



The  
University  
Of  
Sheffield.

# **Efficiency Optimised Control of Interior Permanent Magnet Machine Drives in Electric Vehicle Applications**

---

**Hawa K A Aorith**

---

A thesis submitted for degree of Doctor of Philosophy

Department of Electronic and Electrical Engineering  
University of Sheffield  
Mappin Street, Sheffield, S1 3JD, UK  
August 2014

---

# Acknowledgements

I would like to express my sincere and great appreciation to my supervisor, Professor Jiabin Wang for his guidance, supervision, discussion, and support during the preparation of this work. His supervision indeed helped me to overcome arising problems throughout this research.

I would also convey much gratitude to Dr. Khoa D. Hoang for his assistance in this research. I would also to express much thankfulness to Mr. Panagiotis Lazari who developed the IPMSM motor used in this thesis. Assistance from the technical staffs is gratefully acknowledged for their indispensable help. I owe my deepest gratitude to Mr Andy Race, Mr Richard Garraway, and Mr John Wilkinson for their help on building and testing my experimental test-bed. Without their help, this work may never complete.

Many thanks for my colleagues at the Department of Electronic and Electrical Engineering, the University of Sheffield for their helpful discussions and friendship during my stay at the department.

I am grateful to the Libyan Government for their financial support.

I do feel under obligation to record the word of encouragement from my family and for them a few words of thankfulness would not cover the genuine affection, absolute support, remarkable encouragement and profound prayers especially of my husband Farij and my children, Mariam, Mukhtar and Amaleed. I am thankful to them, without their cooperation, it would have been impossible for me to devote so much of time and attention to this study. Also, I would like to place on record sincere thanks to my parent for her support and encouragement during my study.

# Abstract

The thesis focuses on the losses minimisation of an interior permanent magnet synchronous machine (IPMSM) drive in electric vehicle applications. As drive losses are a combination of the IPMSM losses and the inverter losses, this thesis is mainly divided into two parts: the first part deals with minimising the copper and iron losses of the IPMSM with due account of machine parameters variations and the voltage drop across the stator winding resistance. A new losses minimisation algorithm (LMA) which considers these issues is presented in this research. A comprehensive off-line simulation study based on this LMA is performed in order to evaluate the effect of the parameters variations, resistive voltage drop and iron losses on the IPMSM optimal efficiency operation. It is shown that the parameters variations and resistive voltage drop should be included in the losses minimisation to achieve IPMSM optimal efficiency operation. On the other hand, the minimum losses operation points are not significantly affected by the utilised IPMSM iron losses. The proposed LMA is implemented with non-linear look-up tables (LUTs) using the current commands developed for both constant torque and field weakening operations. Good matching between the simulation and experimental results has been achieved. Reducing the inverter switching losses is the aim of the second part of this PhD research in addition to decrease the common mode voltage (CMV) which may lead to undesirable motor bearing current and electromagnetic interference. A comparative study between up-to-date PWM techniques for CMV reduction with the conventional space vector PWM (SVPWM technique) through simulation studies are presented. Due to its advantages on reducing both the switching losses and CMV of the inverter over all  $(\alpha\beta)$  voltage hexagon modulation regions, the LuPWM technique is selected for the tested IPMSM drive. Firstly, the scalar implementation of this LuPWM technique using the sine triangle waveform modulation technique on a simulation model of a resistor-inductor (R-L) inductive load is validated with sinusoidal current waveforms. However, implementation of the LuPWM in the closed loop control system of the tested IPMSM drive results in a considerable unexpected distortion in the phase current waveforms especially at low demanded torques. A study on this issue shows that due to the unavoidable ripples on the electrical angle position information leading to the malfunction on determining the  $(\alpha\beta)$  voltage hexagon sectors, the sector transition point of the LuPWM pulses especially when the state of the LuPWM pulse is changed between On-state and Off-state is strongly affected. Consequently, the current

waveforms for a closed-loop drive system under the LuPWM technique during the sectors transition period become seriously distorted. In this thesis, the LuPWM current waveforms distortion problem is proposed to be addressed by modifying the pulse pattern of the traditional LuPWM technique around the  $(\alpha\beta)$  voltage hexagon sectors transition points associated with significant current waveforms distortion as aforementioned. Under this proposed PWM technique denoted as Mod-LuPWM technique, the switching state of each LuPWM pulse is suggested to be hold for an optimum small period around each transition period. Hence, the adverse effects of the angular ripple and the voltage error will be evened out between the “Turn-On” and “Turn-Off” transitions. Therefore, sinusoidal current waveforms can be obtained for closed-loop drive system under the proposed Mod-LuPWM. In addition, similar to the traditional LuPWM the Mod-LuPWM technique own the ability of on reducing the peak-to-peak common mode voltage value to one sixth of the DC-link voltage compared with the traditional PWMs. On the other hand, due to its switching characteristics, the switching losses of the drive system under the Mod-LuPWM technique are also reduced by one third during the switching period leading to an increase on the switching device life-time. Furthermore, as its implementation does not require any additional hardware, the proposed Mod-LuPWM can be employed for any existing drive system without any increase in the total drive cost. The proposed Mod-LuPWM has been validated with well-matched between simulation and experimental results showing significant current waveform improvements and considerable CMV reduction.

# Table of Contents

Acknowledgements .....	i
Abstract .....	ii
Table of Contents .....	iv
List of Figures .....	viii
List of Tables .....	xviii
Nomenclature .....	xxi
1. INTRODUCTION .....	1
1.1 Fundamentals of Electrical Vehicles .....	1
1.1.1 EV Requirements .....	3
1.1.2 Overview of Existing EV Drives .....	4
1.1.3 PMSM Drive Control .....	10
1.1.3.1 Inverter .....	11
1.1.3.2 PM BLAC (PMSM) Topologies .....	14
1.1.3.3 High Performance Control Strategies for PMSM Drives .....	16
1.1.3.4 Constant Torque and Flux Weakening Control Techniques .....	19
1.2 Minimisation of PMSM Drive Losses .....	25
1.2.1 Minimisation of Motor Losses .....	26
1.2.2 Minimisation of Inverter Losses .....	31
1.3 Thesis Outlines, Contributions and Publications .....	39
1.3.1 Thesis Aims and Outlines .....	39
1.3.2 Contributions .....	42
1.3.3 Publications .....	43
2. MINIMISATION OF THE INVERTER LOSSES AND REDUCTION OF THE COMMON MODE VOLTAGE .....	45
2.1 Introduction .....	45
2.2 Inverter Common Mode Voltage .....	46
2.3 PWM Strategies for Switching Losses and CMV Reduction .....	47
2.4 Implementation of Switching Losses and Common Mode Voltage Reduction PWM Strategies .....	54
2.5 Simulation Results .....	60
2.6 Summary on Comparison between the Investigated PWM Techniques .....	67
2.7 Chapter Summary .....	69

3.	LOSSES MINIMISATION OF INTERIOR PERMANENT MAGNET MACHINE	71
3.1	Introduction .....	71
3.2	Dynamic Model of IPMSM .....	72
3.2.1	IPMSM in the D-Q Rotating Reference Frame .....	72
3.2.2	Constant Torque and Constant Power Regions of an IPMSM .....	76
3.2.2.1	Current and Voltage Constraints .....	76
3.2.2.2	Constant Torque Control .....	79
3.2.2.3	Constant Power or Flux Weakening Control .....	79
3.3	Non-Linear Parameters of IPMSM .....	80
3.4	Formulation of the Losses Optimisation Problem .....	84
3.4.1	Copper and Iron Losses Models .....	84
3.4.2	Optimisation Function and Constraints .....	86
3.5	Losses Minimisation Process .....	87
3.5.1	Inputs Values of the Proposed LMA .....	87
3.5.1	Losses Minimisation Algorithm (LMA) .....	89
3.6	Off-Line Simulation Results of the LMA .....	89
3.7	Chapter Summary .....	95
4	INFLUENCE OF IPMSM PARAMETERS NONLINEARITY, STATOR RESISTIVE VOLTAGE DROP AND IRON LOSSES ON THE LOSSES MINIMISATION .....	96
4.1	Introduction .....	96
4.2	Influence of Parameters Variations .....	97
4.2.1	Constant Torque Region .....	97
4.2.2	Flux Weakening Region (FWR) .....	104
4.3	Influence of Stator Resistor Voltage Drop .....	108
4.4	Influence of Iron Losses .....	111
4.4.1	Constant Torque Region .....	112
4.4.2	Flux Weakening Region .....	121
4.5	Chapter Summary .....	124
5	IPMSM CONTROL BASED ON THE LOSSES MINIMISATION ALGORITHM	126
5.1	Introduction .....	126
5.2	IPMSM Control Scheme .....	127
5.3	Generation of Non-Linear Look Up Tables .....	128

5.3.1	Selection of Torque and Speed Operating Points .....	129
5.3.2	Generation of Base Flux, D-Axis and Q-Axis Currents LUTs .....	129
5.4	Simulation Results .....	134
5.3.3	Simulation Results with SVPWM Technique .....	136
5.3.4	LuPWM Simulation Results, Identified Switching Problems and Proposed Solutions.....	144
5.3.4.1	Proposed solution of the LuPWM current waveform distortion.....	153
5.3.4.2	Simulation results of the Mod-LuPWM .....	160
5.3.5	Comparative Simulation Study of SVPWM, LuPWM and Mod-LuPWM 162	
5.5	Chapter Summary .....	170
6	EXPERIMENTAL VALIDATION .....	172
6.1	Introduction .....	172
6.2	Hardware of the Experimental Work .....	172
6.2.1	Inverter .....	173
6.2.2	PWM Control Signals Dead Time and Inversion Board.....	177
6.2.3	Voltage and Current Transducers.....	178
6.2.4	Inverter Power and Control Circuits .....	180
6.2.5	Encoder.....	184
6.2.6	dSPACE Control System .....	187
6.3	Experimental Results .....	194
6.3.1	Constant Torque and Flux Weakening Experimental Results .....	194
6.3.2	Experimental Comparative Study of SVPWM and Mod-LuPWM Techniques .....	205
6.3.3	Comparison of Simulated And Experimental Power Losses .....	219
6.3.3.1	Constant and Flux Weakening Region .....	219
6.3.3.2	Inverter Losses with SVPWM and LuPWM Techniques .....	223
6.4	Chapter summary.....	230
7	CONCLUSION AND FUTURE WORK .....	232
7.1	Conclusion.....	232
7.2	Future Works .....	236
	Appendix A: Experimental Set Up.....	238
A.1.	Isolated Interface Layout .....	238
A.2.	Layout of The CT's And VT's Measuring Board .....	238

A.3. PWM Dead Time and Inversion Boards .....	238
A.4. dSPACE ADC to Simulink Interface BLOCKS .....	238
Appendix B: Additional Experimental Results .....	242
B.1. Encoder Signals .....	242
B.2. Inductive Load Results with SVPWM .....	243
B.3. IPMSM Drive Results with SPWM Technique .....	244
B.4. IPMSM Drive Results with Negative Torque .....	245
Appendix C: LuPWM implementation .....	247
References .....	249



# List of Figures

Figure 1.1 Schematic of all-EVs power trains [3].	2
Figure 1.2 A battery pack of Toyota Prius 2004 [4].	2
Figure 1.3 Typical torque-speed and power-speed characteristics of electrical motor drives in EVs [3, 8].	3
Figure 1.4 Configuration of the EV drives [9].	5
Figure 1.5 Configuration of common electrical machine dedicated for EV drives [8]. (a) DC motor. (b) IM. (c) PM BL motor. (d) SRM.	6
Figure 1.6. Torque-speed characteristics of the PM BL drives (a) with and without control (b) BLAC versus BLDC [9].	8
Figure 1.7. Theoretical waveforms of PM BL operations. (a) BLAC (b) BLDC[9].	8
Figure 1.8 EV drives applications in the automotive industry [8].	9
Figure 1.9 Evaluation of the EV drive systems [8].	10
Figure 1.10 Six-switch three-phase voltage source inverter fed PM BLAC machine [12].	11
Figure 1.11 Principles of PWM for three-phase bridge inverter.	12
Figure 1.12 Implementation of the PWM technique [16, 17]	13
Figure 1.13 Scalar implementation of PWM with the injection of zero sequence signal [16, 17].	13
Figure 1.14 SVPWM voltage space vectors [18].	14
Figure 1.15 Rotor configuration studied for: a) SPMSM; b) IPMSM.	15
Figure 1.16 PMSM in a) stationary $\alpha\beta$ reference frame b) in rotational $dq$ reference frame [12].	16
Figure 1.17 Block diagrams of PM BL Control systems [9]. (a) FOC. (b) DTC. (c) AIC. (d) PSC.	18
Figure 1.18 FOC based PM BLAC machine drive for MTPA control [32].	20
Figure 1.19 Optimum current profile of SPMSM under MTPA and FW operations [12, 20].	22
Figure 1.20 Optimum current profile of IPMSM under MTPA and FW operations [12, 20].	23

Figure 1.21 Block diagram of FF- FW control system of PMSM [19].	24
Figure 1.22 Block diagram of FB- FW control system of PMSM [19].	24
Figure 1.23 Block diagram of FF- FW and FB-FW control system of PMSM [56].	25
Figure 1.24 Optimal vector controlled of SPMSM [57, 58].	27
Figure 1.25 Optimal vector controlled of IPMSM [57, 58]	28
Figure 1.26 Equivalent circuit: a) SPMSM; b) $dq$ -axis of IPMSM [57, 58].	29
Figure 1.27 CMV of a VSI fed three phase load [12].	32
Figure 1.28 Switching pattern and peak-to-peak CMV of a VSI with SVPWM [75].	32
Figure 1.29 Modulation waveforms of (a) CPWM (b) DCPWM [17].	34
Figure 1.30 Space vector PWM (a) Reference voltage within SV hexagon, b) Constructing of $V_{com}$ vector [78].	35
Figure 1.31 Switching pattern and peak-to-peak CMV of a VSI with NSPWM [75].	36
Figure 1.32 Switching pattern and peak-to-peak CMV of a VSI with (a) SVPWM (b) AZPWM1 [75].	36
Figure 1.33 Switching pattern and Peak-to-peak CMV of a VSI with (a) AZPWM2 (b) RSPWM3 [75].	37
Figure 1.34 Modulation region of NSPWM [79].	38
Figure 1.35 Switching pattern and peak-to-peak CMV of a VSI with LuPWM [79]. (a) L-region. (b) H-region.	39
Figure 2.1 Voltage source inverter (VSI) connected to PM BLAC [12].	47
Figure 2.2 Space vector hexagon formed by the two zero vectors ( $V_0$ and $V_7$ ) and the six active vectors ( $V_1$ to $V_6$ ) [78].	48
Figure 2.3 Switching sequence and generated CMV of (a) SVPWM and (b) AZPWM1 [75].	49
Figure 2.4 Voltage vector and the definitions of A- and B- sectors of the studied PWMs [75].	50
Figure 2.5 Space vector hexagon with the definition of high and low modulation regions [76, 80, 83].	51
Figure 2.6 Switching sequence and produced CMV of (a) NSPWM (b) LuPWM L-region (c) LuPWM H-region [75, 76, 80, 83].	52
Figure 2.7 Scalar implementation of PWM with the injection of zero sequence signal $V_o$ [17].	55
Figure 2.8 Modulation waveforms of SVPWM and AZPWM1.	56

Figure 2.9 Modulation waveforms of LuPWM in $L$ -region.....	57
Figure 2.10 Modulation waveforms of NSPWM and LuPWM in $H$ -region.....	57
Figure 2.11 Scalar implementation of LuPWM (a) $L$ -region (b) $H$ -region.....	58
Figure 2.12 PWMs under study phase “a” voltage in $L$ -region. ....	61
Figure 2.13 PWMs under study phase “a” voltage in $L$ -region .....	62
Figure 2.14 PWMs under study phase “a” current in $L$ -region. ....	63
Figure 2.15 PWMs under study phase “a” current in $H$ -region. ....	64
Figure 2.16 Phase “a” voltage FFT analysis of PWMs under study in $L$ -region. ....	64
Figure 2.17 Phase “a” voltage FFT analysis of PWMs under study in $H$ -region. ....	65
Figure 2.18 PWMs under study peak to peak CMV in $L$ -region. ....	65
Figure 2.19 PWMs under study peak to peak CMV in $H$ -region.....	66
Figure 2.20 Modulation waveforms and phase “a” inverter output of SVPWM. ....	66
Figure 2.21 Modulation waveforms and phase “a” inverter output of LuPWM. ....	67
Figure 2.22 Voltage linearity of the PWM techniques under study [75]. ....	68
Figure 3.1 PMOB IPMSM topology. ....	77
Figure 3.2 Maximum torque-per-ampere current vector trajectory and voltage limited maximum-output current vector trajectory for the IPMSM [20]. ....	78
Figure 3.3 Variations of d-axis flux linkage $\lambda_d$ with $i_d$ and $i_q$ .....	82
Figure 3.4 Variations of q-axis flux linkage $\lambda_q$ with $i_d$ and $i_q$ .....	82
Figure 3.5 Variations of q-axis inductance $L_q$ with $i_q$ at constant $i_d$ .....	83
Figure 3.6 Variations of d-axis inductance $L_d$ with $i_d$ at constant $i_q$ .....	83
Figure 3.7 Variations of flux linkage $\lambda_m$ with $i_q$ at $i_d = 0$ . ....	84
Figure 3.8 Phasor diagram of PMSM relating to field weakening operation [81, 82]....	86
Figure 3.9 Torque-speed profile of IPMSM drive. ....	88
Figure 3.10 Flowchart of losses minimisation algorithm (LMA). ....	90
Figure 3.11 Variations of losses with $i_d$ and $T_d$ at $\omega_m = 200rpm$ obtained by the LMA. ....	91
Figure 3.12 Variations of losses with $i_d$ and $T_d$ at $\omega_m = 1350rpm$ obtained by the LMA. .....	92

Figure 3.13 Variations of losses $i_q$ with $i_d$ and $T_d$ at $\omega_m = 200$ and $1350rpm$ obtained by the LMA. ....	92
Figure 3.14 Resultant minimum losses variations with $\omega_m$ and $T_e$ obtained by the LMA. ....	93
Figure 3.15 Variations of losses with $i_d$ and $T_d$ at $\omega_m = 2000rpm$ obtained the LMA. ...	93
Figure 3.16 Variations of losses with $i_d$ and $T_d$ at $\omega_m = 3000rpm$ obtained the LMA. ...	94
Figure 3.17 Variations of losses with $i_d$ and $T_d$ at $\omega_m = 4000rpm$ obtained the LMA. ...	94
Figure 4.1 Variations of losses with $i_d$ and $T_d$ at $\omega_m = 200rpm$ obtained with linear (constant) and non-linear (varying) parameters. ....	98
Figure 4.2 Variations of losses with $i_d$ and $T_d$ at $\omega_m = 1350rpm$ obtained with linear (constant) and non-linear (varying) parameters. ....	99
Figure 4.3 Variations of $i_q$ with $i_d$ and $T_d$ at $\omega_m = 200rpm$ obtained with linear (constant) and non-linear (varying) parameters. ....	101
Figure 4.4 Variations of $i_q$ with $i_d$ and $T_d$ at $\omega_m = 1350rpm$ obtained with linear (constant) and non-linear (varying) parameters. ....	102
Figure 4.5 Resultant minimum losses variations with $\omega_m$ and $T_d$ obtained from linear (constant) parameters. ....	103
Figure 4.6 Resultant minimum losses variations with $\omega_m$ and $T_d$ obtained from non-linear (variable) parameters. ....	103
Figure 4.7 Resultant minimum losses differences variations with $\omega_m$ and $T_d$ obtained from linear (variable) and non-linear (constant). ....	104
Figure 4.8 Variations of losses with $i_d$ and $T_d$ at $\omega_m = 2000rpm$ obtained with linear (constant) and non-linear (varying) parameters. ....	105
Figure 4.9 Variations of losses with $i_d$ and $T_d$ at $\omega_m = 3000rpm$ obtained with linear (constant) and non-linear (varying) parameters. ....	107
Figure 4.10 Variations of losses with $i_d$ and $T_d$ at $\omega_m = 4000rpm$ obtained with linear (constant) and non-linear (varying) parameters. ....	107
Figure 4.11 Variations of losses with $i_d$ and $T_d$ at $\omega_m = 2000rpm$ obtained with and without $V_R$ . ....	109
Figure 4.12 Variations of losses with $i_d$ and $T_d$ at $\omega_m = 3000rpm$ obtained with and without $V_R$ . ....	110
Figure 4.13 Variations of losses with $i_d$ and $T_d$ at $\omega_m = 4000rpm$ obtained with and without $V_R$ . ....	111
Figure 4.14 Variations of losses with $i_d$ and $T_d$ at $\omega_m = 200rpm$ obtained with and without considering iron losses. ....	113

Figure 4.15 Variations of losses with $i_d$ and $T_d$ at $\omega_m = 1350rpm$ obtained with and without considering iron losses. ....	114
Figure 4.16 Variations of $i_q$ with $i_d$ and $T_d$ at $\omega_m = 200rpm$ obtained with considering and not considering iron losses in total losses. ....	116
Figure 4.17 Variations of $i_q$ with $i_d$ and $T_d$ at $\omega_m = 1350rpm$ obtained with considering and not considering iron loss in total losses. ....	116
Figure 4.18 Variations of iron losses with $i_d$ and $T_d$ at $\omega_m = 200rpm$ .....	117
Figure 4.19 Variations of total losses $P_t$ and copper loss $P_{cu}$ with $i_d$ and $T_d$ at $\omega_m = 200rpm$ . ....	118
Figure 4.20 Variations of iron losses with $i_d$ and $T_d$ at $\omega_m = 1350rpm$ . ....	118
Figure 4.21 Variations of total losses $P_t$ and copper losses $P_{cu}$ with $i_d$ and $T_d$ at $\omega_m = 1350rpm$ . ....	119
Figure 4.22 Resultant total minimum power losses variation with $\omega_m$ and $T_d$ obtained when iron losses is considered. ....	119
Figure 4.23 Resultant total minimum power losses variation with $\omega_m$ and $T_e$ obtained when iron losses is neglected. ....	120
Figure 4.24 Differences between total minimum power losses with and without considering iron losses .....	120
Figure 4.25 Variations of losses with $i_d$ and $T_d$ at $\omega_m = 2000rpm$ obtained with and without iron losses. ....	122
Figure 4.26 Variations of losses with $i_d$ and $T_d$ at $\omega_m = 3000rpm$ obtained with and without iron losses. ....	122
Figure 4.27 Variations of losses with $i_d$ and $T_d$ at $\omega_m = 4000rpm$ obtained with and without iron losses. ....	123
Figure 5.1 Schematic of IPMSM drive based on non-linear lookup tables generated by LMA [51]. ....	128
Figure 5.2 Input speed and torque for selected operating points $(\omega_m, T_d)$ of the IPMSM. ....	130
Figure 5.3 Variations of $i_q$ with $i_d$ and $T_d$ . ....	131
Figure 5.4 Variations and limitation of $\lambda_{dq}$ with $i_d$ and $T_d$ . ....	132
Figure 5.5 Look-up tables of variations of $i_d$ with $\lambda_{dq}$ and $T_d$ . ....	133
Figure 5.6 Look-up tables of variations of $i_q$ with $\lambda_{dq}$ and $T_d$ . ....	133
Figure 5.7 Look-up table of variations of $\lambda_{base}$ with $T_d$ .....	134
Figure 5.8 Torque and speed steady state response at $\omega_m = 1350rpm$ and $T_d = 35Nm$ . ....	136

Figure 5.9 $i_d$ and $i_q$ currents steady state response at $\omega_m = 1350rpm$ and $T_d = 35Nm$ ..	137
Figure 5.10 Phase currents response at $\omega_m = 1350rpm$ and $T_d = 35Nm$ .....	137
Figure 5.11 Torque and speed steady state response at $\omega_m = 1350rpm$ and $T_d = 60Nm$ .....	138
Figure 5.12 $i_d$ and $i_q$ currents response at $\omega_m = 1350rpm$ and $T_d = 60Nm$ .....	138
Figure 5.13 Phase currents response at $\omega_m = 1350rpm$ and $T_d = 60Nm$ .....	139
Figure 5.14 $i_d$ and $i_q$ currents response at $\omega_m = 1350rpm$ and $T_d$ varied from 10 to 60Nm .....	140
Figure 5.15 Torque response at $\omega_m = 1350rpm$ and $T_d$ varied from 10 to 60Nm .....	140
Figure 5.16 Phase current response at $\omega_m = 1350rpm$ and $T_d$ varied from 10 to 60Nm .....	141
Figure 5.17 $i_d$ and $i_q$ currents response at $\omega_m = 2000rpm$ and $T_d$ varied from 10 to 40Nm .....	141
Figure 5.18 Torque response at $\omega_m = 2000rpm$ and $T_d$ varied from 10 to 40Nm .....	142
Figure 5.19 $i_d$ and $i_q$ currents response at $\omega_m = 3000rpm$ and $T_d$ varied from 10 to 20Nm .....	142
Figure 5.20 Torque response at $\omega_m = 3000rpm$ and $T_d$ varied from 10 to 20Nm .....	143
Figure 5.21 $i_d$ and $i_q$ currents response at $\omega_m = 4000rpm$ and $T_d = 10Nm$ .....	143
Figure 5.22 Torque and speed response at $\omega_m = 4000rpm$ and $T_d = 10Nm$ .....	144
Figure 5.23 LuPWM phase current response at $\omega_m = 600rpm$ and $T_d = 10Nm$ .....	145
Figure 5.24 LuPWM $i_d$ and $i_q$ currents response at $\omega_m = 600rpm$ and $T_d = 10Nm$ .....	146
Figure 5.25 LuPWM torque response at $\omega_m = 600rpm$ and $T_d = 10Nm$ .....	146
Figure 5.26 LuPWM phase current response at $\omega_m = 600rpm$ and $T_d = 10Nm$ for one hexagon period. ....	147
Figure 5.27 Switching sequence of LuPWM and SVPWM .....	148
Figure 5.28 Fluctuation of sectors transition point in LuPWM (low region) .....	149
Figure 5.29 LuPWM electrical angle ripple .....	149
Figure 5.30 SVPWM phase current response at $\omega_m = 600rpm$ and $T_d = 10Nm$ .....	150
Figure 5.31 SVPWM $i_d$ and $i_q$ currents response at $\omega_m = 600rpm$ and $T_d = 10Nm$ .....	151
Figure 5.32 SVPWM torque response at $\omega_m = 600rpm$ and $T_d = 10Nm$ .....	151
Figure 5.33 SVPWM phase current response at $\omega_m = 600rpm$ and $T_d = 10Nm$ .....	152

Figure 5.34 Fluctuation of sectors transition point in SVPWM (low region).....	152
Figure 5.35 LuPWM phase current response at $\omega_m = 600rpm$ and $T_d = 10Nm$ without dead time .....	153
Figure 5.36 Linear and Non-linear regions of the LuPWM. ....	154
Figure 5.37 LuPWM and SVPWM in H-region at $\omega_m = 1000rpm$ and $T_d = 10Nm$ ....	155
Figure 5.38 LuPWM and Mod-LuPWM switching pattern in low region.....	156
Figure 5.39 Variations of the distortion angle with the modulation index in sector 5 ..	159
Figure 5.40 Mod-LuPWM phase current response at $\omega_m = 600rpm$ and $T_d = 10Nm$ ....	160
Figure 5.41 Mod-LuPWM $i_d$ and $i_q$ currents response at $\omega_m = 600rpm$ and $T_d = 10Nm$	161
Figure 5.42 Mod-LuPWM Torque response at $\omega_m = 600rpm$ and $T_d = 10Nm$ .....	161
Figure 5.43 $i_a$ current of the studied PWMs at $\omega_m = 600rpm$ and $T_d = 40Nm$ .....	163
Figure 5.44 $i_d$ and $i_q$ currents of the studied PWMs at $\omega_m = 600rpm$ and $T_d = 40Nm$ ...	163
Figure 5.45 Torque response of studied PWMs at $\omega_m = 600rpm$ and $T_d = 40Nm$ .....	164
Figure 5.46 CMV of studied PWMs at $\omega_m = 600rpm$ and $T_d = 40Nm$ .....	164
Figure 5.47 Phase voltage harmonic of studied PWMs at $\omega_m = 600rpm$ and $T_d = 40Nm$ .....	165
Figure 5.48 Phase current harmonic of the studied PWMs at $\omega_m = 600rpm$ and $T_d = 40Nm$ .....	165
Figure 5.49 Phase current harmonic of studied PWMs at $\omega_m = 600rpm$ and $T_d = 40Nm$ .....	167
Figure 5.50 $i_a$ current of the studied PWMs at $\omega_m = 1000rpm$ and $T_d = 35Nm$ .....	167
Figure 5.51 $i_d$ and $i_q$ currents of the studied PWMs at $\omega_m = 1000rpm$ and $T_d = 35Nm$ .	168
Figure 5.52 Torque response of the PWMs at $\omega_m = 1000rpm$ and $T_d = 35Nm$ .....	168
Figure 5.53 CMV of the studied PWMs at $\omega_m = 1000rpm$ and $T_d = 35Nm$ .....	169
Figure 5.54 Phase voltage harmonics of studied PWMs at $\omega_m = 1000rpm$ and $T_d = 35Nm$ .....	169
Figure 5.55 Phase current harmonics of the studied PWMs at $\omega_m = 1000rpm$ and $T_d = 35Nm$ .....	170
Figure 6.1 Experimental setup of the IPMSM drive. ....	174
Figure 6.2 PM300CA060 situated on a heat sink. ....	175

Figure 6.3 Intelligent power module interface BP7B-LB. ....	176
Figure 6.4 The DC link voltage power supply. ....	177
Figure 6.5 Developed drive system for IPMSM drive. ....	178
Figure 6.6 PWM dead time and inversion circuit for upper switch of phase “a”. ....	179
Figure 6.7 (a) Current transducers scaling circuits, (b) Voltage transducer scaling circuit. ....	179
Figure 6.8 First-order unity-gain low-pass-filter. ....	180
Figure 6.9 Power circuit of the inverter .....	181
Figure 6.10 Control circuit of the inverter. ....	182
Figure 6.11 Control circuit of DC link capacitor power dissipation resistor. ....	183
Figure 6.12 sine and cosine encoder signals. ....	184
Figure 6.13 Block diagram of the utilised PLL. ....	185
Figure 6.14 LUT of the electrical angular position offset. ....	186
Figure 6.15 Final resultant electrical angular position after adding the delay offset. ..	187
Figure 6.16 Alignment of back-emf of phase <i>a</i> with the electrical angular position. ...	188
Figure 6.17 Control Algorithm of the IPMSM drive under torque control mode. ....	190
Figure 6.18 dSPACE Real-Time Control Desk. ....	191
Figure 6.19 Connection between IPMSM, inverter, AVL dynamometer. ....	191
Figure 6.20 Torque transducer and coupling. ....	192
Figure 6.21 Torque waveform and power analyser displays. ....	192
Figure 6.22 Torque transducer display. ....	193
Figure 6.23 Connections between dSPACE, encoder and inverter. ....	193
Figure 6.24 Torque and speed steady state response at $\omega_m = 1350rpm$ and $T_d = 35Nm$ .....	196
Figure 6.25 $i_d$ and $i_q$ currents steady state response at $\omega_m = 1350rpm$ and $T_d = 35Nm$	196
Figure 6.26 Phase currents response at $\omega_m = 1350rpm$ and $T_d = 35Nm$ .....	197
Figure 6.27 Torque and speed steady state response at $\omega_m = 1350rpm$ and $T_d = 60Nm$ .....	197
Figure 6.28 $i_d$ and $i_q$ currents response at $\omega_m = 1350rpm$ and $T_d = 60Nm$ .....	198



Figure 6.29 Phase currents response at $\omega_m = 1350rpm$ and $T_d = 60Nm$ .....	198
Figure 6.30 $i_d$ and $i_q$ currents response at $\omega_m = 1350rpm$ and $T_d$ varied from 10 to 60Nm .....	199
Figure 6.31 Torque response at $\omega_m = 1350rpm$ and $T_d$ varied from 10 to 50Nm .....	199
Figure 6.32 Phase current response at $\omega_m = 1350rpm$ and $T_d$ varied from 10 to 50Nm .....	200
Figure 6.33 MTPA to FW line for $V_{dc} = 120V$ .....	201
Figure 6.34 $i_d$ and $i_q$ currents and torque response at $\omega_m = 2000rpm$ and $T_d = 10Nm$ ..	202
Figure 6.35 $i_d$ and $i_q$ currents and torque response at $\omega_m = 2000rpm$ and $T_d = 20Nm$ ..	202
Figure 6.36 $i_d$ and $i_q$ currents and torque response at $\omega_m = 2000rpm$ and $T_d = 30Nm$ ..	203
Figure 6.37 Phase currents at $\omega_m = 2000rpm$ and $T_d = 10 Nm, 20 Nm$ and $30Nm$ .....	203
Figure 6.38 $i_d$ and $i_q$ currents and torque response at $\omega_m = 3000rpm$ and $T_d = 10Nm$ ..	204
Figure 6.39 $i_d$ and $i_q$ currents and torque response at $\omega_m = 3000rpm$ and $T_d = 20Nm$ ..	204
Figure 6.40 Phase currents at $\omega_m = 3000rpm$ and $T_d = 10 Nm$ and $20Nm$ .....	205
Figure 6.41 Voltage and current phases of the inductive load with LuPWM in the $L$ -region .....	206
Figure 6.42 Voltage and current phases of the inductive load with LuPWM in the $H$ -region .....	207
Figure 6.43 Electrical angular position generated by the Simulink repeating sequence block for open loop test with inductive load. ....	208
Figure 6.44 Phase currents of LuPWM and Mod-LuPWM at $\omega_m = 200rpm$ and $T_d = 10Nm$ .....	209
Figure 6.45 DC link current of LuPWM at $\omega_m = 200rpm$ and $T_d = 10Nm$ .....	210
Figure 6.46 Torque response of LuPWM and Mod-LuPWM at $\omega_m = 200rpm$ and $T_d = 10Nm$ .....	210
Figure 6.47 $i_a$ phase current of SVPWM and Mod-LuPWM at $\omega_m = 600rpm$ and $T_d = 40Nm$ .....	211
Figure 6.48 $i_d$ and $i_q$ currents of SVPWM and Mod-LuPWM at $\omega_m = 600rpm$ and $T_d = 40Nm$ .....	211
Figure 6.49 Torque response of SVPWM and Mod-LuPWM at $\omega_m = 600rpm$ and $T_d = 40Nm$ .....	212
Figure 6.50 Simulation (Sim.) and experimental (Exp.) phase voltage harmonic of SVPWM and Mod-LuPWM at $\omega_m = 600rpm$ and $T_d = 40Nm$ .....	212

Figure 6.51 Simulation (Sim.) and experimental (Exp.) phase current harmonic of SVPWM and Mod-LuPWM at $\omega_m = 600rpm$ and $T_d = 40Nm$ .....	213
Figure 6.52 CMV of SVPWM and Mod-LuPWM at $\omega_m = 600rpm$ and $T_d = 40Nm$ ....	213
Figure 6.53 $i_a$ phase current of SVPWM and Mod-LuPWM at $\omega_m = 1000rpm$ and $T_d = 35Nm$ .....	214
Figure 6.54 $i_d$ and $i_q$ currents of SVPWM and Mod-LuPWM at $\omega_m = 1000rpm$ and $T_d = 35Nm$ .....	215
Figure 6.55 Torque response of SVPWM and Mod-LuPWM at $\omega_m = 1000rpm$ and $T_d = 35Nm$ .....	215
Figure 6.56 CMV of SVPWM and Mod-LuPWM at $\omega_m = 1000rpm$ and $T_d = 35Nm$ ..	216
Figure 6.57 Simulation (Sim.) and experimental (Exp.) phase voltage harmonic of SVPWM and Mod-LuPWM at $\omega_m = 1000rpm$ and $T_d = 35Nm$ .....	216
Figure 6.58 Simulation (Sim.) and experimental (Exp.) phase current harmonic of SVPWM and Mod-LuPWM at $\omega_m = 1000rpm$ and $T_d = 35Nm$ .....	217
Figure 6.59 Phase voltage, phase current and torque waveforms of SVPWM $\omega_m = 600rpm$ and $T_d = 40Nm$ .....	217
Figure 6.60 Phase voltage, phase current and torque waveforms of Mod-LuPWM $\omega_m = 600rpm$ and $T_d = 40Nm$ .....	218
Figure 6.61 Phase voltage, phase current and torque waveforms of Mod-LuPWM $\omega_m = 1000rpm$ and $T_d = 35Nm$ .....	218
Figure 6.62 Phase voltage, phase current and torque waveforms of Mod-LuPWM $\omega_m = 1000rpm$ and $T_d = 35Nm$ .....	219
Figure 6.63 MTPA to FW line for $V_{dc} = 80V$ .....	222
Figure 6.64 Determining of the initial voltage and resistance values from the graph of (a) Transistor (b) Diode [73]. .....	225
Figure A. 1 Isolated interface layout model BP7B-LB. ....	239
Figure A. 2 Complete circuit of the PWM signals dead time and inversion board. ....	240
Figure A. 3 CTs and VTs scaling measuring board. ....	240
Figure A. 4 dSPACE Simulink interface blocks (a) input signal (b) PWM signals. ....	241
Figure B. 1 Encoder sin and cos signals. ....	242
Figure B. 2 Electrical and mechanical position calculated by the PLL. ....	242
Figure B. 3 Alignment of back-emf phase “a” with the electrical angle. ....	243

Figure B. 4 Voltage and current phases of the inductive load with SVPWM in the $L$ -region.....	243
Figure B. 5 Voltage and current phases of the inductive load with LuPWM in the $H$ -region.....	244
Figure B. 6 $i_d$ and $i_q$ current waveforms of the IPMSM drive with SPWM.....	244
Figure B. 7 Torque waveforms of the IPMSM drive with SPWM. ....	245
Figure B. 8 $i_d$ and $i_q$ current of the IPMSM drive with SVPWM.....	245
Figure B. 9 Negative torque waveforms of the IPMSM drive with SVPWM. ....	246
Figure C. 1 Phase $a$ , $b$ and $c$ inverter legs output voltages, and sector transition.....	247
Figure C. 2 Switching of low region sector 1 to 6 .....	248
Figure C. 3 Switching of high region sector 1 to 6 .....	248

## List of Tables

Table 1.1 Comparison of PM BL control strategies.....	19
Table 1.2 Switching states of three phase inverter .....	35
Table 2.1 Switching sequence of AZPWM1, NSPWM and LUPWM [75].....	53
Table 2.2 Dependency of the selected triangular waveforms on sector number .....	59
Table 2.3 Comparison of SVPWM, AZPWM1, NSPWM and LuPWM [75] .....	68
Table 3.1 Parameters of IPMSM drive.....	78
Table 3.2 Parameters of iron losses model.....	85
Table 3.3 Input operating point to LMA .....	88
Table 3.4 Resultant MTPA trajectories at 200 and 1350rpm.....	91
Table 4.1 Resultant linear and non-linear optimal ( $i_d, P_t$ ) at 200rpm.....	99
Table 4.2 Resultant linear and non-linear optimal ( $i_d, P_t$ ) at 1350rpm.....	100
Table 4.3 Resultant linear and non-linear optimal $i_q$ .....	102
Table 4.4 Resultant linear and non-linear optimal ( $i_d, P_t$ ) at 2000rpm.....	106
Table 4.5 Resultant linear and non-linear optimal ( $i_d, P_t$ ) at 3000rpm.....	106
Table 4.6 Resultant linear and non-linear optimal ( $i_d, P_t$ ) at 4000rpm.....	108

Table 4.7 Resultant linear and non-linear optimal $i_q$ .....	108
Table 4.8 Optimal solution $(i_d, P_t)$ with and without $VR$ $(i_d, P_t)$ at 2000rpm.....	109
Table 4.9 Optimal solution $(i_d, P_t)$ with and without $VR$ $(i_d, P_t)$ at 3000rpm.....	109
Table 4.10 Optimal solution $(i_d, P_t)$ with and without $VR$ at 4000rpm .....	110
Table 4.11 Resultant linear and non-linear optimal $i_q$ .....	110
Table 4.12 Optimal solution $(i_d, P_t)$ with and without $P_{fe}$ at 200rpm.....	112
Table 4.13 Optimal solution $(i_d, P_t)$ with and without $P_{fe}$ at 1350rpm.....	113
Table 4.14 Resultant optimal $i_q$ with and without $P_{fe}$ .....	115
Table 4.15 Variations of $P_{fe}$ , $P_{cu}$ and $P_t$ with $t_d$ and $\omega_m$ .....	115
Table 4.16 Optimal solution $(i_d, P_t)$ with and without $P_{fe}$ at 2000rpm.....	121
Table 4.17 Optimal solution $(i_d, P_t)$ with and without $P_{fe}$ at 3000rpm.....	121
Table 4.18 Optimal solution $(i_d, P_t)$ with and without $P_{fe}$ at 4000rpm.....	123
Table 4.19 Resultant optimal $i_q$ with and without $P_{fe}$ .....	124
Table 4.20 Variations of $P_{fe}$ , $P_{cu}$ and $P_t$ with $T_d$ and $\omega_m$ .....	124
Table 5.1 Parameters of IPMSM drive .....	135
Table 5.2 Sector transition point and distorted phase .....	150
Table 5.3 Calculated distortion angle in each sector at $m_a = 0.7$ .....	158
Table 5.4 LuPWM and Mod-LuPWM pulse pattern selection .....	159
Table 6.1 PM300CA060/DC-AC inverter specifications .....	176
Table 6.2 Gains of the phase locked loop PI controller .....	185
Table 6.3 Experimental results of the IPMSM drive in CT and FW regions .....	220
Table 6.4 Simulation and experimental results of IPMSM drive power losses $P_t$ .....	221
Table 6.5 Experimental results of the IPMSM drive in CTR and FWR .....	222
Table 6.6 Simulation and experimental results of the IPMSM drive total power losses $P_t$ .....	222
Table 6.7 Simulation and experimental results of the IPMSM drive total power losses $P_t$ at 120VDC.....	228
Table 6.8 Experimental results of the inverter losses, IPMSM power losses and the IPMSM drive power losses at 120VDC .....	228

Table 6.9 Simulation and predicted results of the studied IPMSM total power losses $P_t$ at 120VDC and 600VDC .....	229
---	-----

# Nomenclature

AIC	Artificial intelligent control	
AZPWM1,2,3	Active zero state PWM 1, 2 and 3	
ADC	Analogue to digital converter	
$a_h, a_j, b_h, b_j$	Hysteresis and eddy current losses coefficients	
$B$	Viscous friction coefficient	N.m.s
CTR	Constant torque region	
CPR	Constant power region	
CMV	Common mode voltage	V
CMC	Common mode current	A
CPWM	Continuous PWM	
$C_{dc}$	DC-link capacitive filter	F
CT VT	Current and voltage transducers	
$\cos(\varphi)$	Power factor	
DC	Direct current	
DTC	Direct torque control	
DPWM	Discontinuous PWM	
$d_{max}$	Maximum duty cycle	
EV	Electrical vehicles	
EMF	Electromagnetic force	
$E_{onT}, E_{onD}$	Turn-on energy losses of the IGBT and diode	J
$E_{offT}, E_{offD}$	Turn-off energy losses of the IGBT and diode,	J
$E_{onTref}, E_{offTref}$	Typical turn-on and turn-off energy values,	J
FW	Flux weakening control	
FF-FW	Feed-forward control FW control	
FB-FW	Feed-back control FW control	

FFT	Fast Fourier transform	
FEM	Finite element method	
FWR	Flux weakening region	
FOC	Field oriented control	
$f_s$	Fundamental frequency	Hz
$f_c$	Carrier frequency	Hz
$f_{sw}$	Switching frequency	Hz
$\phi_1$	Magnetizing flux component	Wb
$\phi_2$	Demagnetizing flux component	Wb
HEV	Hybrid electrical vehicles	
$H$ -region	High modulation region of $\alpha\beta$ voltage hexagon	
$I_a$	Armature current	A
$i_d^*, i_q^*$	Direct and quadrature axis demand current components	
$i_{d,q}$	dq-axis currents	A
ICE	Internal combustion engine	
IM	Induction motor	
IPMSM	Interior Permanent magnet synchronous motor	
IGBT	Insulated-gate bipolar transistors	
$I_{cav}, I_{Dav},$	IGBT and diode average currents	A
$I_{Crms}, I_{Drms}$	IGBT and diode root mean square values currents	A
$I_{in}$	Input current	A
$I_o$	Peak output current	A
$I_{am}$	Maximum current	A
$I_{ref}$	Maximum current of the utilised intelligent power module	A
$i_{a,b,c}$	Phase a, b, c stator currents	A
$J$	Moment of inertia.	Kg.m <sup>2</sup>
$k_{id}, k_{iq}$	d- and q-axis current controller integral terms	

$k_{id}, k_{iq}$	d- and q-axis current controller proportional terms	
$k_{pdave}, k_{pqave}$	d- and q-axis current controller average proportional terms	
$L_d, L_q$	Direct and quadrature axis inductances	$mH$
$L_{dmin}, L_{qmin}$	d- and q-axis minimum inductances	$mH$
$L_{dmax}, L_{qmax}$	d- and q-axis maximum inductances	$mH$
$L_{dave}, L_{qave}$	d- and q-axis average inductances	$mH$
$L_{dqave}$	d- and q-axis total average inductances	$mH$
LMC	Losses model controllers	
LUT	Look up table	
$L$ -region	Low modulation region of $\alpha\beta$ voltage hexagon	
LMA	Losses minimisation algorithm	
$L_{aa}, L_{bb}, L_{cc}$	Phase a, b, c stator self-inductances	H
Mod-LuPWM	Modified Lu PWM	
$L, M$	Self-inductance and mutual inductance average value	H
$L_2, M_2$	Self-inductance and mutual inductance with considering the saliency effect	H
$m_a$	Modulation index	
$M_{ab}, M_{ac}, M_{ba}, M_{bc}, M_{ca}, M_{cb}$	Mutual inductances	H
MTPA	Maximum torque per ampere	
$n$	Alpha-beta ( $\alpha\beta$ ) voltage hexagon sector number	
NSPWM	Near state PWM	
$P_{cu}$	Copper losses	W
RCMV-PWM	CMV reduction PWM techniques	
$P_{CT/D}$	Conduction losses of IGBT and diode	W
$P_{inp}$	Drive input power	W
$P_{out}$	Drive output power	W
$P_{Diod}$	Diode power losses	W



$P_{fe}$	Iron losses	W
$P_{IGBT}$	Insulated-gate bipolar transistors power losses	W
$p$	Number of pole pairs	
PM BLAC	Permanent magnet brushless AC motor	
$P_{a,b,c}$	Phase $a$ , $b$ and $c$ inverter output power	W
PA	Power analyser	
PMSM	PM synchronous motors	
PM BLDC	Permanent magnet brushless DC motor	
PWM	Pulse width modulation	
PSC	Position-sensorless control	
PLL	Phase locked loop	
$P_{swT/D}$	Switching losses of IGBT and diode	W
$P_t$	Total power losses	W
$r_C, r_D$	On-state resistance of the IGBT and diode	$\Omega$
RSPWM	Remote state PWM	
$R$	Stator resistance,	$\Omega$
SRM	Switched reluctance motor	
SPMSM	Surface mounted Permanent magnet synchronous motor	
SPWM	Sinusoidal pulse width modulation	
SVPWM	Space vector pulse width modulation	
SC	Search control	
$T_d$	Demand torque	Nm
$T_{em}$	Electromagnetic torque	Nm
$T_{MPW}$	Minimum pulse width	$\mu s$
$T_{sw}$	PWM switching time	$\mu sec$
$T_s$	Sampling time	$\mu s$
$\bar{V}_{com}$	Command voltage vector	V

$V_{dc}$	DC-link voltage	V
$v_{d,q}$	dq-axis voltages	V
$V_d^*$	Demagnetizing voltages	V
$V_d^{r*}, V_q^{r*}$	d- and q-axis input voltage	V
$V_d^r, V_q^r$	d- and q-axis output voltage vector of the over modulation block	V
$V_{ao,bo,co}$	Inverter phase-to-zero output voltages	V
$V_{in}$	Input voltage	V
$V_{com}$	Magnitude of command voltage vector	V
$V_{am}$	Maximum voltage	V
$V_m$	Magnetizing voltage	V
$V_{ref}$	Maximum voltage of the utilised intelligent power module	V
$V_{CE0}$	On-state forward voltage of the IGBT	V
$V_{D0}$	On-state forward voltage of the diode	V
$V_{a,b,c}$	Phase voltages	V
$V_{an,bn,cn}$	Phase-to-neutral voltages across the load	V
$v_{a,b,c}$	Phase a, b, c stator voltages IPMSM	V
$V_R$	Resistive voltage	V
$V_{tri}$	Triangle carrier signal	V
$V_a$	Terminal voltage	V
$v_o$	Zero-sequence signal	V
VSI	Voltage source inverter	
VT	Voltage transducer	
$\omega_{cc}$	Cut-off frequency of the current controller	Rad/sec
$\omega_e$	Electrical angular speed	Rad/sec
$\omega_b$	Rated speed	rad/s
$\omega_{Micon}$	Tuning factor	rad/sec

$\delta_{com}$	Direction of command voltage vector	<i>rad</i>
$\lambda_{d,q}$	dq-axis flux linkage	Wb
$\lambda_{dq}$	d- and q-axis flux magnitude	V/rad/sec
$\lambda_{base}$	Stator base flux	V/rad/sec
$ \lambda _{ff}$	Feed-forward flux component	Wb
$ \lambda _{fb}$	Feedback flux component	Wb
$ \lambda _{max}$	Maximum flux magnitude	Wb
$\lambda_{a,b,c}$	Phase a, b, c stator flux linkages	Wb
$\lambda_{ma,b,c}$	Phase a, b, c PM flux linkages	Wb
$\lambda_m$	PM flux linkage	Wb
$\theta_{dis}$	Distortion angle	rad
$\theta_e$	Electrical angular position	Rad
$\alpha$	Normalized factor	

## 1. INTRODUCTION

### 1.1 Fundamentals of Electrical Vehicles

Nowadays, electrical vehicles (EVs) are increasingly gaining importance due to their lower fuel consumption, and lower environmental pollution. In fact, EVs were presented for the first time in the UK in 1873 [1]. However, due to the limitation of the battery technique at the time, the importance of this invention decreased gradually, especially after the invention of the internal combustion engines (ICEs) at 1885 [1]. ICE has become a strong competitive alternative to EV owing to their relatively low production cost, better performance and higher reliability as it can be driven for long distance compared with the limited distance that can be achieved by EV [2]. More importantly, the availability of the petrol as a source of energy helps to spread the ICE widely [2] after its invention.

However, as the oil prices are in increase and the ICEs have a negative effect on the environment caused by the CO<sub>2</sub> and pollutant emissions, the importance of all-electric vehicles (i.e. no gasoline fuel is used) and hybrid electrical vehicles (HEV) (i.e. both fossil fuel and electricity are used) has been significantly focused in recent years as an attractive environmental option which uses sustainable energy sources instead of gasoline [1, 2]. A great number of studies have been introduced to improve these EVs' performances in terms of batteries efficiency, motors efficiency and their control strategies; together with reducing the production cost and increasing the safety limits [1, 2]. A typical all-EV power train system schematic is shown in Figure 1.1[3].

Usually, EVs are powered by a battery pack including a set of battery cells configured in a mix of series and parallel connections, Figure 1.2 [4]. Thus, the development of the EVs is strongly constrained by the battery characteristics such as power performance, life time, weight and cost [5]. Theoretically, safety and environmental impacts are other considered aspects on battery development. Basically, battery improvements are in progress aiming to fast charging time, cost decrease, weight reduction, high capability, and less environmental impact [6]. On the other hand, battery management techniques

to deal with unbalanced battery cell voltages which result from the difference in their characteristics and strongly affect the battery life are also proposed in [5].

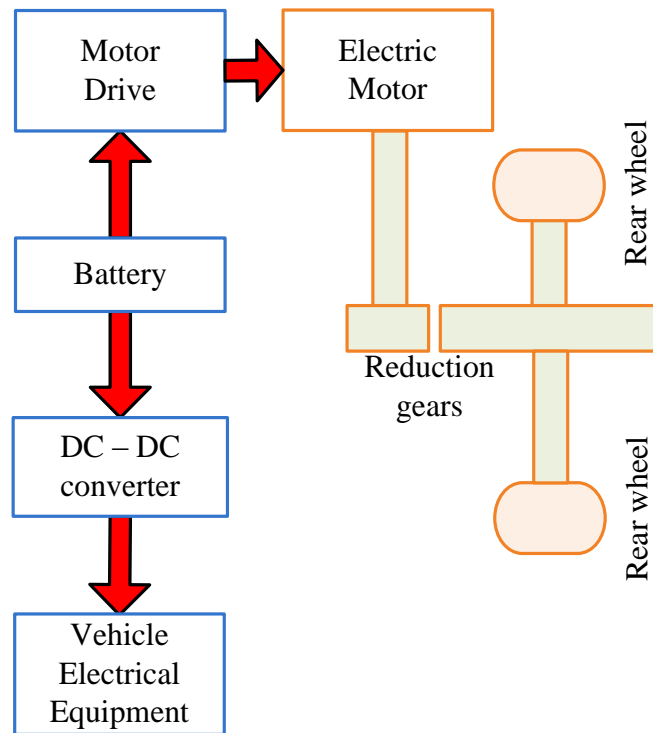


Figure 1.1 Schematic of all-EVs power trains [3].



Figure 1.2 A battery pack of Toyota Prius 2004 [4].

### 1.1.1 EV Requirements

Basically, high power density, high starting torque, high efficiency, a wide speed range and low kW/\$ cost metric are the main requirements for an EV traction motor [7] which defines the vehicle performance, as the driven torque to the wheels is generated only by this traction motor [3, 8]. As a result, the torque-speed or power-speed characteristics of the traction motor govern the EVs behaviour [3, 8]. The typical torque-speed and power-speed characteristics of motor drives for EVs are depicted in Figure 1.3 [3, 8].

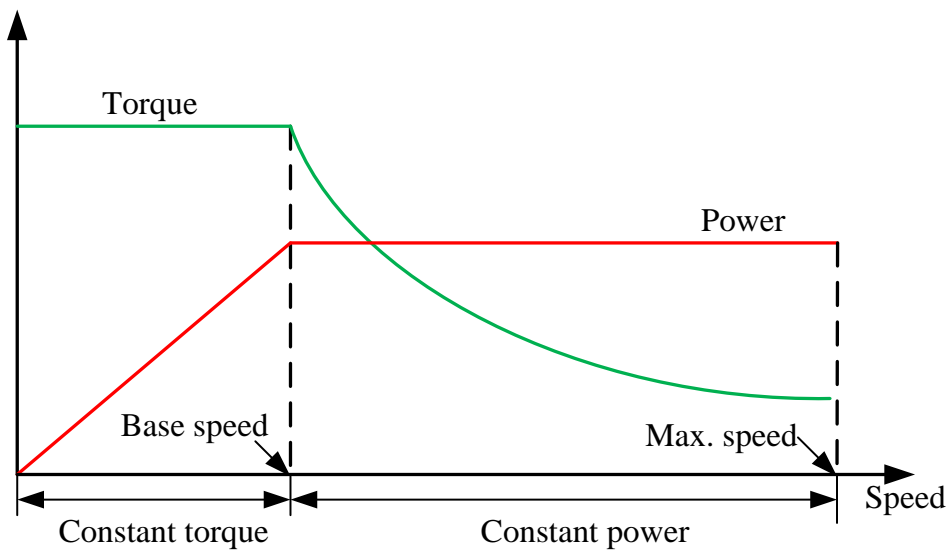


Figure 1.3 Typical torque-speed and power-speed characteristics of electrical motor drives in EVs [3, 8].

Two control regions can be identified from this figure: the constant torque region CTR where the torque is only limited by the machine current rating (i.e. motor is driven below rated speed) and the constant power region CPR (or flux weakening region FWR) where the torque is limited by both the machine current rating and inverter voltage rating [3, 8]. The acceleration time also needs to be considered in the evaluation of EVs performance [3, 8]. This is defined as the time that the vehicle requires to reach to a given speed starting from standstill (i.e. start of acceleration) or from a low speed to a predetermined high speed (i.e. the capability of overtaking) [3, 8]. Another factor often used to evaluate the EV performance is the level of the vehicle quality [3, 8]. This is

measured by the maximum distance that the vehicle can achieve at a given speed and the maximum speed it can reach [3, 8].

Theoretically, electrical motor drives dedicated for traction application should be designed to satisfy the aforementioned requirements. For the starting and acceleration, the motor drive should be able to operate at the maximum torque while the speed and consequently power increasing from zero to their rated values [3, 8]. The motor drives also should be designed to operate at the maximum available power as the speed increasing beyond the rated speed towards the maximum speed (i.e. for cruising) [3, 8].

### 1.1.2 Overview of Existing EV Drives

For a machine drive system designed for EVs, it should be able to meet a set of requirements to name but just a few [3, 7, 8]:

- High efficiency and high power density.
- High constant torque at low speed for starting and hill climbing as well as high constant power at high speed for cruising.
- Simple construction with low cost.
- Good fault tolerance.
- A wide speed range with constant power, fast torque response, low torque ripple and low noise.
- The ability to operate in harsh environments.
- Easy to be controlled and low maintenance requirements.

A lot of electrical machine drives have been designed and developed to meet the aforementioned EVs requirements such as brushed direct current DC machine drive, induction machine IM drive, permanent magnet brushless AC machine drive PM BLAC [also called PM synchronous machine (PMSM)], permanent magnet brushless DC machine drives (PM BLDC), and switched reluctance machine (SR) drive [3, 7].

Figure 1.4 summarises the classifications of the existing EV drives [9]. The common topologies of the DC, IM, PM BL, and SR motor drives are illustrated in Figure 1.5[8].

The torque-speed characteristics of brushed DC machines are ideal for EV traction applications as they are able to achieve high torque at low speed [3, 7, 10]. Owing to their simple control and torque-speed characteristics, they have been widely used in EVs in the past. The self-excited brushed DC machine has two main configurations: the series windings and shunt field windings.

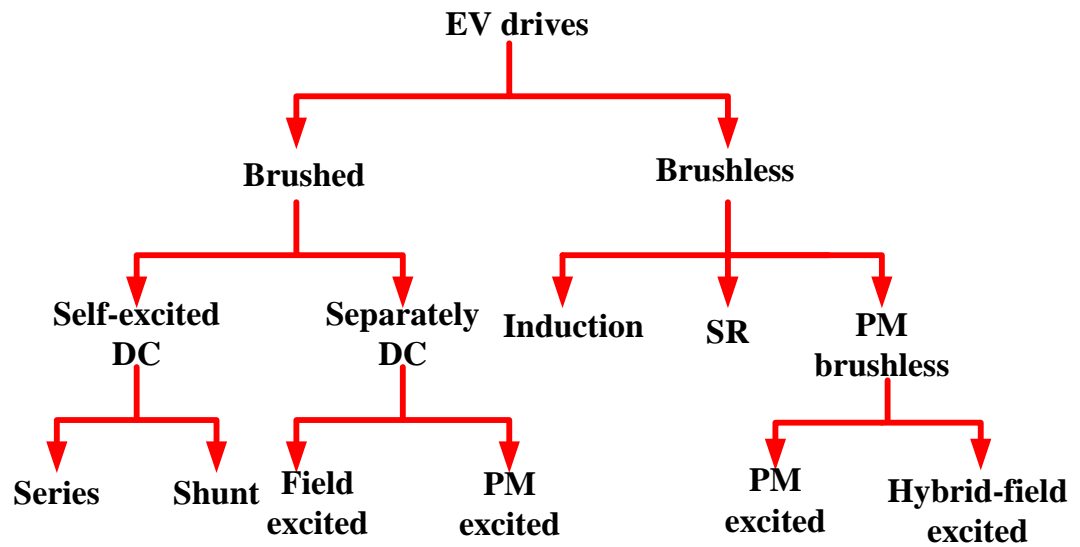


Figure 1.4 Configuration of the EV drives [9].

The constant power operation is achievable in the separately excited brushed DC machine due to their flux control and decoupled torque characteristics. However, the size of these machines is considerably large making them heavy and expensive. Furthermore, these machines are low efficiency, low reliability, and required frequent maintenance for the brushes, springs and commutator due to the mechanical friction. Finally, the maximum speed of these machines is constrained by the friction between the brushes and commutator [3, 7, 10].



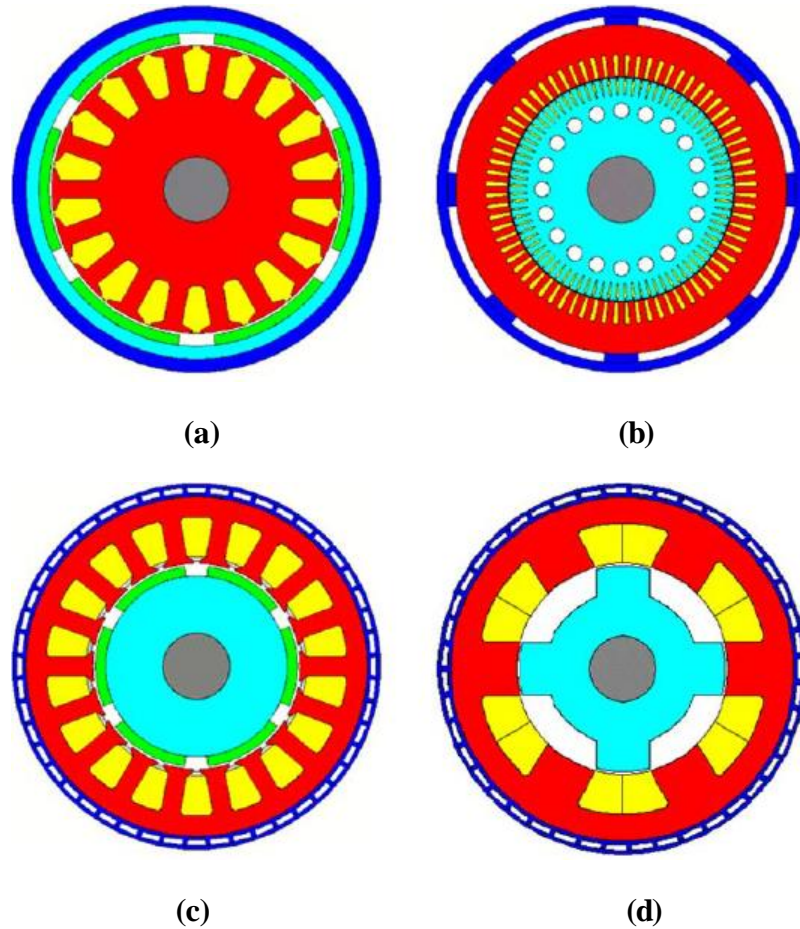


Figure 1.5 Configuration of common electrical machine dedicated for EV drives [8].  
(a) DC motor. (b) IM. (c) PM BL motor. (d) SRM.

On the other hand, the IM machines have several advantages over the DC brushed machines such as the maintenance requirements are much less frequent compared with the DC brushed machines. In addition to their construction is simple, and relatively cheap. Moreover, they offer better reliability, low torque ripple, high overload capacity, and they have the ability to operate in harsh environments. The IM can operate in high speeds as there is no friction for the brushes. The field oriented control technique (FOC, discussed later) [3, 7, 10] is often used to decouple the torque control and the field control from each other. This leads to the machine operation is similar to that of the separately excited DC machine. Theoretically, the flux weakening technique [3, 7, 10] is used in order to increase the speed beyond the rated speed. Thus, the speed can be expanded to 2-5 times of the rated speed via a suitable control. Nevertheless, the

controllers of the IM drives are relatively expensive compared with that of the brushed DC machine as well as its efficiency and power density are low especially at high speeds. On the other hand, the efficiency and power density of both two kind of machines are lower than that of PM machine which will be discussed later [3, 7, 10].

The SR motors are simple and reliable in their constructions as brushes, commutator, windings and magnets are not involved in the rotor structure. The absence of these parts makes the SR motors relatively cheap, light, and able to operate in harsh environments. Its cooling is eased and the influence of high temperature on its operation is less significant. They can be accelerated very rapid as well as the operational speed is very high. They also have a good fault tolerance, high starting torque, high torque-to-inertia ratio and easy to be controlled. The EVs load requirements are well satisfied in SR motors torque-speed characteristics and the speed can be expanded to 2-3 times of the rated speed with constant power. However, the saturation of the SR motors magnetic circuits is very high. Moreover, they suffer from high acoustic noise and high torque ripple in comparison with other machines. The SRM machines also exhibit low efficiency and medium power density [3, 7, 10].

High efficiency and high power density are the main advantage of the PMSM machines [7, 11]. Since the magnetic field essential for electro-mechanical energy conversion is provided by permanent magnets (PM) with no energy losses, they give higher efficiency and higher power density than IM, DC and SRM machines. This kind of machine also enjoys maintenance-free as brushes are not a part of their construction and thus its operating speed is not restricted by brush friction [3, 7, 8]. It is also small in size and the heat dissipation is good [3, 7, 8]. The expansion of the machine speed over the base speed is an available feature by weakening the permanent magnet flux when the machine enters the constant power operation mode (Figure 1.6 (a)) [9]. By employing FW control technique [3, 8], the speed is expandable to 2-3 times of the rated speed. However, the use of PM materials considerably raises its production cost [3, 8]. Moreover, demagnetization consideration of the magnet constraints the ability to weaken the flux [3, 7, 8]. As the PM BLAC operates with sinusoidal current and airgap

flux (Figure 1.7 (a)) [9], it requires a high resolution position signal for closed loop control therefore, an accurate encoder or resolver is required. This also raises the cost of this drive. On the other hand, PM machines may operate in the brushless DC (BLDC) mode [9, 11] with square wave current and a trapezoidal airgap flux (see Figure 1.7 (b)) [9]. For this operation, an inexpensive encoder may use to obtain the rotor position for the commutation of the phase-current. Unlike the PM BLAC, the PM BLDC machines presents poor ability to expand the speed range in the constant power region [9]. Figure 1.6 (b) compares the power capability of the BLAC and BLDC. It shows that the  $120^\circ$ -BLDC (two-phase  $120^\circ$  conduction) offers lower torque and power capability than the BLAC drive. The PM BLDC high speed-power capability is improved by implementing the  $180^\circ$ -BLDC (three-phase  $180^\circ$  conduction), but it shows low- speed torque capability [9].

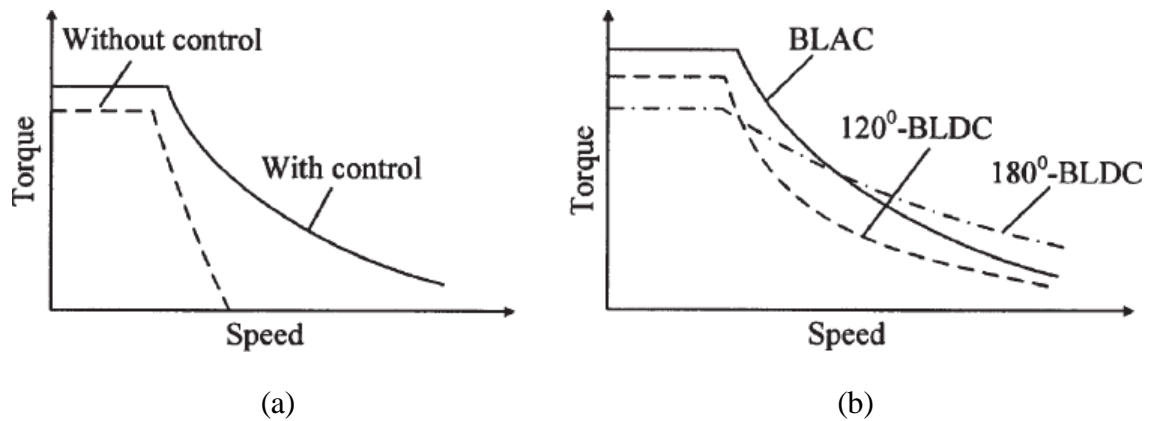


Figure 1.6. Torque-speed characteristics of the PM BL drives (a) with and without control (b) BLAC versus BLDC [9].

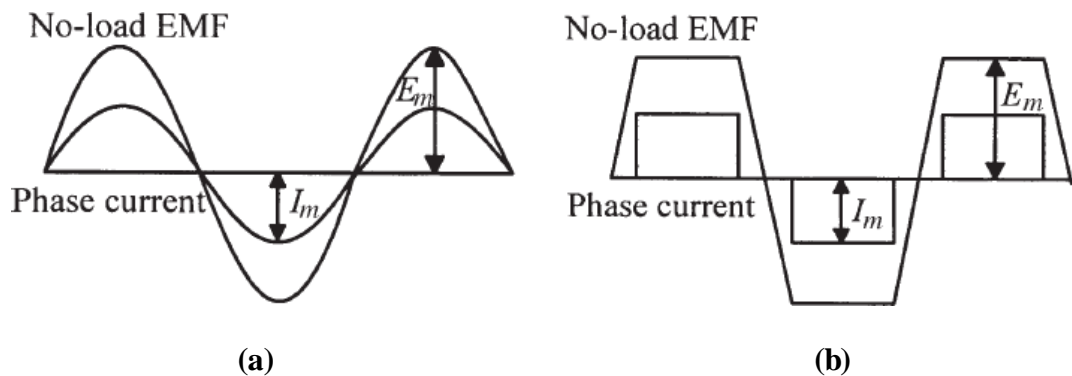


Figure 1.7. Theoretical waveforms of PM BL operations. (a) BLAC (b) BLDC [9].

Figure 1.8 [8] gives a brief description of some automotive applications of the aforementioned electrical machines. A comparison between these machines is illustrated in Figure 1.9 [8] where they are scored from 1 to 5 with 1 means the worst and 5 means the best. This comparison show that the PM BL has the highest efficiency and power density amongst the mentioned machines, but its cost is relatively high due to the PM materials utilised in the construction of these machines. Although, the IMs present considerably lower cost than PM BL, SRM and DC machines, their efficiency and power density are low.

HEV Model	Propulsion System
 PSA Peugeot-Citroën/Berlingo (France)	Dc Motor
 Holden/ECOMmodore (Australia)	Switched Reluctance Motor
 Nissan/Tino (Japan)	Permanent Magnet Synchronous Motor
 Honda/Insight (Japan)	Permanent Magnet Synchronous Motor
 Toyota/Prius (Japan)	Permanent Magnet Synchronous Motor
 Renault/Kangoo (France)	Induction Motor
 Chevrolet/Silverado (USA)	Induction Motor

Figure 1.8 EV drives applications in the automotive industry [8].

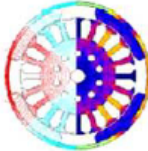
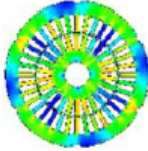
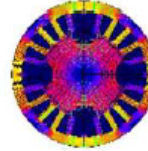
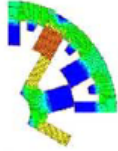




<i>Propulsion Systems</i>				
<i>Characteristics</i>	DC	IM	PM	SRM
<i>Power Density</i>	2.5	3.5	5	3.5
<i>Efficiency</i>	2.5	3.5	5	3.5
<i>Controllability</i>	5	5	4	3
<i>Reliability</i>	3	5	4	5
<i>Technological maturity</i>	5	5	4	4
<i>Cost</i>	4	5	3	4
<b><math>\Sigma</math> Total</b>	 <b>22</b>	 <b>27</b>	 <b>25</b>	 <b>23</b>

Figure 1.9 Evaluation of the EV drive systems [8].

From the above discussion, it is obvious that the PMSM can be considered as a very strong candidate for EV tractions due to their high power density, high efficiency and good controllability over a wide operating speed range which are the main requirements of an EV application.

### 1.1.3 PMSM Drive Control

As the PMSMs operate with sinusoidal current waveforms and sinusoidal airgap flux linkages (see Figure 1.7), a three phase voltage source inverter VSI is usually used to generate sinusoidal stator phase current waveforms in order to smoothly produce the electromagnetic torque. Thus, a high performance control strategy is often employed.

### 1.1.3.1 Inverter

Recently, the six-switches three-phase VSIs with the pulse width modulation PWM technique have been widely used in industrial applications and can be considered as industrial standard, Figure 1.10 [12]. However, for a high switching frequency application, the switching of the VSIs generates high transient of  $dv/dt$  which affects harmfully the insulation of the machine [13-15]. This impact depends on the impedance of the feeder and the distance that separate the inverter from the machine. If these transient effects are not completely removed via filtering technique, the lifetime of the machine will be significantly affected. Another issue related to this inverter configuration is that the producing of the common-mode voltage CMV which has negative effects on the machine insulations and bearings [13-15].

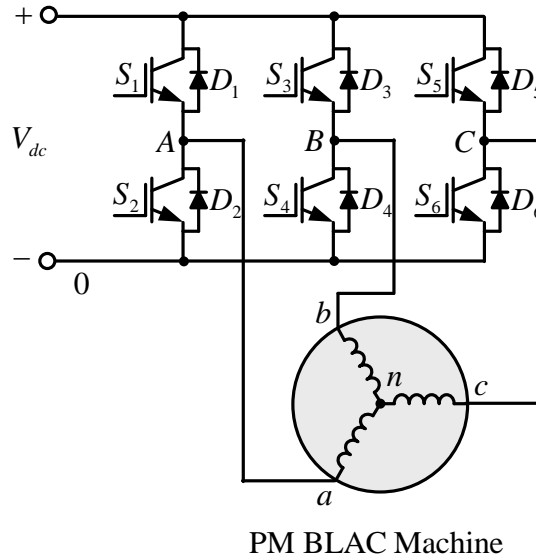


Figure 1.10 Six-switch three-phase voltage source inverter fed PM BLAC machine [12].

The common topology of three-phase VSI in Figure 1.10 includes six switching devices together with six freewheeling diodes. These controllable devices are chosen based on the voltage and current rating together with switching frequency. For a high voltage industrial application with low switching frequency, the insulated-gate bipolar transistors (IGBTs) are the best candidate [16]. For the VSIs, modulation techniques are

often employed to produce sinusoidal voltages at the inverter output terminals. Conventionally, two common PWM techniques are used: the sinusoidal PWM (SPWM) technique and the space vector PWM (SVPWM) technique. The principle of the PWM technique is illustrated in Figure 1.11 [16, 17] where sinusoidal voltage reference waveforms ( $V_a$ ,  $V_b$  and  $V_c$ ) with the desired magnitude and frequency  $f_s$  are compared with a triangle carrier signal ( $V_{tri}$ ) with a carrier frequency  $f_c$ . The crossing points defined the switching points of the power device [16, 17].

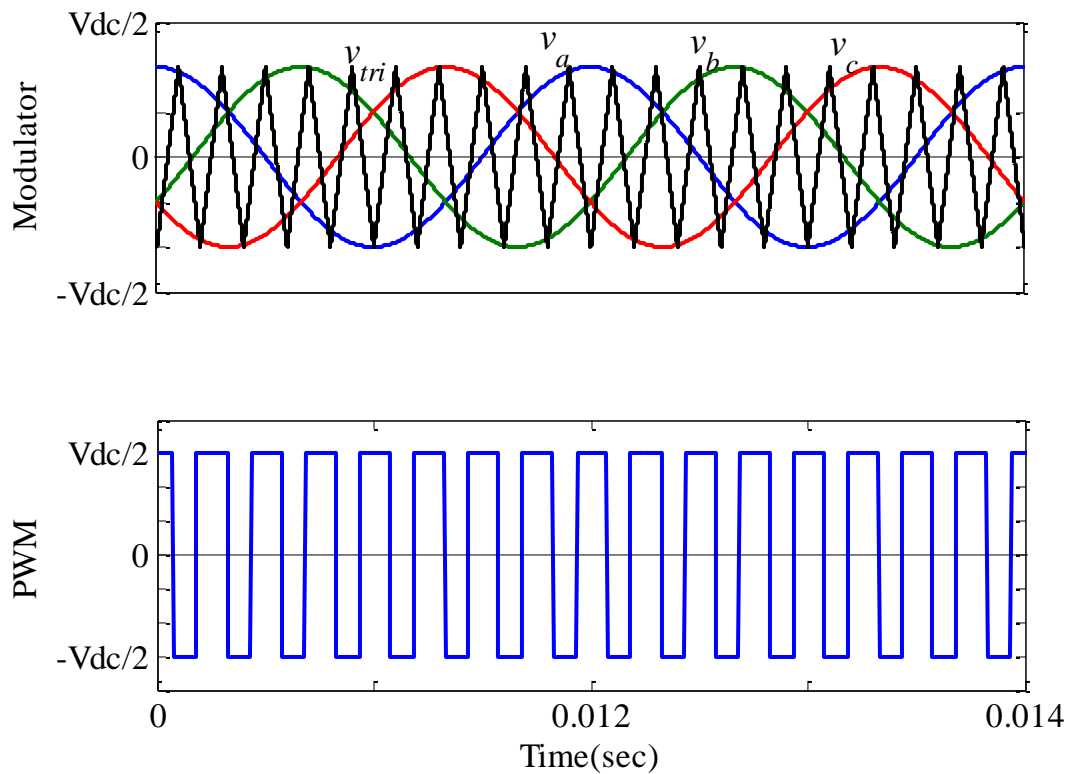


Figure 1.11 Principles of PWM for three-phase bridge inverter.

The SPWM technique is a simple technique and easy to implement, Figure 1.12 [16, 17]. However the utilisation of the available DC-link voltage is limited. In practice, the voltage range of the SPWM technique can be extended by injecting suitable zero sequence signal into the reference voltages as shown in Figure 1.13 [16, 17]. This leads to improving the quality of the waveform and reducing the switching losses



considerably [16, 17]. On the other hand, the SVPWM technique is an advanced modulation strategy which generates a modulated voltage vector that is matched with the reference voltage vector by controlling the switching sequence (i.e. On-Off) of the switches in each leg of the three-phase inverter as shown in Figure 1.10. In comparison, the SVPWM technique method produces 15.5% higher output [18] than SPWM technique [18]. However, the implementation of the SVPWM technique is much more complicated than the SPWM technique, Figure 1.14 [18].

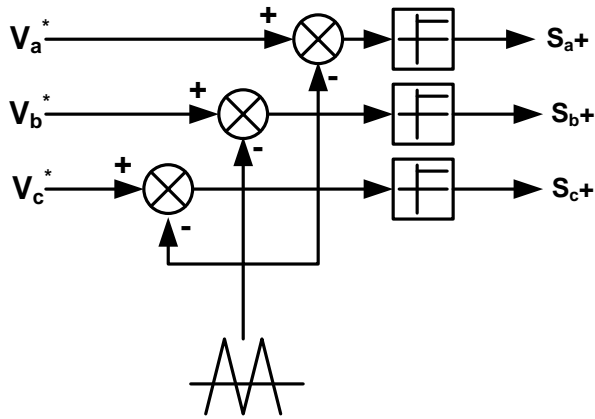


Figure 1.12 Implementation of the PWM technique [16, 17]

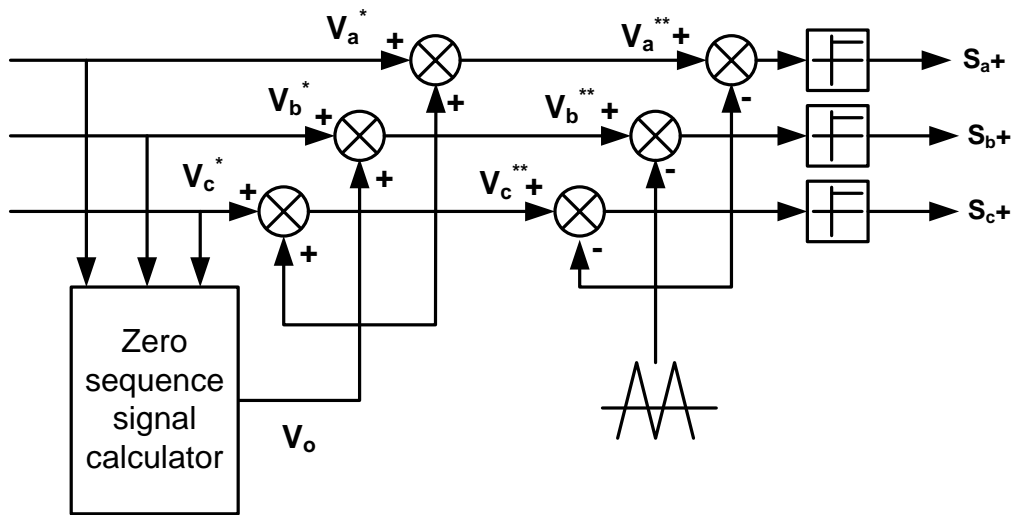


Figure 1.13 Scalar implementation of PWM with the injection of zero sequence signal [16, 17].



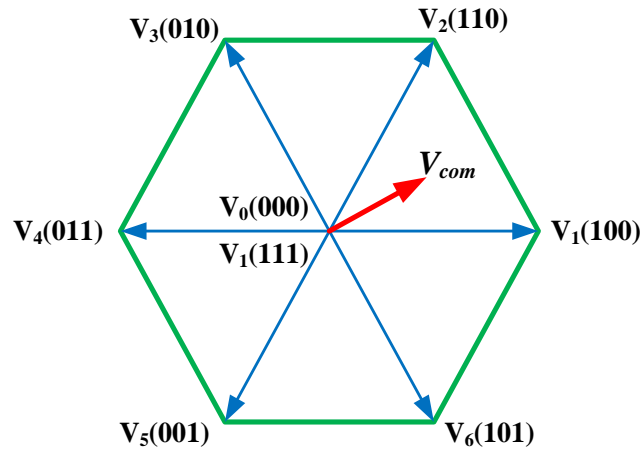


Figure 1.14 SVPWM voltage space vectors [18].

### 1.1.3.2 PM BLAC (PMSM) Topologies

As mentioned in item 1.1.2 the rotating magnetic field of the PMSMs is produced by the PM materials which are mounted on/in the rotor. Consequently, the PMSM stator phase currents are related to the production of the torque. Based on the construction of the PMSM rotor, several PMSM topologies have been presented in previous work [9, 19]. The most major topologies are the surface mounted permanent magnet synchronous machine SPMSM and the interior permanent magnet synchronous machine IPMSM, Figure 1.15. From Figure 1.15 (a) it can be seen that in the SPMSM the magnets are mounted on the rotor surface where the permeability of the PM materials and the air space are almost equal. Therefore, the SPMSM is classified as a non-salient PM BLAC machine in which the production of the electromagnetic torque results from the reaction between the stator phase currents and their related stator flux linkages regardless the rotor saliency impacts [9, 11]. In the IPMSM, on the other hand, the magnets are structured inside the rotor, Figure 1.15 (b). As a result, the IPMSM is classified as a salient PM BLAC machine due to the difference of the flux paths in the iron core where the permeability of the rotor iron core is higher than that of the PM materials [9, 11]. Therefore, the electromagnetic torque generated by the IPMSM is contributed by two components which are the torque resulted from the interaction of the stator phase

currents with their relevant stator flux linkages and the reluctance torque which is related to the saliency of the IPMSM [11].

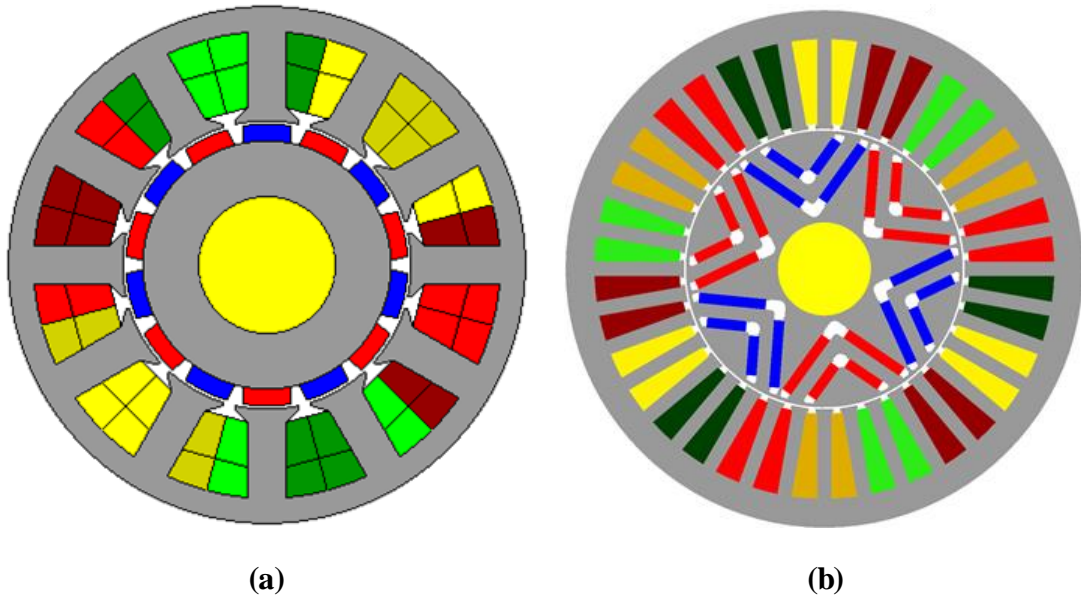


Figure 1.15 Rotor configuration studied for: a) SPMSM; b) IPMSM.

The degree of machine saliency is evaluated using the saliency coefficient [20]. This coefficient is usually expressed in the dq-axis rotating reference frame of the PMSM, which is less complicated and time consumed than the stationary  $abc$  reference frame [21], Figure 1.16 (a) [12]. This dq-rotating reference frame can be obtained from the stationary  $abc$  reference frame using Clark-Park mathematical transformation [22, 23] where the stationary  $abc$  reference frame ( $abc$  varying with time) is transferred to the stationary  $\alpha\beta$  reference frame ( $\alpha\beta$  varying with time) using Clark transformation [22] and then the stationary  $\alpha\beta$  reference frame is transferred to dq-rotating reference frame using Park transformation [23], Figure 1.16 (b) [12]. Finally, the saliency coefficient is expressed as the ratio of the quadrature axis ( $q$ -axis) inductance  $L_q$  to the direct axis ( $d$ -axis) inductance  $L_d$  of the PMSM [20]. The inductances  $L_d$  and  $L_q$  of the SPMSM are almost equal (i.e.  $L_d = L_q$ ). Unlike the SPMSM, the  $L_d$  and  $L_q$  inductances of the IPMSM are not equal ( $L_d < L_q$ ) [20].

It is obvious that the IPMSM has advantages over the SPMSM due to its ability of generating the reluctance torque, but it is noted that this reluctance torque component increases the difficulties of machine control compared with the SPMSM [24].

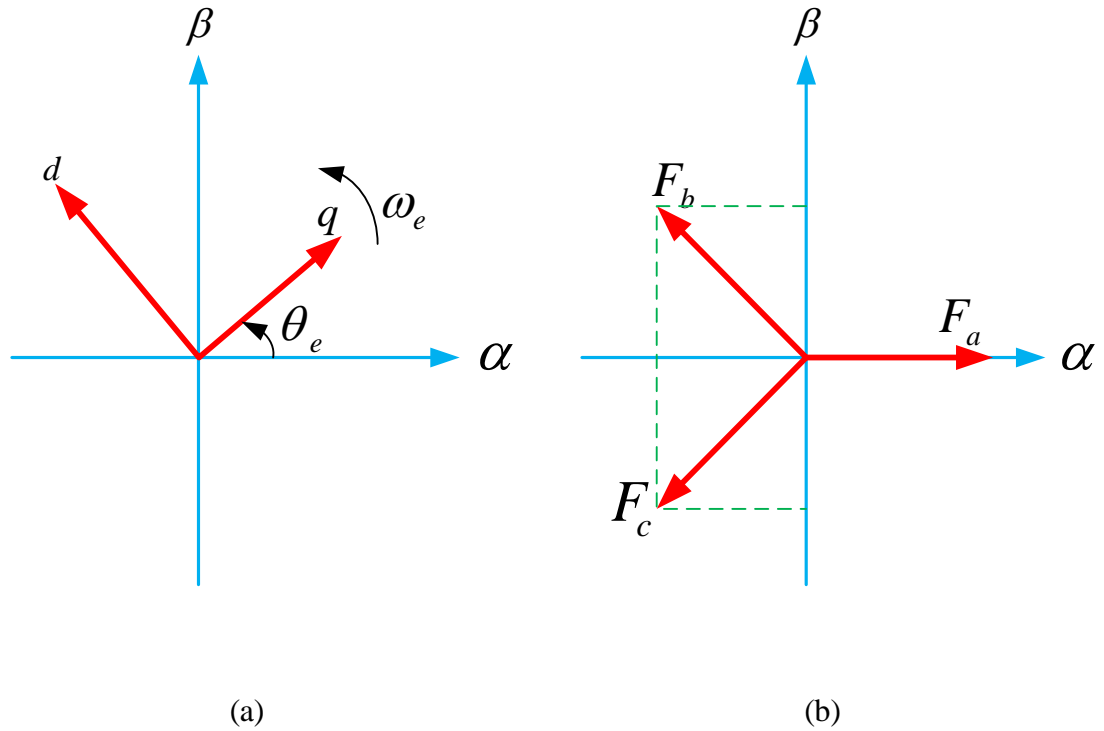


Figure 1.16 PMSM in a) stationary  $\alpha\beta$  reference frame b) in rotational  $dq$  reference frame [12].

### 1.1.3.3 High Performance Control Strategies for PMSM Drives

In literature, high performance operation of PMSMs is often achieved by control techniques such as [9]:

- Field oriented control (FOC) or vector control (VC).
- Direct torque control (DTC),
- Artificial intelligent control (AIC)
- Position sensorless control (PSC) to enhance performance of the aforementioned techniques.

The strategies of these control systems and their main advantages and drawbacks are briefly highlighted as follows.

- The FOC of the PMSM (see Figure 1.17(a)) [9] is based on the rotating  $dq$  reference frame model [25-27]. The stator current is decomposed into two decoupled  $dq$  components, Figure 1.16 (a) [12]. These components are the quadrature axis current component  $i_q^*$  and it controls the torque, and the direct axis current component  $i_d^*$  that governs the flux. Based on this technique, the FOC provides two current control loops that can be controlled separately. This control strategy has the advantage of minimising the total power losses (usually copper and iron losses) where  $i_d^*$  is online regulating in order to minimise both the copper and iron losses [9, 25-27]. Moreover, it has high dynamic performance and the ability to accomplish short response times. However, FOC presents some disadvantages such as requirement of the rotor position information, sensitive to motor parameters variations and intensive computation for coordinate transformations is required [25-27].
- The DTC technique (see Figure 1.17(b)) [9] independently controls the torque and stator flux linkage. The stator flux linkage and the torque independent controllers are followed by an optimum switching table to select a suitable voltage space vector applied to the inverter. Comparing with FOC technique, DTC technique has the merit of simple principle and easy implementations [28-31] since current controllers, coordinate transformations, and PWM modulator that are essential for FOC technique are not required in the DTC. Subsequently the sensor of the position is not needed but torque and flux observers are essentially required. As a result, the entire delay phenomenon associated with rotor position sensor can be removed which leads to that the dynamic torque response under DTC technique is very fast. In addition, DTC technique has a simple structure which is insensitive to motor parameter variation, less sensitive to the external disturbance and only needs information about the sector which the rotor is located in. Furthermore, because the possibilities of direct control of the stator flux linkage, the flux weakening operation

under DTC technique can be achieved quite easily [28-31]. However, stator flux estimation with pure integration in the conventional DTC technique may cause inaccurate results due to the integration drift and stator resistance variation [9].

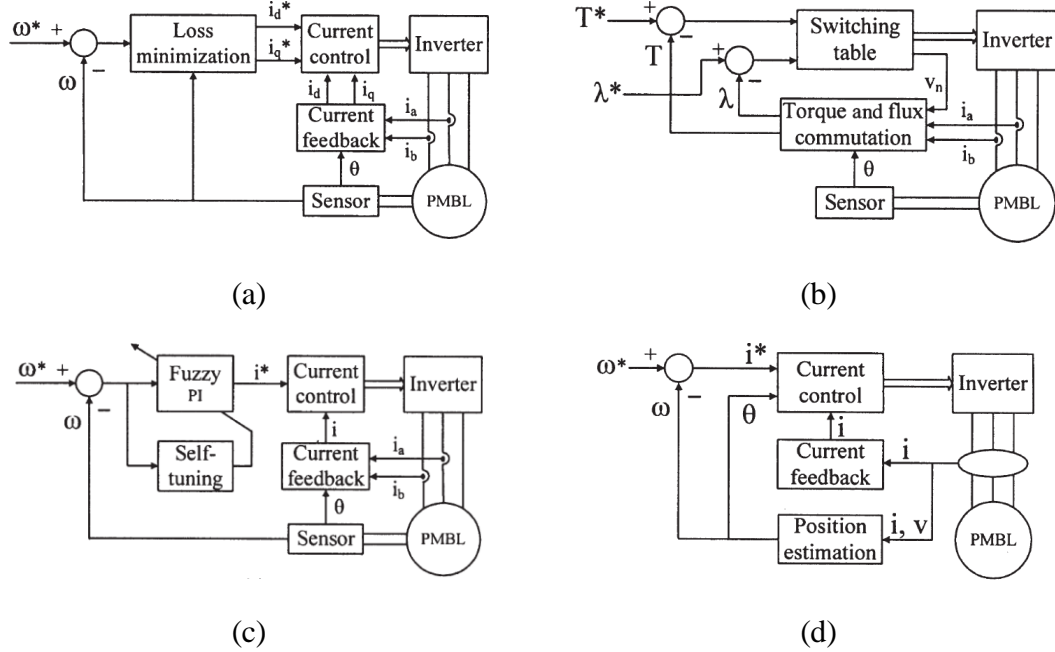


Figure 1.17 Block diagrams of PM BL Control systems [9]. (a) FOC. (b) DTC. (c) AIC. (d) PSC.

- The AIC (see Figure 1.17(c)) utilises the intelligent control theories such as fuzzy logic, neural network, neuro-fuzzy and genetic algorithm control strategies in order to control the PMSM [9]. The most popular AIC are the fuzzy logic and neural network control owing to their ability to deal with the nonlinearities of the system and parameters saturations [9]. The main disadvantage of the AIC is that it requires intensive computational work and additional hardware for implementation.
- PSC (see Figure 1.17(d)) is a control technique which can be combined with the aforementioned control strategies which are the FOC, DTC and AIC to help to reduce the drive cost and size by avoiding using a position sensor to obtain the instantaneous rotor position information [9]. In the PSC strategy the rotor position of the PMSM is obtained by analysing the voltages and currents in the windings of

the machine [9]. The PSC techniques are classified as flux-linkage variations, inductance variation, and the motional back EMF [9]. Similar to AIC, PSC needs demanding computational work and require specific knowledge [9].

Table 1.1 summarises the advantages, disadvantages and the control strategies of FOC, DTC, AIC and PSC of the PMSM drive [9].

Table 1.1 Comparison of PM BL control strategies			
	Advantages	Disadvantages	Control strategies
<b>FOC</b>	Minimize the overall losses ; no need to accurate losses model; work for wide speed and torque ranges	Originate system oscillation or convergence problem	Control the input voltage or d-axis armature current; control DC field current
<b>DTC</b>	Fast torque response; no need for current control; less parameter dependence	Causing errors due to drift in stator flux linkage estimation and stator resistance variation	Generating the voltage vector using independent torque and flux computations
<b>AIC</b>	Flexible control algorithms, adapt nonlinearities and parameter variations	Require expert knowledge, or intensive computation and sophisticated hardware	Incorporate fuzzy logic or neural network or other AI into traditional control
<b>PSC</b>	Eliminate the position sensor, hence reducing the system size and cost, Readily merge into other control	Require intensive computation and sophisticated hardware	Estimate position into the EMF, inductance variation or flux linkage variation

#### 1.1.3.4 Constant Torque and Flux Weakening Control Techniques

Theoretically, PMSM should be controlled based on whether the drive is in the CTR or FWR (CPR) operation modes, Figure 1.3.

- Constant torque control:

The CTR mode of operation is common in industrial applications where the PMSM operates below its rated speed. In this case, the FOC technique is simply used to control the machine, Figure 1.18 [32]. It is noted that due to its rotor structures

which causes unequal inductances in the  $d$ -axis inductances, reluctance torque can be only achieved for the IPMSM [24]. As a result, in the CTR, the  $d$ -axis current of the SPMSM does not contribute to the electromagnetic torque production [9, 11]. Therefore, the control of the SPMSM in the CTR is conventionally achieved by maintaining zero  $d$ -axes current and regulating the  $q$ -axes current to meet the demand torque [32, 33]. Generally, this control strategy is known as the maximum torque per ampere (MTPA) control technique as the torque is generated with minimum current requirement [20]. However, for the IPMSM,  $d$ -axes current contributes to the electromagnetic torque production by generating the reluctance torque components [9, 11]. Consequently, controlling of the IPMSM in the CTR is more complicated compared by SPMSM and it is accomplished by regulating both the  $d$ - and  $q$ -axis current components at the same time [24]. This is one of the main topics of this thesis.

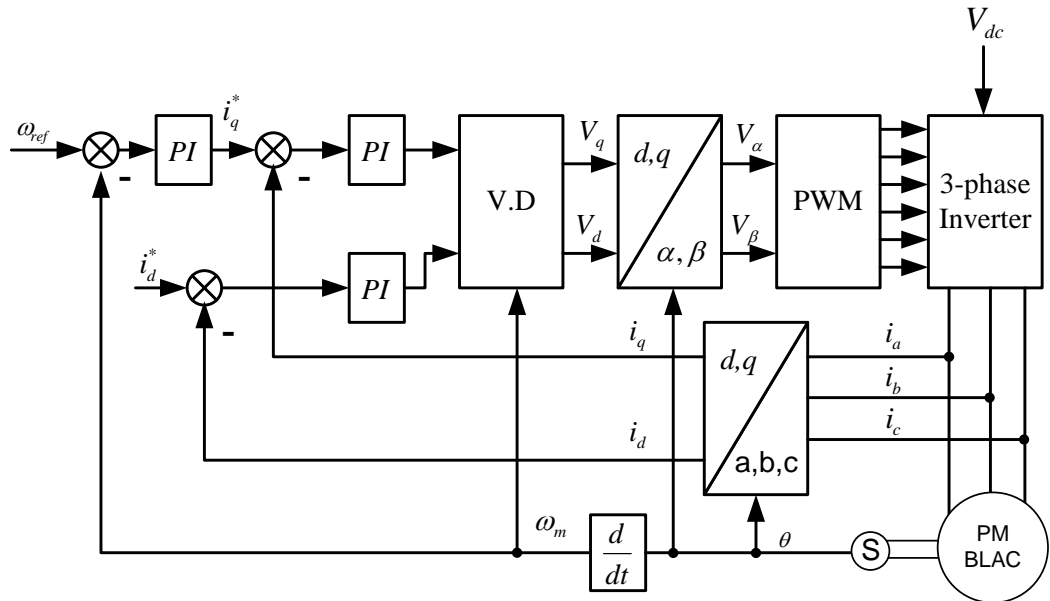


Figure 1.18 FOC based PM BLAC machine drive for MTPA control [32].

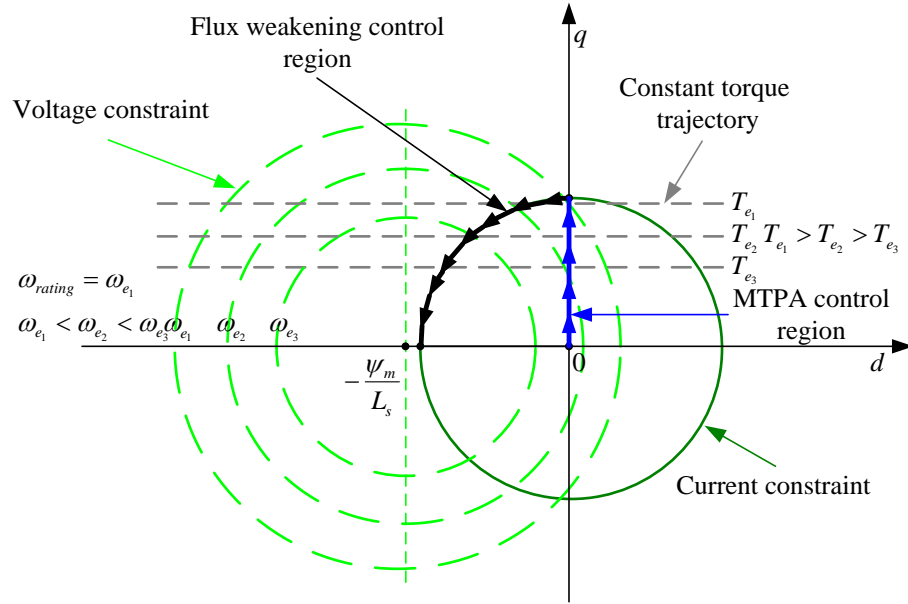
- **Flux weakening control:**

Typically, when the speed of the PMSM increases, the induced voltage (back-EMF) due to the rotating rotor is also increased. For a drive system with a constant DC-link voltage, there is a maximum modulated voltage associated with the fixed DC-

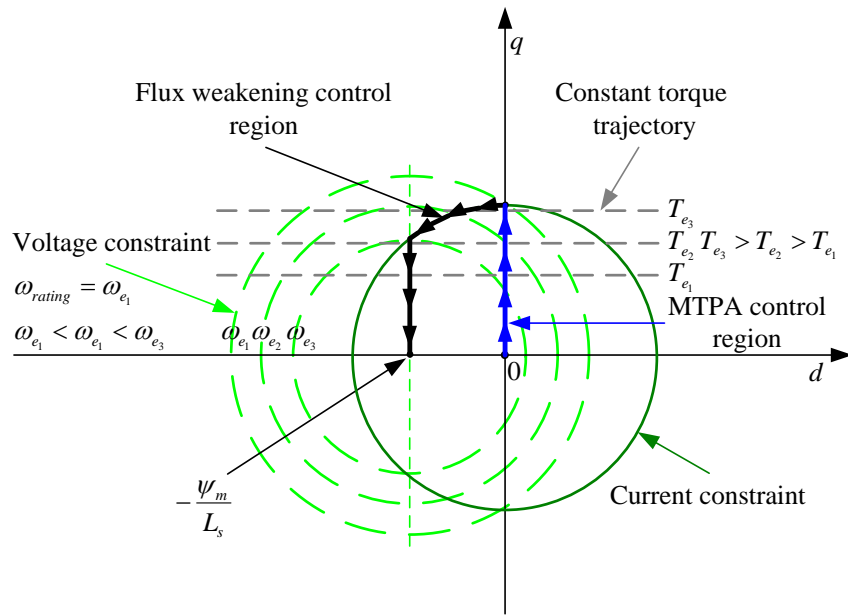
link voltage value and the employed modulation technique. When the back-EMF value reach the maximum modulated voltage of the PMSM drive, this operating speed is defined as rated speed of the drive system. Driving the PMSM beyond this rated speed is not possible without employing an appropriate control strategy, Figure 1.6 (a) [9, 20, 34]. Theoretically, to increase the speed of a PMSM above the rated speed, it has been suggested that a proper negative d-axes current value needs to be injected to demagnetise the PM flux linkage and consequently maintaining the stator phase voltage constant at the voltage limits of the drive [20, 34]. This control strategy is defined by the flux weakening FW control technique. Again, due to the differences in the design of SPMSM and IPMSM, the FW control is classified as SPMSM FW control and IPMSM FW control as shown in Figure 1.19 and Figure 1.20 respectively [12, 20]. From these figures one can easily note that voltage constraint of an SPMSM is a circle loci and the IPMSM is described as an ellipse loci Figure 1.20. This is due to the fact that the dq-inductances ( $L_d$  and  $L_q$ ) of the IPMSM are not equal.

Many researches have been presented in literature aiming to develop and improve the FW control schemes. Generally, the proposed schemes can be categorized as feed-forward FW control (FF-FW), feed-back FW control (FB-FW) and a combination of the FF-FW and FB-FW control [19, 35]. The FF-FW [20, 35-39] approaches (see Figure 1.21) [19] generate good stability and transient response, and they provide the possibility to introduce optimisation criteria [8]. On the other hand, the control algorithm is strongly dependent on the motor parameters as it has been mostly assumed that these parameters are known and do not change with the operation conditions such as material characteristics changing with time, temperature and saturation effects [8].



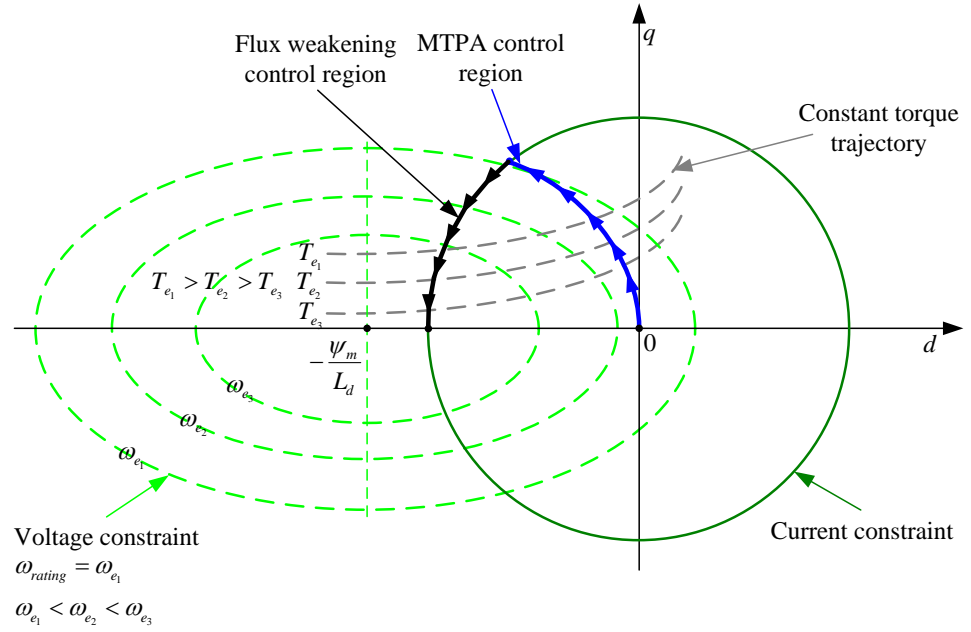


(a)  $\psi_m > L_s I_{rating}$

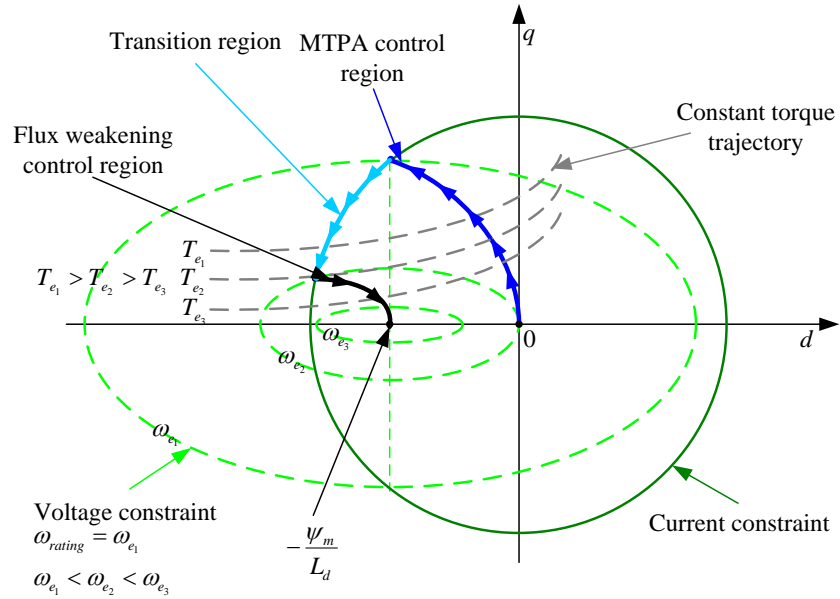


(b)  $\psi_m < L_s I_{rating}$

Figure 1.19 Optimum current profile of SPMSM under MTPA and FW operations [12, 20].



(a)  $\psi_m > L_s I_{rating}$



(b)  $\psi_m < L_s I_{rating}$

Figure 1.20 Optimum current profile of IPMSM under MTPA and FW operations [12, 20].

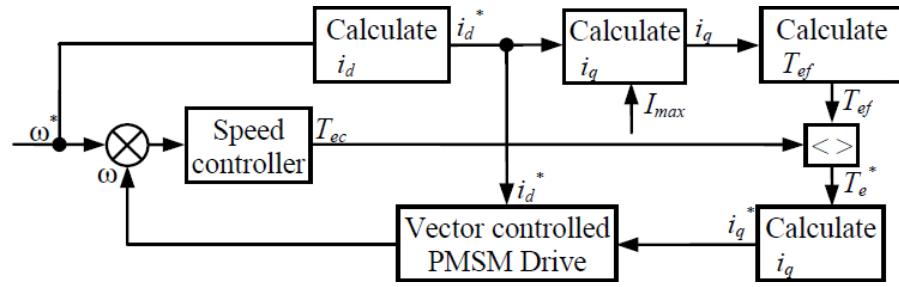


Figure 1.21 Block diagram of FF- FW control system of PMSM [19].

The FB-FW [40-50] (see Figure 1.22) [19] is not sensitive to the parameter changes as it does not use these parameters and therefore the steady state error no longer occur. Moreover, their implementation is uncomplicated and it presents better utilise of the DC-link voltage. It also guarantees a smooth transition between motor operation regions via anti-windup action. On the other hand, the poor transient response of the closed loop voltage controller represents the main drawback of this approaches as well as the tuning of the regulator gains is not easy due to the operation in the closeness of voltage saturation region.

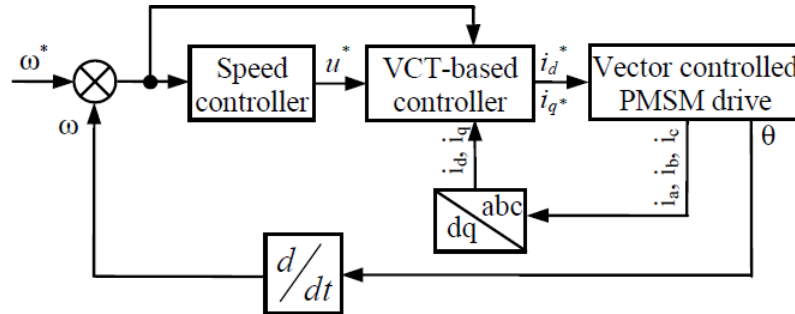


Figure 1.22 Block diagram of FB- FW control system of PMSM [19].

The FF-FW and FB-FW [51-55] control (see Figure 1.23) [56] are combined in one scheme in order to produce a system that utilises the advantages of both the FF-FW and FB-FW control systems. This flux weakening control technique is robust to the variations of the parameters and the back-calculations of the anti-wind up for the current controller are no longer needed. It also shows good response, less torque ripple, better maximum torque is achieved compared with conventional methods

specially under flux weakening control as well as windup phenomena is completely avoided. On the other hand, the implementation of these control systems tends generally to be complex due to the dependency on the look up tables LUTs to accomplish this implantation and therefore bulky memories are required. Additionally, hard off-line computational work is required to establish the necessary data to fill in the LUTs [19, 35, 56].

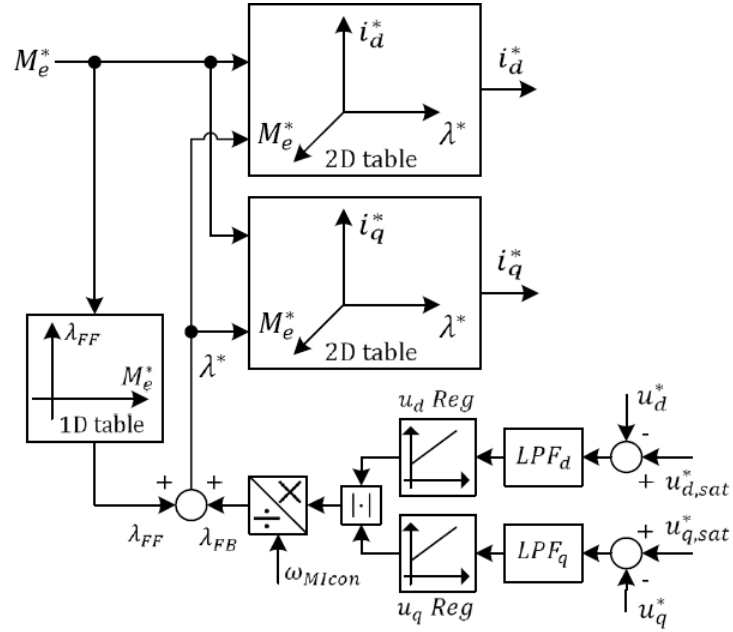


Figure 1.23 Block diagram of FF-FW and FB-FW control system of PMSM [56].

## 1.2 Minimisation of PMSM Drive Losses

As mentioned in section 1.1, PMSM drives are increasingly used in the industrial applications such as EVs due to their advantages over IM and DC machines drives such as high power factor, high power density and high efficiency [7]. Therefore, the improvement of the efficiency of these drives has been an attractive subject of researchers in order to reduce the energy cost. The total drive losses are mainly contributed by both the PMSM and the inverter. In the following two sections, the strategies for the motor and inverter losses minimisation are reviewed and discussed.

### **1.2.1 Minimisation of Motor Losses**

The power losses of the PMSMs which have been reported in literature [57, 58] can be summarised as follows:

- Copper losses due to the current which flows through the motor stator winding.
- Iron losses in the motor core due to the hysteresis and eddy current effects.
- Mechanical losses owing to the friction and windage losses.
- Harmonic losses that are produced by the non-sinusoidal voltage and current in the stator windings. The current harmonics raise the copper losses of the stator and the voltage harmonics increase the iron losses.
- Stray losses include all losses that cannot be quantified accurately by the above terms, such as eddy current losses in the rotor magnets.

The mechanical losses are not able to be controlled as for a given motor, those losses mainly depends on speed not the electrical variables [57, 58]. The harmonic losses are usually reduced by the decrease of the voltage harmonics [57, 58]. The losses which can be directly controlled are the copper, iron and stray losses [57, 58]. The minimisation of the copper losses can be achieved by the maximum torque per ampere (MTPA) control technique [59]. This is due to the fact that the copper loss is caused by the stator windings resistance and it is directly proportion to the stator current power [60]. On the other hand, the MTPA control actually represents the current vector with the minimum magnitude among the solutions that generate a given torque [60]. Therefore, the MTPA can be considered as the copper-losses minimizing solution. However, the iron and stray losses rely on the operating speed and the machine material [60].

Fundamentally, the optimal efficiency control of a machine can be implemented by two main techniques, Figure 1.24 and Figure 1.25, respectively [57, 58]: The first approach is the search control (SCs) techniques in which the input power is measured and control variables such as current or voltage is adjusted by using a search algorithm until the minimum power is detected. The main advantage of this technique is that the motor parameters are not required to be known as it is independent on the motor losses model. Therefore it is not sensitive to the parameter variations and an accurate model is not

required [57, 61]. On the other hand, this optimization strategy cannot find the minimum point very fast and it suffers from some difficulties to reach to the true minimum point. This is due to the fact that the power curves of a PMSM close to the minimum point for a given torque tend to be flat [57, 61]. Moreover, it presents poor steady state performance owing to the oscillations in the air-gap magnetic field caused by this search technique which leads to additional torque ripple/disturbance [57, 61].

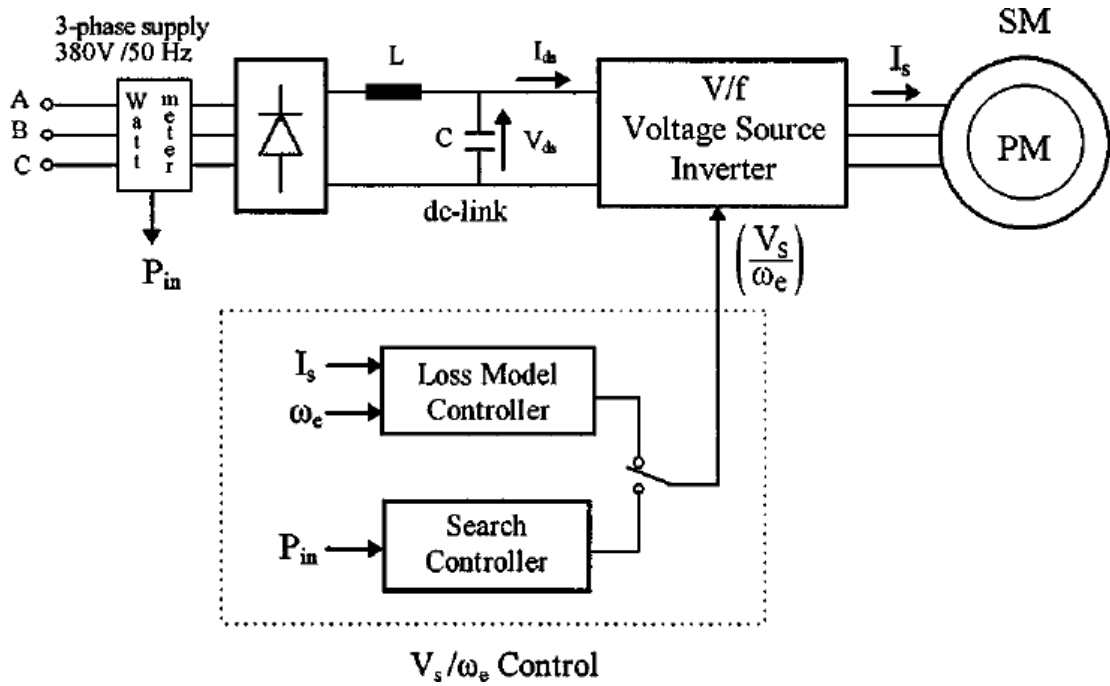


Figure 1.24 Optimal vector controlled of SPMSM [57, 58].

The second approach is that the losses model controllers (LMCs) [54, 55, 60-64] where the optimal stator voltage is determined by the motor losses-model according to the measured speed and armature current. In [61-64] a LMC accounting for the core losses and copper losses is developed based on the IPMSM equivalent circuit under a given operating condition, Figure 1.26 [57, 58]. The losses function is then differentiated and the optimum value of the d-axis current  $i_d$  is found. The drive systems based on these control techniques show efficiency improvement compared with the conventional control with  $i_d = 0$ . However, the methods presented in [61, 62] do not consider the flux weakening operation. The optimization model in [60] is developed in the same

manner as those in [61, 62] with considering the FW control and neglecting the parameters saturation effect. In [63] it is argued that the saturation of the q-axis inductance has negligible effect on the machine efficiency and therefore its effect is neglected. The developed method in [64] follows similar manner of [61-63] and it considers both MTPA and FW control but, again it does not account for the parameters saturation effect of the IPMSM machine. Look up tables (LUTs) are used in [54, 55] to implement the optimal current control in CTR and the FWR. It is noted that the optimisation algorithm in [54, 55] are developed based on the motor parameters which leads to increases its sensitivity towards parameters variations. Unlike SC method, the LMC method can reach to the optimal point very fast. However, it requires an accurate knowledge of the motor parameters. Consequently, it is very sensitive to parameters variations. Generally, LUTs require time consuming and intensive experimental work and calculations to generate them.

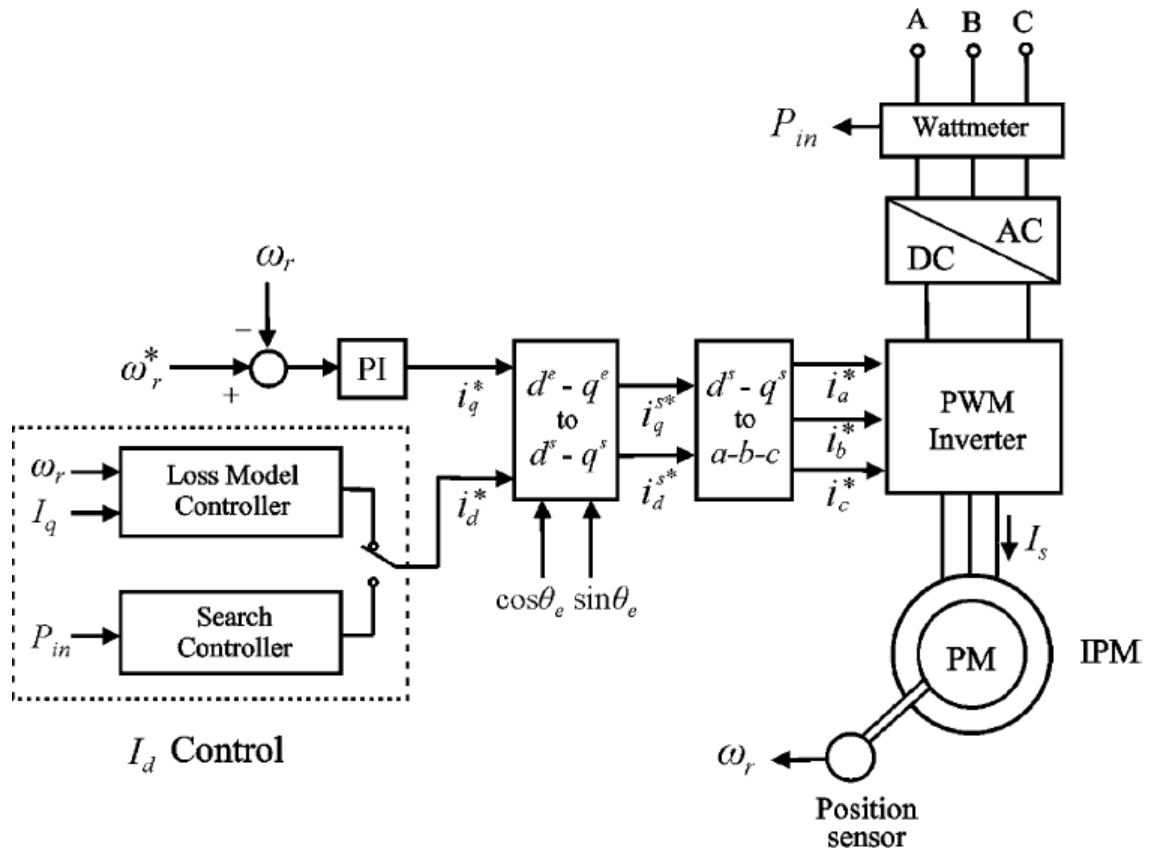
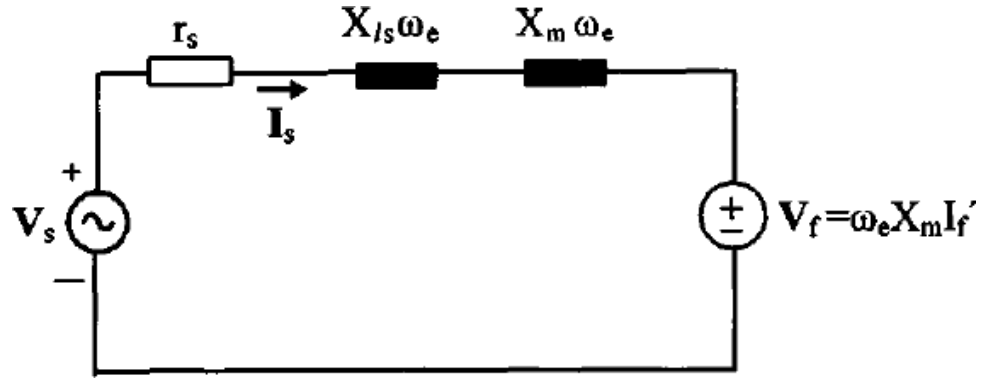
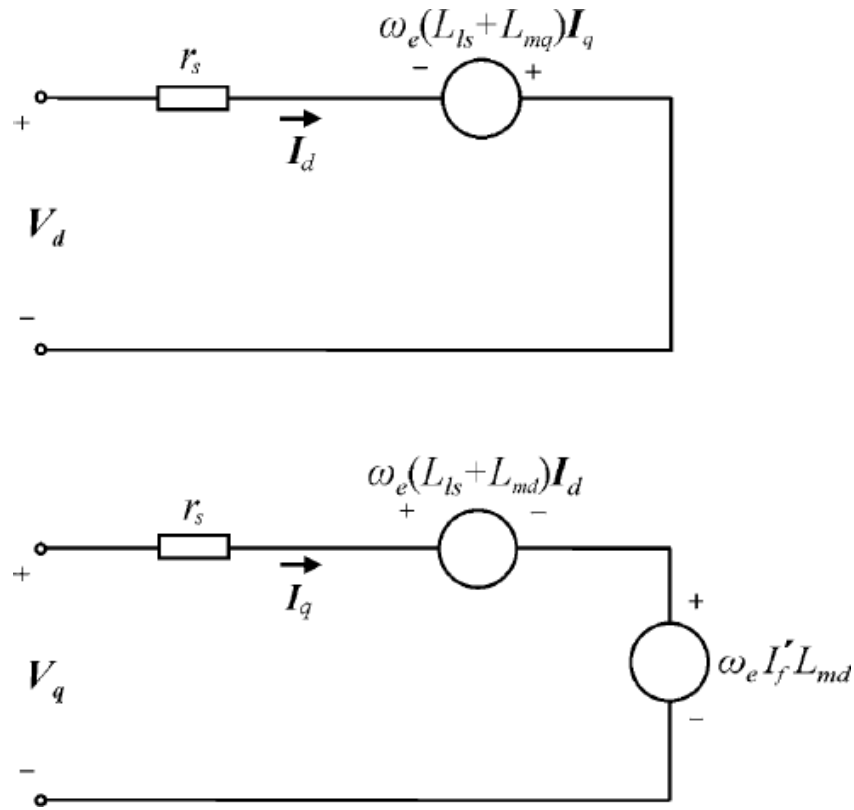


Figure 1.25 Optimal vector controlled of IPMSM [57, 58]



(a)



(b)

Figure 1.26 Equivalent circuit: a) SPMSM; b)  $dq$ -axis of IPMSM [57, 58].

In reality, the variation in high performance IPMSM parameters especially due to saturation is considerable. This parameter variations have a significant influence on the minimum losses operation of the motor where a difference between the simulated and measured optimal  $d$ -axis current points is reported [65]. The torque per ampere ratio tends to be reduced by these variations as the armature current increases and



consequently the electrical losses [65]. Additionally, the decrease in the iron losses due to a demagnetizing effect of the d-axis current  $i_d$  is offset by the increase in the flux harmonic losses [65]. Therefore, the losses are greater leading to an increase in the input power with the d-axis current. As a result, the optimal point of the d-axis current will shift slightly to the right [65]. Some research has been presented in order to solve the problem of IPMSM parameter variation using adaptive losses minimisation controller as described in [65, 66] where the demagnetizing current is continuously adjusted in order to minimise the total input power. In [65] the system results show smooth performance of the drive. However, additional computational work is needed and more memories are required to store the resultant values of the input power. In addition to it does not consider the flux weakening control of IPMSM. The losses minimisation algorithm presented in [66] also does not consider the FW region of the IPMSM and since it accounts for the parameters variations by estimating the torque and the fraction coefficient by using an adaptive algorithm, inaccurate estimation results may be obtained.

Another solution is proposed in [59] where a LMC is developed based on a polynomial approximations. The author investigated the  $L_d$  and  $L_q$  inductances saturation and it is reported that the saturation effect of  $L_q$  is significantly higher than that of the  $L_d$  which remains almost constant with the direct axis current. Therefore,  $L_q$  saturation is only considered in the proposed LMC [59]. The minimisation is achieved in two different steps depending on whether the optimal solution is in the interior (MTPA) or on the boundary (FW). The LMC is implemented in the vector control environment without the need of LUTs. The system presents good performance and the energy saving is considerably increased. However, intensive mathematical computation in real time is required and, more importantly, the saturation effect of  $L_q$  is only considered in the constant torque region which may lead to oscillation at the boundary between the constant torque and constant power regions. The saturation effect of the flux linkage has been also neglected in [59]. Considering the dq-inductances and the flux linkage saturation effect is one of the aims of this thesis.

Other approaches such as losses minimisation controls based on on-line parameter estimation [67-69] were investigated. However, the performance is also affected by estimation errors and uncertainty in the model structure. Recently, a parameter independent MTPA control technique [70] based on signal injection for IPMSM drives has been reported. The concept is to perturb the current reference angle such that the MTPA point, at which mechanical power variation with respect to the angle is zero, and is tracked. However, FW control is not considered under this method and a speed control loop is required which is not suitable for EVs applications as the EVs drive system needs to be operated in the torque mode [71].

### **1.2.2 Minimisation of Inverter Losses**

The losses of an inverter mainly consist of the conduction losses and the switching losses of the inverter switches [72, 73]. Although the inverter losses represents a significant part of the total drive losses, the including of the inverter losses in a losses minimization process, is not necessary [74]. This is due to the fact that it almost does not have any influence on the minimum losses operation point of the drive as a very tiny difference has been noticed between the d-axis currents obtained with and without considering the inverter losses [74]. Therefore, the inverter losses do not need to be considered in losses minimisation control [74]. However, the use of the PWM technique to control the output of a VSI increases the switching losses which rise with switching frequency [75, 76]. The increase of the switching losses decreases the efficiency of the VSI and affects the safe operation and life of the switching devices [75, 76]. Additional problem which is needed to be considered is the adverse effect of the neutral-to-zero voltage  $V_{no}$  (see Figure 1.27) [12], (alternatively called common-mode-voltage CMV) under the traditional employed PWM techniques such as SVPWM technique, Figure 1.28. In the AC motors, a high level of the CMV leads to excessive quantity of common-mode current leakage (CMC) [75]. This, in turn, may lead to motor bearing failure, electromagnetic interference noise that causes undesirable trip of the inverter drive, or interference with other electronic equipment in locality [75, 76]. Therefore, it is desirable to reduce the switching losses and the peak-to-peak CMV

value for better efficiency of the VSI, long life for the switching device and motor bearings, and better control of electromagnetic compatibility.

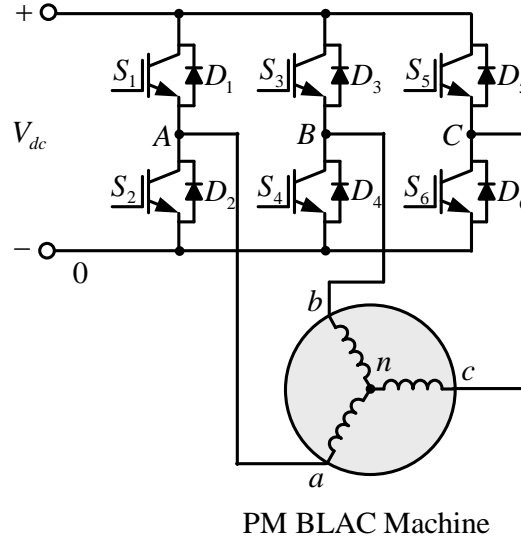


Figure 1.27 CMV of a VSI fed three phase load [12]

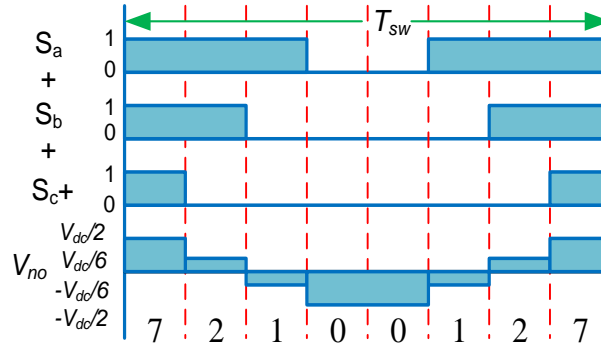


Figure 1.28 Switching pattern and peak-to-peak CMV of a VSI with SVPWM [75].

The switching losses linearly change with the switching frequency [73]. Carefully studying of Figure 1.28, it can be seen that each phase has two switching events (i.e. “On” to “Off” and “Off” to “On”) during the switching time  $T_{sw}$ . Therefore, it is possible to reduce switching losses by decreasing the number of the switching events per phase during the switching time  $T_{sw}$ . In previous work, this has been achieved by implementing modern PWM techniques where two phases are switched and the state of the third phase is kept constant at On/Off during  $T_{sw}$  [75]

In terms of the CMV, it is reported that this undesirable voltage can be reduced by employing filters [75, 77]. Four CMV reduction methods were reported in literature, which are passive CMV filter, active CMV filter, isolation transformer, and modification of the existing PWM techniques such as SPWM and SVPWM techniques [75, 77]. As the equivalent circuit of the CMV filter and differential mode filter are identical, it is not easy to satisfy the requirements for different frequency characteristics [77]. Therefore, the passive CMV filter is not highly recommended. On the other hand, the active CMV filter is only available for high voltage levels [77]. In general, the reduction of the CMV by using filters required additional hardware equipment which increases the system cost, weight/size, and complexity [75]. Thus, due to the fact that the PWM techniques are relatively simple to be modified without any additional hardware or cost, it is quite common to reduce both the switching losses and CMV at the same time by modifying or employing new PWM strategies, [75].

According to [17], PWM techniques can be classified into continuous PWM (CPWM) techniques, and discontinuous PWM (DPWM) techniques. In the CPWM methods such as SPWM and SVPWM (see Figure 1.29) [17], the modulation waves are always within the triangle peak limits and within every carrier cycle triangle and modulation waves intersect, and, therefore, “On” and “Off” switching occur. In the DPWM methods such as DPWM0,1,2 and 3 (see Figure 1.29), the modulation wave of a phase has at least one segment which is clamped to the positive or negative DC rail for at most a total of 120, therefore, within such intervals the corresponding inverter leg discontinues modulation. Since no modulation implies on switching losses, the switching loss characteristics of CPWM and DPWM methods are different. Detailed studies indicated the waveform quality and linearity characteristics are also significantly different [17].

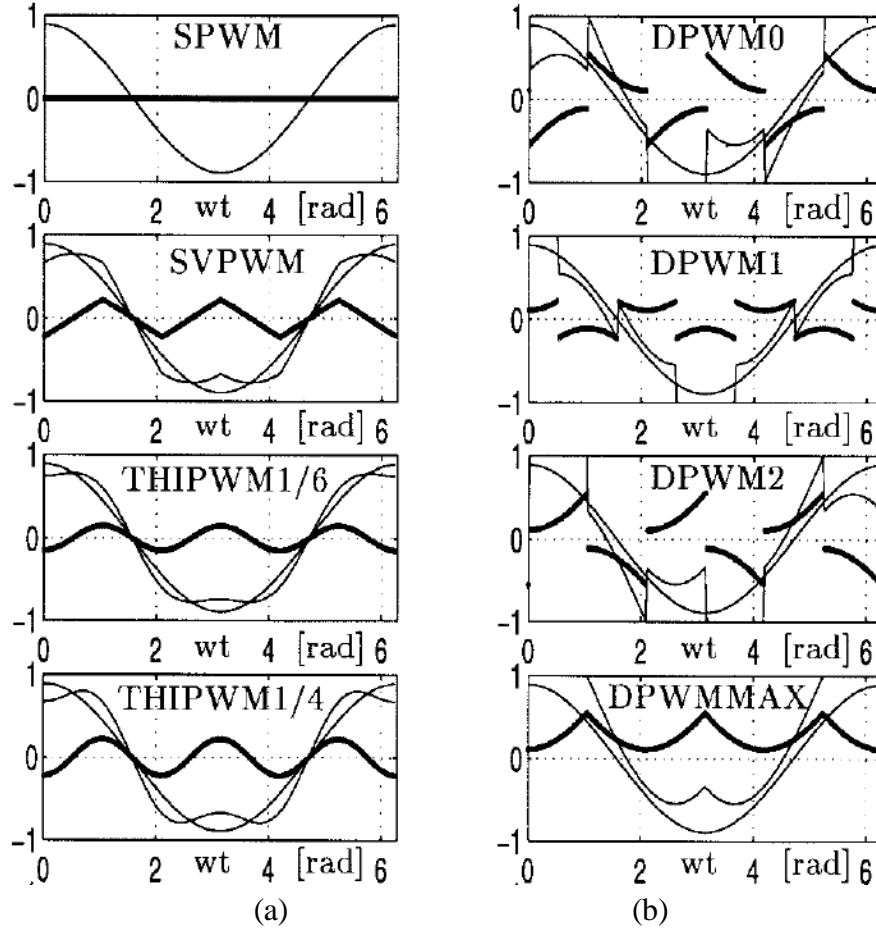


Figure 1.29 Modulation waveforms of (a) CPWM (b) DCPWM [17]

It is noted that the zero state vectors ( $V_0(000)$  and  $V_7(111)$ ), Figure 1.30 [78], which are utilised in the CPWM techniques (see Figure 1.28) to construct the command voltage vector  $\vec{V}_{com}$  expressed by its magnitude  $V_{com}$  and direction  $\delta_{com}$ , produces a CMV whose peak-to-peak value is  $\pm V_{dc}/2$ . This value is three times larger than that produced by the non-zero state vectors ( $\pm V_{dc}/6$ ), Figure 1.28. The non-zero state vectors are denoted by  $V_n$  and  $V_{n+1}$  respectively, Figure 1.30 (b). The states of these zero and non-zero vectors are shown in Table 1.2 [75]. Thus, it is possible to reduce the CMV if only non-zero states are used to construct the command voltage,  $\vec{V}_{com}$  [75]. Based on this phenomenon, the CMV reduction PWM techniques (RCMV-PWM) discussed in [75] use only non-zero state to produce  $\vec{V}_{com}$ . These RCMV-PWM techniques are referred to as active zero state PWM 1, 2 and 3 techniques (AZPWM1, AZPWM 2, and AZPWM 3), remote state PWM techniques (RSPWM) and near state PWM technique (NSPWM). The difference between these techniques is in the switching sequence they used to produce

$V_{com}$  [75]. It is noted that the peak-to-peak CMV is mostly reduced from  $\pm V_{dc}/2$  of the conventional PWM technique to  $\pm V_{dc}/6$  by the aforementioned RCMV-PWMs strategies [75].

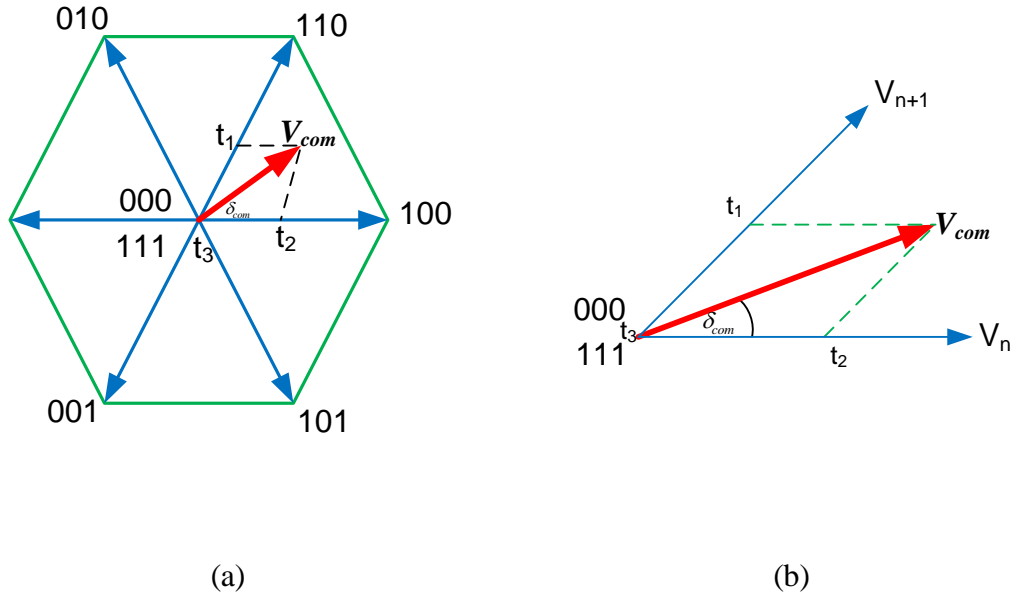


Figure 1.30 Space vector PWM (a) Reference voltage within SV hexagon, b) Constructing of  $V_{com}$  vector [78].

Table 1.2 Switching states of three phase inverter						
Index	a	b	c	$v_{an}$	$v_{bn}$	$v_{cn}$
$V_1$	0	0	0	0	0	0
$V_2$	1	0	0	$2/3$	$-1/3$	$-1/3$
$V_3$	1	1	0	$1/3$	$1/3$	$-2/3$
$V_4$	0	1	0	$-1/3$	$2/3$	$1/3$
$V_5$	0	1	1	$-2/3$	$1/3$	$1/3$
$V_6$	0	0	1	$-1/3$	$-1/3$	$2/3$
$V_7$	1	0	1	$1/3$	$-2/3$	$1/3$
$V_8$	1	1	1	0	0	0

According to the pulse pattern of DPWM1 and NSPWM techniques illustrated in [75], one of the inverter legs is kept “On” or ”Off” over the PWM period (i.e. only two phases are commutated). Therefore, the switching losses are expected to be reduced by one third per one switching period. For instance, Figure 1.31 [75] shows the pulse

pattern and the CMV of the NSPWM technique where phase “a” and “b” are switched and phase “c” is kept “Off” over the switching period. The peak-to-peak CMV voltage is reduced to  $\pm V_{dc}/6$  compared with the SVPWM technique ( $\pm V_{dc}/2$ ). The AZPWM1/2/3 techniques successfully reduce the CMV[75]. For example, AZPWM1 technique reduces the peak-to-peak of the CMV to be 3 times lower than that produced by the traditional SVPWM technique, Figure 1.32 [75]. However, an AZPWM1/2/3 technique fails in reducing the switching losses due to the fact that all the three inverter legs are switched during one switching period Figure 1.32 (b).

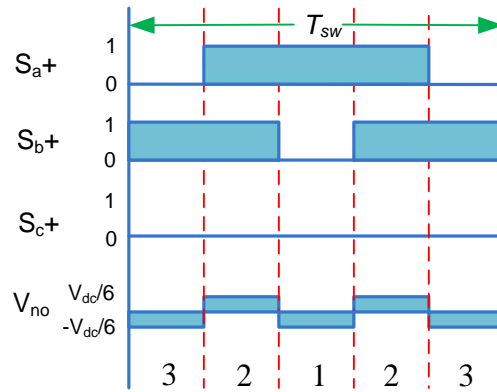


Figure 1.31 Switching pattern and peak-to-peak CMV of a VSI with NSPWM [75].

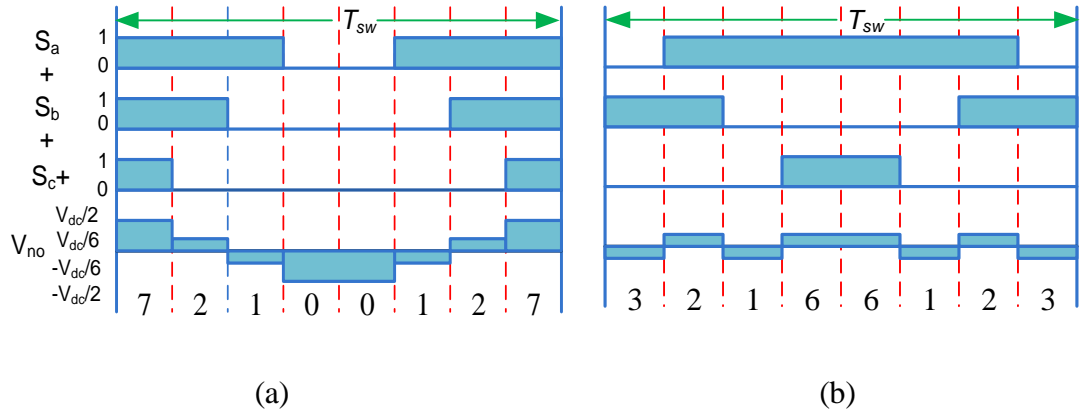


Figure 1.32 Switching pattern and peak-to-peak CMV of a VSI with (a) SVPWM (b) AZPWM1 [75].

Obviously, in order to satisfy the pulse pattern of AZSPWM2, AZSPWM3 and RSPWM3 techniques (see Figure 1.33) [75] presented in [75], two inverter legs are required to be switched at the same time. However, in reality, it is usually not possible

to switch two legs simultaneously due to the inverter dead time and disparity between the electronic components [75]. However, even if two legs are switched at the same time, a significant overvoltage may be created at the terminals of the motor which may damage the machine [75].

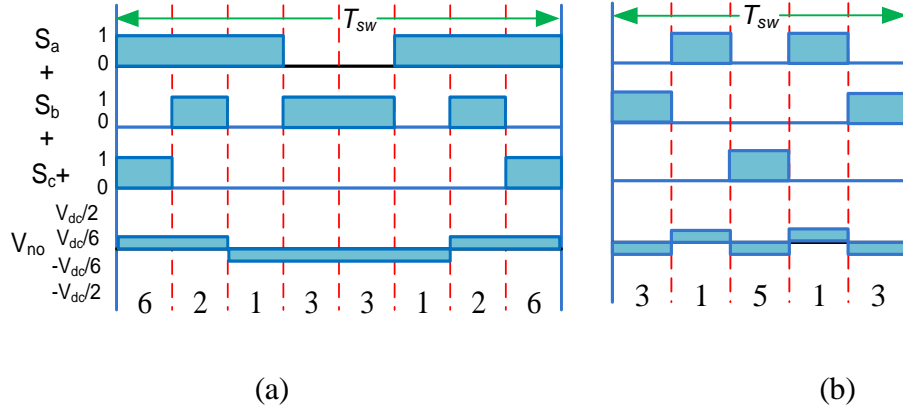


Figure 1.33 Switching pattern and Peak-to-peak CMV of a VSI with (a) AZPWM2 (b) RSPWM3 [75].

Usually, the  $(\alpha\beta)$  voltage hexagon space (see Figure 1.14) is divided into two regions depending on the value of the modulation index  $m_a$  which represents the ratio of the magnitude of the command voltage-to-the maximum modulated voltage [79]. These regions are defined as low modulation region ( $L$ -region) and high modulation region ( $H$ -region), and therefore:

- If  $m_a$  is lower than or equal to 0.6, then the command voltage is in the low modulation regions ( $L$ -region), Figure 1.34 [79].
- If  $m_a$  is greater than 0.6, then the command voltage is in the high modulation regions ( $H$ -region), Figure 1.34 [79].

Fundamentally, the ability of a PWM technique to modulate overall the  $(\alpha\beta)$  voltage hexagon low and high modulation regions (see Figure 1.34) [79] is defined as the voltage linearity of the PWM technique [75]. In other words, a PWM can be implemented in the low, high or both low and high modulation regions if its duty cycles have a valid solution in that region. It is noted that all the aforementioned PWM



techniques such as SVPWM and AZPWM1 techniques are able to modulate in the  $L$ - and  $H$ -region of the  $(\alpha\beta)$  voltage hexagon space except NSPWM technique which can only employed in the  $H$ -region due to the fact that its duty cycles can be only solved in this region [79].

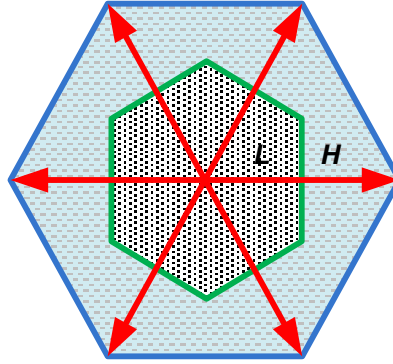


Figure 1.34 Modulation region of NSPWM [79].

Generally, implementation of non-zero RCMV-PWM techniques results in high current ripple especially in the  $L$ -region. This is due to the fact that they avoid using the zero states to construct  $\bar{V}_{com}$ . The current ripple is caused by the current harmonics resultant from the difference between the machine currents and the fundamental currents [78]. This difference is due to the deviation of the machine voltages from the fundamental voltages. Optimum PWM modulation requires the maximum difference of the current vector for several switching states becomes as small as possible to reduce the current harmonics, and therefore the current ripple [78]. This can only be realised if the three vectors adjacent to the command vector  $\bar{V}_{com}$  including the zero state vectors (see Figure 1.30) are used to construct this vector during a switching period. Therefore, avoiding of using the zero state vectors in the AZPWM1 and NSPWM techniques increases the deviation of the machine currents from the fundamental currents and consequently increases the current harmonics and the current ripple [80].

To reduce the effects of the problem of high current ripple produced by the non-zero RCMV-PWM techniques, a new PWM technique called LuPWM technique is proposed

in [80]. In the  $L$ -region, one zero voltage vector is used with the active vectors to the right and left of the reference vector to construct the command vector. The use of the zero vectors is avoided in the  $H$ -region where they have been replaced by the nearest active vector to the reference vector. This is due to the fact that current harmonics in high modulation region are significantly reduced due to high on-time duration of the PWM pulses. Theoretically, implementation of LuPWM technique reduces the peak-to-peak CMV to  $\pm V_{dc}/3$  and  $\pm V_{dc}/6$  in the  $L$ - and  $H$ -regions respectively, Figure 1.35[80]. In addition, it is expected that the switching losses will be reduced by one third in both modulation regions due to the fact that one phase is not switching during the whole switching period, Figure 1.35. Comparing with the NSPWM technique, the LuPWM technique can be employed in the  $L$ - and  $H$ -regions in addition to, it reduces the switching losses in both  $L$ - and  $H$ -regions unlike to the AZPWM1 technique which can only reduce the CMV.

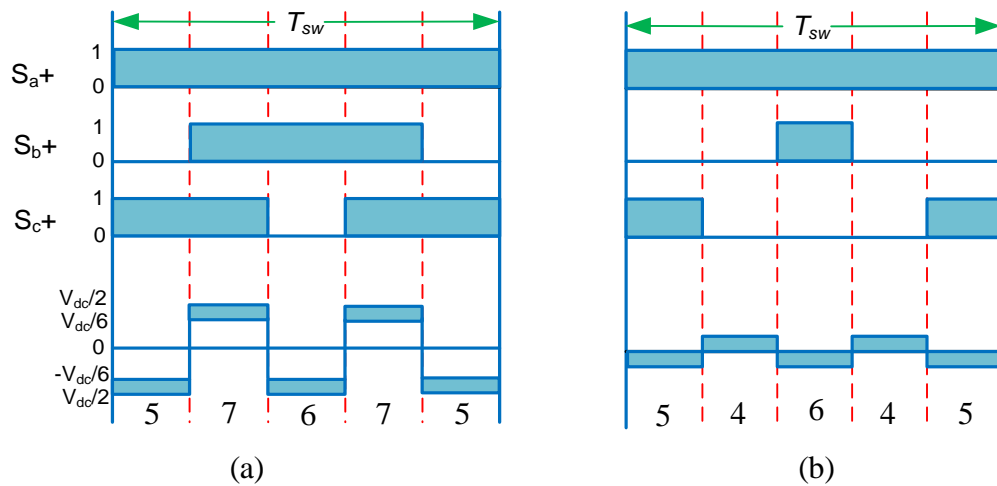


Figure 1.35 Switching pattern and peak-to-peak CMV of a VSI with LuPWM [79]. (a) L-region. (b) H-region.

## 1.3 Thesis Outlines, Contributions and Publications

### 1.3.1 Thesis Aims and Outlines

The thesis research is focusing on the minimisation of the power losses of an IPMSM drive for traction applications in order to increase the efficiency of the drive. The

IPMSM is characterised by high efficiency and high power density in addition to their ability to expand their operating speed to more than 2 or 3 times of the rated speed by weakening the flux [3, 7, 8]. These advantages make the IPMSM a very attractive option in traction applications. As mentioned in section 1.1, EV traction drives are fed by a set of battery packs which suffers from some limitations such as high cost, short life time and long charging time [5] therefore, minimising the power losses through the EV drive may lead to improve the battery performance and increases its life time which in turn decreases the need to maintenance, replace or recharge these batteries. Therefore, the aims of the thesis can be summarised as follows:

- The research aims to minimise both the IPMSM and inverter losses in order to improve the overall efficiency of the IPMSM drive for the whole operating speed range (both CTR and FWR).
- It is also aimed to consider the saturation effects of the IPMSM parameters which result in machine parameter variations associated with the operation conditions. These parameters are the dq-axis inductances and the flux linkage.
- Considering the effects of the voltage drop across the stator winding resistance which were almost neglected in previous works.
- One purpose of this research is to evaluate the impact of the parameters variations, resistive voltage drop and iron losses on the optimal operation of the IPMSM drive in order to clearly show the benefit of including these factors in the optimization criteria.
- In terms of the inverter, the research aims to achieve three goals:
  1. Scalar implementation of a LuPWM technique.
  2. Reduces the switching losses, which can shorten the inverter switching device life, without any additional hardware or increasing the drive system complication.
  3. As the CMV has negative effects on the drive performance such as it may damage the motor bearings and cause electromagnetic interference [75, 80], it is also aimed to reduce the CMV of the VSI via PWM technique.

The thesis is organised as follows:

**Chapter 1** introduces the thesis by giving a brief introduction to the EVs, the existing EVs drive technologies, literature review of motor losses minimisation algorithms for the control of IPMSM drive, and the existing switching losses and CMV reduction PWM techniques. Finally, the thesis research aims, outlines, contributions and publications are highlighted.

**Chapter 2** presents a detailed study for the latest switching losses and CMV reduction PWM techniques. The PWM techniques under study are also compared using a simulation study in terms of their switching pattern, switching losses, voltage linearity, implementation possibility, current and voltage waveforms and fast Fourier transform FFT.

**Chapter 3** gives a brief description of the topology, mathematical model, parameters and parameters nonlinearity of the utilised IPMSM. A losses minimisation algorithm (LMA) is developed in order to minimise the copper and iron losses taken into consideration of the parameter saturation effects and the stator winding resistive voltage. A simple and accurate iron losses model [81, 82] is utilised in order to accurately calculate the iron losses under the given operation point.

**Chapter 4** performs an intensive study in order to evaluate the influence of the IPMSM parameters variations, resistive voltage drop and finally the iron losses on the optimal operation point under specific speed and demand torque.

**Chapter 5** illustrates how to utilise the LMA presented in chapter 3 in controlling the IPMSM drive by generating non-linear LUTs of the dq current command based on this the LMA. The LuPWM, the modified LuPWM (Mod-LuPWM) and SVPWM techniques are implemented and their performances are compared by simulating the closed loop control Simulink model of the IPMSM drive.

**Chapter 6** deals with the experimental validation of the developed losses minimisation control algorithm described in Chapter 5. The SVPWM and Mod-LuPWM techniques are implemented and the obtained experimental results are compared. Agreement between the simulation and experimental results is illustrated.

**Chapter 7** summarises the thesis research and gives a conclusion of the developed work. It also illustrates the thesis outcome of the PhD research. The future works that can be extended from the research of this thesis is also presented.

### **1.3.2 Contributions**

The thesis contributions can be summarised as follows:

- The scalar implementation of the LuPWM technique is achieved in Chapter 2.
- A new IPMSM losses minimisation algorithm (LMA) is developed in Chapter 3. The copper and iron losses are minimised in both the constant torque and flux weakening regions. The IPMSM dq inductance variations, flux linkage variation and the voltage drop across the stator winding resistance are considered by the LMA. The LMA is initiated by using the constant (linear) parameters which are the parameters at the rated speed and maximum torque obtained by the finite element method (FEM). The LMA can be modified to be suitable for different brushless motor types, and it is very flexible and simple to implement.
- According to the intensive off-line simulation study presented in Chapter 4, the parameters variations have the most significant influence on the optimal operation point of the IPMSM especially at high torques and therefore it should be considered in used optimisation criteria. The impact of the iron losses in the optimal operation of the IPMSM is depending on the IPMSM machine design and the materials used in the motor constructions.
- Non-linear look up tables of the  $i_d$  and  $i_q$  current commands are generated in Chapter 5 based on the LMA in order to utilise the LMA in IPMSM controlling purposes.

- The performance of the LuPWM technique is investigated in Chapter 5 under closed loop control conditions. The simulation investigation shows that the quality of the phase currents produced by the LuPWM technique is highly distorted compared with that generated with SVPWM technique especially in the low voltage modulation region. The distortion in the LuPWM current waveforms is investigated and it is concluded that the ripple of the electrical angular position caused this distortion.
- The pulse pattern of the LuPWM technique is modified by holding the state of the current pulse constant until the command voltage passes the sector transitions point in order to eliminate or reduce the distortion effect.

### **1.3.3 Publications**

- **Papers have been published**

[1] A New Losses Minimization Algorithm for Interior Permanent Magnet Synchronous Machine Drives. H. Aorith, J. Wang, and P. Lazari

[2] Online feedback-based field weakening control of interior permanent magnet brushless AC drives for traction applications accounting for nonlinear inverter characteristics. K. D. Hoang, J. Wang, and H. Aorith

- **Paper submitted to reviewer**

[1] Online feedback-based flux weakening control of IPMSM drives considering inverter nonlinearities for traction application. K. D. Hoang, J. Wang, and H. Aorith on IEEE Transaction on Vehicular Technology

- **Papers to be considered**

[1] A New Losses Minimization Algorithm for IPMSM drives with the accounting for parameters saturation and stator winding resistive voltage drop. H. Aorith, J. Wang, and K. D. Hoang (on IEEE Transaction on Vehicular Technology)

- [2] The influence of IPMSM parameters saturation effect, stator windings resistive voltage drop and iron losses on the optimal operation of the IPMSM drive. H. Aorith, J. Wang, and K. D. Hoang
- [3] Comparative study of recent CMR-PWM techniques and LuPWM technique scalar implementation. H. Aorith, J. Wang, and K. D. Hoang
- [4] Performance evaluation of the LuPWM technique in driving EV drive system. H. Aorith, J. Wang, and K. D. Hoang

## 2. MINIMISATION OF THE INVERTER LOSSES AND REDUCTION OF THE COMMON MODE VOLTAGE

### 2.1 Introduction

The machine losses and the inverter losses are the two main losses components of a machine drive system contributing to the total drive losses. As the machine losses will be discussed in Chapter 3, this Chapter deals with the inverter losses as well as common mode voltage (CMV) reduction by using different modern pulse width modulation (PWM) techniques.

Basically, the increase in inverter losses strongly affects the drive cost. Therefore, for a well-designed drive system, the inverter losses should be evaluated in order to improve the inverter efficiency and reduce the drive cost. However, it has been reported that [74] the inverter losses almost do not affect the optimal operation of a given drive where the difference between the drive optimal current levels, with and without considering the inverter losses, is negligible. This is due to the fact that for a given torque, the drive power losses curves in the region close to the minimum tend to be flat. Therefore, a small shift in the optimal current level considering the inverter losses would not affect the resultant drive optimal power losses point. Consequently, considering the inverter losses in a power losses minimisation criteria will not result in significant difference in the drive minimum operation points [74]. However, in a high switching frequency application, which may cause significant switching losses, the efficiency of the inverter may decrease and results in damaging the inverter switching devices. Minimisation of the inverter losses, especially the switching losses can increase the power electronics semiconductor devices' life and consequently reduce the cost of the drive maintenance. As mentioned in section 1.2.2, high switching frequency and CMV can lead to generate high common mode leakage current (CMC) across the voltage source inverter [75]. The CMC may damage the motor bearings and the insulation system of the motor windings, create electromagnetic interference noises which cause undesirable trip of the inverter drive, or interfere other electronic equipment in locality [75, 76]. In practice, the CMV



can mainly be reduced by using the passive or active filters [75]. However, this will lead to considerable increase in the drive system cost and complexity since extra hardware devices will be required [75]. Therefore, instead of employing extra hardware devices, reduction of the CMV is often achieved by modifying the PWM techniques [75, 77].

In this Chapter, a brief mathematical description of the CMV of a voltage source inverter (VSI) is presented in section 2.2. Then, CMV reduction PWM (RCMV-PWM) techniques [75, 80] are described in section 2.3 where their advantages and disadvantages over the conventional PWM strategies such as SVPWM technique are highlighted. The implementation of the LuPWM techniques, which was proposed for better achievement in switching losses and CMV reduction [76, 80, 83], is presented in section 2.4. Simulation results using Matlab/Simulink with SimPowerSystems of the studied PWM techniques such as phase voltage waveforms, current waveforms, and CMV waveforms are discussed in section 2.5. A comparative study in terms of voltage linearity, current ripple, the peak-to-peak CMV, the switching pattern and the reduction in the switching losses of these PWM strategies is presented in section 2.6. The Chapter content is summarised in section 2.7.

## **2.2 Inverter Common Mode Voltage**

The CMV of a VSI with three legs and six insulated-gate bipolar transistors IGBT switches ( $S_1$  to  $S_6$ ) connected to a star-connection PMSM Figure 2.1 [12], is defined by the voltage across the PMSM neutral point and inverter zero voltage level. From Figure 2.1, the CMV can be calculated according to Eqns. 2.1 to 2.7 [75].

$$V_{ao} = V_{an} + V_{no} \quad 2.1$$

$$V_{bo} = V_{bn} + V_{no} \quad 2.2$$

$$V_{co} = V_{cn} + V_{no} \quad 2.3$$

where,  $V_{ao}$ ,  $V_{bo}$  and  $V_{co}$  are the inverter phase-to-zero output voltages,  $V_{an}$ ,  $V_{bn}$  and  $V_{cn}$  are the phase-to-neutral voltages across the load and  $V_{no}$  is the neutral-to-zero voltage or the CMV. The summation of the inverter phase-to-zero output voltages is given by:

$$V_{ao} + V_{bo} + V_{co} = V_{an} + V_{bn} + V_{cn} + 3V_{no} \quad 2.4$$

For a balanced three phase star connection machine:

$$V_{an} + V_{bn} + V_{cn} = 0 \quad 2.5$$

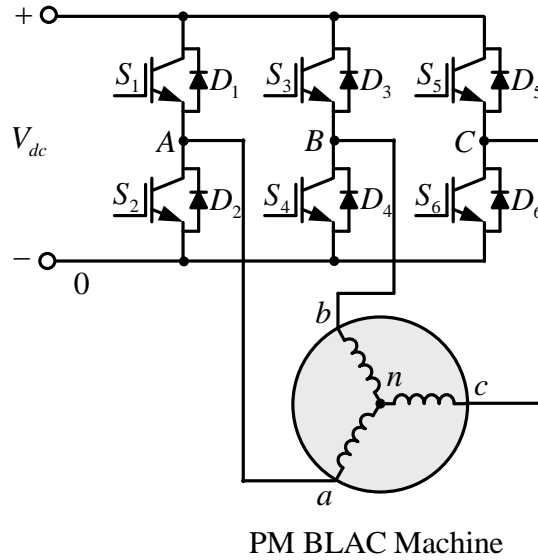


Figure 2.1 Voltage source inverter (VSI) connected to PM BLAC [12].

Substituting from 2.5 into 2.4, Eqn. 2.5 yields to Eqn. 2.8 and therefore, the CMV is given by Eqn. 2.7:

$$V_{ao} + V_{bo} + V_{co} = 3V_{no} \quad 2.6$$

$$V_{no} = (V_{ao} + V_{bo} + V_{co})/3 \quad 2.7$$

## 2.3 PWM Strategies for Switching Losses and CMV Reduction

Traditional PWM methods is based on the space vector hexagon with the six active vectors and two zero vectors shown in Figure 2.2 [78]. For notational convenience, the

voltage vectors are denoted by  $V_j$  where  $j$  is the voltage vector number corresponding to the three-bit binary code associated with a given switching state, Table 1.2. For example, the voltage vector associated with switching state (101) is denoted by  $V_5$ . These PWM methods such as SVPWM technique produces high CMV especially during switching periods of the zero vectors  $V_0$  (000) and  $V_7$  (111) [84]. Figure 2.3(a) [75] illustrates the switching pattern of phases  $a$ ,  $b$  and  $c$  in the first sector of the hexagon of the SVPWM technique for one switching period ( $T_{sw}$ ).

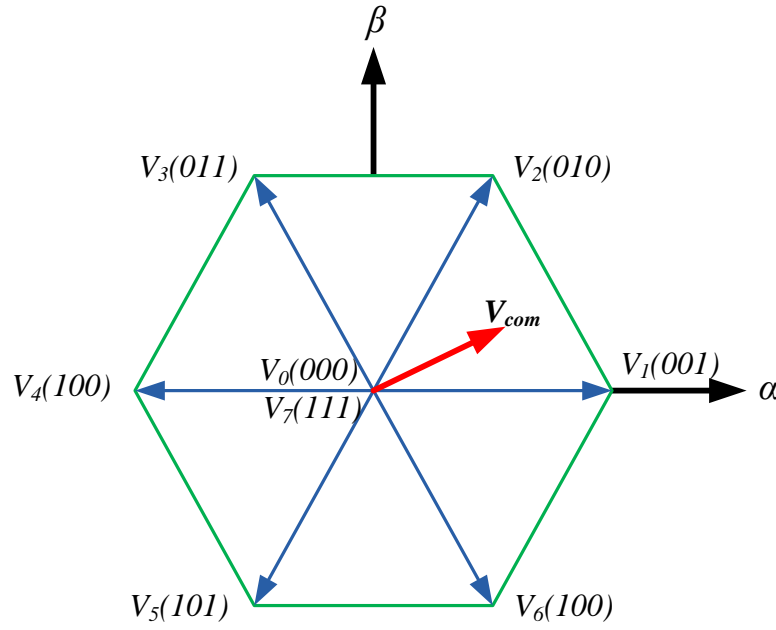


Figure 2.2 Space vector hexagon formed by the two zero vectors ( $V_0$  and  $V_7$ ) and the six active vectors ( $V_1$  to  $V_6$ ) [78].

Using Eqn. 2.7, it is obvious that the employing of the two zero vectors shows the highest peak-to-peak value of the generated CMV during  $T_{sw}$ . Therefore, if the employment of the zero vectors can be avoided during the switching period, the CMV can be reduced. Most CMV reduction PWM strategies such as Active-Zero PWM1 (AZPWM1) [75], Near-state PWM (NSPWM) [79] and LuPWM [76, 80, 83] techniques follow this methodology to reduce the CMV. These RCMV-PWM techniques are defined based on the selected active vector strategy employed to generate the reference voltage vector  $\bar{V}_{com}$ . Generally, these PWM techniques are classified into

two types depending on the defined angle of the first sector in the  $(\alpha\beta)$  voltage hexagon space, Figure 2.2. Basically, PWM techniques with the first sector starts at zero angle referred to the  $\alpha$ -axis such as SVPWM and AZPWM1 techniques are defined as A-type sector as shown in Figure 2.4 (a) (sector  $A_1$  to  $A_6$ ). On the other hand, PWM techniques with the starting angle of each sector of the hexagon is shifted by 30 degrees referred to the  $\alpha$ -axis (such as NSPWM and LuPWM techniques) are defined by B-type sector PWMs (sector  $B_1$  to  $B_6$ ) as shown in Figure 2.4 (b) [75].

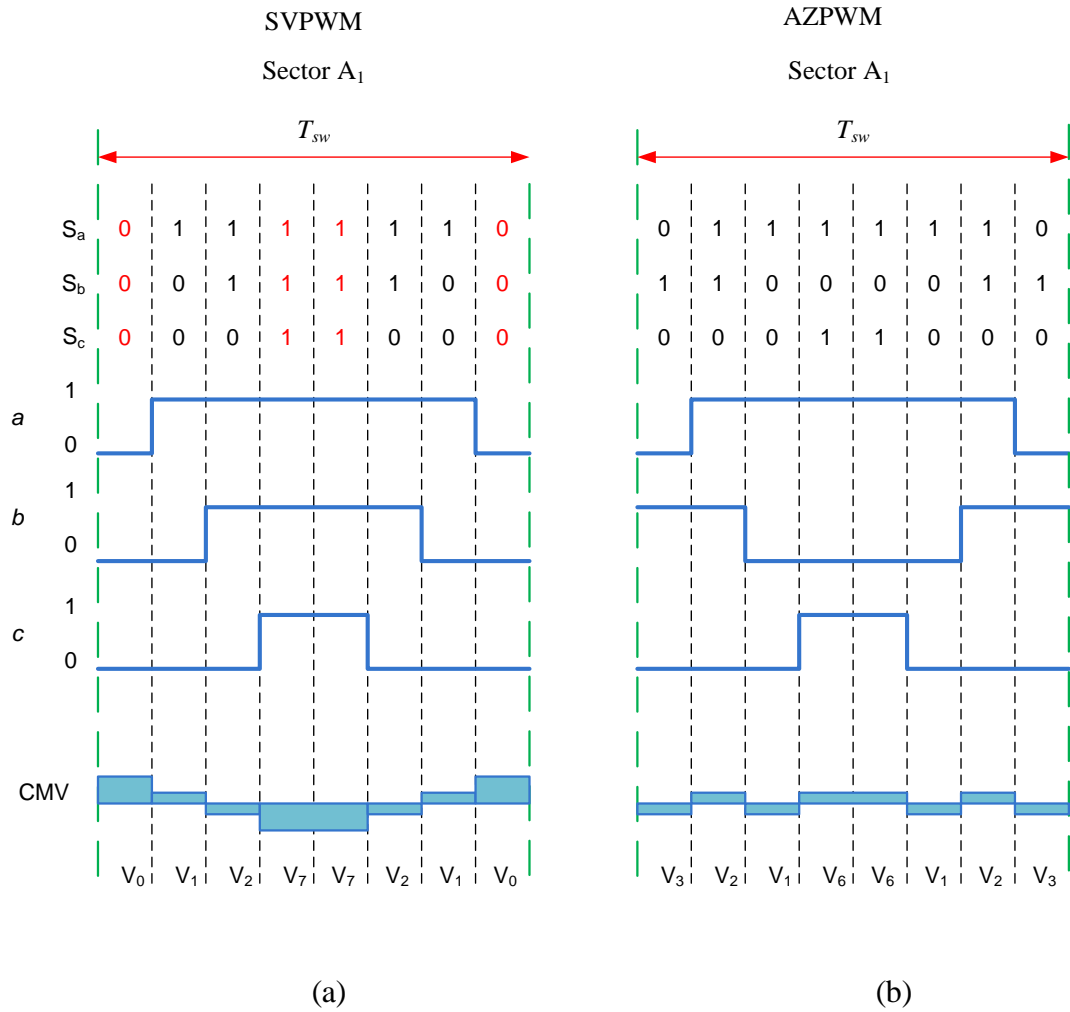


Figure 2.3 Switching sequence and generated CMV of (a) SVPWM and (b) AZPWM1[75].

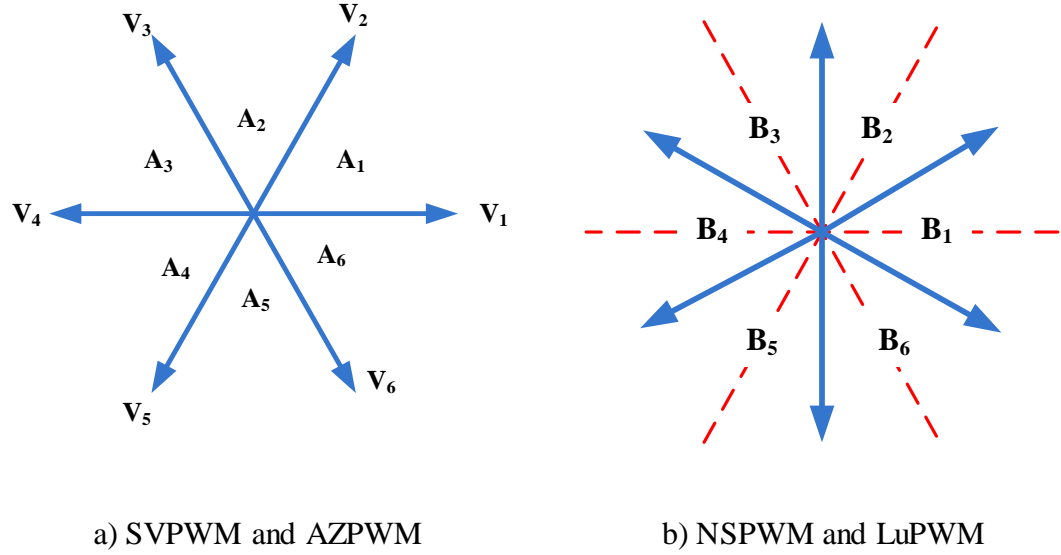


Figure 2.4 Voltage vector and the definitions of A- and B- sectors of the studied PWMs [75].

Figure 2.3 shows the switching vectors of the SVPWM and AZPWM1 techniques in sector  $A_1$ . Both SVPWM and AZPWM1 techniques have eight switching states in one switching period  $T_{sw}$  with all inverter legs performing switching during the switching period  $T_{sw}$ . However, inverter legs of drive system under SVPWM and AZPWM1 techniques are switched with different strategies. In the well-know SVPWM technique, the voltage command vector  $\vec{V}_{com}$  (see Figure 2.2) will be constructed by switching two zero vectors  $V_0$  and  $V_7$  and the two active vectors regarding the sector where the voltage reference vector is located. By way of example, when the voltage reference vector is in sector  $A_1$  (see Figure 2.4 (a)) vectors  $V_1$  and  $V_2$  are chosen for the modulation. As can be seen from Figure 2.3 (a), the zero vectors create high level of the peak-to-peak CMV which is about  $\pm V_{dc}/2$  compared to  $\pm V_{dc}/6$  produced by the two active vectors  $V_1$  and  $V_2$ . However, in the AZPWM1 technique, by replacing the two zero vectors  $V_0$  and  $V_7$  by  $V_6$  (101) and  $V_3$  (010), which are the closest opposing vectors to the active vectors  $V_1$  and  $V_2$ , the CMV is reduced to about  $\pm V_{dc}/6$  during the switching time of these two new vectors, Figure 2.3(b).

As mentioned in item 1.2.2, the  $(\alpha\beta)$  voltage hexagon space is divided into two regions which are the high modulation region ( $H$ -region) and low modulation region ( $L$ -region)

depending on the value of the modulation index  $m_a$ , Figure 2.5 [76, 80, 83]. It is also mentioned that the duty cycles of the SVPWM and AZPWM1 techniques have a valid solution in the overall region of the  $(\alpha\beta)$  voltage hexagon space therefore; they can be employed in both the  $L$ - and  $H$ -regions [75]. Conversely, the NSPWM technique cannot be employed in the  $L$ -region as its duty cycles yield invalid solution in this region [79]. Consequently, the NSPWM technique can be employed to generate  $\bar{V}_{com}$  in the  $H$ -region only. Figure 2.6(a) [75] illustrates the active voltage vectors that are used to construct  $\bar{V}_{com}$  in sector  $B_I$  of the NSPWM technique ( $H$ -regions) [75] where three active vectors which are the nearest active vector to  $\bar{V}_{com}$  and its two nearby vectors to the left and right are used to develop this reference voltage vector. For instance, if the reference voltage vector occurs in sector  $B_I$ , then vectors  $V_1$ ,  $V_2$  and  $V_6$  are used to form this reference voltage (see Figure 2.6 (a)). The NSPWM technique switching method reduces the peak of the CMV to  $V_{dc}/6$  during the switching period, Figure 2.6 (a) [75].

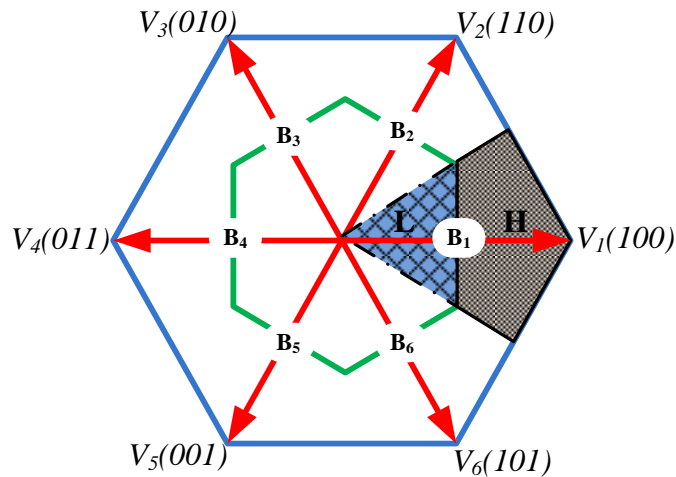


Figure 2.5 Space vector hexagon with the definition of high and low modulation regions [76, 80, 83].

The switching sequence of the SVPWM, AZPWM1, NSPWM and LuPWM techniques (LuPWM technique will be discussed later in this section) in the different  $A$ - and  $B$ -regions is given in Table 2.1 [75], where the series numbers given for every region represents the voltage vector numbers and their switching sequence which should be used to form the command voltage vector [75, 80]. For example, if the command

voltage lay in region  $A_3$  then the voltage vectors  $V_2$ ,  $V_3$ ,  $V_4$  and  $V_5$  should be chosen for AZPWM1 technique and the switching sequence is denoted as 5432345, and so on.

In [75] it is concluded that the NSPWM technique has better performance than AZPWM1 technique in the  $H$ -region, but due to the limitation of the NSPWM technique in the  $L$ -region it is suggested that the AZPWM1 technique should be utilised in the  $L$ -region and the NSPWM technique should be employed in the  $H$ -region in order to reduce the CMV in the whole modulation regions of the hexagon space.

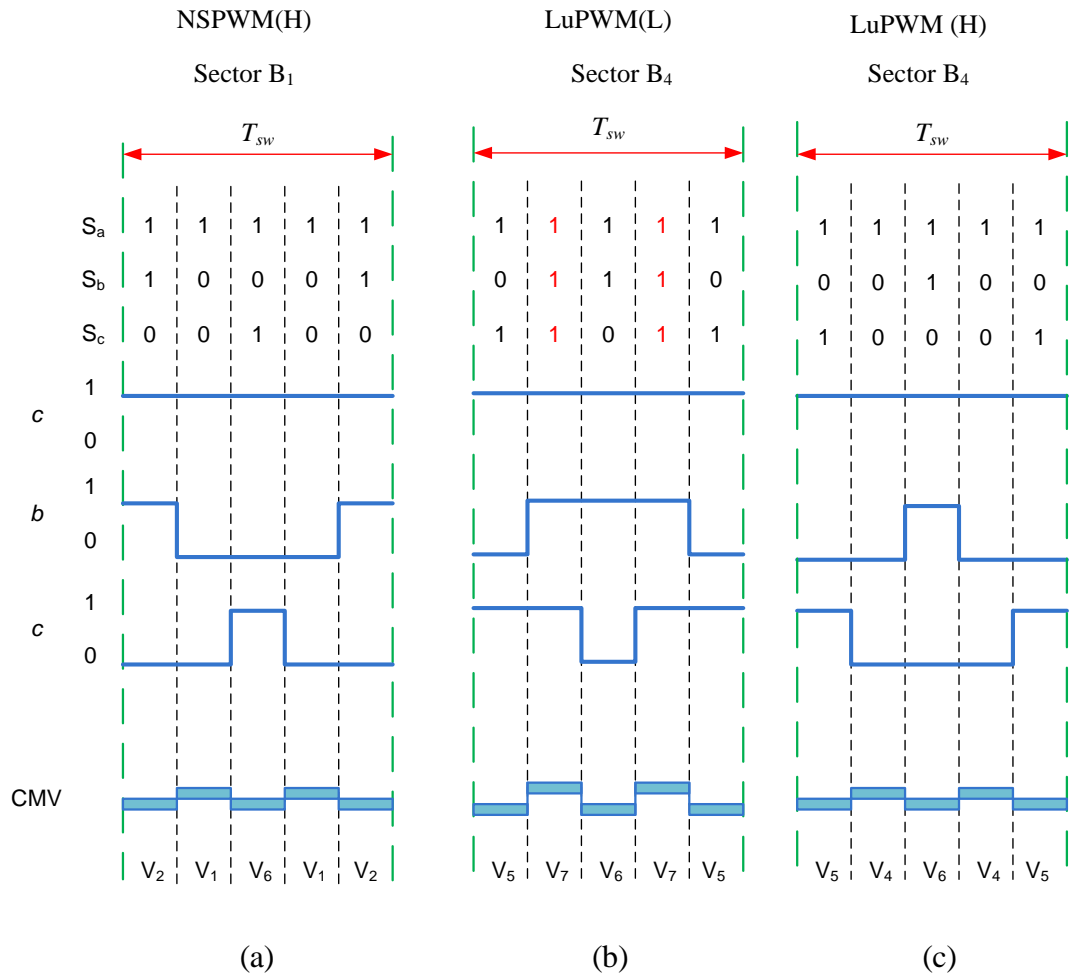


Figure 2.6 Switching sequence and produced CMV of (a) NSPWM (b) LuPWM  $L$ -region (c) LuPWM  $H$ -region [75, 76, 80, 83].

Form Table 2.1 it is noted that, the using of the zero vectors are totally avoided in both the NSPWM and AZPWM1 techniques in order to reduce the CMV. According to [78],

this leads to increase the current ripple which in turns will cause an undesirable torque ripple especially in the  $L$ -region where AZPWM1 technique is utilised. As mentioned in Chapter 1, the current ripple results from the current harmonics which are produced by the difference between the machine currents and the fundamental currents [78]. This difference should be as small as possible in order to reduce the current harmonics and therefore optimum PWM modulation can be obtained. This can only be achieved by including the non-zero vectors as well as the zero vectors adjacent to the command vector  $\bar{V}_{com}$  in the production process of this command vector. For instance, if  $\bar{V}_{com}$  is located in sector  $A_1$  and the SVPWM technique is implemented, then the vectors  $V_0$ ,  $V_7$ ,  $V_1$  and  $V_2$  (see Figure 2.2) should be used to generate the reference voltage  $\bar{V}_{com}$ . In this case, the switching of the inverter legs starts from one zero state and ending in the other zero state, Figure 2.3 (a) (i.e. the switching sequence should be 0127210 in order to reduce the current harmonics and shorten the cycle time).

Table 2.1 Switching sequence of AZPWM1, NSPWM and LUPWM [75]

	A <sub>1</sub>	A <sub>2</sub>	A <sub>3</sub>	A <sub>4</sub>	A <sub>5</sub>	A <sub>6</sub>
SVPWM	0127210	0327230	0347430	0547450	0567650	0167610
AZPWM1	3216123	4321234	5432345	5432345	6543456	2165612
	B <sub>1</sub>	B <sub>2</sub>	B <sub>3</sub>	B <sub>4</sub>	B <sub>5</sub>	B <sub>6</sub>
NSPWM	21612	32123	43234	54345	65456	16561
LuPWM (L)	37573	67376	20102	57675	10401	40204
LuPWM (H)	35153	62326	23132	54645	15451	46264

In addition to the current ripple problem, AZPWM1 technique does not reduce the switching losses as all the three inverter legs are switched in one switching period, Figure 2.3 (b). Basically, LuPWM technique [76, 80, 83] is presented as a solution of both the limitation of AZPWM1 and NSPWM techniques where unlike the NSPWM technique, the duty cycles of the LuPWM technique have a valid solution in both the  $L$ -region and  $H$ -region and therefore, it can modulate overall the  $\alpha\beta$  voltage hexagon space. Moreover, it is expected to reduce the current ripple in the  $L$ -region compared with AZPWM1 technique by utilising one zero vector in addition two active vectors to



the right and left of the command vector [80] in order to construct  $\bar{V}_{com}$ . In the LuPWM technique, the selection of the active vectors (see Table 2.1) used to form the  $\bar{V}_{com}$  is  $m_a$  dependant and to do so the hexagon  $L$ - and  $H$ -region definitions are also utilised, Figure 2.5. Basically, in the  $L$ -region of LuPWM technique, a zero vector and the vectors to the right and left of the command vector are switched while the closest vector to the reference voltage is omitted, Figure 2.6 (b) [76, 80, 83]. Conversely, the nearest active voltage vector is used instead of the zero vectors, if the reference voltage occurs in  $H$ -region (see Figure 2.6 (c)) [76, 80, 83]. From Figure 2.6 (b) and (c) [76, 80, 83], it is noted that one phase status under LuPWM technique is kept constant (totally On or totally Off) during  $T_{sw}$  in both  $L$ -region and  $H$ -region. Therefore, unlike AZPWM1 and NSPWM techniques, the switching losses will be reduced in both regions by the LuPWM technique. The transition between the  $L$ - and  $H$ -regions is governed by the conditions statements given by Eqn. 2.8 and 2.9 respectively [79].

$$\text{If } m_a \leq 0.61 \text{ then } L\text{-region LuPWM is chosen} \quad 2.8$$

$$\text{If } 0.61 > m_a > 0.907 \text{ then } H\text{-region LuPWM is chosen} \quad 2.9$$

## 2.4 Implementation of Switching Losses and Common Mode Voltage Reduction PWM Strategies

The duty cycles as well as the theory and implementation of the SVPWM, NSPWM and AZPWM1 techniques have been discussed in the previous studies [79, 84-88]. The implementation of the LuPWM technique is proposed in [80] and the focus was on the derivation of its duty cycles. Less attention has been paid to the details of the scalar implementation of this modern PWM technique where the PWM On/Off switching events is defined by the intersections of a triangular carrier wave with the reference modulation waveforms [17]. Therefore, the scalar implementation of the LuPWM technique is discussed in detail in this section.

According to [17], the LuPWM technique can be classified as a discontinuous carrier-based PWM technique (DPWM) where one phase is kept constant (totally On or totally

Off) during one  $T_{sw}$  as shown in Figure 2.6 (b) and (c). In carrier-based PWM techniques [17], the reference modulation waveforms are injected by a zero-sequence signal which is selected depending on the PWM technique voltage linearity, the quality of the waveforms and the switching losses [17]. The principles of scalar implementation of a PWM technique with the injection of a zero sequence signal is illustrated in Figure 2.7 [17] where the zero-sequence signal is denoted by  $V_o$ , the reference voltage waveforms are denoted by  $V_a^*$ ,  $V_b^*$  and  $V_c^*$ , and the modulation waveforms are denoted by  $V_a^{**}$ ,  $V_b^{**}$  and  $V_c^{**}$  ( $V_a^{**} = V_a^* + V_o$ ,  $V_b^{**} = V_b^* + V_o$  and  $V_c^{**} = V_c^* + V_o$ ). The zero-sequence of SVPWM and AZPWM1 techniques are identical and it is given by 2.10.

$$V_o = 0.5 * V_a^* \quad 2.10$$

It is noted that the same zero-sequence signal, which is given by Eqn. 2.11, is usually used to implement the DPWM techniques such as DPWM1, DPWM2 and NSPWM techniques [17, 79]. It has been reported that the zero-sequence signal extends the voltage linearity, exhibits superior quality of the waveforms and considerably reduces the inverter switching losses [17].

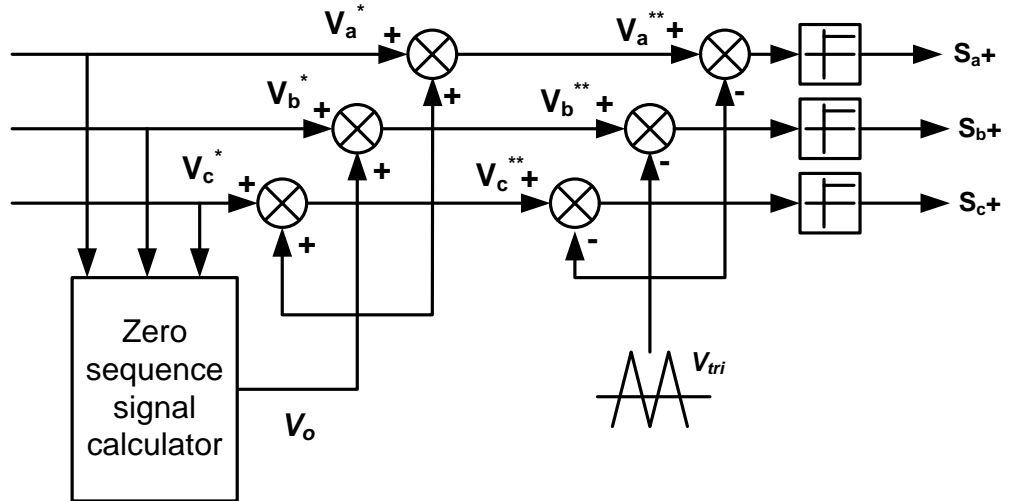


Figure 2.7 Scalar implementation of PWM with the injection of zero sequence signal  $V_o$  [17].

$$V_o = \text{sign}(V_a^*) \left( \frac{V_{dc}}{2} \right) - V_a^* \quad 2.11$$

As LuPWM technique can be classified as a DPWM technique [17], the zero-sequence signal given by Eqn. 2.11 is selected to be used to implement it [17]. The reference (fundamental) waveforms, modulation waveforms (modulator) and the zero-sequence signals of the PWM techniques under study are shown in Figure 2.8, Figure 2.9 and Figure 2.10, respectively taken in consideration that the waveforms of SVPWM and AZPWM1 techniques in  $L$ -region are identical, and the waveforms of the LuPWM and NSPWM techniques in the  $H$ -region (see Figure 2.10) are similar. The modulation waveforms of the LuPWM technique in the  $L$ -region and  $H$ -region (see Figure 2.9 and Figure 2.10, respectively) are almost following the same trend and the difference is only in their magnitudes due to the difference in command voltage magnitude in the two regions.

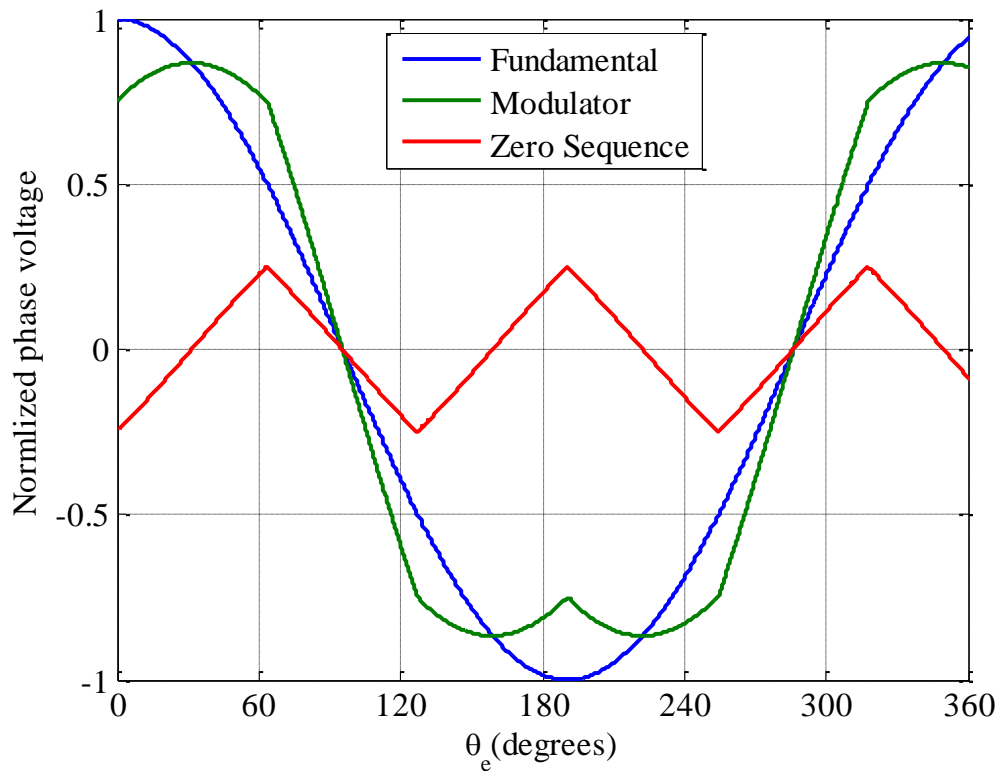


Figure 2.8 Modulation waveforms of SVPWM and AZPWM1.

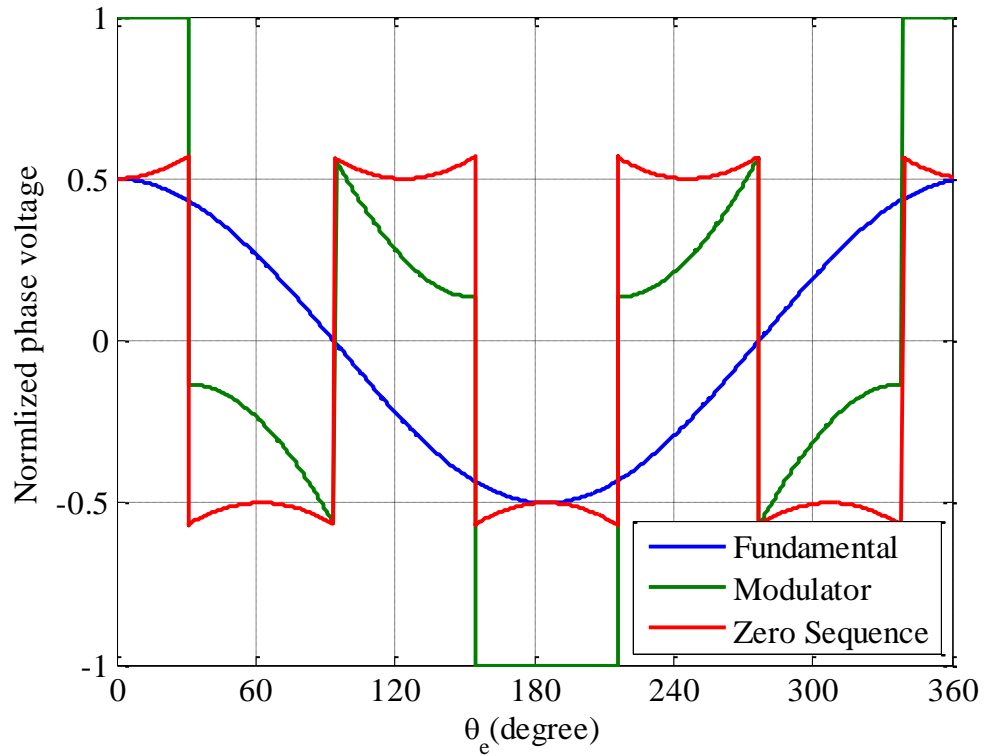


Figure 2.9 Modulation waveforms of LuPWM in *L*-region.

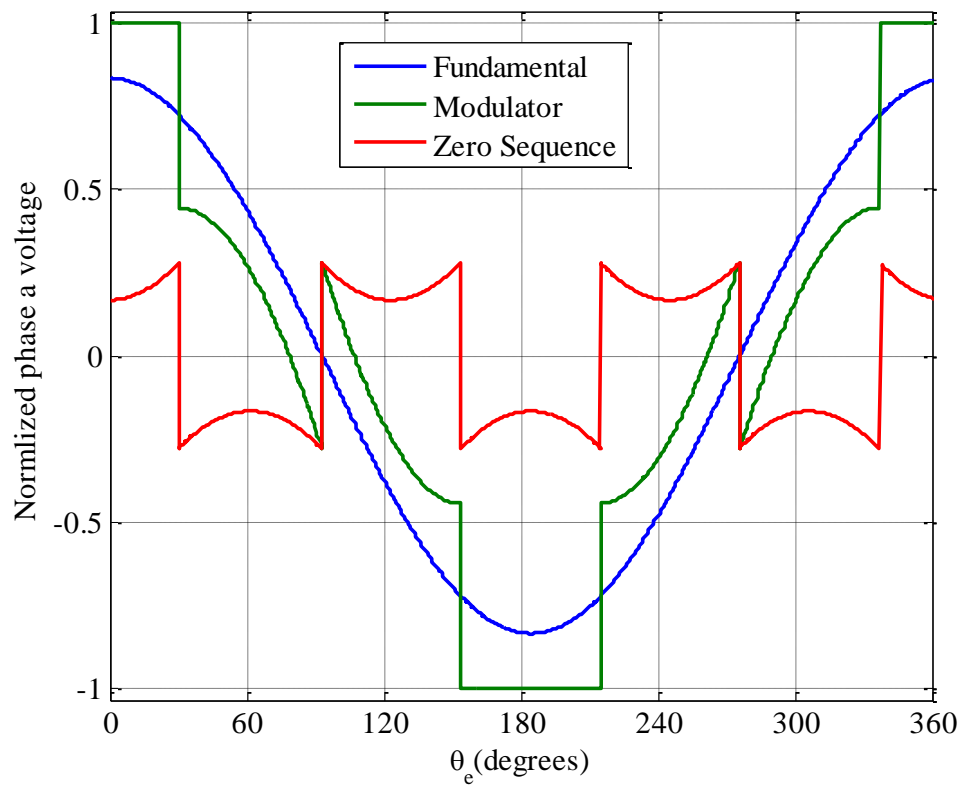


Figure 2.10 Modulation waveforms of NSPWM and LuPWM in *H*-region.

The scalar implementation of the LuPWM technique can be achieved by comparing its modulator waveforms in the  $L$ -region and  $H$ -region with positive and negative triangular carrier waves ( $V_{tri}$  and  $-V_{tri}$  respectively) with a magnitude of  $\pm V_{dc}/2$  and a frequency equal to the switching frequency  $f_{sw}$  as shown in Figure 2.11.

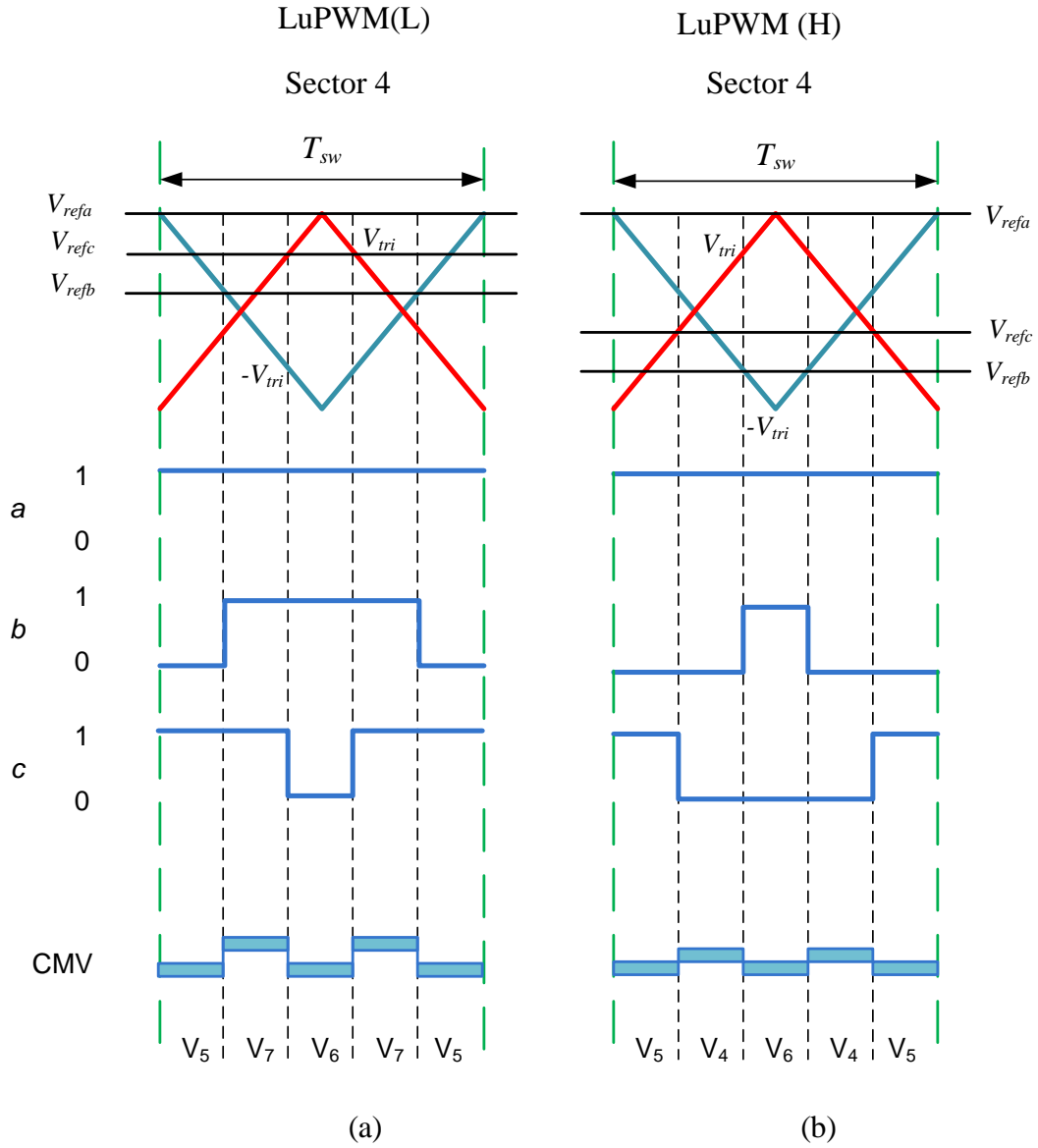


Figure 2.11 Scalar implementation of LuPWM (a)  $L$ -region (b)  $H$ -region.

The comparing of the modulator waveforms (see Figure 2.9 and Figure 2.10) with  $V_{tri}$  or  $-V_{tri}$  is depending on the sector number “ $n$ ” ( $n = 1$  to 6) and the pulse pattern that is required to be generated in the current sector. The general rule of this comparison is that

at the switching instance, if the modulation waveform is greater than  $V_{tri}$  ( $-V_{tri}$ ), the upper switch of the inverter leg of the associated phase is turned “On” (i.e. the upper PWM pulse is “1”) and the lower switch is turned “Off” (i.e. the lower PWM pulse is “0”). The state of each switch is kept constant until the  $V_{tri}$  ( $-V_{tri}$ ) become greater than the modulation waveforms, then the switches state will be reversed. For each switching period of the LuPWM, the PWM pulse in the  $L$ -region and  $H$ -region consists of five segments (see Figure 2.11) with five states (0/1). The waveforms  $V_{tri}$  or  $-V_{tri}$  which will be compared with the modulator during the switching period should be selected to produce the right state for each segment. For example, in the  $L$ -region of sector 4 (see Figure 2.11 (a)) the required states of the five segments for phase “a” are “1 1 1 1 1”, for phase “b” are “0 1 1 1 0” and for phase “c” are “1 1 0 1 1”. Careful studying of Figure 2.11 (a), one can identify that the modulator of phase “a” can be either compared with  $V_{tri}$  or  $-V_{tri}$  as both of them are smaller than phase “a” modulator for the whole switching period of sector 4. The modulator of phase “b” is needed to be greater than the triangular carrier wave for the three middle segments denoted by  $V_7$ ,  $V_6$  and  $V_7$  respectively (see Figure 2.11 (a)) in order to generate the right pulse pattern of this phase. The triangular carrier wave which satisfies this condition is  $-V_{tri}$ , therefore it is selected. Phase “c” modulator should be smaller than the triangular carrier wave for the middle segment denoted by  $V_6$  (see Figure 2.11(a)) to produce the required pulse pattern of this phase in sector 4. The triangular carrier wave which satisfies this condition is the  $V_{tri}$ ; therefore it is chosen to be compared with phase “c” sector 4.

Similar procedure can be done in order to select the right triangular carrier wave for each sector in the  $L$ -region and  $H$ -region of the hexagon (see Figure 2.5). The modulation waveforms are simulated in each sector for  $L$ -region and  $H$ -region and the triangular wave  $V_{tri}$  or  $-V_{tri}$  which produce the right switching pattern for each phase is given in Table 2.2.

Table 2.2 Dependency of the selected triangular waveforms on sector number						
$n$	1	2	3	4	5	6
a	$-V_{tri}$	$V_{tri}$	$V_{tri}$	$V_{tri}$	$-V_{tri}$	$V_{tri}$
b	$V_{tri}$	$V_{tri}$	$V_{tri}$	$-V_{tri}$	$V_{tri}$	$-V_{tri}$
c	$V_{tri}$	$-V_{tri}$	$-V_{tri}$	$V_{tri}$	$V_{tri}$	$V_{tri}$

## 2.5 Simulation Results

The PWMs under study are implemented using Simulink and SimPower system Matlab toolboxes. The VSI model is connected to a three phase star connection inductive load. The resistor and inductor values of each phase of the R-L inductive load is  $0.0521\Omega$  (the phase resistor of the utilised IPMSM) and  $3mH$  (the summation of the average values of the dq-axis inductances of the utilised IPMSM) respectively. The switching frequency  $f_{sw}$  and the DC-link voltage  $V_{dc}$  is 8 kHz and 120V, respectively. The phase “a” voltage referred to the neutral star point of the SVPWM, AZPWM1, NSPWM and LuPWM techniques in the hexagon regions are shown in Figure 2.12 to Figure 2.13, respectively taken in consideration that the phase voltage waveforms of the SVPWM and AZPWM1 techniques in the  $L$ -region and  $H$ -region are similar. The phase current waveforms produced by the abovementioned PWMs in the  $L$ -region and  $H$ -region are depicted in Figure 2.14 and Figure 2.15, respectively. In the  $L$ -region, the results show that the current ripple of the AZPWM1 technique (see Figure 2.14) is higher than that of SVPWM and LuPWM techniques current waveforms. The PWM voltage waveforms in the low and high modulation regions are analysed by the fast Fourier transform FFT (see Figure 2.16 and Figure 2.17). It is noted that the FFT analysis is done by a computer program DADiSP 6.5. For a balanced three phases, square-wave voltage supply, only the odd harmonics should be considered. The third and its multiple (tripplen) harmonics are in the same phase (co-phrasal-often defined as zero sequence component), and therefore cannot cause any triplen harmonic current in a wye- or delta-connected machine winding with isolated neutral [21]. The FFT analysis show a fundamental (i.e. useful) and undesirable harmonic components. The voltage harmonics of the AZPWM1 in the  $L$ -region (see Figure 2.16) are higher than the voltage harmonics of SVPWM and LuPWM techniques due to the absence of the zero vectors in the AZPWM1 technique. The voltage harmonics of the LuPWM technique is however, higher than that of the SVPWM technique indicating that the LuPWM technique has higher current ripple than that produced by the SVPWM technique but lower current ripple than AZPWM1 technique. This is due to the fact that the SVPWM technique uses

two zero vectors and the LuPWM technique uses only one zero vector to construct the command voltage therefore, the deviation between the fundamental voltage and machine voltage in the LuPWM technique will be higher than that in the SVPWM technique [78]. A further reduction in the current ripple can be seen in the simulation results of the AZPWM1 technique in the  $H$ -region due to decreasing in the voltage harmonic (see Figure 2.17). The peak-to-peak value of the resultant CMV of the SVPWM technique is equal to  $\pm V_{dc}/2$  in both  $L$ -region and  $H$ -region voltage region (see Figure 2.18 and Figure 2.19). This value is reduced to  $\pm V_{dc}/6$  by AZPWM1 (see Figure 2.18 and Figure 2.19). The NSPWM technique reduces the peak-to-peak value of the CMV to  $\pm V_{dc}/6$  in the  $H$ -region (see Figure 2.19). The LuPWM technique decreases the CMV peak-to-peak value to  $\pm V_{dc}/3$  in the  $L$ -region (see Figure 2.18 and to  $\pm V_{dc}/6$  in the  $H$ -region (see Figure 2.19).

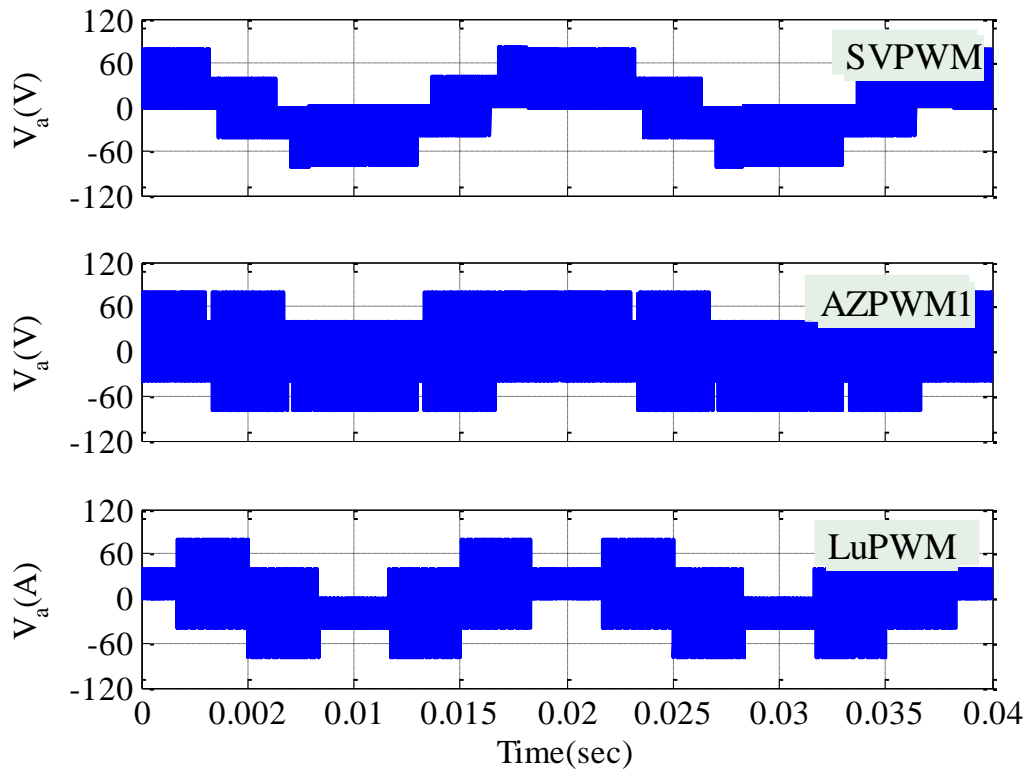


Figure 2.12 PWMs under study phase “a” voltage in L-region.

From Figure 2.3 and Figure 2.6, it is noted that in the LuPWM and NSPWM techniques one phase remains totally “On” or totally “Off” during the full switching period unlike



SVPWM and AZPWM1 techniques. Therefore, in addition to the reduction in the CMV, the switching events per one period are reduced by the NSPWM and LuPWM techniques compared with SVPWM and AZPWM1 techniques over the switching period  $T_{sw}$ . This phenomenon can be seen clearly in the simulation results shown in Figure 2.20 and Figure 2.21 of phase “a” output voltage referred to the neutral star point of the inverter leg and the relevant modulator wave forms of the AZPWM1 and LuPWM techniques respectively. Consequently, it is expected that the switching losses of the switching devices (IGBTs and diodes) will be reduced during the switching period. From Figure 2.20 the SVPWM technique On/Off switching events per one fundamental period is about 325. The switching events are reduced to 214 in the LuPWM technique (see Figure 2.21), therefore the reduction of the switching events can be given by:

$$\text{Reduction of the switching events} = \frac{325-214}{325} * 100 = 34\% \quad 2.12$$

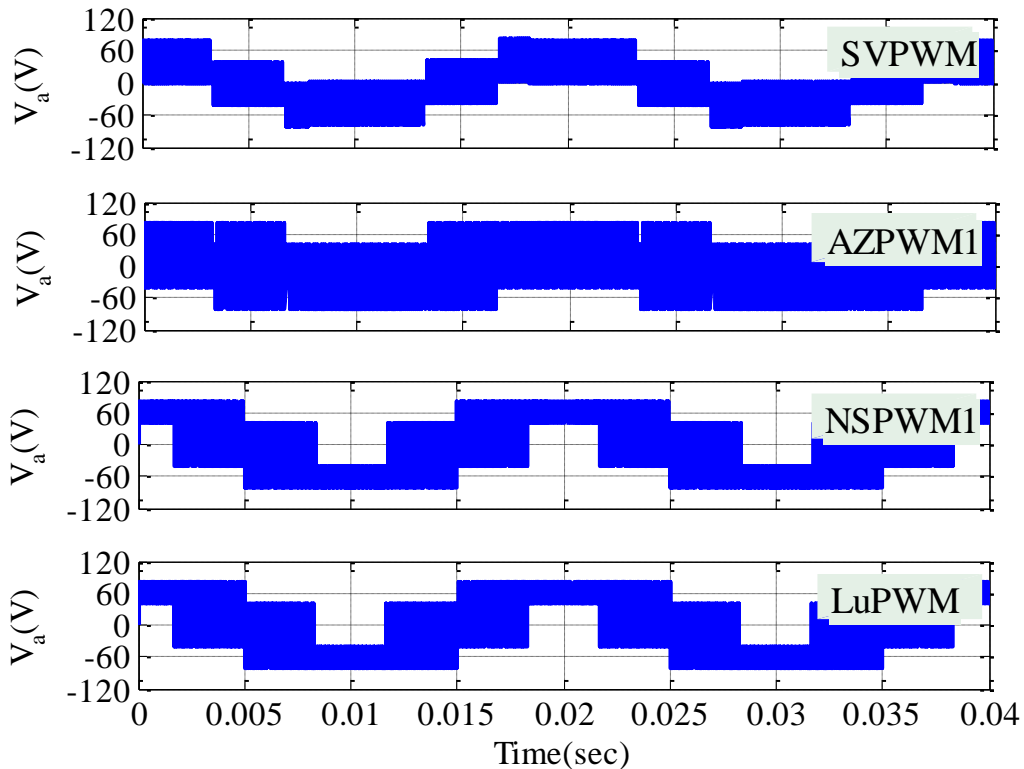


Figure 2.13 PWMs under study phase “a” voltage in  $L$ -region

From equation 2.12 it can be seen that the switching losses in the LuPWM technique is reduced by about one third compared with SVPWM technique. Similarly, the switching losses of NSPWM technique are also reduced to one third whereas the AZPWM1 technique has almost the same switching losses of the SVPWM technique.

Based on what has been discussed before, it can be concluded that although the NSPWM technique has approximately the same current ripple of the LuPWM technique, it cannot be employed in the low modulation region due to its invalid duty cycles solution in this region. The AZPWM1 technique produces lower peak-to-peak CMV ( $\pm V_{dc}/6$ ) than LuPWM technique ( $V_{dc}/3$ ) in the  $L$ -region but it has larger current ripple than the LuPWM technique and it does not reduce the switching losses. On the other hand, LuPWM technique does reduce the CMV as well as the switching losses and it exhibits superior current ripple reduction. In addition to it can be used to modulate in both the  $L$ - and  $H$ -regions. On the other hand, the conventional SVPWM technique has the highest CMV value and higher switching losses than LuPWM technique.

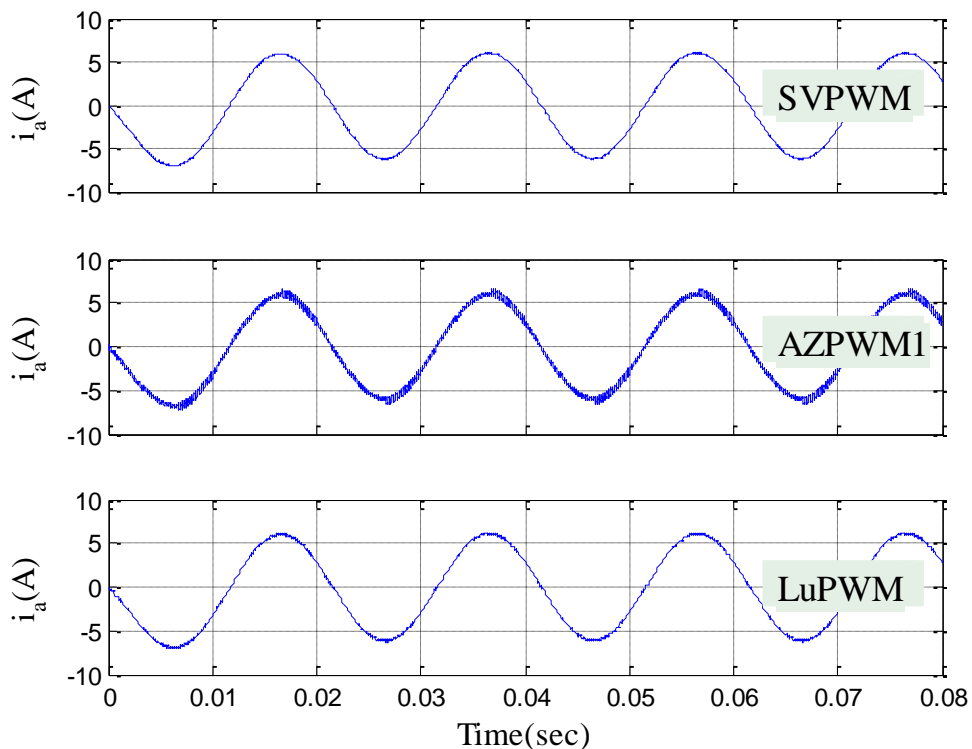


Figure 2.14 PWMs under study phase “a” current in  $L$ -region.

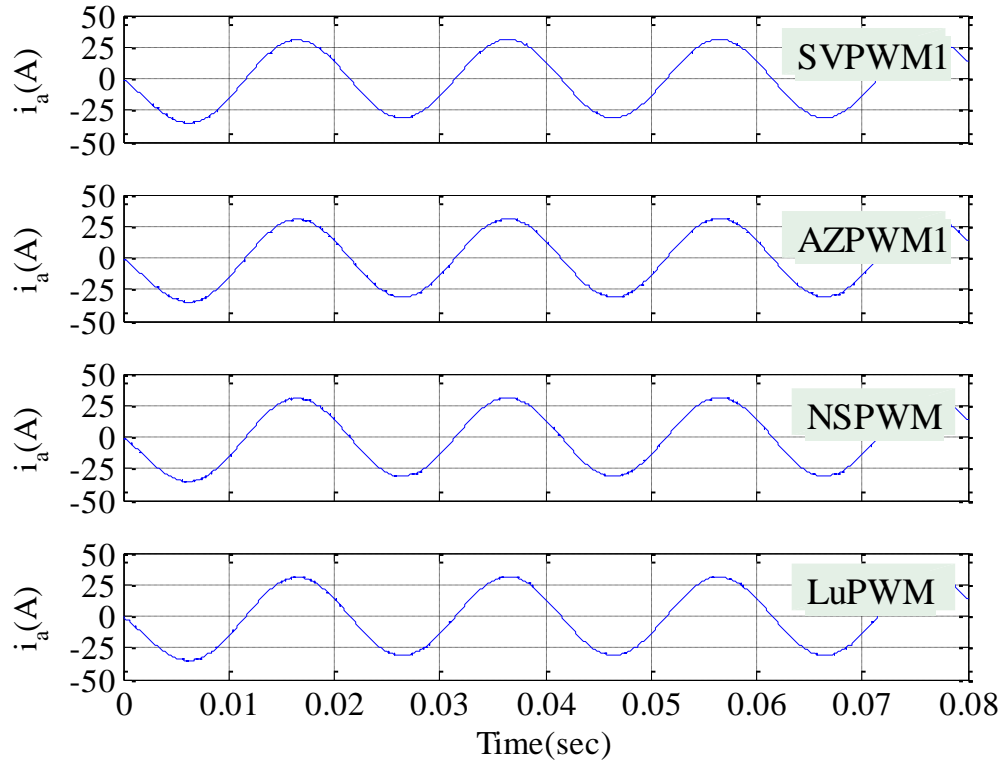


Figure 2.15 PWMs under study phase "a" current in  $H$ -region.

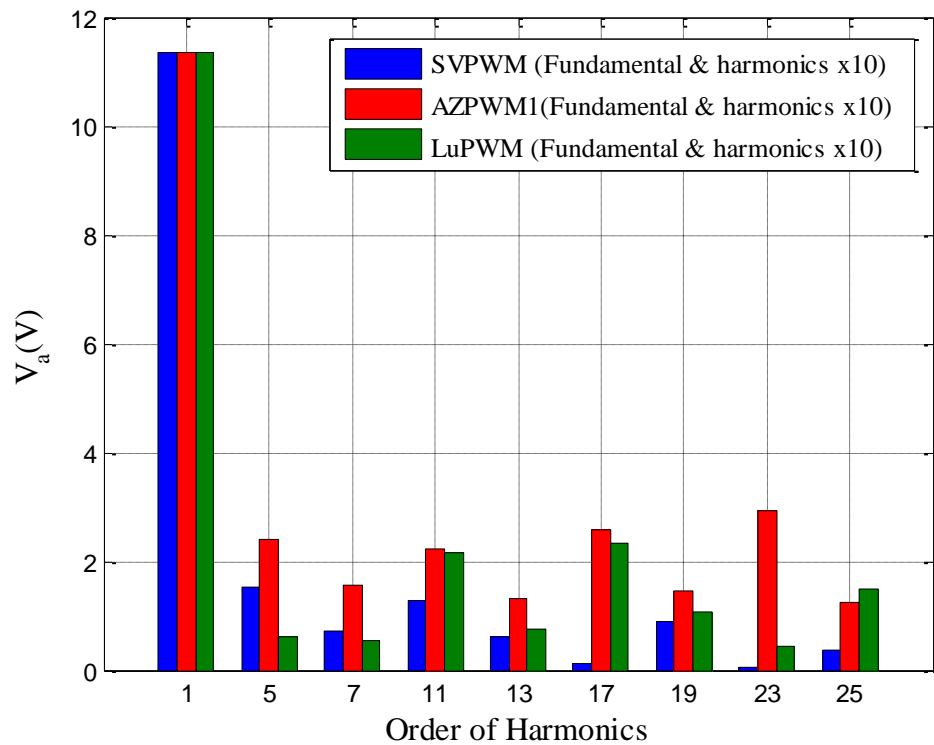


Figure 2.16 Phase "a" voltage FFT analysis of PWMs under study in  $L$ -region.

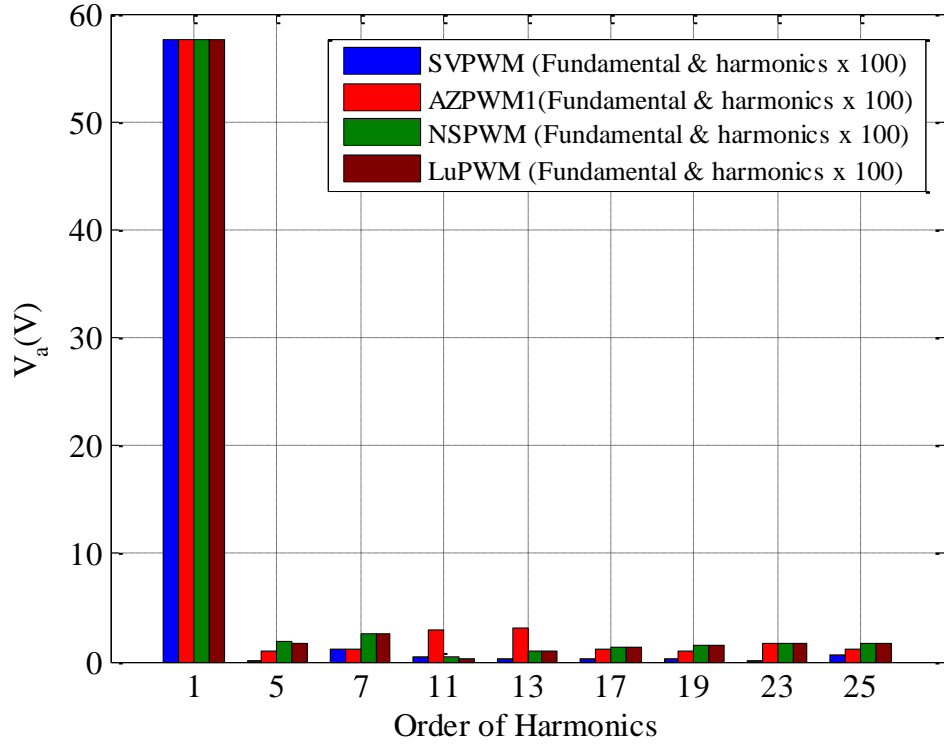


Figure 2.17 Phase “a” voltage FFT analysis of PWMs under study in *H*-region.

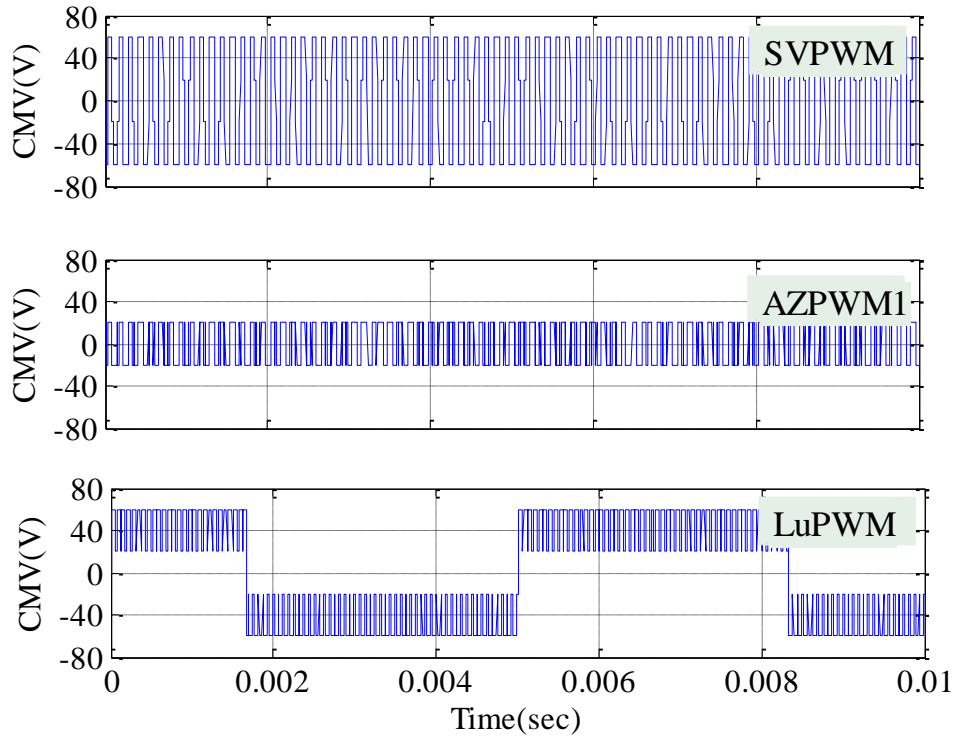


Figure 2.18 PWMs under study peak to peak CMV in *L*-region.

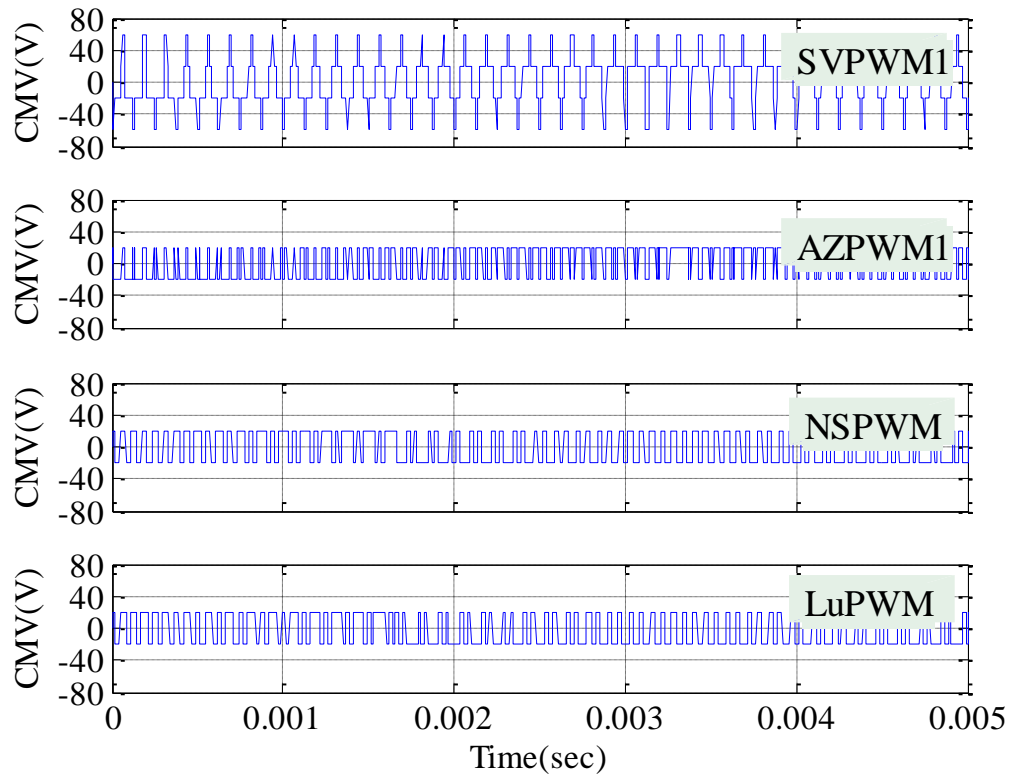


Figure 2.19 PWMs under study peak to peak CMV in H-region.

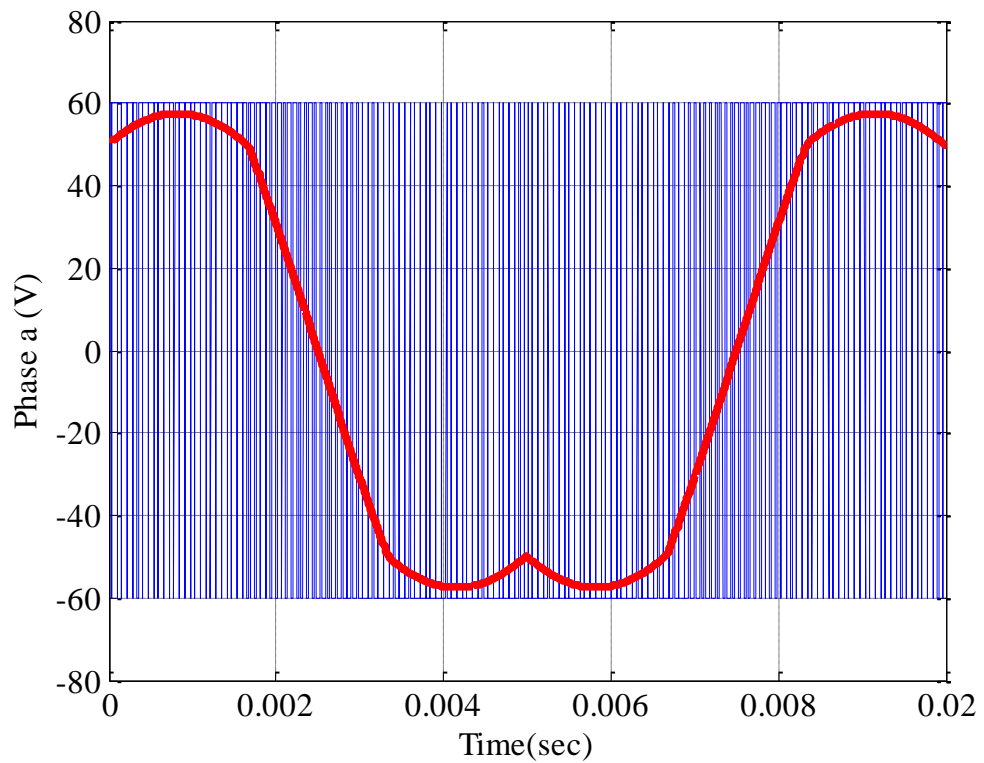


Figure 2.20 Modulation waveforms and phase "a" inverter output of SVPWM.

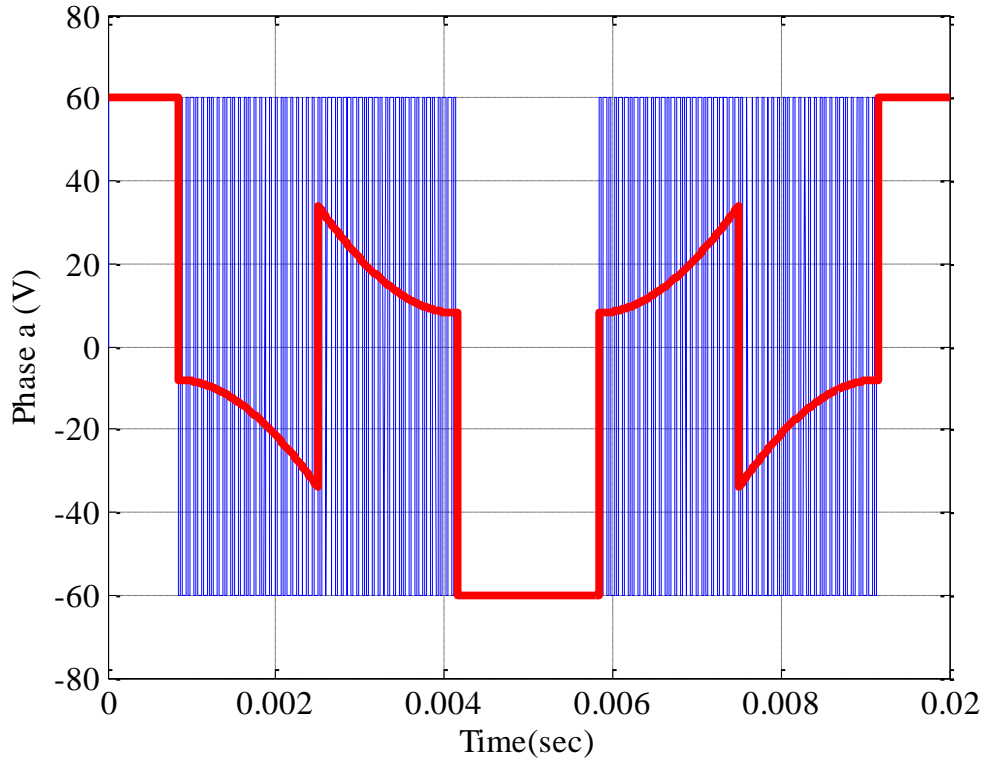
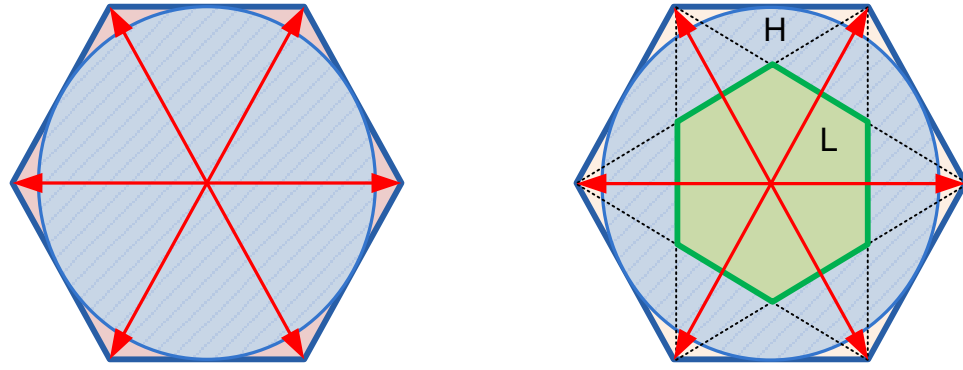


Figure 2.21 Modulation waveforms and phase “a” inverter output of LuPWM.

## 2.6 Summary on Comparison between the Investigated PWM Techniques

It is noted that the performance of SVPWM and LuPWM techniques was compared in [76, 80] but no comparative study between LuPWM, AZPWM1 and NSPWM techniques have been done to date in terms of CMV reduction and switching losses. Therefore, performance of SVPWM, AZPWM1, NSPWM and LuPWM techniques will be compared with each other. One factor used to evaluate a PWM technique is the voltage linearity which defined the ( $\alpha\beta$ ) voltage hexagon regions where the duty cycles of a PWM technique have a veiled solution. In other words, voltage linearity means the ability of a PWM technique to modulate in all the SV hexagon regions [75]. The linear voltage operation region of the SVPWM, AZPWM1, NSPWM and the LuPWM techniques are shown in Figure 2.22 [75]. The limitation of the NSPWM technique can be seen clearly from Figure 2.22 (b) since it can only operate in the  $H$ - region (light blue hashed area) in comparison with the other three PWM strategies shown in Figure 2.22 (a).



A) SVPWM, AZPWM and LuPWM

b) NSPWM

Figure 2.22 Voltage linearity of the PWM techniques under study [75].

Table 2.3 compares the studied PWM techniques where it can be seen that the peak-to-peak value of the CMV of the RCMV PWM techniques is reduced to one third in the  $H$ -region compared with the traditional SVPWM technique. The pulse patterns of the investigated PWM strategies (Figure 2.3 and Figure 2.6) show that in NSPWM and LuPWM techniques one inverter leg is kept “On” or “Off” for one switching period which leads to reduce the switching losses by one third. However, the switching losses of the AZPWM1 technique method remains as high as that of the SVPWM technique. The reduction of the switching losses is due to the fact that the switching events in a PWM cycle in NSPWM and LuPWM techniques is decreased to four rather than six in the SVPWM and AZPWM1 techniques (see Figure 2.3 and Figure 2.6).

Table 2.3 Comparison of SVPWM, AZPWM1, NSPWM and LuPWM [75]

	SVPWM	AZPWM1	NSPWM	LuPWM (L)	LuPWM (H)
Switching / $T_s$	6	6	4	4	4
Switching losses	High	High	Reduced by 1/3	Reduced by 1/3	Reduced by 1/3
CMV ( $V_{pp}$ )	$\pm V_{dc}/2$	$\pm V_{dc}/6$	$\pm V_{dc}/6$	$\pm V_{dc}/3$	$\pm V_{dc}/6$
Simultaneous switching	No	No	No	No	No
Implementation	possible	possible	possible	possible	possible
Voltage linearity	0 – 0.91	0 – 0.91	0.61 – 0.91	0.0 – 0.61	0.61 – 0.91

As mentioned in section 1.2.2, it is usually not possible to switch two legs simultaneously due to the inverter dead time and disparity between the electronic components [75]. The switching pattern of the PWMs under study (Figure 2.3 and Figure 2.6) illustrates that any two legs in a VSI will not switch at the same time therefore, the implementation of these PWMs is practically possible.

From the above discussion it is obvious that the LuPWM technique presents better performance in the low voltage region in comparison with AZPWM1 technique which produce high current ripple and is not able to reduce the switching losses. However, unlike NSPWM technique, LuPWM technique can operate in high region with the ability to reduce the switching losses as well as the CMV. In high voltage regions, the performance of the LuPWM and NSPWM techniques is almost similar.

The performance of the LuPWM technique is investigated in this chapter with the help of stationary load (inductive load). In Chapter 5, the LuPWM technique will be implemented in a closed loop control system of an IPMSM to evaluate it.

## **2.7 Chapter Summary**

In this Chapter, traditional SVPWM technique and CMV reduction modern PWM techniques such as AZPWM1, NSPWM and LuPWM techniques are investigated and their performances in terms of voltage waveforms, current waveforms, produced peak-to-peak CMV and switching losses are compared. The scalar implementation of the LuPWM technique, which has not been clearly highlighted in the previous works, is discussed. The studied PWM techniques are implemented and simulated with inductive load using Matlab/Simulink. The simulation results show that compared with the conventional SVPWM technique, the AZPWM1, NSPWM and LuPWM techniques can be employed to reduce the peak-to-peak value of the CMV. Additionally, the switching losses are also reduced by about one third when the NSPWM or LuPWM techniques are employed. Since the NSPWM technique cannot be utilised in the low modulation region Figure 2.22 (b), the LuPWM technique seems to be the best choice amongst the studied



PWM techniques. This conclusion is based on its ability to be implemented in both the low and high modulation region of the voltage hexagon, lower current ripple in the low modulation region compared with the AZPWM1 technique, and its reduction of the switching losses by one third. The performance of the LuPWM technique will be furthermore investigated and compared with the performance of the conventional SVPWM technique in machine drive applications in Chapter 5.

### 3. LOSSES MINIMISATION OF INTERIOR PERMANENT MAGNET MACHINE

#### 3.1 Introduction

The power losses of an IPMSM drive mainly consists of inverter losses and the IPMSM losses. Chapter 2 discussed the inverter switching losses and investigated a number of PWM techniques which have been suggested in literature in order to minimise the switching losses as well as reduce the CMV produced by VSIs. This chapter deals with the second part of the drive losses associated with the IPMSM. It focuses on minimising the controllable IPMSM power losses (copper and iron losses) as they are current and speed dependant [57, 58] in order to improve the efficiency of the tested machine. As mentioned in section 1.2.1, the copper losses is related to the motor armature current and winding resistance therefore its minimisation can be directly achieved by the well-known MTPA control strategy when the motor operates in the CTR under the armature current limit only [60]. The iron losses at a given speed is influenced by the magnetic flux in the machine and hence also dependent on the current [60]. Basically, the optimal efficiency control techniques of a machine are classified into two methods [57, 58] which are the SCs and the LMCs. The SCs [57, 61] has advantageous such as it is not sensitive to the IPMSM parameters variations and no need to develop an accurate core losses model. In practice, the SCs approach suffer from difficulties of reaching the actual minimum point due to the flat shape of the IPMSM power curves in addition to its poor steady state response. The (LMCs) method [54, 55, 60-64] characterised by its smooth performance, very fast in terms of finding the minimum power losses and effectively utilizing the reluctance torque and the  $d$ -axes armature reaction. It is, however, very sensitive to parameters variations, expensive, time consumed and comprehensive experimental work is required. Basically, the parameters of an IPMSM vary with operation condition due to magnetic saturation [9, 11] and the iron losses is highly non-linear, both of which increase the difficulties of searching the true minimum losses solution. In the previous work of the IPMSM losses minimisation criteria the IPMSM parameters variation has been mostly neglected [60, 63, 64], considered only in

the CTR [59, 65, 66] or accounted for parameters variations using on-line parameters estimation [67-69] but with estimation errors and uncertainty in the model structure. Most recent approach is a parameter independent MTPA control technique [70] based on signal injection where a speed control loop is required. However, this is not applicable for EVs applications as the EVs drive system needs to be operated in the torque mode [71].

The parameter non-linearity of an IPMSM used in the study and formulation of the IPMSM losses minimisation problem including copper and iron losses models are discussed in section 3.3 and 3.4, respectively. A new losses minimisation algorithm (LMA) which aims to minimise copper and/or iron losses in the constant and the flux weakening regions of an IPMSM is presented in section 3.5. The LMA generates optimal direct and quadrature axis currents for a given torque and speed operating points according to the actual IPMSM parameters ( $L_d$ ,  $L_q$  and  $\lambda_m$ ). The resistive voltage drop across the stator winding resistances, which has been commonly neglected in previous work, is taken into consideration in the LMA [20, 34]. A high fidelity iron losses model that presented in [81, 82] is employed to quantify the iron losses as close as possible to the actual iron losses value at a given operation condition. The IPMSM mathematical model, MTPA and flux weakening control strategies are discussed in section 3.2 [89]. The off-line simulation results of the LMA are illustrated in section 3.6. Chapter 3 is summarised in section 3.7.

## **3.2 Dynamic Model of IPMSM**

The dynamic model of IPMSM in the d-q rotating reference frame, the MTPA and FW control strategies are briefly discussed in this section. This model based on the assumption that the employed machine is designed with conventional distributed winding.

### **3.2.1 IPMSM in the D-Q Rotating Reference Frame**

An IPMSM has three stator windings and permanent magnet structured inside the rotor, Figure 1.15. As a result of this design, the IPMSM inductances in the dq reference

frame ( $L_d$  and  $L_q$ ) introduced in Chapter 1 are no longer constant and they vary with the rotor angular position. Therefore, reluctance torque as well as the synchronous motor mutual reaction torque [9, 11] is produced by the IPMSM. Since both magnet and retaining sleeves have high resistivity, rotor-induced currents can be neglected and no damper windings are modelled [90]. Therefore, the phase voltages electrical dynamic equations are given by the following equations [89, 90]:

$$v_a = Ri_a + \frac{d\lambda_a}{dt} \quad 3.1$$

$$v_b = Ri_b + \frac{d\lambda_b}{dt} \quad 3.2$$

$$v_c = Ri_c + \frac{d\lambda_c}{dt} \quad 3.3$$

where  $R$  is the stator resistance,  $v_{a,b,c}$ ,  $i_{a,b,c}$  and  $\lambda_{a,b,c}$  are the phase  $a$ ,  $b$ ,  $c$  stator voltages, phase  $a$ ,  $b$ ,  $c$  stator currents and phase  $a$ ,  $b$ ,  $c$  stator flux linkages, respectively. The stator flux linkage is given by Eqn. 3.4 to 3.6 [90] taking in consideration that the mutual inductances  $M_{ab}$ ,  $M_{ac}$ ,  $M_{ba}$ ,  $M_{bc}$ ,  $M_{ca}$  and  $M_{cb}$  are symmetrical (i.e.  $M_{ab} = M_{ba}$ ,  $M_{ac} = M_{ca}$  and  $M_{bc} = M_{cb}$ ).

$$\lambda_a = L_{aa}i_a + M_{ab}i_b + M_{ac}i_c + \lambda_{ma} \quad 3.4$$

$$\lambda_b = M_{ab}i_a + L_{bb}i_b + M_{bc}i_c + \lambda_{mb} \quad 3.5$$

$$\lambda_c = M_{ac}i_a + M_{bc}i_b + L_{cc}i_c + \lambda_{mc} \quad 3.6$$

where  $L_{aa}$ ,  $L_{bb}$ ,  $L_{cc}$  are phase  $a$ ,  $b$ ,  $c$  stator self-inductances and  $\lambda_{ma,b,c}$  are phase  $a$ ,  $b$ ,  $c$  PM flux linkages. The phase voltage (Eqns. 3.1 to 3.3) and the stator flux linkage (Eqns. 3.4 to 3.6) can be expressed in the matrix form for simplicity reasons, as follows [90]:

$$\begin{bmatrix} v_a \\ v_b \\ v_c \end{bmatrix} = R \begin{bmatrix} i_a \\ i_b \\ i_c \end{bmatrix} + \frac{d}{dt} \begin{bmatrix} \lambda_a \\ \lambda_b \\ \lambda_c \end{bmatrix} \quad 3.7$$

$$\begin{bmatrix} \lambda_a \\ \lambda_b \\ \lambda_c \end{bmatrix} = \begin{bmatrix} L_{aa} & M_{ab} & M_{ac} \\ M_{ab} & L_{bb} & M_{bc} \\ M_{ac} & M_{bc} & L_{cc} \end{bmatrix} \begin{bmatrix} i_a \\ i_b \\ i_c \end{bmatrix} + \begin{bmatrix} \lambda_{ma} \\ \lambda_{mb} \\ \lambda_{mc} \end{bmatrix} \quad 3.8$$

As the IPMSM inductances are functions in the rotor electrical angular position ( $\theta_e$ ). This inductance matrix is expressed by Eqn. 3.9 where,  $L$  and  $M$  are the self-inductance and mutual inductance average value respectively,  $L_2$  and  $M_2$  are the self-inductance and mutual inductance with considering the saliency effect of the IPMSM indicating by the term  $2\theta_e$ . The values of  $L_2$  and  $M_2$  are almost zero in a non-salient PM BLAC machine [90]:

$$\begin{bmatrix} L_{aa} & M_{ab} & M_{ac} \\ M_{ab} & L_{bb} & M_{bc} \\ M_{ac} & M_{bc} & L_{cc} \end{bmatrix} = \begin{bmatrix} L & M & M \\ M & L & M \\ M & M & L \end{bmatrix} + \begin{bmatrix} L_2 \cos(2\theta_e) & M_2 \cos(2\theta_e - \frac{2\pi}{3}) & M_2(2\theta_e - \frac{4\pi}{3}) \\ M_2 \cos(2\theta_e - \frac{2\pi}{3}) & L_2 \cos(2\theta_e - \frac{4\pi}{3}) & M_2 \cos(2\theta_e) \\ M_2(2\theta_e - \frac{4\pi}{3}) & M_2 \cos(2\theta_e) & L_2 \cos(2\theta_e - \frac{2\pi}{3}) \end{bmatrix} \quad 3.9$$

The PM stator flux linkages can be given by Eqn. 3.10 where,  $\lambda_m$  is the PM flux linkage:

$$\begin{bmatrix} \lambda_{ma} \\ \lambda_{mb} \\ \lambda_{mc} \end{bmatrix} = \begin{bmatrix} \lambda_m \cos(\theta_e) \\ \lambda_m \cos(\theta_e - \frac{2\pi}{3}) \\ \lambda_m \cos(\theta_e - \frac{4\pi}{3}) \end{bmatrix} \quad 3.10$$

Assume  $x$  is a symbol which represents a variable which is needed to be transformed from  $abc$  stator reference frame to dq rotating reference frame where  $x$  could be voltage, current or flux linkage. This can be achieved using Clark-Park transformation [22, 23] given by [90]:

$$\begin{bmatrix} x_d \\ x_q \end{bmatrix} = \frac{2}{3} \begin{bmatrix} \cos(\theta_e) & \cos(\theta_e - 120) & \cos(\theta_e + 120) \\ -\sin(\theta_e) & -\sin(\theta_e - 120) & -\sin(\theta_e + 120) \end{bmatrix} \begin{bmatrix} x_a \\ x_b \\ x_c \end{bmatrix} \quad 3.11$$

Any variable  $x$  in dq frame can be transformed to  $abc$  stator reference frame by using the inverse Clark-Park transformation which is the inverse transformation of Eqn. 3.11 [90].

$$\begin{bmatrix} x_a \\ x_b \\ x_c \end{bmatrix} = \begin{bmatrix} \cos(\theta_e) & -\sin(\theta_e) \\ \cos(\theta_e - 120) & -\sin(\theta_e - 120) \\ \cos(\theta_e + 120) & -\sin(\theta_e + 120) \end{bmatrix} \begin{bmatrix} x_d \\ x_q \end{bmatrix} \quad 3.12$$

The dq reference frame model equations of an IPMSM can be obtained by applying Eqn. 3.11 to the voltages, currents and flux linkages equations given by Eqns. 3.7 and 3.8. The mathematical representation of the resultant dq voltages of the IPMSM in the dq reference frame is given by Eqn. 3.13 and 3.14 [90].

$$v_d = Ri_d + \frac{d\lambda_d}{dt} - \omega_e \lambda_q \quad 3.13$$

$$v_q = Ri_q + \frac{d\lambda_q}{dt} + \omega_e \lambda_d \quad 3.14$$

where  $v_{d,q}$  are respectively the d- and q-axis voltages,  $i_{d,q}$  are respectively the d- and q-axis currents,  $L_d$  and  $L_q$  are respectively the d- and q-axis inductances,  $\omega_e$  is the electrical angular speed,  $\lambda_d$  and  $\lambda_q$  are respectively the d- and q-axis flux linkage and they are given by:

$$\lambda_d = L_d i_d + \lambda_m \quad 3.15$$

$$\lambda_q = L_q i_q \quad 3.16$$

Substituting from Eqns. 3.15 and 3.16 into Eqns. 3.13 and 3.14 and representing the resultant equations in matrix form:

$$\begin{bmatrix} v_d \\ v_q \end{bmatrix} = \begin{bmatrix} R & -\omega_e L_q \\ \omega_e L_d & R \end{bmatrix} \begin{bmatrix} i_d \\ i_q \end{bmatrix} + \begin{bmatrix} L_d & 0 \\ 0 & L_q \end{bmatrix} \frac{d}{dt} \begin{bmatrix} i_d \\ i_q \end{bmatrix} + \begin{bmatrix} 0 \\ \lambda_m \omega_e \end{bmatrix} \quad 3.17$$

The electromagnetic torque  $T_{em}$  in d-q reference frame is given by Eqn. 3.18:

$$T_{em} = \frac{3}{2\omega_m} (v_d i_d + v_q i_q) = \frac{3p}{2} [\lambda_m i_q + (L_d - L_q) i_d i_q] \quad 3.18$$

where  $p$  is the number of pole pairs and  $\omega_m$  the mechanical speed. From the torque equation it is noted that the torque  $T_{em}$  consists of two components: The first components is the mutual reaction torque produced by  $i_q$  and the permanent magnet. The second component is the reluctance torque due to the difference between the d- and q-axis inductances [90]. The torque produced in the second term of Eqn. 3.18 is positive if the d-axis current  $i_d$  is negative. The equation of motion of an IPMSM is [90]:

$$J \frac{d\omega_m}{dt} = (T_{em} - T_d - B\omega_m) \quad 3.19$$

where,  $J$  is the moment of inertia,  $B$  is the viscous friction coefficient and  $T_d$  is the demand torque.

### 3.2.2 Constant Torque and Constant Power Regions of an IPMSM

#### 3.2.2.1 Current and Voltage Constraints

The inverter capacity should be taken into account during the IPMSM control action as the terminal voltage  $V_a$  is constrained by the available DC-link voltage and the armature current  $I_a$  is however, limited by the maximum available inverter current [20]. The current and voltage limits of the converter are given by Eqns. 3.20 and 3.21:

$$I_a = \sqrt{i_d^2 + i_q^2} \leq I_{am} \quad 3.20$$

$$V_a = \sqrt{v_d^2 + v_q^2} \leq V_{am} \quad 3.21$$

where,  $I_{am}$  is the maximum current which is decided by the continuous armature current rating and the available output current of the inverter. The voltage  $V_{am}$  is the maximum voltage which is decided depending on the DC-link voltage of the inverter. An interior permanent magnet synchronous machine for EV traction, referred as PMOB IPM has been designed and constructed by the Electrical Machines and Drives group in the Electronic and Electrical Department at Sheffield University. This machine is used in this thesis in order to evaluate the LMA performance. The PMOB IPM topology is shown Figure 3.1 where it employs a conventional distributed double layer winding with a V-shape interior permanent magnet rotor. The machine has 6 poles and 36 slots, and utilizes NdFeB permanent magnets. The parameters of this PMOB IPM machine are listed in Table 3.1. The  $L_d$ ,  $L_q$  and  $\lambda_m$  parameters are calculated by the FEM at rated speed and maximum torque.

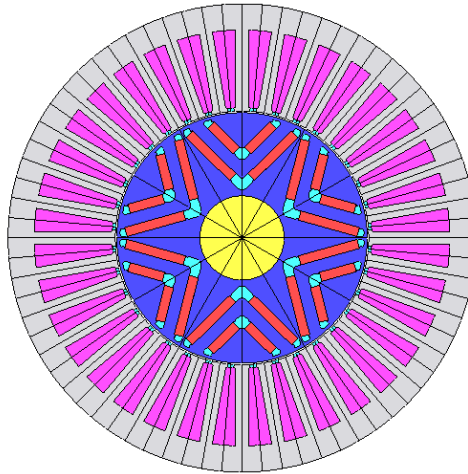


Figure 3.1 PMOB IPMSM topology.

For the PMOB IPM, equation 3.20 represents a circle with a radius equal to the maximum current in the  $(i_d, i_q)$  plane, Figure 3.2 [20]. Equation 3.21, however, represents an ellipse and its size is decided by the maximum voltage and instantaneous rotor speed Figure 3.2 [20].



Input DC link voltage ( $V_{dc}$ )[V]	120.0
Maximum output power [kw]	9.9
Maximum speed ( $\omega_{max}$ )[rpm]	5000
Rated speed ( $\omega_{base}$ )[rpm]	1350
Maximum torque ( $T_{max}$ )[Nm]	70.0
Rated Torque [Nm]	35.0
Maximum phase current [A]	120.0
Number of pole pairs $P$ [V]	3
Flux linkage $\lambda_m$ [Wb]	0.127
d axis inductance ( $L_d$ )[mH]	0.64
q axis inductance ( $L_q$ )[mH]	1.594
Stator resistance ( $R$ )[ $\Omega$ ]	0.0521

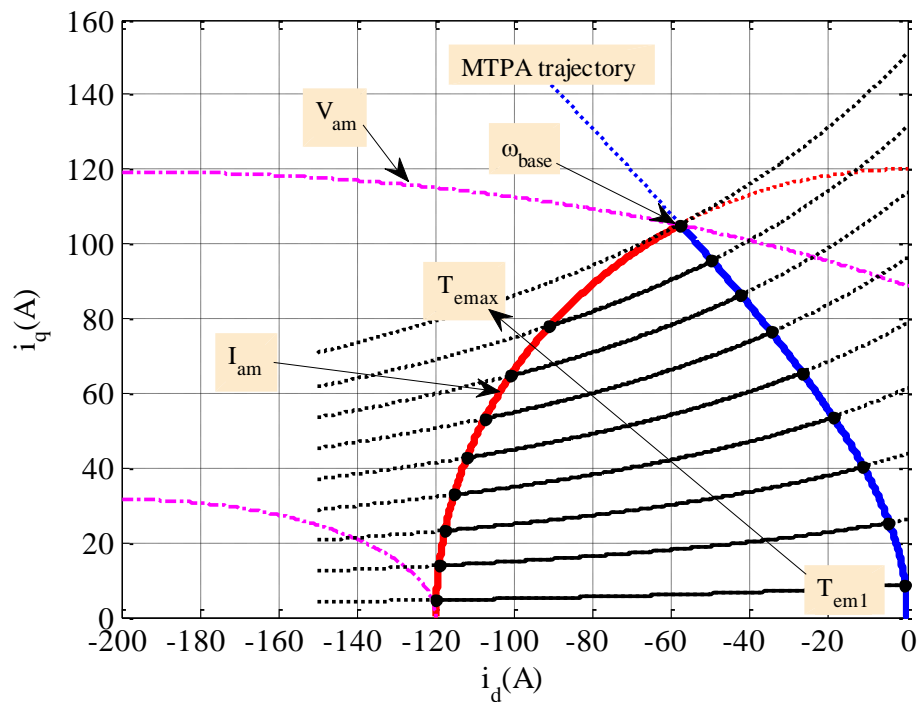


Figure 3.2 Maximum torque-per-ampere current vector trajectory and voltage limited maximum-output current vector trajectory for the IPMSM [20].

### 3.2.2.2 Constant Torque Control

In the constant torque region where the speed is below rated speed  $\omega_b$ , the current vector  $(i_d, i_q)$  is only restricted by the current limit circle [20]. As the  $i_d$  and  $i_q$  current component both associated with the electromagnetic torque production, the MTPA control of the IPMSM can be only achieved by regulating both  $i_d$  and  $i_q$  by the drive system at the same time [24]. The MTPA trajectory which is denoted by the solid bold blue curve in Figure 3.2, represents the crossing points of the  $T_{em}$  curves ( $T_{em1}$  to  $T_{emax}$ ) with the minimum current circles formed by the current vector  $(i_d, i_q)$  as  $I_a$  increases gradually toward its maximum value  $I_{am}$ .

### 3.2.2.3 Constant Power or Flux Weakening Control

Operating beyond the base speed of an IPMSM is possible by injecting a negative d-axis current (FW control) [20, 34]. Fundamentally, the FW control system is derived based on two main assumptions for simplicity purpose. First, is the assumption of steady state circumstance ( $\frac{di_d}{dt} = \frac{di_q}{dt} = 0$ ). As a result Eqns. 3.13 and 3.14 refer to:

$$v_d = Ri_d - \omega_e L_q i_q \quad 3.22$$

$$v_q = Ri_q + \omega_e (L_q i_d + \lambda_m) \quad 3.23$$

Second, armature resistance is neglected as it is assumed that the effect of the resistance voltage drop is very small at high speed therefore Eqns. 3.22 and 3.23 yields to:

$$v_d = -\omega_e L_q i_q \quad 3.24$$

$$v_q = \omega_e (L_q i_d + \lambda_m) \quad 3.25$$

The second term in Eqn. 3.25, explains the idea behind the flux weakening control method as the smaller the factor  $(L_q i_d + \lambda_m)$  the higher the motor speed, taken into account the demagnetisation limit. In the constant power or flux weakening region where the speed is beyond  $\omega_b$ , the current vector  $(i_d, i_q)$  is limited by both the maximum available current and voltage. The crossing points of the torque curves with the current

circular limits (solid bold red curve in Figure 3.2) and maximum elliptical voltage limits (dash magenta curves in Figure 3.2) defined the  $(i_d, i_q)$  current vector components that satisfies both the current and voltage limits. Therefore, there is only one pair of  $(i_d, i_q)$  at specific speed and torque that satisfies these limits in FWR [20]. Basically, the voltage limit ellipse shrinks toward zero as IPMSM speed increases to higher values [20]. The new losses minimisation algorithm (LMA) proposed in this thesis [91] considers the resistive voltage drop across the stator windings resistance therefore, Eqns. 3.22 and 3.23 are utilised. As the parameters variations effect is also taken into consideration in the new LMA, the parameters  $L_d$ ,  $L_q$  and  $\lambda_m$  are no longer constant and varying with  $(i_d, i_q)$  therefore Eqns. 3.22 and 3.23 yields to:

$$v_d(i_d, i_q) = Ri_d - \omega_e L_q(i_d, i_q) i_q \quad 3.26$$

$$v_q(i_d, i_q) = Ri_q + \omega_e (L_d(i_d, i_q) i_d + \lambda_m(i_q)) \quad 3.27$$

Consequently, Eqns. 3.24, 3.25 and 3.21 become:

$$v_d(i_d, i_q) = -\omega_e L_q(i_d, i_q) i_q \quad 3.28$$

$$v_q(i_d, i_q) = \omega_e (L_d(i_d, i_q) i_d + \lambda_m(i_q)) \quad 3.29$$

$$V_a(i_d, i_q) = \sqrt{v_d(i_d, i_q)^2 + v_q(i_d, i_q)^2} \leq V_{am} \quad 3.30$$

### 3.3 Non-Linear Parameters of IPMSM

The d- and q-axis voltage components given by Eqns. 3.26 and 3.27 can be rewritten in terms of d- and q-axis flux linkage components as follows:

$$v_d(i_d, i_q) = Ri_d - \omega_e \lambda_q(i_d, i_q) \quad 3.31$$

$$v_q(i_d, i_q) = Ri_q + \omega_e (\lambda_d(i_d, i_q) + \lambda_m(i_q)) \quad 3.32$$

where  $\lambda_d$  and  $\lambda_q$  are given by Eqns. 3.33 and 3.34 respectively:

$$\lambda_d(i_d, i_q) = L_d(i_d, i_q) i_d \quad 3.33$$

$$\lambda_q(i_d, i_q) = L_q(i_d, i_q) i_q \quad 3.34$$

Hence, Eqns. 3.28 and 3.29 become:

$$v_d(i_d, i_q) = -\omega_e \lambda_q(i_d, i_q) \quad 3.35$$

$$v_q(i_d, i_q) = \omega_e (\lambda_d(i_d, i_q) + \lambda_m(i_q)) \quad 3.36$$

Equations 3.31 and 3.32 show that the flux linkage components ( $\lambda_d$  and  $\lambda_q$ ) vary with  $i_d$  and  $i_q$  currents. In Eqn. 3.32 it is assumed that  $\lambda_m$  is independent of  $i_d$  and only varies with  $i_q$ . Figure 3.3 and Figure 3.4 show the variation of  $\lambda_d$  and  $\lambda_q$  calculated by finite element method (FEM) as functions of  $i_d$  and  $i_q$  for the IPMSM machine. It can be seen that the core saturation is gradually increased as the currents increase. The saturation in  $\lambda_d$  is almost negligible along the negative  $i_d$  axes. Conversely, it becomes significant in  $\lambda_q$  as  $i_q$  increases. Based on the FEM results, the inductances  $L_d$  and  $L_q$  are calculated according to equations 3.37 and 3.38:

$$L_q = \left. \frac{\lambda_q}{i_q} \right|_{\text{constant } i_d} \quad 3.37$$

$$L_d = \left. \frac{\lambda_d - \lambda_m}{i_d} \right|_{\text{constant } i_q} \quad 3.38$$

The resultant curves of  $L_q$  vs.  $i_q$  at constant  $i_d$ ,  $L_q$  vs.  $i_d$  at constant  $i_q$  and  $\lambda_m$  vs.  $i_q$  are shown in Figure 3.5, Figure 3.6 and Figure 3.7, respectively. It can be seen that the relationships between  $(L_d, i_d)$ ,  $(L_q, i_q)$  and  $(\lambda_m, i_q)$  are not linear. The  $q$ -axis inductance  $L_q$  shown in Figure 3.5 decreases as  $i_q$  increases over the full range of  $i_d$ . However, for a given  $i_q$ , the variation of  $L_d$  is lower when the  $d$ -axis current is sufficiently large in the negative direction, as shown in Figure 3.6. The flux  $\lambda_m$  is steadily decreased as  $i_q$  is increased when  $i_d$  is kept at zero level (see Figure 3.7).

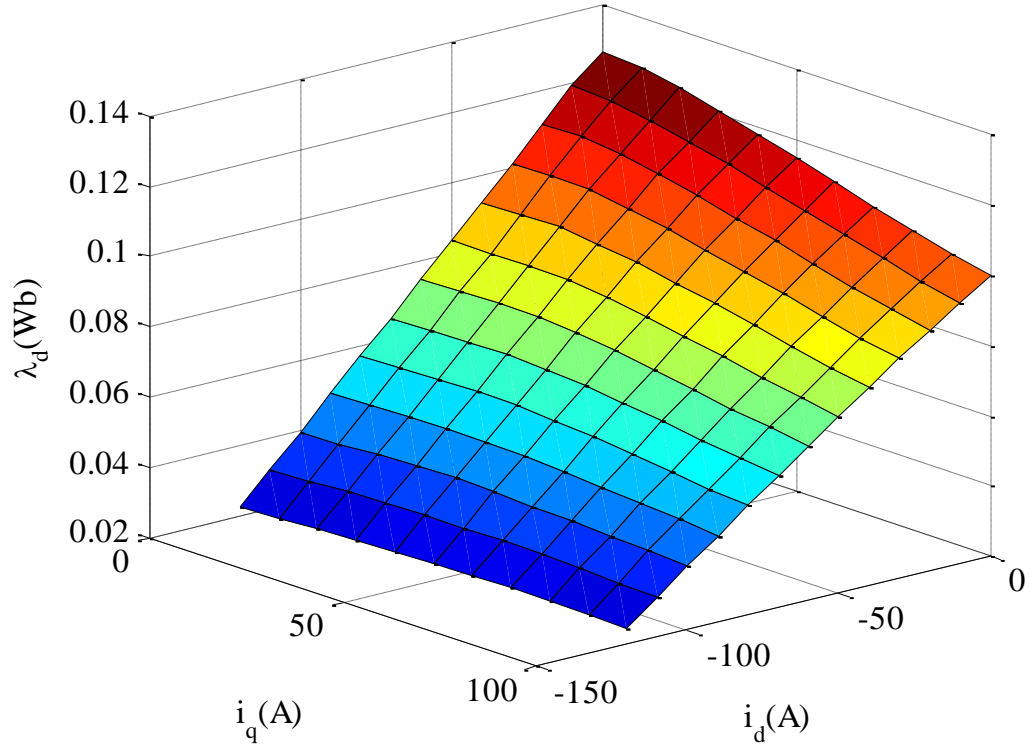


Figure 3.3 Variations of d-axis flux linkage  $\lambda_d$  with  $i_d$  and  $i_q$

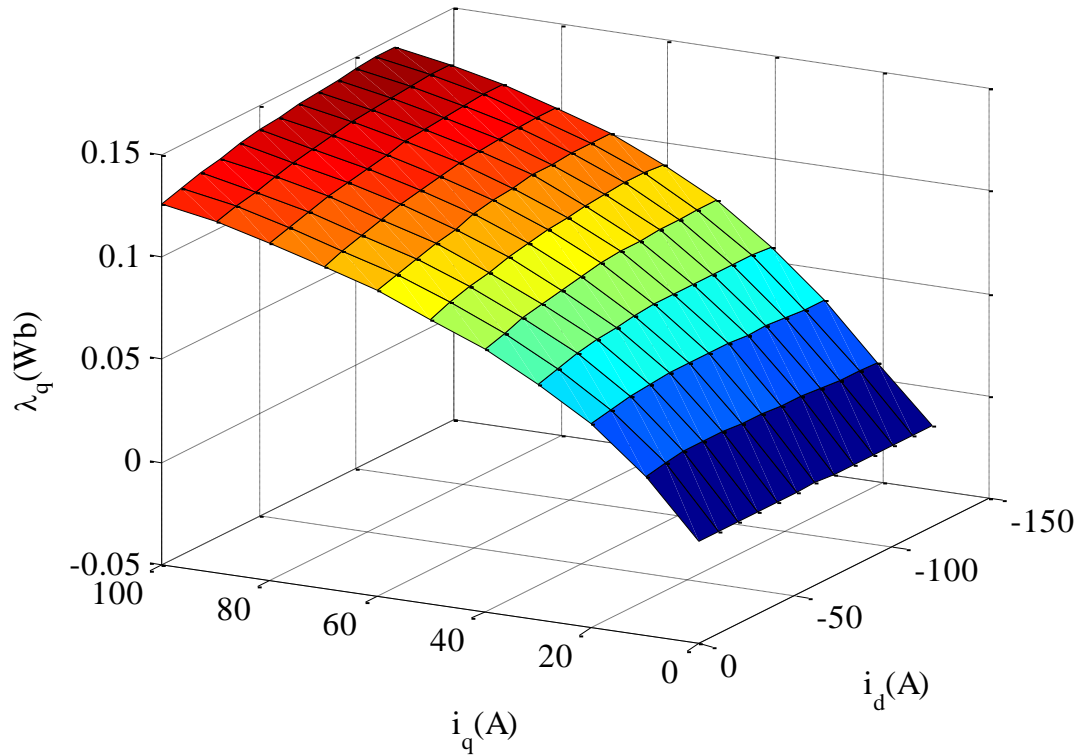


Figure 3.4 Variations of q-axis flux linkage  $\lambda_q$  with  $i_d$  and  $i_q$

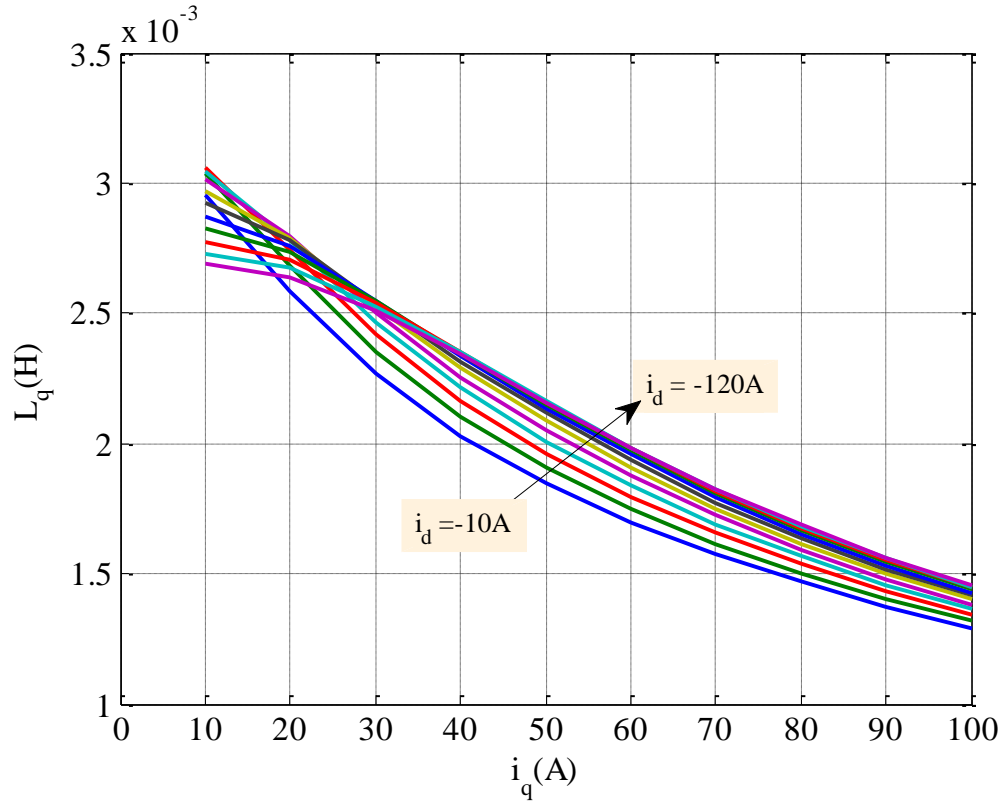


Figure 3.5 Variations of q-axis inductance  $L_q$  with  $i_q$  at constant  $i_d$

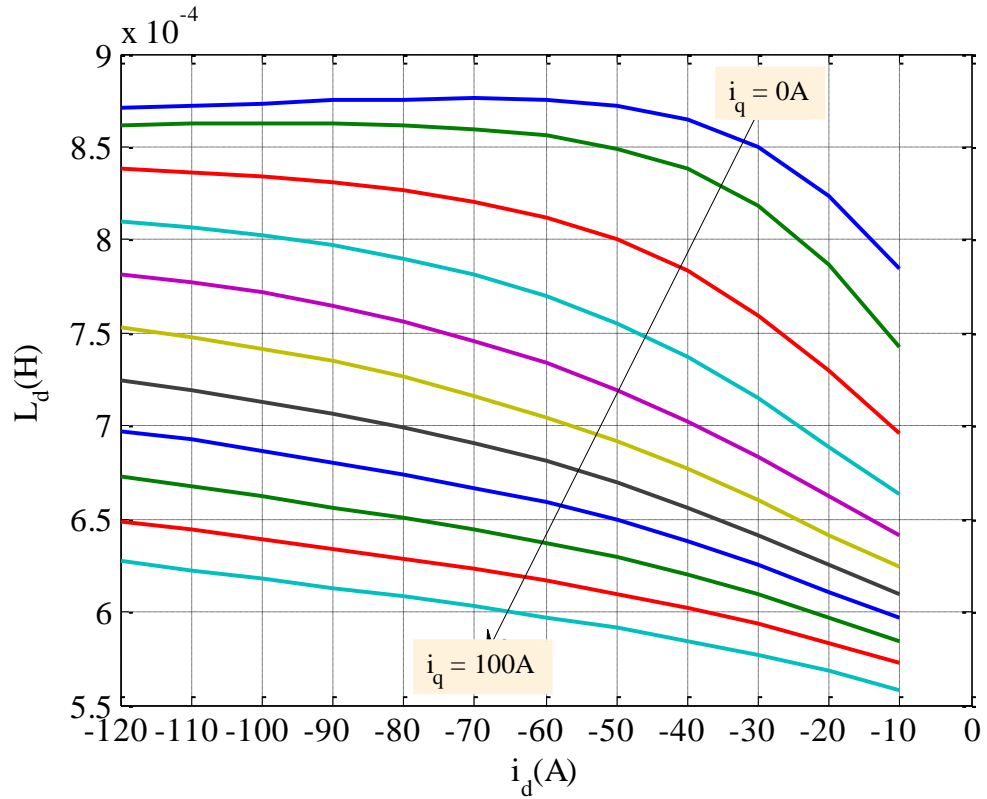


Figure 3.6 Variations of d-axis inductance  $L_d$  with  $i_d$  at constant  $i_q$

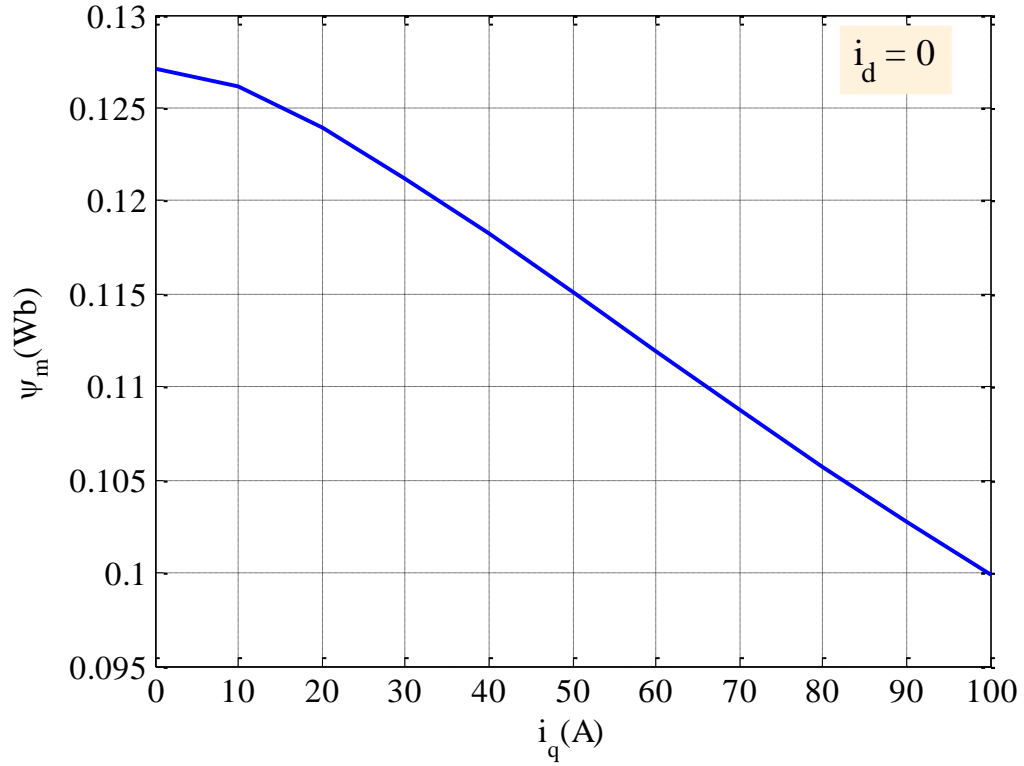


Figure 3.7 Variations of flux linkage  $\lambda_m$  with  $i_q$  at  $i_d = 0$ .

### 3.4 Formulation of the Losses Optimisation Problem

The main goal of the proposed LMA is to achieve minimum power losses which consists of the copper  $P_{cu}$  and iron losses  $P_{fe}$  at a given operating point ( $\omega_m$ ,  $T_d$ ) within the current ( $I_{am}$ ) and voltage ( $V_{am}$ ) limits of the IPMSM taken into consideration the parameter variations and resistive voltage drop. This section deals with the formula of the optimisation problem which usually consists of an objective function and constraints that restrict the optimal solution.

#### 3.4.1 Copper and Iron Losses Models

Copper losses is directly related to the stator resistance ( $R$ ) and  $(i_d, i_q)$  current vector as given by Eqn. 3.39 [59]:

$$P_{cu}(i_d, i_q) = \frac{3}{2} R (i_d^2 + i_q^2) \quad 3.39$$

where,  $P_{cu}(i_d, i_q)$  is the copper losses as a function of  $i_d$  and  $i_q$  components. The iron losses model that is used in the LMA to quantify the iron losses value of the IPMSM, is developed based on the model given in [81, 82] as it is simple and more accurate and it can predict the iron loss in both the CTR and FWR regions. This model is based on the operation of the short and open circuits of the IPMSM machine. In this approach, the total iron loss  $P_{fe}(i_d, i_q)$  is separated into two components. The first component is the one associated with the main magnetizing flux path ( $g_1$ ) and the second is based on the demagnetizing flux path ( $g_2$ ) in the flux weakening region. These two components are expressed as functions in the magnetising voltage  $V_m$  and the demagnetising voltage  $V_d^*$  as given in Eqns. 3.40 and 3.41 respectively [81, 82]. :

$$g_1(V_m) + g_2(V_d^*) = \left( \frac{a_h}{K_e} V_m + \frac{a_J}{K_e^2} V_m^2 \right) + \left( \frac{b_h}{K_e} V_d^* + \frac{b_J}{K_e^2} V_d^{*2} \right) \quad 3.40$$

$$P_{fe}(i_d, i_q) = g_1(V_m) + g_2(V_d^*) \quad 3.41$$

where  $a_h, a_J, b_h, b_J$  are hysteresis and eddy current losses coefficients, and  $K_e$  is the emf constant. The voltages  $V_m$  and  $V_d^*$  can be obtained from PMSM dq-axis phasor diagram which describes the machine AC operation shown in Figure 3.8 where  $L_{lend}$  is the leakage ending inductance [81, 82].

The parameters of the losses model can be determined by two dimensional finite element FEM analyses [8] and they are given in Table 3.2 for the prototype motor under investigation.

Table 3.2 Parameters of iron losses model

$a_h$	21.76	$b_h$	13.88
$a_J$	10.55	$b_J$	28.25
$K_e$	92.38		



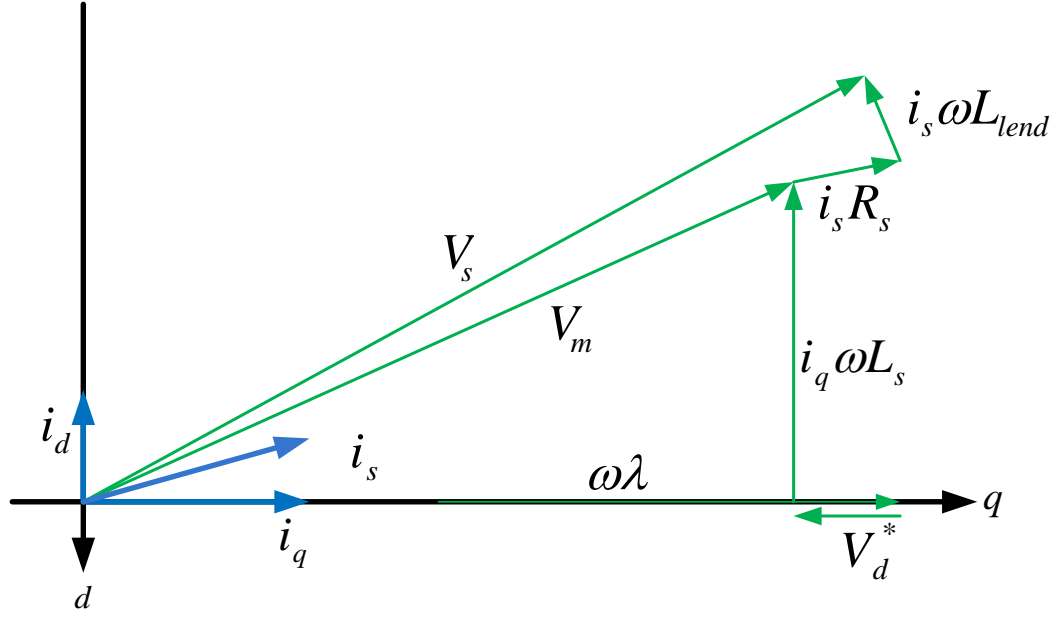


Figure 3.8 Phasor diagram of PMSM relating to field weakening operation [81, 82].

### 3.4.2 Optimisation Function and Constraints

In the losses minimisation problem, the total losses are the summation of the copper losses  $P_{cu}(i_d, i_q)$  and/or iron losses  $P_{fe}(i_d, i_q)$  given by Eqns. 3.39 and 3.41, respectively. Therefore, total power losses objective function  $P_t(i_d, i_q)$  is given by the following equation:

$$\text{Min}[P_t(i_d, i_q)] = \min\left[\frac{3}{2}R(i_d^2 + i_q^2) + P_{fe}(i_d, i_q)\right] \quad 3.42$$

Subject to the following constraints:

$$\frac{3P}{2}(\lambda_m(i_d, i_q)i_q + (L_d(i_d, i_q) - L_q(i_d, i_q))i_d i_q - T_d = 0 \quad 3.43$$

$$(Ri_q + L_d(i_d, i_q)i_d\omega_e + \lambda_m(i_q)\omega_e)^2 + (Ri_d - L_q(i_d, i_q)i_q\omega_e)^2 \leq V_{am}^2 \quad 3.44$$

$$i_d^2 + i_q^2 \leq I_{am}^2 \quad 3.45$$

where  $T_d$  is the demand torque. In the constant torque operating region, the voltage limit of Eqn. 3.44 will not be reached, and the minimisation process will only be constrained by the torque demand equation Eqn. 3.43 and current limit equation Eqn. 3.45. As long as the current magnitude is below the maximum limit, there is an optimal current vector which yields minimum losses for a given torque demand. When the IPMSM drive operates in the flux weakening region, the minimum losses current vector lies at the intersection of the torque equation Eqn. 3.43 and the voltage equation of Eqn. 3.43, subject to the current limit of Eqn. 3.45. As can be seen, when the complex non-linear inductance characteristics and non-linear iron losses model are taken into account together with the effect of phase resistance, it is not possible to determine the optimal solution analytically in closed form. A numerical optimisation process has to be used instead.

### **3.5 Losses Minimisation Process**

This section presents a new losses minimisation algorithm (LMA) which is aiming to minimise the copper and iron losses of the IPMSM machine taken into consideration of the parameters saturation effect as well as the resistive voltage drop through the stator resistance.

#### **3.5.1 Inputs Values of the Proposed LMA**

The inputs values to the LMA can be divided into two types which are constant inputs ( $\omega_m$ ,  $T_d$ ) and variable inputs ( $L_d$ ,  $L_q$  and  $\lambda_m$ ). The constant inputs do not change during the optimisation process for the same operating point ( $\omega_m$ ,  $T_d$ ). These operating points (see Table 3.3) are chosen according to the torque-speed profile of the IPMSM drive, which is calculated by FEM and depicted in Figure 3.9. By doing this, the chosen operating points listed in Table 3.3 will cover the whole motor operation speed and torque ranges. According to the torque speed profile given in Figure 3.9, in the constant torque region for example  $\omega_m$  points is chosen to be changed from 200 to 1350rpm in a 200rpm step basis and  $T_d$  is changed from 10 to 60Nm in a 10Nm step basis. In the flux weakening region,  $\omega_m$  is changed from 2000 to 4000rpm in a 1000rpm step basis in

order to examine the LMA performance in a wide speed range. However, the range of  $T_d$  which is used at each given speed is chosen according to the maximum available torque at that speed according to the torque-speed profile given in Figure 3.9.

Table 3.3 Input operating point to LMA			
Constant torque region		Flux weakening region	
$T_d(Nm)$	$\omega_m(rpm)$	$T_d(Nm)$	$\omega_m(rpm)$
10 to 60	200	10 to 40	2000
10 to 60	400	10 to 20	3000
10 to 60	600	10	4000
10 to 60	800		
10 to 60	1000		
10 to 60	1200		
10 to 60	1350		

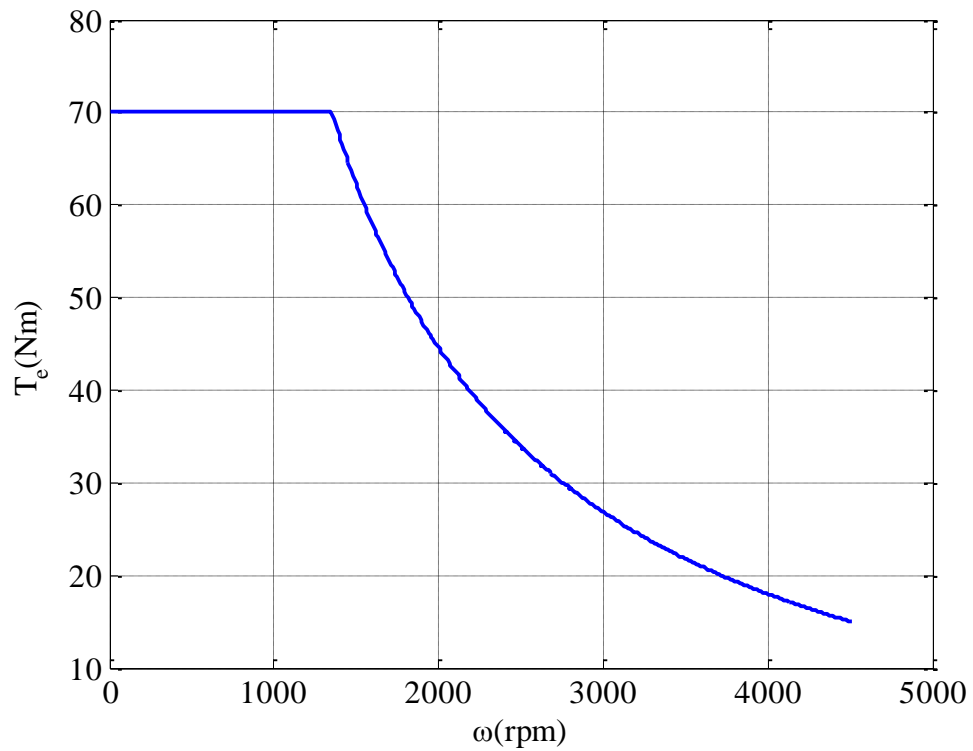


Figure 3.9 Torque-speed profile of IPMSM drive.

The variable (nonlinear) inputs of the LMA are the parameters  $L_d$ ,  $L_q$  and  $\lambda_m$  that are changed as the iterations of the LMA change. Initially, these parameters are assumed to

be constant and they are chosen to be the parameter values at the rated speed and maximum torque given in Table 3.1. The optimal currents ( $i_d$ ,  $i_q$ ) under these initial parameters are referred to as linear values as they have been calculated with the assumption of linear (constant) parameters.

### 3.5.1 Losses Minimisation Algorithm (LMA)

The optimisation process is performed off-line using Matlab optimisation toolbox as shown in Figure 3.10. The inputs to the LMA are  $T_d$ ,  $\omega_m$  and the parameters of  $L_d(n)$ ,  $L_q(n)$  and  $\lambda_m(n)$  at the  $n^{th}$  iteration where  $n = 1, 2, 3, \dots$ . The outputs of the LMA are the optimal values of ( $i_d$ ,  $i_q$ ). Firstly, the values of the objective function as well as constraints given by Eqns. 3.42 to 3.45 respectively are calculated according to the aforementioned initial inputted values. The Matlab optimisation toolbox will then generate the first linear solution ( $i_d(n)$ ,  $i_q(n)$ ) of the losses minimisation problem that satisfies the given constraints. This solution is then used to interpolate new values of the parameters  $L_d(n+1)$ ,  $L_q(n+1)$  and  $\lambda_m(n+1)$  from a set of pre-calculated parameters that are determined using the FEM. For each parameter vector  $X$ , where,  $X = L_d, L_q$  and  $\lambda_m$  if the difference between the previous  $X(n)$  and current  $X(n+1)$  values is within a predefined tolerance  $\varepsilon = 10^{-4}$  for each parameter, then ( $i_d(n)$ ,  $i_q(n)$ ) is the non-linear optimal solution ( $i_d$ ,  $i_q$ ) under the given conditions. Otherwise the previous parameters will be replaced by the new interpolated parameters and the iteration repeats.

### 3.6 Off-Line Simulation Results of the LMA

Figure 3.11 and Figure 3.12 show the variations of the total power losses in the constant torque region with  $i_d$  and  $T_d$  at a mechanical speed of 200rpm (below rated speed) and 1350rpm (rated speed), respectively where the resultant optimal values of  $i_d$  which give the minimum total power losses are denoted by the red triangle. Figure 3.13 shows the variations of  $i_q$  with  $i_d$  and  $T_d$  at 200rpm and 1350rpm in the form of MTPA trajectory. The differences in the ( $i_d$ ,  $i_q$ ) points of the two MTPA trajectories calculated at constant torque (see Table 3.4) are caused by the iron losses as it increases with speed where the copper losses is current-dependent.

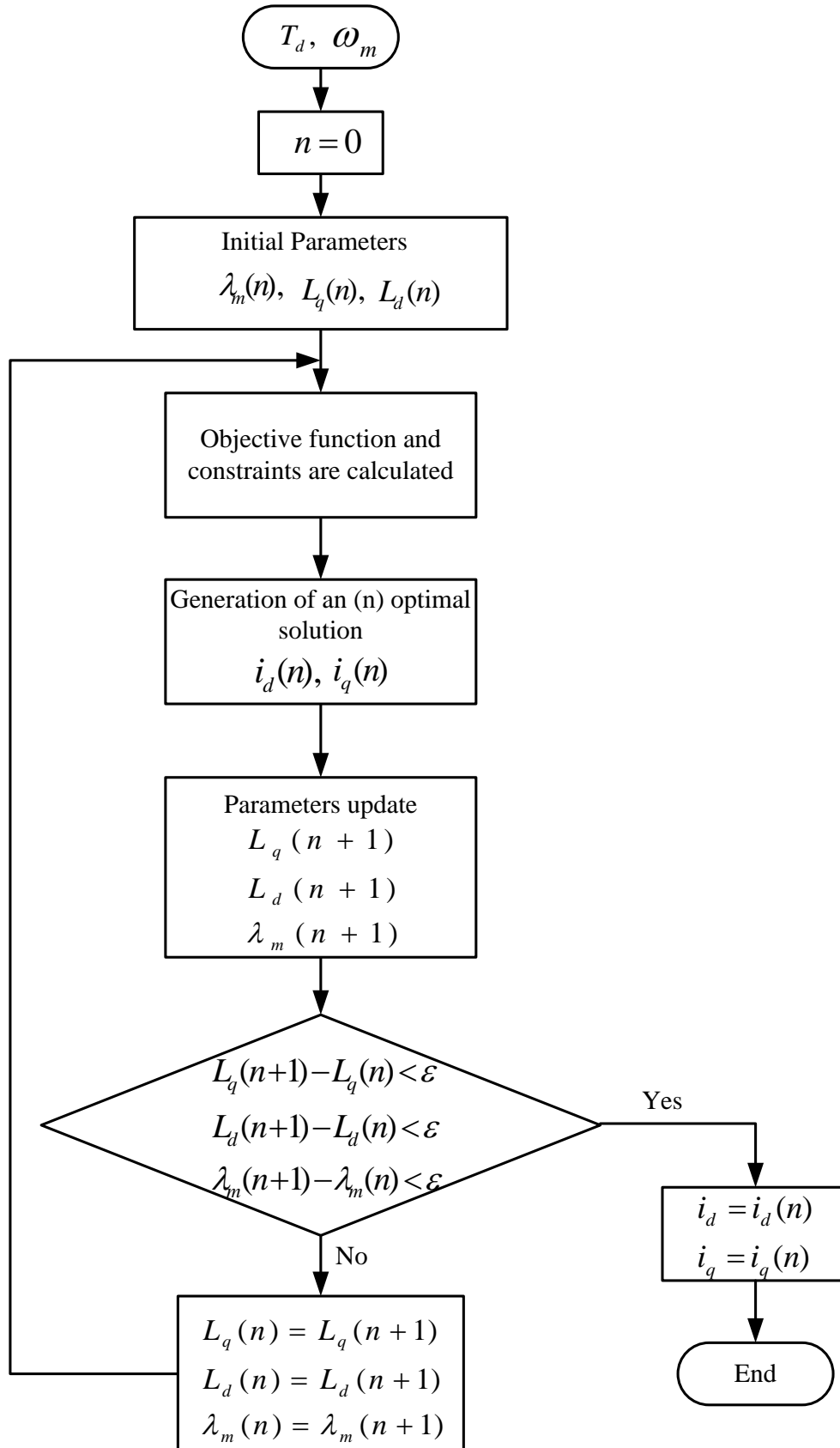


Figure 3.10 Flowchart of losses minimisation algorithm (LMA).

Table 3.4 Resultant MTPA trajectories at 200 and 1350rpm						
$T_d(Nm)$	$i_q(A)$			$i_d(A)$		
	200rpm	1350rpm	% diff.	200rpm	1350rpm	% diff.
10	16.801	16.377	2.50	-4.07	-5.75	41.30
20	32.05	31.34	2.23	-11.64	-13.29	14.18
30	46.737	45.878	1.84	-20.23	-21.75	7.51
40	61.304	60.328	1.60	-29.53	-30.91	4.67
50	76.414	75.386	1.35	-39.44	-40.61	2.97
60	92.119	91.099	1.11	-50.04	-51.00	1.92

It should be noted that the MTPA refers the current trajectory obtained from the losses minimisation algorithm which takes into account the iron losses. Figure 3.14 depicts the variations of the calculated minimum power losses with  $T_d$  and  $\omega_m$  in the CTR. Figure 3.15, Figure 3.16 and Figure 3.17 show the obtained results in the FWR at speed 2000, 3000 and 4000rpm (deep flux weakening region) respectively where the optimal values of  $i_d$  (denoted by red circles) are chosen to be the values that satisfy both the current and voltage constraints.

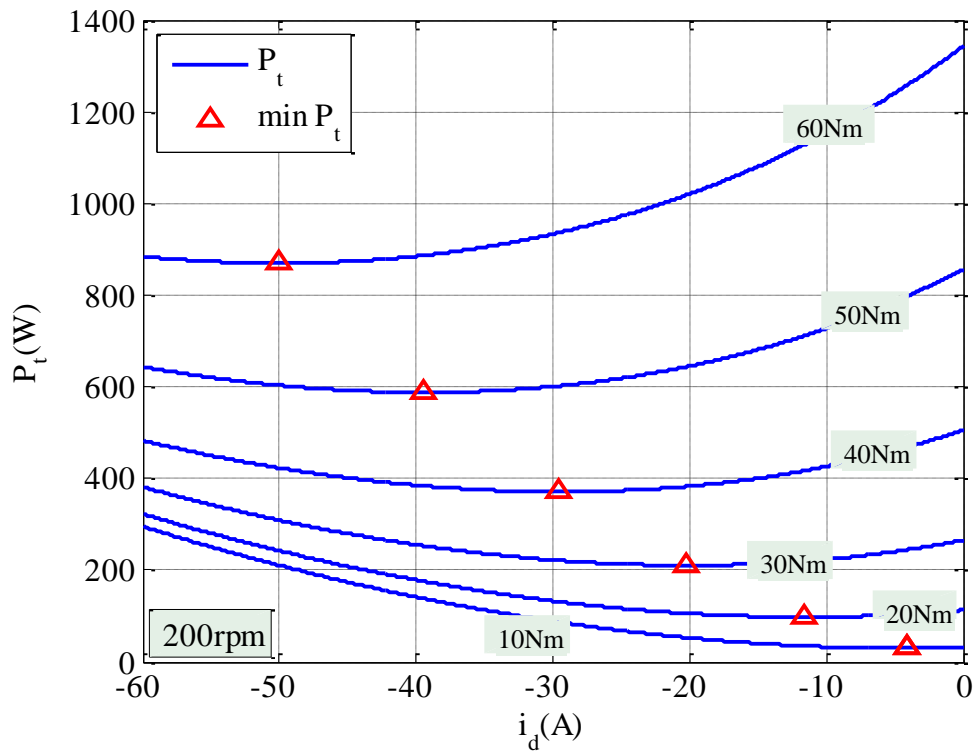


Figure 3.11 Variations of losses with  $i_d$  and  $T_d$  at  $\omega_m = 200rpm$  obtained by the LMA.

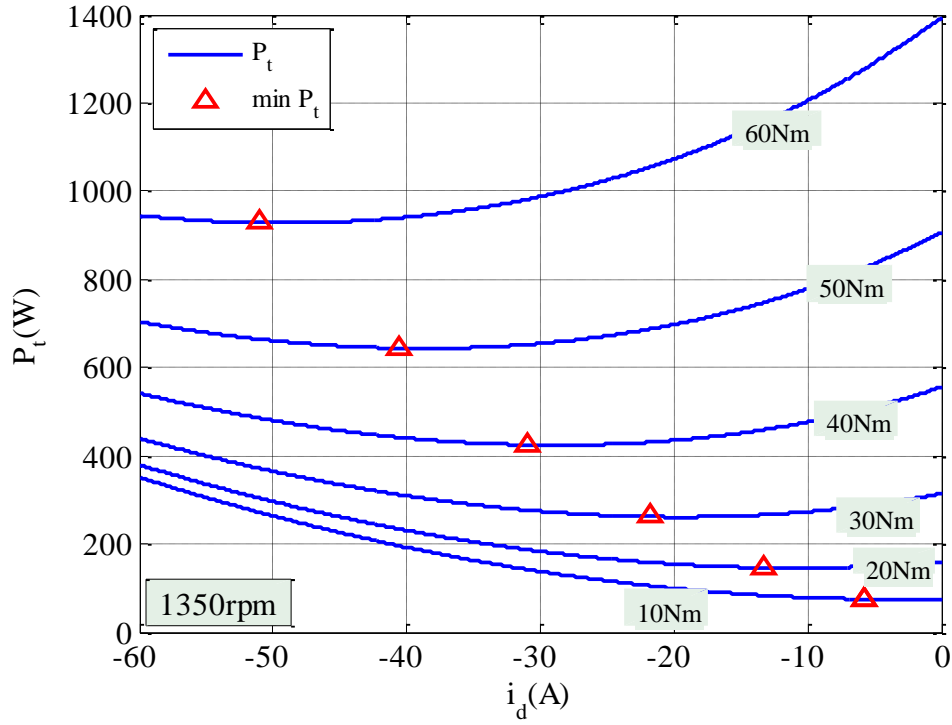


Figure 3.12 Variations of losses with  $i_d$  and  $T_d$  at  $\omega_m = 1350 \text{ rpm}$  obtained by the LMA.

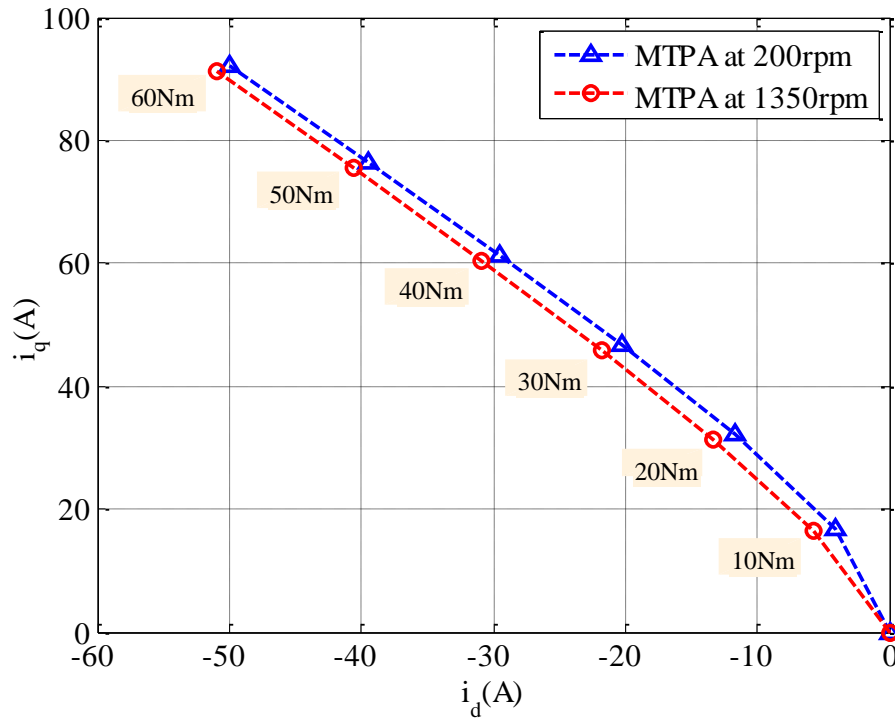


Figure 3.13 Variations of losses  $i_q$  with  $i_d$  and  $T_d$  at  $\omega_m = 200$  and  $1350 \text{ rpm}$  obtained by the LMA.

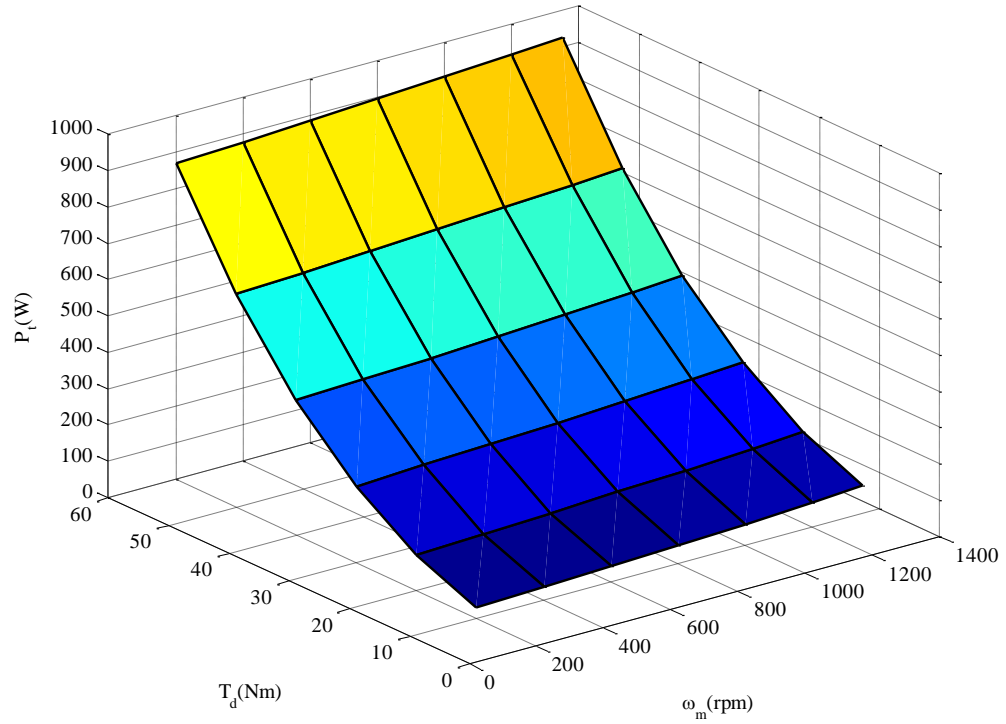


Figure 3.14 Resultant minimum losses variations with  $\omega_m$  and  $T_e$  obtained by the LMA.

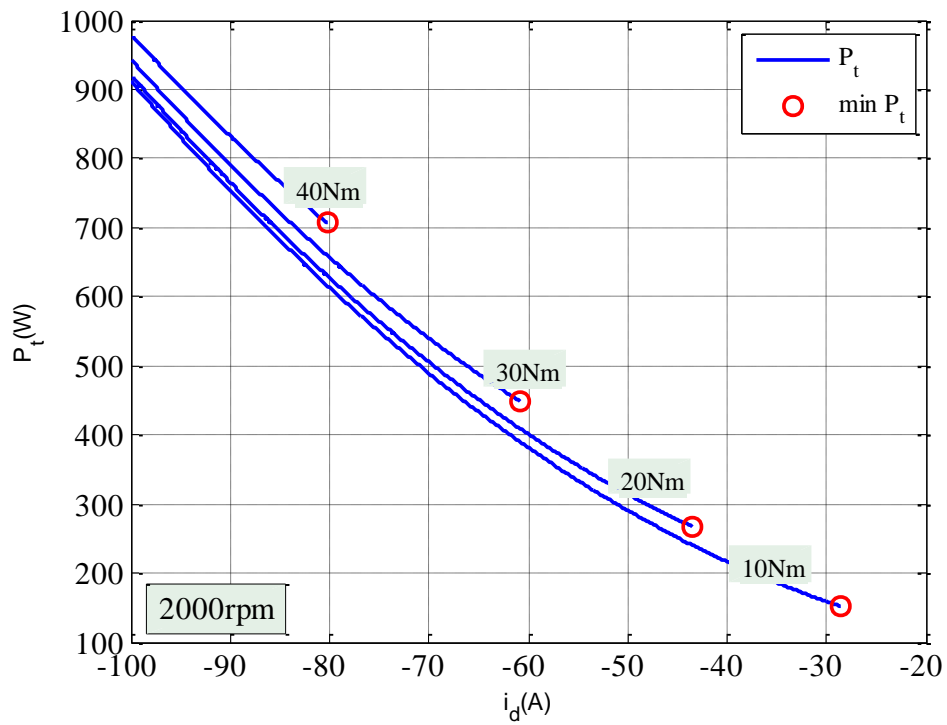


Figure 3.15 Variations of losses with  $i_d$  and  $T_d$  at  $\omega_m = 2000$  rpm obtained the LMA.



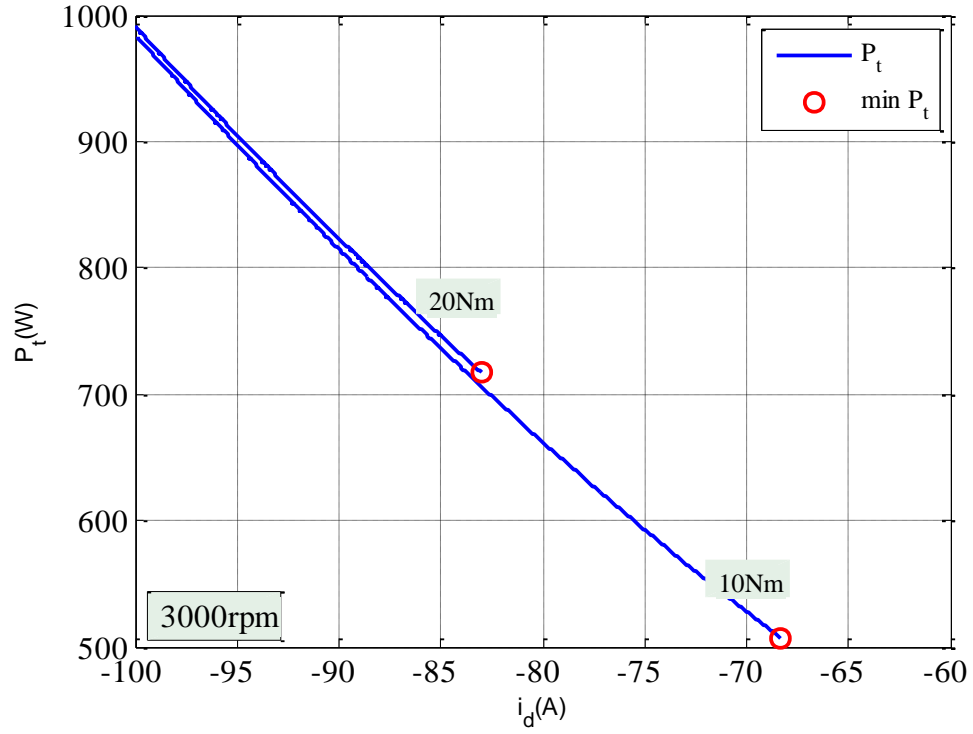


Figure 3.16 Variations of losses with  $i_d$  and  $T_d$  at  $\omega_m = 3000rpm$  obtained the LMA.

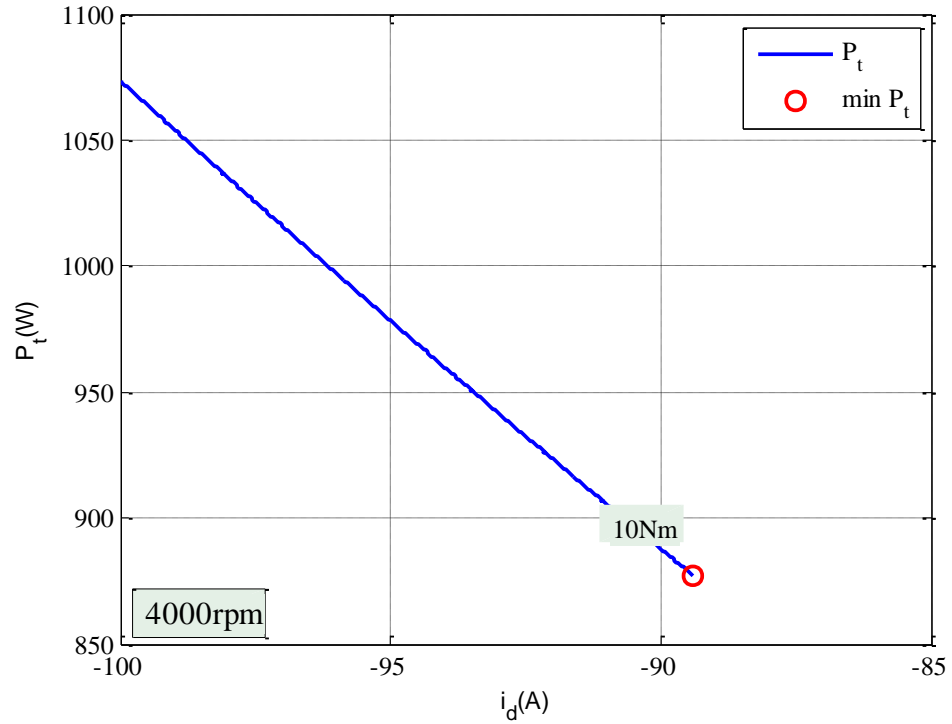


Figure 3.17 Variations of losses with  $i_d$  and  $T_d$  at  $\omega_m = 4000rpm$  obtained the LMA.

The results in both CTR and FWR show that the non-linear optimal operating points calculated by the LMA give the minimum power losses over the power losses curve at a specific speed and demand torque.

### **3.7 Chapter Summary**

In this Chapter a new losses minimisation algorithm LMA of IPMSM machine, is presented. This LMA calculates the optimal current vector  $(i_d, i_q)$  that yields the minimum power losses (copper and/or iron losses) at a given operating point  $(\omega_m, T_d)$  while taking into consideration of the IPMSM parameters variations  $(L_d, L_q$  and  $\lambda_m)$  and the voltage drop in the stator resistance which has been neglected in most previous work. The traditional IPMSM mathematical model is used but the motor inductances and flux linkages are expressed as non-linear functions of the current vector  $(i_d, i_q)$ . The off-line calculations of the LMA in the constant torque region show that the obtained optimal current solution at a given speed and torque yields the minimum operating power losses. In the flux weakening region the results show that the minimum power losses is restricted by the maximum available voltage and current at the given operating point  $(\omega_m, T_d)$  therefore, the optimal current solution lies on the intersection point which satisfies both the torque demand and voltage limits. The proposed LMA is flexible as it has the ability to generate an optimal solution for the IPMSM losses minimisation problem with no restriction on the non-linear characteristics and with due account of the resistive voltage drop which are often neglected in literature. Therefore the proposed LMA is ideal to be used in comprehensive studies such as an assessment of the influence of parameters variations, neglecting of the resistive voltage drop and iron losses on the obtained optimal solution under specific given speed and torque as will be shown in Chapter 4.

## 4 INFLUENCE OF IPMSM PARAMETERS NONLINEARITY, STATOR RESISTIVE VOLTAGE DROP AND IRON LOSSES ON THE LOSSES MINIMISATION

### 4.1 Introduction

Chapter 3 presents a new LMA that is able to account for the well-known parameters variations problem of IPMSMs and voltage drop across the stator resistance. The losses which are aimed to be minimised are the copper and iron losses in both CTR and FWR. Losses minimisation techniques such as LMCs which are depending on IPMSM machine parameters [54, 55, 60-64] has the advantage of fast finding of the optimal solution under given operation conditions however, their performance is strongly depending on the accurate knowledge of the motor parameters. Basically, parameter variations problem of IPMSMs makes the searching of the true minimum losses solution difficult. Parameters saturations have been sometimes considered [65] but neglected in most literature especially in the flux weakening region due to calculation difficulties [59, 65, 66]. It is also common to consider  $L_q$  saturation effect due to its significant change where  $L_d$  is usually assumed to be constant [59] however, the variation of  $\lambda_m$  is most likely to be neglected. Additionally, the resistive voltage drop has been generally ignored in literature for simplification reasons particularly in the flux weakening region where it has been assumed that the voltage drop through the stator winding resistor at high speed is negligible [20, 34]. In terms of considering motor controllable losses, the focus is generally on the minimisation of the copper losses due to some difficulties in iron losses calculation although great efforts have been made in order to present accurate, simple and effective iron losses models [81, 82]. However, the influence of the parameter variation, resistive voltage drop, and iron losses in losses minimisation is not clearly highlighted in literature and as the other studies do not considered all of the nonlinear effects; this chapter investigates the influences of neglecting them and gives a benchmark. Therefore, a comprehensive off-line simulation study based on the LMA described in Chapter 3 is presented. The impact of the parameters ( $L_d$ ,  $L_q$  and  $\lambda_m$ ) non-linearity on minimum losses operation point ( $i_d, P_t$ ) is

described in section 4.2. Section 4.3 highlights the effect of accounting for or neglecting the resistive voltage ( $V_R$ ) on the optimal currents and hence minimum power losses calculated by the LMA. Section 4.4 discusses the influence of neglecting the iron losses  $P_{fe}$  on the optimal solution of the losses minimisation criteria. Finally, the chapter work is summarised in section 4.5. The work described in sections 4.2 and 4.3 has been published in [91].

## 4.2 Influence of Parameters Variations

The influence of  $L_d$ ,  $L_q$  and  $\lambda_m$  variations on the minimum losses operation is evaluated in this section by comparing the optimal  $i_d$  values calculated with linear (constant) parameters and non-linear (actual or varying) parameters under the same operating condition ( $\omega_m, T_d$ ). The saturation affect is inspected in both CTR and FWR in order to ensure that this effect is well-assessed over the full speed and torque ranges of the IPMSM drive. The resistive voltage drop across the stator resistance  $V_R$ , the iron losses and copper losses are considered in this section. The same input operating points given in Table 3.3 are used in the computations in this section.

### 4.2.1 Constant Torque Region

The off-line simulation results in the CTR where the speed is less than or equal to the base speed (1350rpm), are shown in Figure 4.1 and Figure 4.2. The optimal solution obtained in each case is summarised in Table 4.1 and Table 4.2, respectively. From Figure 4.1, it can be seen that the optimal values of  $i_d$  which are calculated at linear and non-linear parameters are not equal at the given torques. As the resultant  $i_d$  currents in both linear and non-linear cases are calculated under the same speed and torque demand the differences between these currents and power losses levels are due to parameter variations. However, the difference in the minimum power losses at relatively low torque ( $T_d$  is 10Nm and 20Nm, Figure 4.1) with and without considering the parameters variations is not noticeable, where the non-linear minimum power losses at 20Nm is

increased by 0.81 per cent compared with that calculated at constant (linear) parameters, Table 4.1.

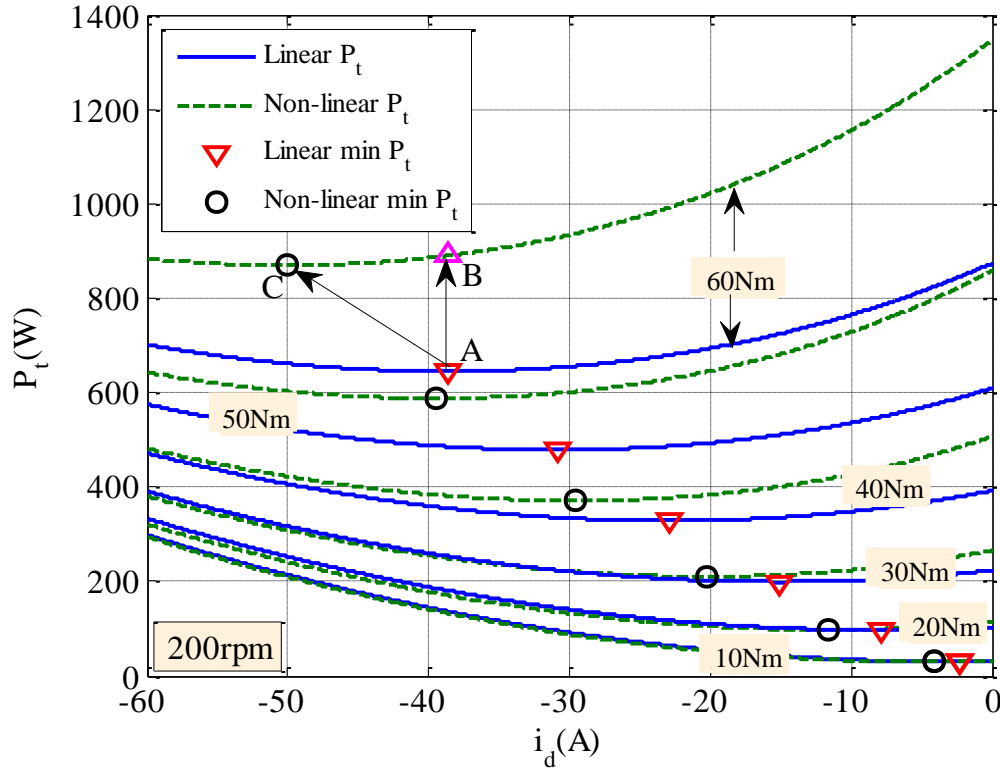


Figure 4.1 Variations of losses with  $i_d$  and  $T_d$  at  $\omega_m = 200\text{rpm}$  obtained with linear (constant) and non-linear (varying) parameters.

As  $T_d$  increases from  $20\text{Nm}$  to  $30\text{Nm}$ , the optimal  $i_d$  point that account for parameters non-linearity moves towards higher negative value with slightly higher minimum power losses than that achieved by constant parameters, Figure 4.1. A further increase in the torque ( $40\text{Nm}$  to  $60\text{Nm}$ , Table 4.1) causes the differences in the linear and non-linear current and power losses levels to be significantly increased.

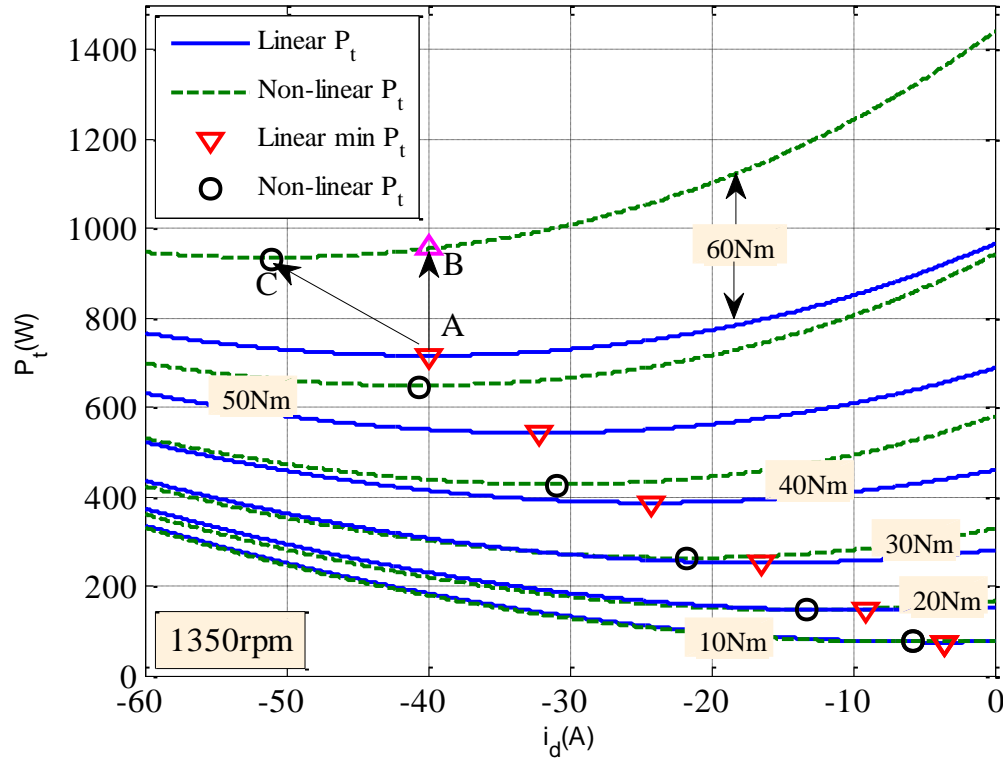


Figure 4.2 Variations of losses with  $i_d$  and  $T_d$  at  $\omega_m = 1350rpm$  obtained with linear (constant) and non-linear (varying) parameters.

$T_d(Nm)$	$i_d(A)$			$P_t(W)$		
	Linear	Non-linear	% diff.	Linear	Non-linear	% diff.
10	2.26	-4.07	80.09	29.51	29.4	0.37
20	-7.83	-11.64	48.66	97.03	97.82	0.81
30	-15.08	-20.23	34.15	199.37	210.58	5.62
40	-22.93	-29.53	28.78	328.54	370.69	12.83
50	-30.86	-39.44	27.80	478.51	587.73	22.83
60	-38.64	-50.04	29.50	644.97	869.66	34.84

By comparing the optimal point A ( $i_d = -38.64A$ ,  $P_t = 644.97W$ ) illustrated in Figure 4.1 which results with the linear parameters and the optimal point C ( $i_d = -50.04A$ ,  $P_t = 869.66W$ ) which results with the non-linear parameters, it can be seen that the parameter variations due to magnetic saturation increases the power losses by about 34.84% at 60Nm. However, if the parameter variations are not taken into account in the optimisation process, the optimal  $i_d$  would be -38.64A and the resultant actual losses is

the value at point B which is 890.65W, Figure 4.1. The difference between power losses point B and C is, however, marginal being about 2.41%. Figure 4.2 shows the variations of power losses with  $i_d$  and  $T_d$  when the IPMSM machine operates at the base speed (1350rpm). From these results it is obvious that the obtained optimal  $i_d$  currents and minimum power losses levels at a given speed and  $T_d$  are following the same trend shown in Figure 4.1 regardless the speed. It is also noted that for a given  $T_d$ , the optimal  $i_d$  at 200rpm (see Table 4.1) and 1350rpm (see Table 4.2) are not equal. This is due to the fact that the iron losses are speed and current dependant whiles the copper losses is proportional to the current. If the copper losses are only considered in the losses minimisation problem, then the  $i_d$  currents will be equal at different speeds as long as the torque is kept constant and the IPMSM machine is running below rated speed (MTPA). This is owing to the fact that the MTPA control is independent of speed [81, 82] when the iron losses is neglected.

Table 4.2 Resultant linear and non-linear optimal ( $i_d, P_t$ ) at 1350rpm						
$T_d(Nm)$	$i_d(A)$			$P_t(W)$		
	Linear	Non-linear	% diff.	Linear	Non-linear	% diff.
10	-3.58	-5.75	60.61	74.608	75.01	0.54
20	-9.15	-13.29	45.25	145.22	146.28	0.73
30	-16.41	-21.75	32.54	251.98	261.86	3.92
40	-24.27	-30.91	27.35	386.55	424.68	9.86
50	-32.20	-40.61	26.74	542.64	644.01	18.68
60	-39.99	-51.00	27.53	715.74	928.28	29.70

The optimal point A ( $i_d = -39.99A$ ,  $P_t = 715.74W$ ) (see Figure 4.2) resultant with linear parameters and the optimal point C ( $i_d = -51.00A$ ,  $P_t = 928.28W$ ) calculated with the nonlinear parameters at 60Nm, are compared. The power losses are higher at both points A and C than that in Figure 4.1 due to the speed increase. The percentage of the difference of the obtained minimum power losses between points A and C is, however, reduced from 34.84% at 200rpm to 29.70% at 1350rpm. This reduction in difference between linear and non-linear minimum power losses is due to the fact that the values of linear parameters and non-linear parameters at the selected operating point (1350rpm, 60Nm) are close. As mentioned in Chapter 3, the linear or constant IPMSM parameters have been selected to be the values at 1350rpm and 70Nm obtained by the FEM, Table 3.1. Neglecting the parameters variations effect, causes the power losses

difference between points B ( $i_d = -39.99A$ ,  $P_t = 955.54W$ ) and C ( $i_d = -51.00A$ ,  $P_t = 928.28W$ ) to be increased to about 2.94% compared with 2.23% at 200rpm and 60Nm, Figure 4.2. The variations of  $i_q$  with  $i_d$  (MTPA trajectory) due to linear and non-linear parameters at speed 200rpm and 1350rpm is illustrated in Figure 4.3 and Figure 4.4, respectively. The figures show that by considering the parameters variations, the MTPA trajectories at the given speeds are pulled towards higher positive levels of  $i_q$  as  $i_d$  increases in the negative direction at a given torque. The differences in  $i_q$  currents levels at the given speeds (200rpm and 1350rpm) and  $T_d$  are summarised in Table 4.3.

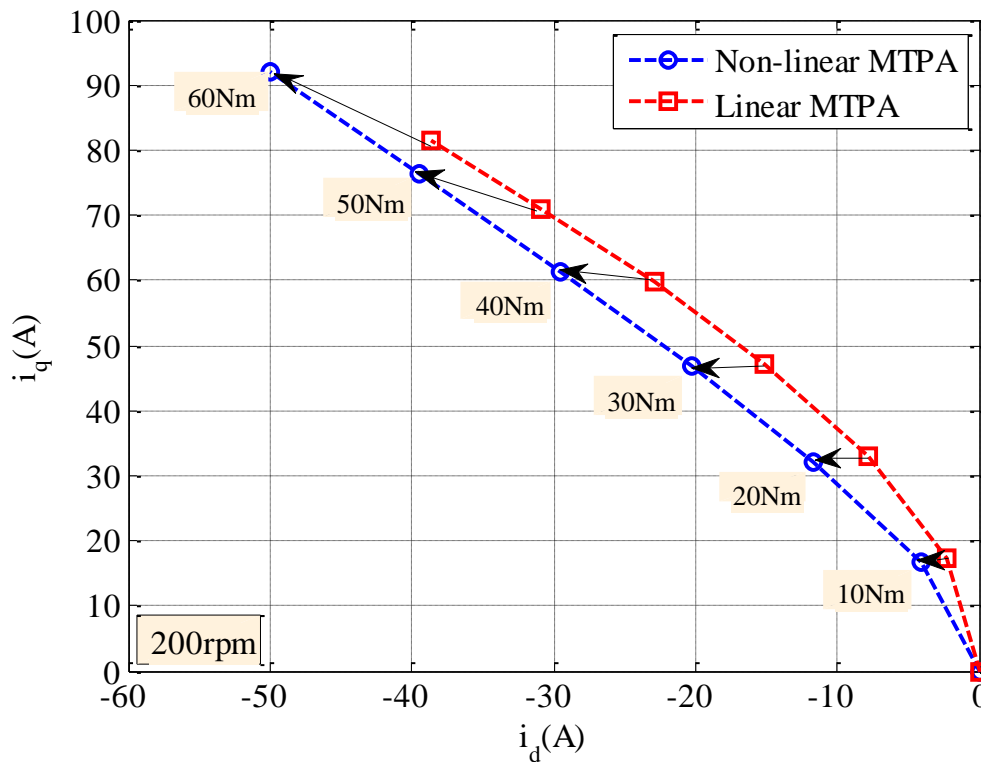


Figure 4.3 Variations of  $i_q$  with  $i_d$  and  $T_d$  at  $\omega_m = 200rpm$  obtained with linear (constant) and non-linear (varying) parameters.

Figure 4.5 and Figure 4.6, respectively, show the variations of the minimum power losses for a set of given operating points ( $\omega_m, T_d$ ) which is calculated under linear and non-linear parameters conditions in the CTR. The resultant difference in linear and nonlinear power losses levels is depicted in Figure 4.7. From this figure it is obviously that the saturation of the IPMSM parameters has slight effect on the achievable



minimum power losses at low torques over the given speed range in the CTR. As the torque increase the difference between the two power levels become obvious. For example at speed  $1350rpm$ , the power losses increases from  $1.06W$  at  $20Nm$  to about  $212W$  at  $60Nm$ , Figure 4.7.

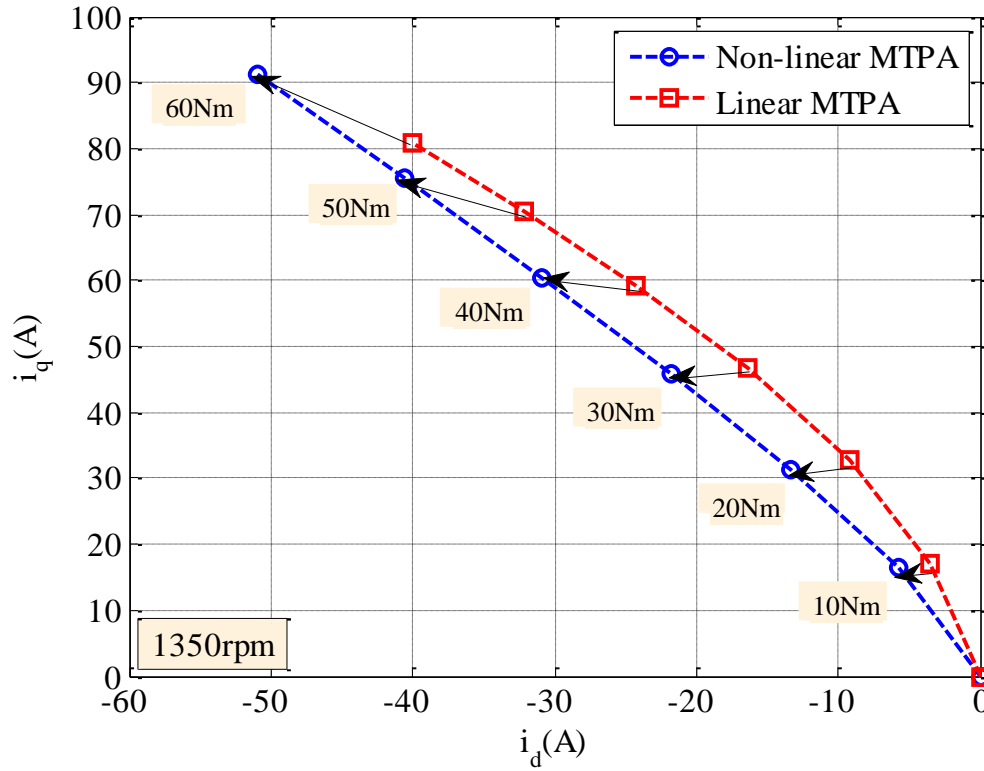


Figure 4.4 Variations of  $i_q$  with  $i_d$  and  $T_d$  at  $\omega_m = 1350rpm$  obtained with linear (constant) and non-linear (varying) parameters.

Table 4.3 Resultant linear and non-linear optimal $i_q$						
$T_d(Nm)$	$i_q(A)$ at $200rpm$			$i_q(A)$ at $1350rpm$		
	Linear	Non-linear	% diff.	Linear	Non-linear	% diff.
10	17.206	16.801	2.35	17.04	16.377	3.90
20	33.053	32.05	3.03	32.746	31.34	4.29
30	47.151	46.737	0.88	46.733	45.878	1.83
40	59.706	61.304	2.68	59.199	60.328	1.91
50	71.025	76.414	7.59	70.448	75.386	6.55
60	81.366	92.119	14.4	80.732	91.099	12.84

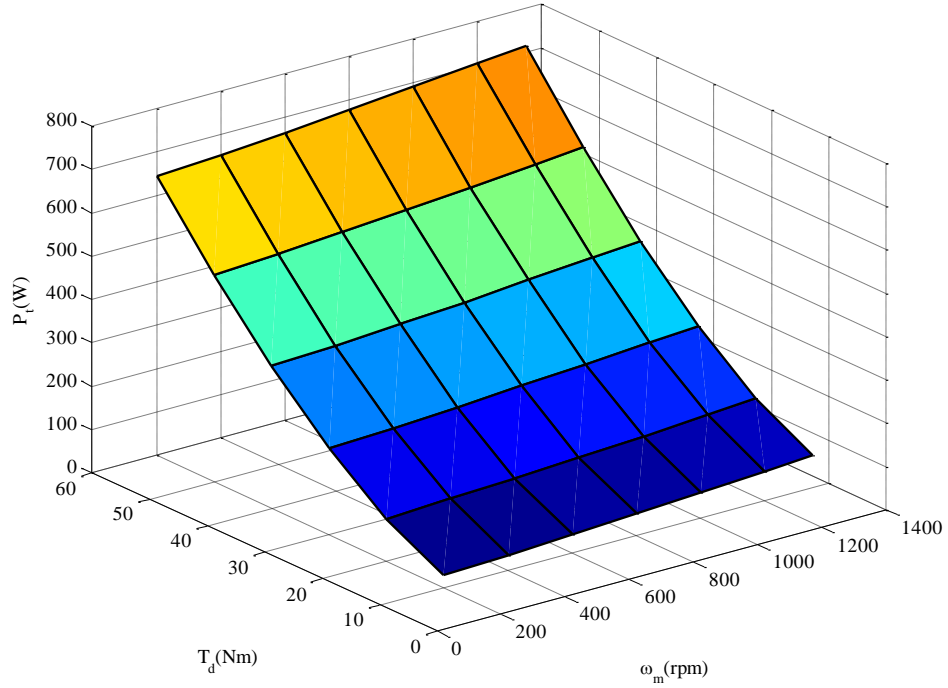


Figure 4.5 Resultant minimum losses variations with  $\omega_m$  and  $T_d$  obtained from linear (constant) parameters.

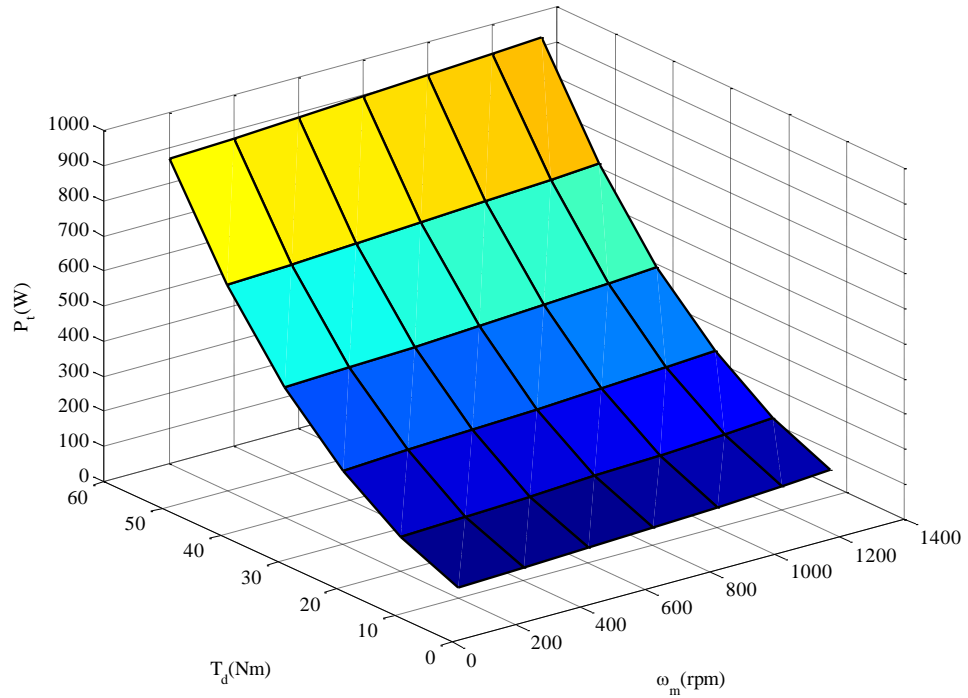


Figure 4.6 Resultant minimum losses variations with  $\omega_m$  and  $T_d$  obtained from non-linear (variable) parameters.

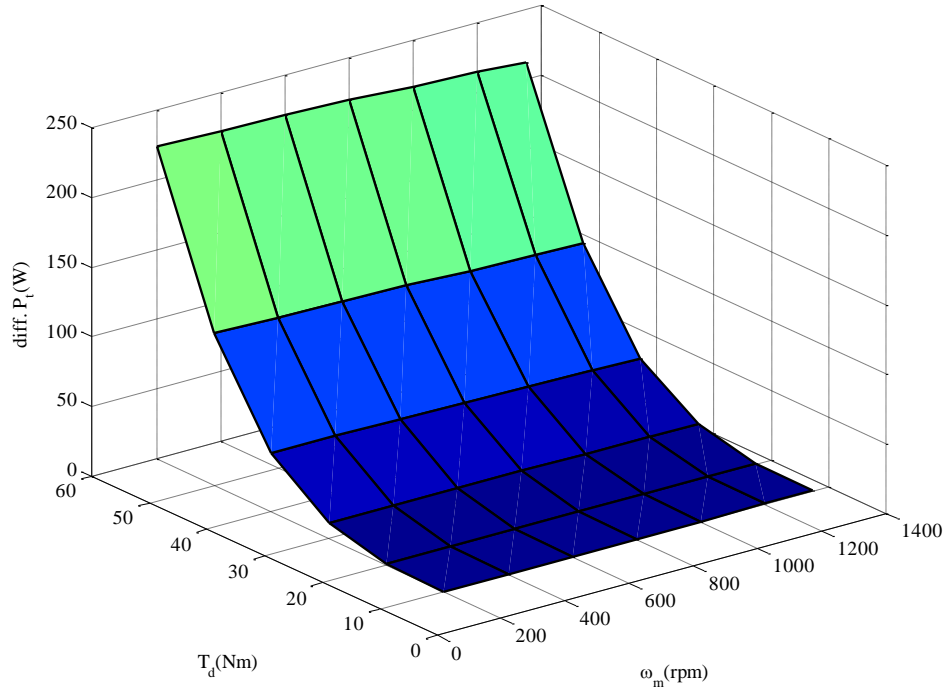


Figure 4.7 Resultant minimum losses differences variations with  $\omega_m$  and  $T_d$  obtained from linear (variable) and non-linear (constant).

#### 4.2.2 Flux Weakening Region (FWR)

Similarly, the LMA is simulated in the FWR ( $\omega_m > 1350\text{rpm}$ ) with and without considering the parameters variations in order to emphasis its effect on the calculated optimal solutions ( $i_d$ ,  $P_t$ ) under flux weakening control. The speed range is chosen to be  $2000\text{rpm}$  to  $4000\text{rpm}$  (deep flux weakening region) in a  $1000\text{rpm}$  step basis. The torque is ranged according to the maximum available torque at specific speed defined by the torque-speed profile depicted in Figure 3.9. The obtained results of the LMA off-line calculations at the given speeds are shown in Figure 4.8, Figure 4.9 and Figure 4.10 respectively. As will be seen, for a given torque the minimum losses point is bounded by the voltage constraint, and hence the magnitude of the  $i_d$  current cannot be below the minimum value which satisfies the voltage constraint. The minimum losses point is on the intersection of the torque and voltage equations. The optimal solutions ( $i_d$ ,  $P_t$ ) in the flux weakening region are strongly affected by the parameter variations at both low and high torques as the speed increases from  $2000\text{rpm}$  to  $4000\text{rpm}$ . This can be seen clearly

in the results summarised in Table 4.4, Table 4.5 and Table 4.6. For example, the percentage of the difference between linear and non-linear power losses levels that is achieved at 2000rpm and 10Nm is about 12.36%, Table 4.4. This percentage is markedly increased to be about 33.98% as the speed increases to 3000rpm and the torque is kept constant at 10Nm, Table 4.5. A further increase in the speed leading to higher differences level between the resultant power losses calculated with the linear and nonlinear parameters as shown in Figure 4.10 where the non-linear power losses is lower than the linear power losses by about 34.94% at 4000rpm and 10Nm, Table 4.6. Due to magnetic saturation, both  $q$ -axes inductance and permanent magnet flux linkage decrease with increase in current, Figure 3.5 and Figure 3.7, respectively. Consequently, the required d-axis current to satisfy the voltage constraints and torque demand is lower in magnitude than that when the parameter variation is neglected, Figure 4.8, Figure 4.9 and Figure 4.10 respectively. Thus, the differences in  $i_d$  current with linear and non-linear parameters reach -29.205A at 4000rpm, Table 4.6.

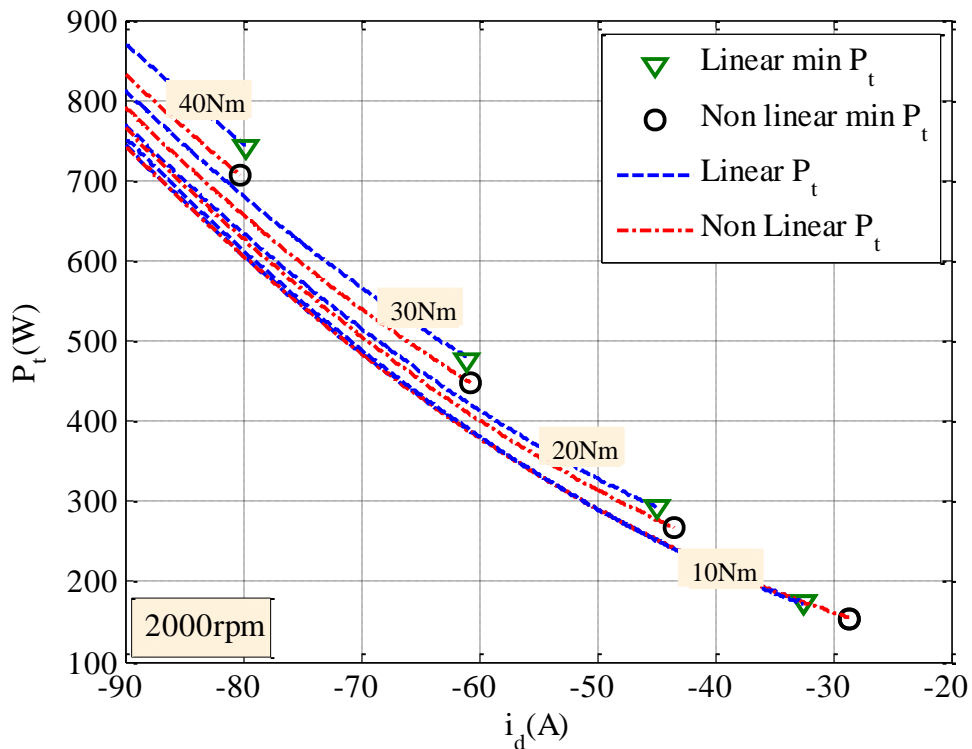


Figure 4.8 Variations of losses with  $i_d$  and  $T_d$  at  $\omega_m = 2000rpm$  obtained with linear (constant) and non-linear (varying) parameters.

Hence, if the parameter variations are neglected in the field weakening operation, excessive d-axes current will be produced by the drive control, and a significant reduction in the drive efficiency will take place.

Table 4.4 Resultant linear and non-linear optimal $(i_d, P_t)$ at 2000rpm						
$T_d(Nm)$	$i_d(A)$			$P_t(W)$		
	Linear	Non-linear	% diff.	Linear	Non-linear	% diff.
10	-32.497	-28.641	11.87	174.41	152.85	12.36
20	-44.851	-43.463	3.09	293.37	267.96	8.66
30	-61.076	-60.767	0.51	475.64	448.75	5.65
40	-80.269	-80.162	0.11	740.99	706.87	4.60

The differences between the achieved linear and non-linear optimal solutions  $(i_d, P_t)$  at 2000rpm, is small, Table 4.4. This is again due to the fact that the linear parameters are chosen to be the values of these parameters at rated speed and maximum torque, Table 3.1. Therefore the differences between  $i_d$  optimal currents calculated at linear parameters and interpolating parameters (non-linear parameters) will be small leading to small differences between linear and non-linear optimal  $i_d$  solutions at this speed especially at high torques where the difference between the maximum torque (70Nm) and a given  $T_d$  is gradually reduced. As the speed increases further the differences between the calculated linear and non-linear optimal current become significant due to the increasing in the deviation of the non-linear parameters from linear parameters at constant speed and torque (see Table 4.5 and Table 4.6). For example, the variations in  $i_q$  due to parameter non-linearity in the flux weakening region at speed 2000rpm and 3000rpm are summarised in Table 4.7. It is noted that the differences between  $i_q$  current levels increases as the torque increases at constant speed.

Table 4.5 Resultant linear and non-linear optimal $(i_d, P_t)$ at 3000rpm						
$T_d(Nm)$	$i_d(A)$			$P_t(W)$		
	Linear	Non-linear	% diff.	Linear	Non-linear	% diff.
10	-89.56	-68.289	23.75	767.57	506.77	33.98
20	-101.17	-83.012	17.95	980.3	717	26.86

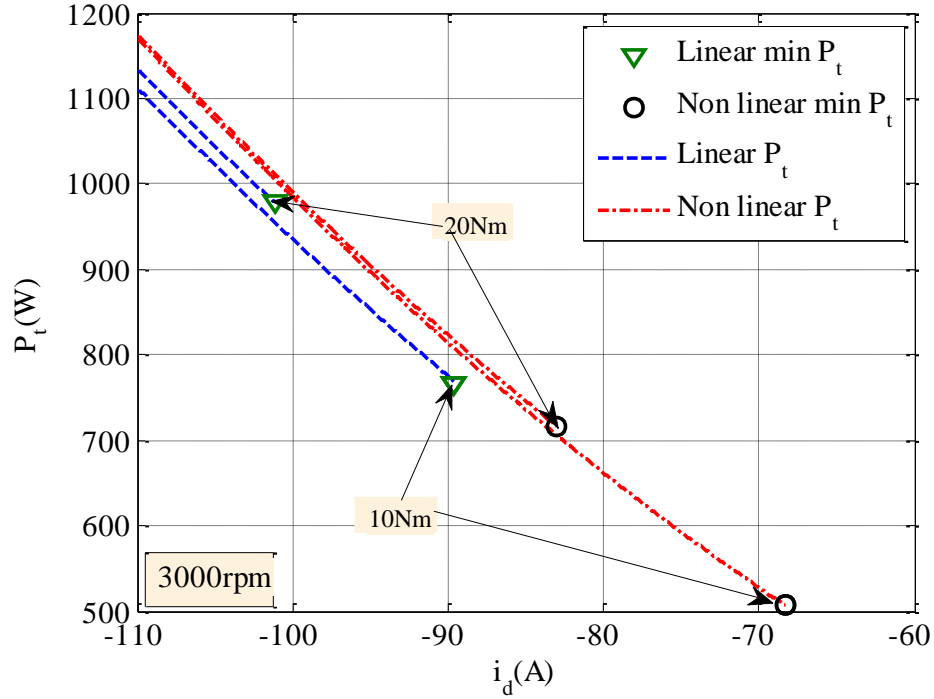


Figure 4.9 Variations of losses with  $i_d$  and  $T_d$  at  $\omega_m = 3000 \text{ rpm}$  obtained with linear (constant) and non-linear (varying) parameters.

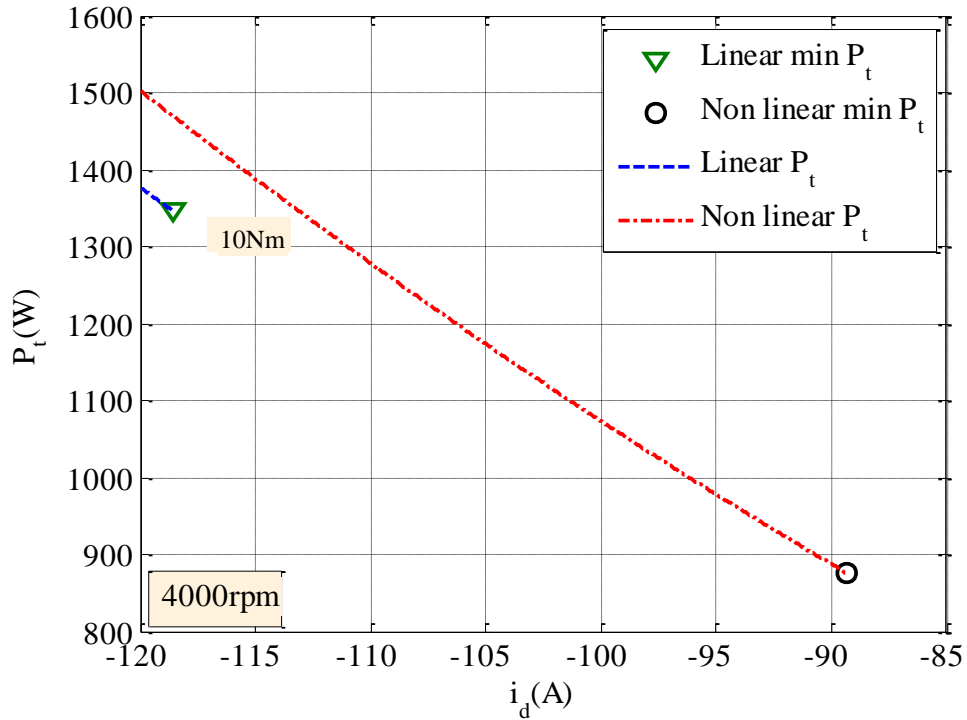


Figure 4.10 Variations of losses with  $i_d$  and  $T_d$  at  $\omega_m = 4000 \text{ rpm}$  obtained with linear (constant) and non-linear (varying) parameters.

Table 4.6 Resultant linear and non-linear optimal  $(i_d, P_t)$  at 4000rpm

$T_d(Nm)$	$i_d(A)$			$P_t(W)$		
	Linear	Non-linear	% diff.	Linear	Non-linear	% diff.
10	-118.56	-89.355	24.63	1347.3	876.56	34.94

Table 4.7 Resultant linear and non-linear optimal  $i_q$ 

$T_d(Nm)$	$i_q(A)$ at 2000rpm			$i_q(A)$ at 3000rpm		
	Linear	Non-linear	% diff.	Linear	Non-linear	% diff.
10	14.064	11.856	15.69	10.46	8.3072	2.1528
20	26.176	21.367	18.37	19.884	15.548	4.336
30	35.984	29.106	19.11			
40	43.755	35.344	19.22			

### 4.3 Influence of Stator Resistor Voltage Drop

This section investigates the influence of the resistive voltage drop  $V_R$  across the stator windings resistance which has been considered negligibly small especially at high speed where the IPMSM is driving under current and voltage limits (i.e., flux weakening operation conditions). The parameters variation effect, copper and iron losses are considered in this study. When the IPMSM drive operates in constant torque region, the voltage saturation has not been reached and consequently, neglecting  $V_R$  will not affect the losses optimisation process. At high speed (FWR), however, the resistive voltage drop would affect the operating point. The off-line calculations with and without  $V_R$  being included at speeds of 2000, 3000 and 4000rpm (deep flux weakening region) shown in Figure 4.11, Figure 4.12 and Figure 4.13 respectively. From these figures, it can be seen that the resistive voltage drop can strongly affect the minimum operating points of the IPMSM at high torque level as neglecting  $V_R$  leads to less negative d-axis current and insufficient field weakening flux. The current control will saturate and consequently the demand torque will not be reached. The voltage deficit will be more significant at high torque level due to  $V_R$  being proportional to current or torque. The results for the three selected speed points are summarised in Table 4.8, Table 4.9 and Table 4.10. For instance, the variations in  $i_q$  with  $i_d$  due to resistive voltage drop in the flux weakening region at speed 2000rpm and 3000rpm are summarised in Table 4.11.

The differences between  $i_q$  current levels increases as the torque increases at constant speed.

Table 4.8 Optimal solution ( $i_d, P_t$ ) with and without $V_R$ ( $i_d, P_t$ ) at 2000rpm						
$T_d(Nm)$	$i_d(A)$			$P_t(W)$		
	with $V_R$	without $V_R$	% diff.	with $V_R$	without $V_R$	% diff.
10	-28.641	-26.772	6.53	152.85	144.63	5.38
20	-43.463	-39.758	8.52	267.96	244.85	8.62
30	-60.767	-55.029	9.44	448.75	400.16	10.83
40	-80.162	-71.983	10.20	706.87	617.78	12.60

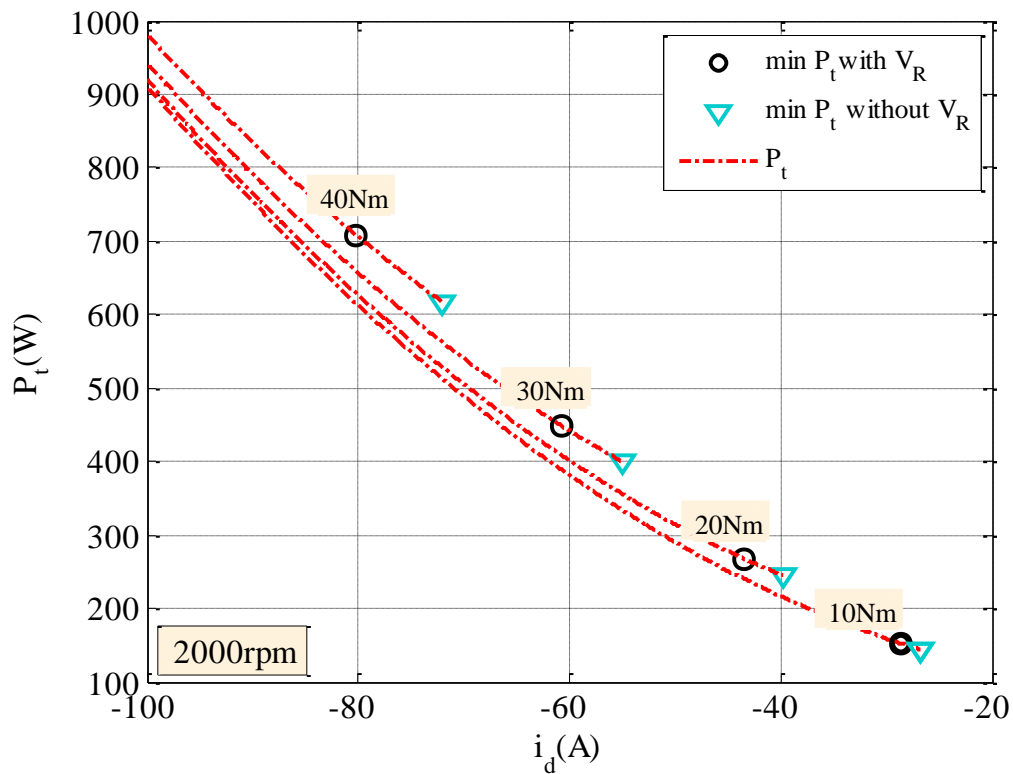


Figure 4.11 Variations of losses with  $i_d$  and  $T_d$  at  $\omega_m = 2000rpm$  obtained with and without  $V_R$ .

Table 4.9 Optimal solution ( $i_d, P_t$ ) with and without $V_R$ ( $i_d, P_t$ ) at 3000rpm						
$T_d(Nm)$	$i_d(A)$			$P_t(W)$		
	with $V_R$	without $V_R$	% diff.	with $V_R$	without $V_R$	% diff.
10	-68.289	-66.291	2.93	506.77	482.48	4.79
20	-83.012	-78.933	4.91	717	658.12	8.21



Table 4.10 Optimal solution ( $i_d, P_t$ ) with and without $V_R$ at 4000rpm						
$T_d(Nm)$	$i_d(A)$			$P_t(W)$		
	with $V_R$	without $V_R$	% diff.	with $V_R$	without $V_R$	% diff.
10	-89.355	-87.225	2.38	876.56	839.6831	4.21

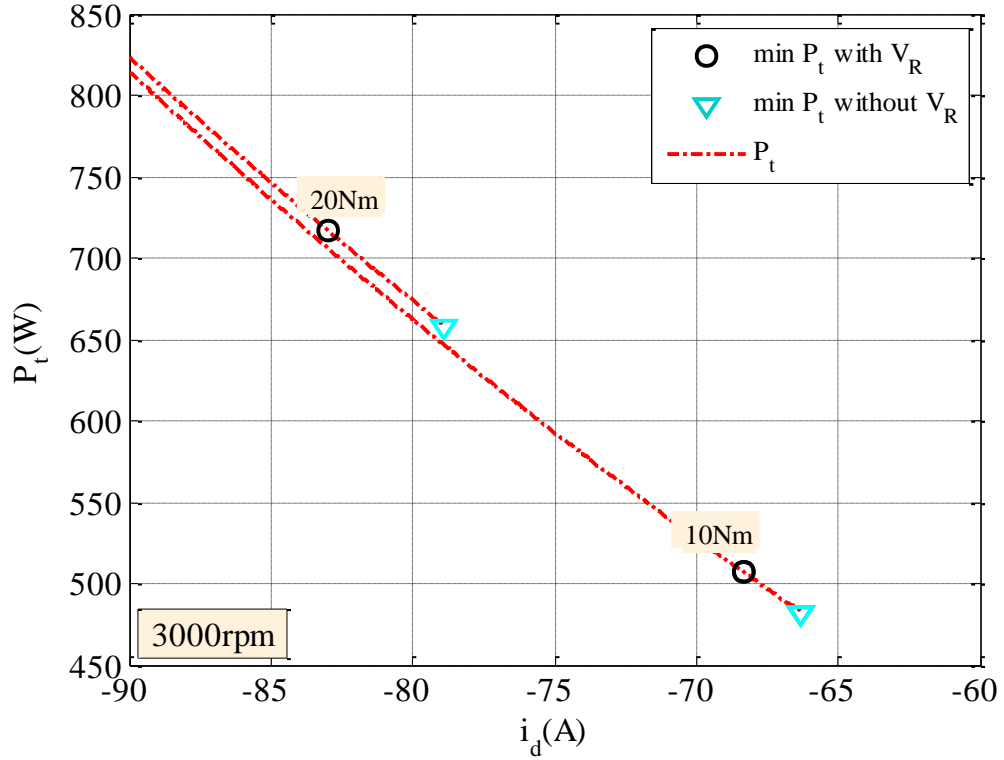


Figure 4.12 Variations of losses with  $i_d$  and  $T_d$  at  $\omega_m = 3000rpm$  obtained with and without  $V_R$ .

Table 4.11 Resultant linear and non-linear optimal $i_q$						
$T_d(Nm)$	$i_q(A)$ at 2000rpm			$i_q(A)$ at 3000rpm		
	without $V_R$	with $V_R$	% diff.	without $V_R$	with $V_R$	% diff.
10	12.145	11.856	2.38	8.416	8.3072	0.1088
20	22.301	21.367	4.19	15.944	15.548	0.396
30	30.843	29.106	5.63			
40	37.993	35.344	6.97			

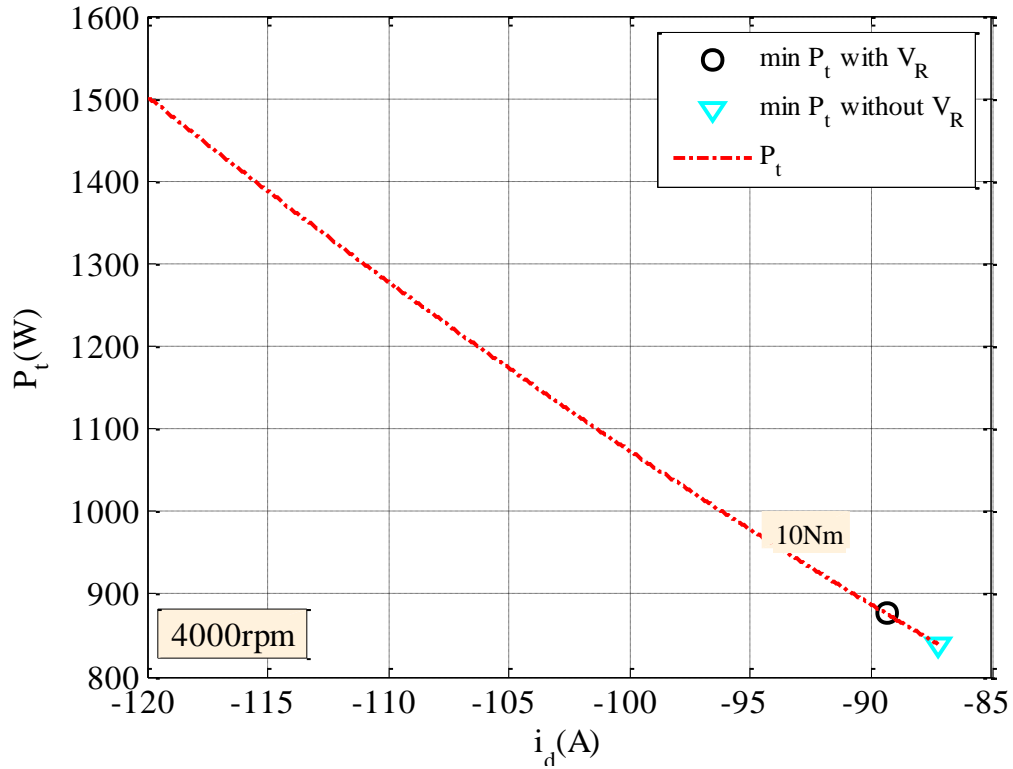


Figure 4.13 Variations of losses with  $i_d$  and  $T_d$  at  $\omega_m = 4000rpm$  obtained with and without  $V_R$ .

#### 4.4 Influence of Iron Losses

This section is focusing on investigating the impact of the iron losses on the minimum losses operation point of the IPMSM in both constant and flux weakening regions. The total power losses consists of the copper and iron losses, therefore the influence of the iron losses on the resultant optimal solution of the IPMSM losses minimisation problem, is evaluated by comparing the optimal points calculated by the LMA with and without considering the iron losses at a given speed and torque. In this stage the parameters variations effects as well as the resistive voltage drop are considered where their influences on the minimum losses operating points of the IPMSM have been evaluated in sections 4.2 and 4.3.

#### 4.4.1 Constant Torque Region

The off-line results of the LMA with and without considering the iron losses in the power losses objective function given by Eqn. 3.42 are compared at low speed (200rpm) and rated speed (1350rpm) as illustrated in Figure 4.14 and Figure 4.15, respectively. Again, the torque is ranged between 10Nm to 60Nm in a 10Nm step basis. At low speed (see Figure 4.14), the results show that the differences between the calculated optimal solutions  $(i_d, P_t)$  with and without considering the iron losses is considerably small. This is owing to that the power losses levels at low speed and low torque is generally small. The simulation results at each given torque with and without considering the iron losses are summarised in Table 4.12. As the speed increases to the base speed (see Figure 4.15), the difference between the optimal solutions  $(i_d, P_t)$  with and without considering the iron losses become progressively visible. As the copper losses are independent of the speed and the optimal current vector  $(i_d, i_q)$  for a given torque is constant, the copper losses should be kept constant as the speed changes. Therefore, the increase in the differences of the  $i_d$  currents and power losses levels over the torque range, Table 4.13, is due to the increase in the iron losses as the speed increases. In Figure 4.15, it is noted that the resultant optimal solutions  $(i_d, P_t)$  with (marked by “Δ”) and without considering  $P_{fe}$  (marked by “□”) both are allocated on the  $P_t$  curves which accounted for the iron loss in order to simplify the comparison between these two optimal solutions. For instance, while the difference between optimal  $i_d$  currents at 200rpm and 60Nm is only about 0.10% (see Table 4.12), it is increased to 1.98% at 1350rpm, Table 4.13. This is because of the dependency of the iron losses on the speed.

Table 4.12 Optimal solution  $(i_d, P_t)$  with and without  $P_{fe}$  at 200rpm

$T_d(Nm)$	$i_d(A)$			$P_t(W)$		
	with $P_{fe}$	without $P_{fe}$	% diff.	with $P_{fe}$	without $P_{fe}$	% diff
10	-4.07	-3.96	2.70	29.40	23.35	20.57
20	-11.64	-11.54	0.86	97.82	90.89	7.08
30	-20.23	-20.15	0.39	210.58	202.79	3.69
40	-29.53	-29.46	0.24	370.69	362.37	2.24
50	-39.44	-39.39	0.13	587.73	578.19	1.62
60	-50.04	-49.99	0.10	869.66	859.16	1.21

The MTPA trajectories at 200rpm and 1350rpm calculated with and without considering the iron losses are depicted in Figure 4.16 and Figure 4.19 respectively. The current trajectory at 200rpm (see Figure 4.16) shows that the neglecting of the iron losses has almost no effect on the optimal current solution ( $i_d$ ,  $i_q$ ). Conversely, at speed 1350rpm ignoring the iron losses leads to small but clear differences between the optimal solution calculated with and without the accounting for iron losses (see Figure 4.17).

$T_d(Nm)$	$i_d(A)$			$P_t(W)$		
	with $P_{fe}$	without $P_{fe}$	% diff.	with $P_{fe}$	without $P_{fe}$	% diff.
10	-5.75	-3.96	31.13	75.01	23.35	68.87
20	-13.29	-11.54	13.16	146.28	90.89	37.86
30	-21.75	-20.15	17.36	261.86	202.79	22.56
40	-30.906	-29.46	0.15	424.68	362.37	14.67
50	-40.612	-39.39	3.00	644.01	578.19	10.22
60	-51.00	-49.99	1.98	928.28	859.16	7.45

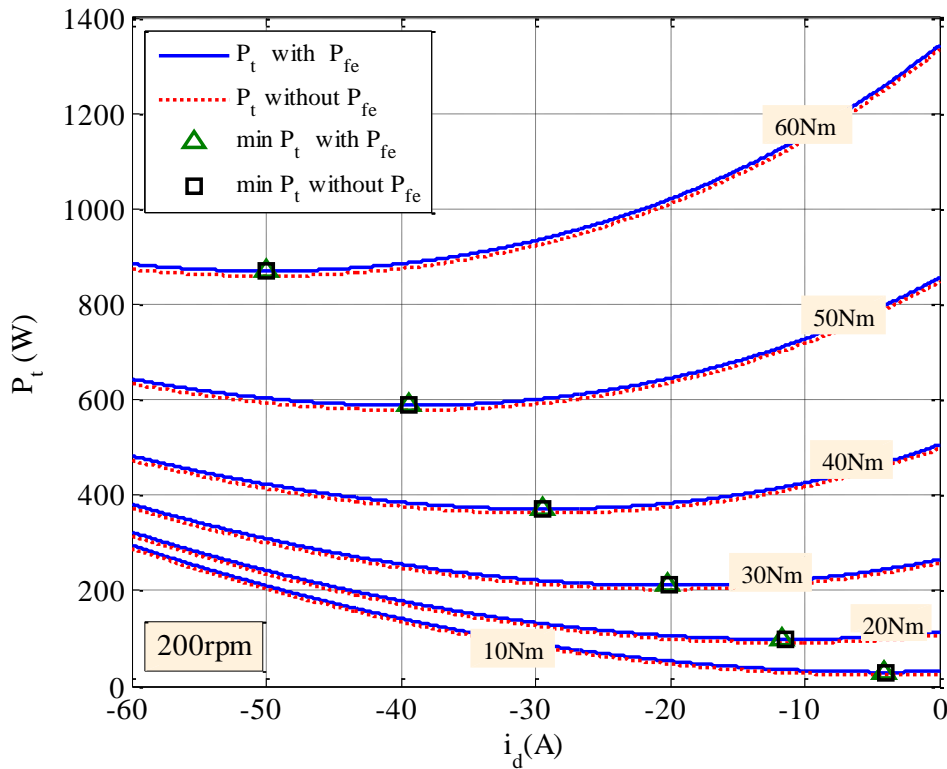


Figure 4.14 Variations of losses with  $i_d$  and  $T_d$  at  $\omega_m = 200rpm$  obtained with and without considering iron losses.

The resultant  $i_q$  current levels as well as the differences in these levels caused by including or neglecting iron losses in the LMA are summarised in Table 4.14. According to the data recorded in Table 4.15, the copper losses ( $P_{cu}$ ) is generally higher than the iron losses ( $P_{fe}$ ). It is noted that at speed  $1350rpm$  and low torque ( $10Nm$ ) the iron losses presented higher level than the copper losses due to the dependency of the iron losses on the speed whilst the copper losses is depending on the current which is relatively low at  $10Nm$ . However, as the torque increases to higher levels (20 to  $60Nm$ ) the copper losses overtake the iron losses due to the increasing of the current.

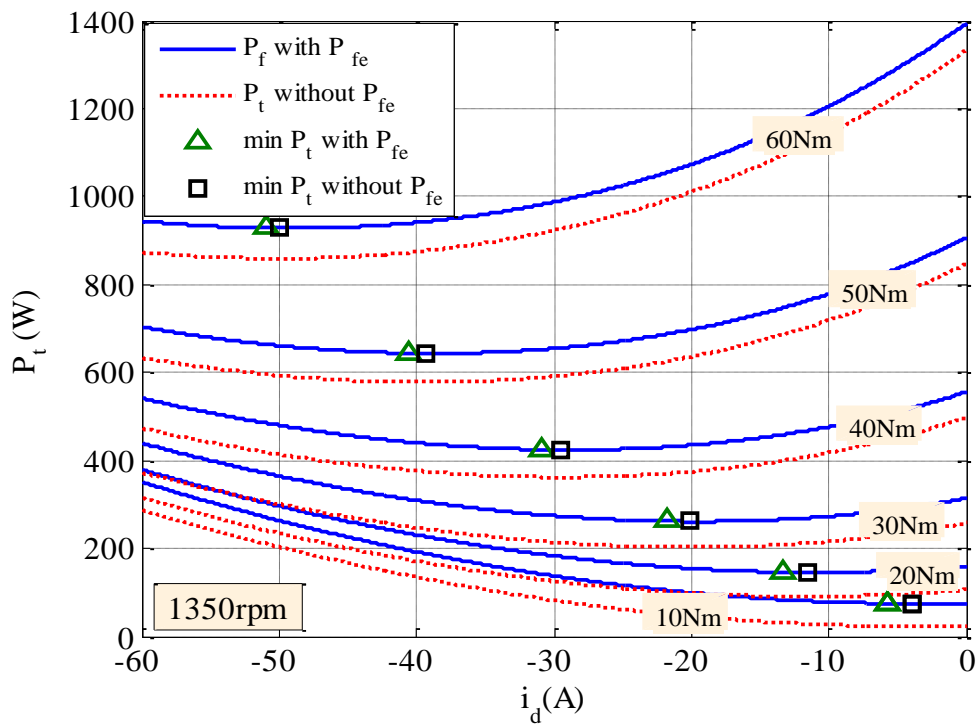


Figure 4.15 Variations of losses with  $i_d$  and  $T_d$  at  $\omega_m = 1350rpm$  obtained with and without considering iron losses.

At low speed (see Table 4.15), the iron losses is lower than the copper loss especially at high torques. As the speed is increased to  $1350rpm$ , significant copper losses levels due to current increase are reported in comparison with iron losses where the iron losses records about  $69.12W$  compared with the copper losses  $859.16W$ . This explains why the iron losses has almost no effect on the IPMSM minimum operating point where it is noticeably small comparing with the copper losses at high torques. This can be clearly

shown in Figure 4.18, Figure 4.19 (Figure 4.20 and Figure 4.21) which depicts the total losses, iron and copper losses over  $i_d$  current at speed 200rpm (1350rpm). Consequently, the copper losses effect is more likely to take over the iron losses effect on the minimum optimal operation point. As a result, the optimal solution ( $i_d$ ,  $i_q$ ) which is decided by the MTPA seems only slightly affected by neglecting iron losses over the selected torque and speed range as shown in Figure 4.16 and Figure 4.17.

Table 4.14 Resultant optimal  $i_q$  with and without  $P_{fe}$ 

$T_d(Nm)$	$i_q(A)$ at 200rpm			$i_q(A)$ at 1350rpm		
	with $P_{fe}$	without $P_{fe}$	% diff.	with $P_{fe}$	without $P_{fe}$	% diff.
10	16.801	16.826	0.15	16.377	16.826	2.74
20	32.05	32.091	0.13	31.34	32.091	2.39
30	46.737	46.786	0.10	45.878	46.786	1.98
40	61.304	61.39	0.14	60.328	61.39	1.76
50	76.414	76.466	0.08	75.386	76.466	1.43
60	92.119	92.165	0.05	91.099	92.165	1.17

Table 4.15 Variations of  $P_{fe}$ ,  $P_{cu}$  and  $P_t$  with  $t_d$  and  $\omega_m$ 

$T_d(Nm)$	200rpm			1350rpm		
	$P_{fe}$	$P_{cu}$	$P_t$	$P_{fe}$	$P_{cu}$	$P_t$
10	6.05	23.35	29.40	51.66	23.35	75.01
20	6.93	90.89	97.82	55.39	90.89	146.28
30	7.79	202.79	210.58	59.07	202.79	261.86
40	8.32	362.37	370.69	62.31	362.37	424.68
50	9.54	578.19	587.73	65.82	578.19	644.01
60	10.5	859.16	869.66	69.12	859.16	928.28

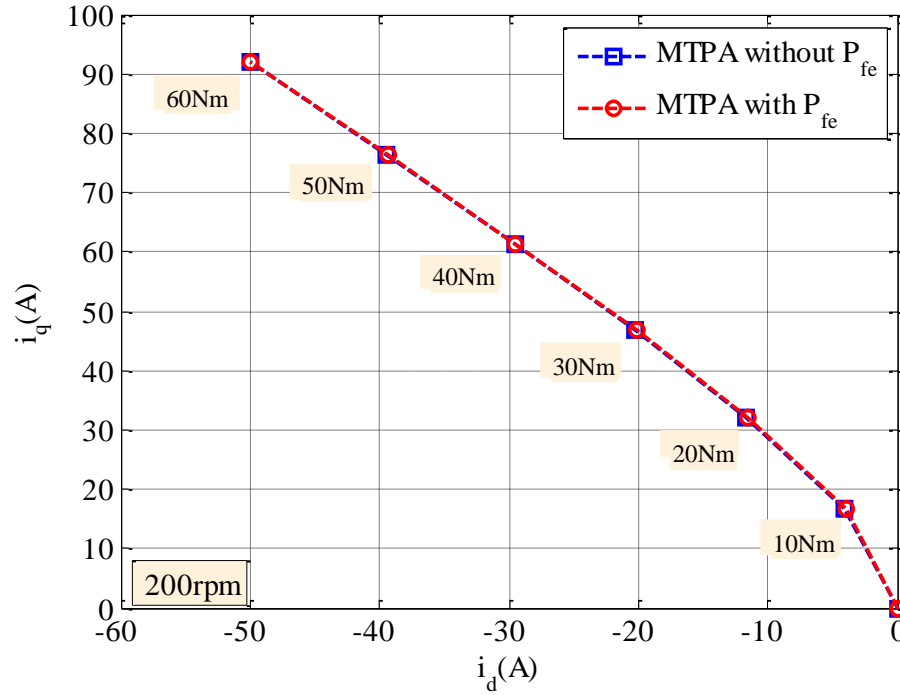


Figure 4.16 Variations of  $i_q$  with  $i_d$  and  $T_d$  at  $\omega_m = 200rpm$  obtained with considering and not considering iron losses in total losses.

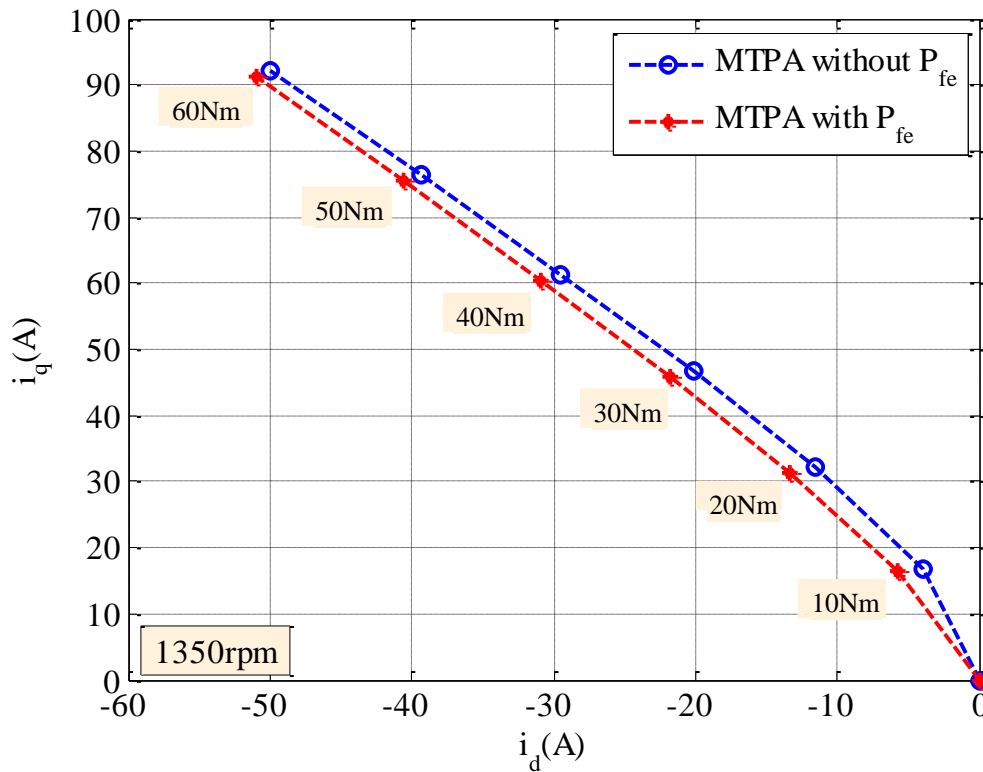


Figure 4.17 Variations of  $i_q$  with  $i_d$  and  $T_d$  at  $\omega_m = 1350rpm$  obtained with considering and not considering iron loss in total losses.

Figure 4.22 and Figure 4.23 depict the resultant power losses level with and without considering the iron losses at different speeds ranging from 200rpm to the base speed, respectively. The according iron losses are shown in Figure 4.24. It can be seen that the resultant iron losses at specific torque and speed is considerably small compare with copper losses. Thus, for the studied IPMSM, the effects of the iron losses on the minimum losses operation are not as important as the copper losses.

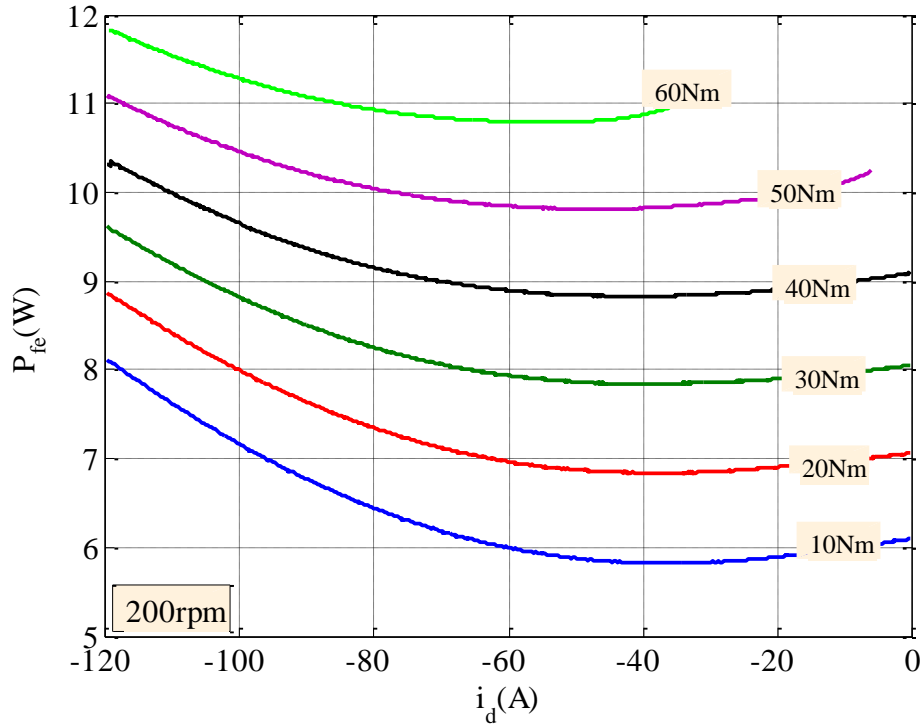


Figure 4.18 Variations of iron losses with  $i_d$  and  $T_d$  at  $\omega_m = 200\text{rpm}$



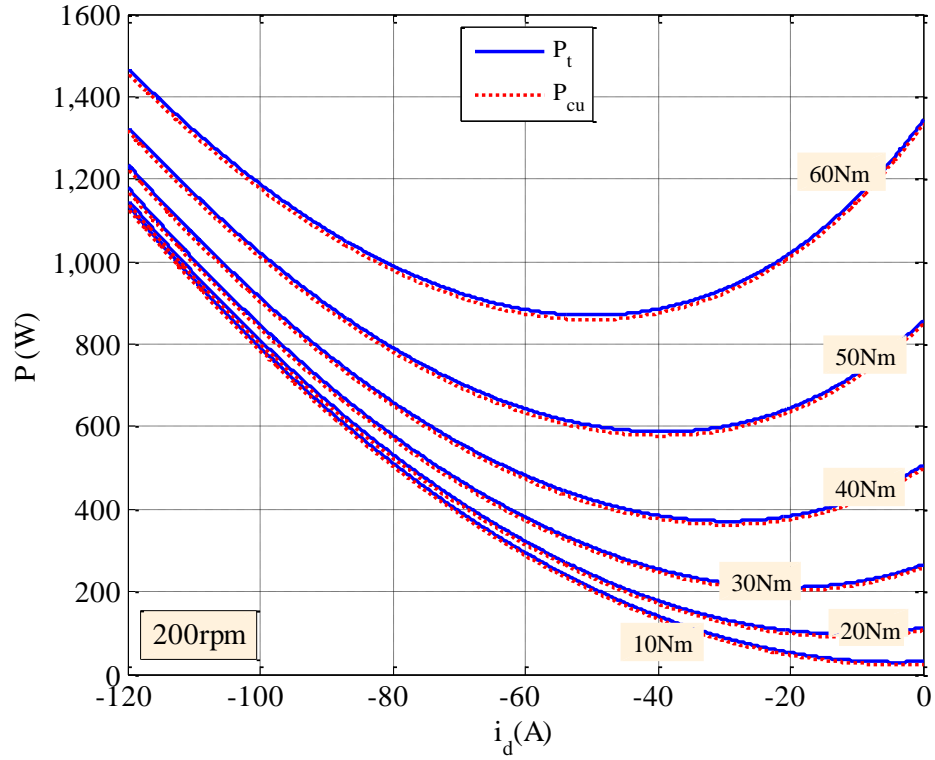


Figure 4.19 Variations of total losses  $P_t$  and copper loss  $P_{cu}$  with  $i_d$  and  $T_d$  at  $\omega_m = 200rpm$ .

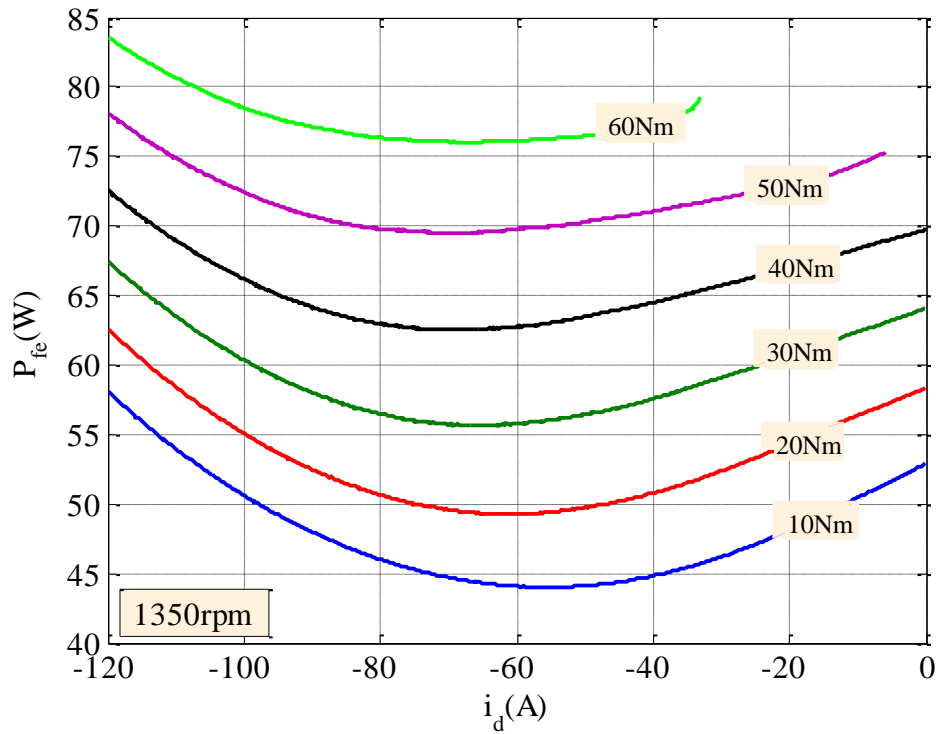


Figure 4.20 Variations of iron losses with  $i_d$  and  $T_d$  at  $\omega_m = 1350rpm$ .

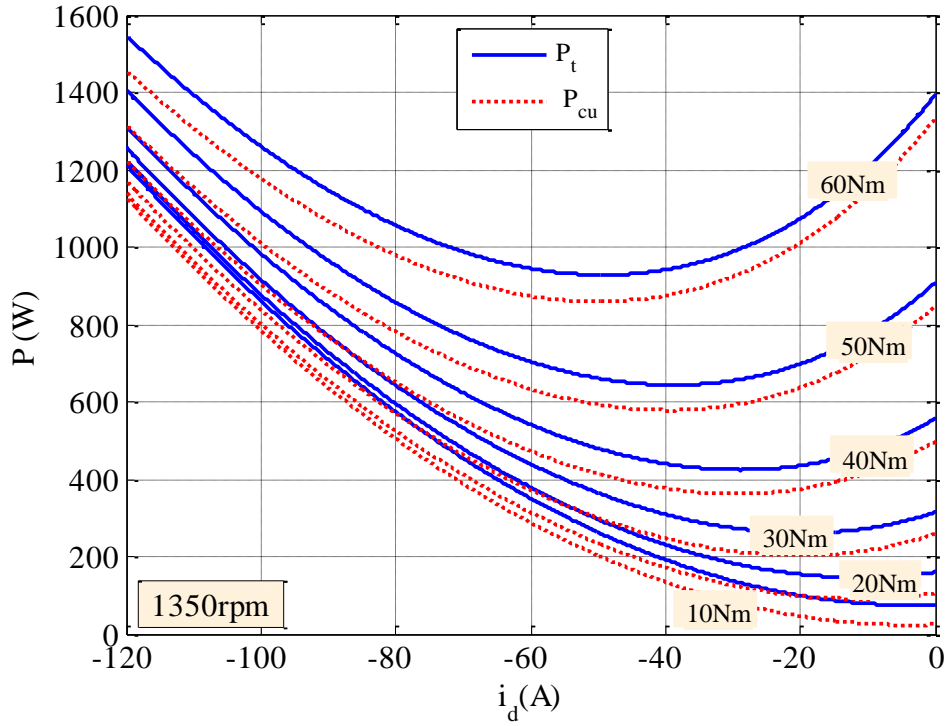


Figure 4.21 Variations of total losses  $P_t$  and copper losses  $P_{cu}$  with  $i_d$  and  $T_d$  at  $\omega_m = 1350\text{rpm}$ .

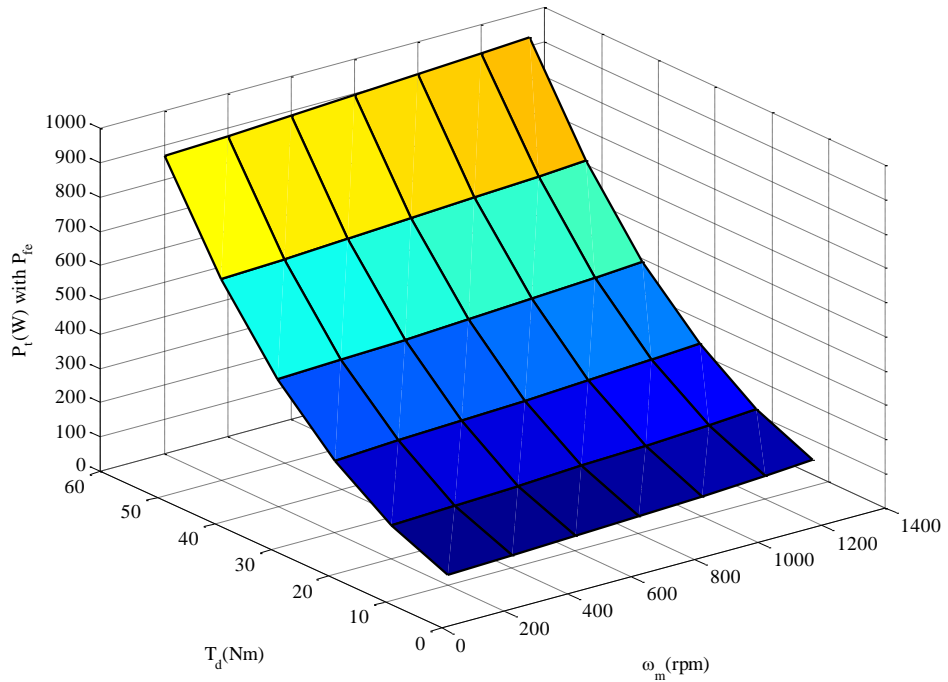


Figure 4.22 Resultant total minimum power losses variation with  $\omega_m$  and  $T_d$  obtained when iron losses is considered.

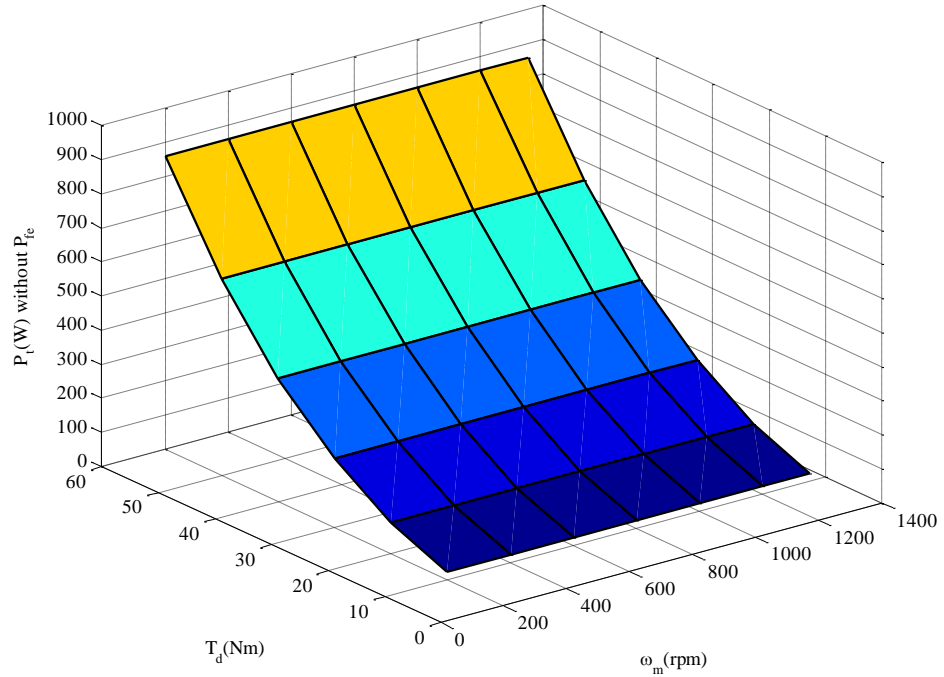


Figure 4.23 Resultant total minimum power losses variation with  $\omega_m$  and  $T_e$  obtained when iron losses is neglected.

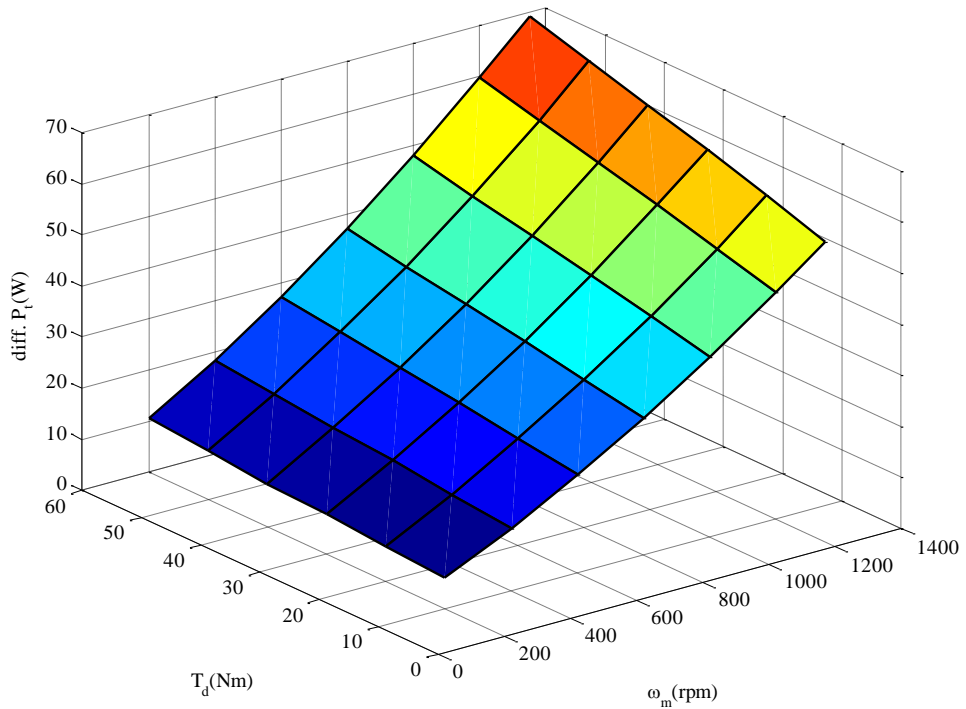


Figure 4.24 Differences between total minimum power losses with and without considering iron losses

#### 4.4.2 Flux Weakening Region

In the CTR the IPMSM is governing under the current limits only. In the FWR, however, the motor is running under both the current and voltage limits. Therefore, for a given operating point ( $\omega_m$ ,  $T_d$ ), there is only one optimal solution that satisfies the voltage and current limits. The off-line simulation results of the proposed LMA in the constant power region are shown in Figure 4.25 (2000rpm), Figure 4.26 (3000rpm) and Figure 4.27 (4000rpm). The resultant optimal solutions in each case are summarised in Table 4.16, Table 4.17 and Table 4.18 respectively. One can easily see that for a given torque demand, accounting or not accounting for the iron losses in the suggested LMA has almost no effect on the minimum operation point in the flux weakening region although higher levels of iron losses is reported (see Table 4.20) under this operating condition (flux weakening) than that in the constant torque region (see Table 4.15) where the values of the resultant  $i_d$  currents remain constant as long as the speed and torque are kept constant. It should be noted that the above results are obtained by assuming that the iron losses does not affect the voltage equation. In reality, the iron losses increase the currents for a given torque, and hence will affect slightly the d- and q-axis voltage.

Table 4.16 Optimal solution ( $i_d, P_t$ ) with and without  $P_{fe}$  at 2000rpm

$T_d(Nm)$	$i_d(A)$			$P_t(W)$		
	with $P_{fe}$	without $P_{fe}$	% diff.	with $P_{fe}$	without $P_{fe}$	% diff
10	-28.641	-28.641	0	152.85	74.9904	50.94
20	-43.463	-43.463	0	267.96	183.6689	31.46
30	-60.767	-60.767	0	448.75	355.0706	20.8
40	-80.162	-80.162	0	706.87	600.0459	15.11

Table 4.17 Optimal solution ( $i_d, P_t$ ) with and without  $P_{fe}$  at 3000rpm

$T_d(Nm)$	$i_d(A)$			$P_t(W)$		
	with $P_{fe}$	without $P_{fe}$	% diff.	with $P_{fe}$	without $P_{fe}$	% diff
10	-68.289	-68.289	0	506.77	369.84	27.02
20	-83.012	-83.012	0	717	557.42	22.26

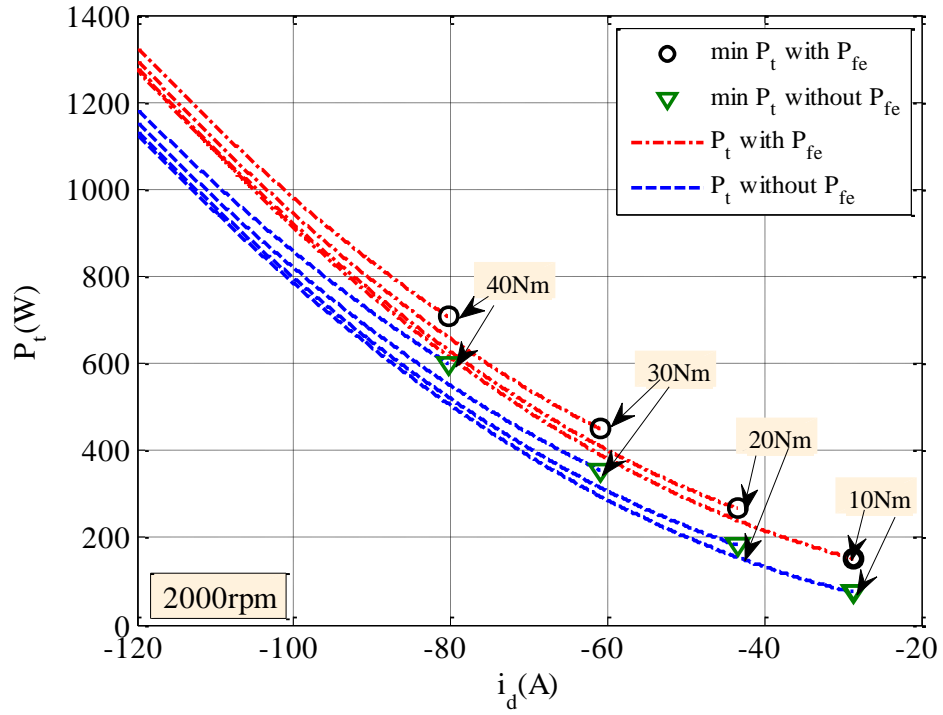


Figure 4.25 Variations of losses with  $i_d$  and  $T_d$  at  $\omega_m = 2000$  rpm obtained with and without iron losses.

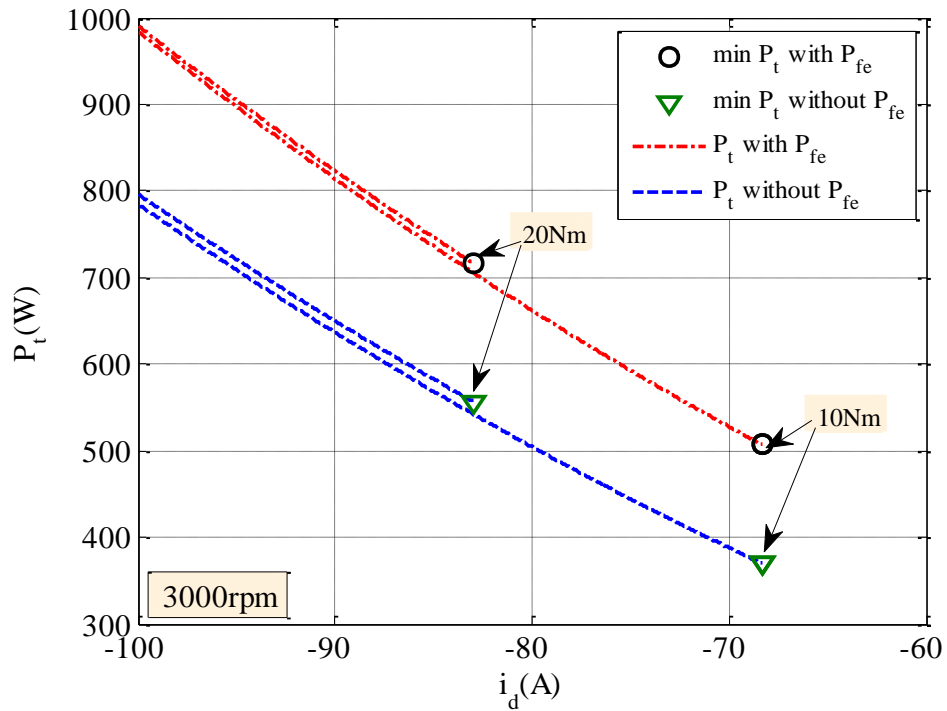


Figure 4.26 Variations of losses with  $i_d$  and  $T_d$  at  $\omega_m = 3000$  rpm obtained with and without iron losses.

Table 4.18 Optimal solution ( $i_d, P_t$ ) with and without $P_{fe}$ at 4000rpm						
$T_d(Nm)$	$i_d(A)$			$P_t(W)$		
	with $P_{fe}$	without $P_{fe}$	% diff.	with $P_{fe}$	without $P_{fe}$	% diff.
10	-89.355	-89.355	0	876.56	628.22	28.33

An example of the resultant optimal  $i_q$  current at 2000 and 3000rpm with and without considering iron losses in the flux weakening region are recorded in Table 4.19. Similarly, the  $i_q$  current levels calculated in the two cases (with and without iron losses) are not affected by the iron losses. Again, this is because the operating of the machine in the flux weakening region is limited by the maximum available voltage and current limit. Therefore, there is only one point that satisfies these limits regardless the iron losses. Table 4.20 illustrates an example of the calculated power losses (iron, copper and total losses) calculated by the LMA in flux weakening region at speed 2000 and 3000rpm.

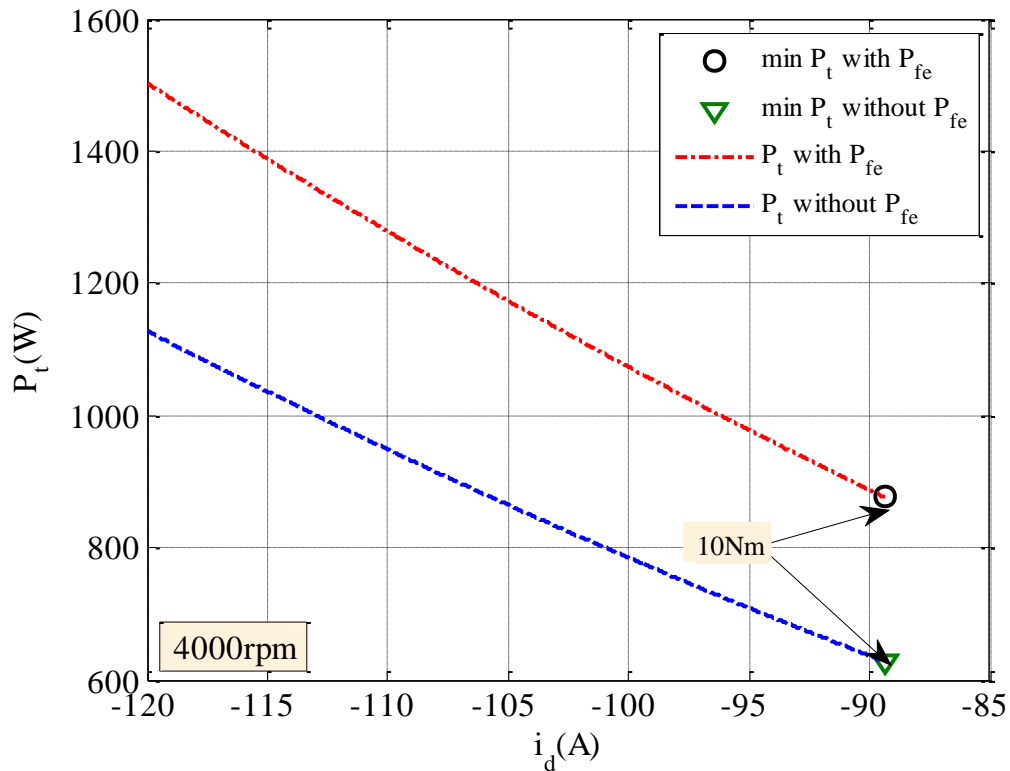


Figure 4.27 Variations of losses with  $i_d$  and  $T_d$  at  $\omega_m = 4000rpm$  obtained with and without iron losses.

According to the above discussion, for the tested IPMSM, the optimised operating points with and without considering the machine iron losses are significantly aligned.

Table 4.19 Resultant optimal  $i_q$  with and without  $P_{fe}$ 

$T_d(Nm)$	$i_q(A)$ at 2000rpm			$i_q(A)$ at 3000rpm		
	with $P_{fe}$	without $P_{fe}$	% diff.	with $P_{fe}$	without $P_{fe}$	% diff.
10	11.856	11.856	0	8.3072	8.3072	0
20	21.367	21.367	0	15.548	15.548	0
30	28.919	28.919	0			
40	35.344	35.344	0			

Table 4.20 Variations of  $P_{fe}$ ,  $P_{cu}$  and  $P_t$  with  $T_d$  and  $\omega_m$ 

$T_d(Nm)$	2000rpm			3000rpm		
	$P_{fe}$	$P_{cu}$	$P_t$	$P_{fe}$	$P_{cu}$	$P_t$
10	77.864	74.9904	152.85	136.81	369.84	506.77
20	84.289	183.6689	267.96	159.85	557.42	717
30	93.677	355.0706	448.75			
40	106.83	600.0459	706.87			

## 4.5 Chapter Summary

This chapter presents a comprehensive simulation study that aiming to evaluate the impact of neglecting of IPMSM parameters variations due to magnetic saturation, resistive voltage drop across the stator resistance and iron losses on the minimum losses operation point of IPMSM at a given speed and torque. The off-line calculations are achieved by the LMA presented in Chapter 3 which has the flexibility to solve the losses minimisation problem with and without these factors. The simulation results show a strong influence of parameters variations in optimal solution in both constant and flux weakening regions. The achieved optimal  $i_d$  currents and power losses levels which account for the parameters variations are higher than those obtained by neglecting the parameters saturation effect. Neglecting the parameters variations would lead to unnecessary high negative d-axis currents under the field weakening region and hence a significant reduction in drive efficiency.

Resistive voltage drop across the stator resistance also has a considerable impact on the minimum d-axis current in the flux weakening region where neglecting of this voltage drop will lead to lower d-axis current magnitude that should be injected in the negative direction in order to weaken the flux. This insufficient field weakening flux causes the current control to be saturated and subsequently demand torque will not be achieved.

The iron losses impact on the optimal solution ( $i_d$ ,  $P_t$ ) in the CTR and FWR has been investigated. In the CTR, comparing with copper losses, the iron losses is considerably small especially at relatively high torques (7.45% at 1350rpm and 60Nm) and therefore the influence of the iron losses on an optimal current vector can be considered negligible ( $i_d$ ,  $i_q$ ) for the studied IPMSM. In the FWR, the iron losses has almost no effect on the IPMSM optimal operation due to the fact that in this region there is only one point that stifles both the current and voltage limits. It is concluded that the impact of the iron losses on an IPMSM machine is depending on the machine design and the materials used in its construction process. Therefore, the optimisation process will be more strongly depending on the copper losses than on the iron losses for the IPMSM machine under study.



## 5 IPMSM CONTROL BASED ON THE LOSSES MINIMISATION ALGORITHM

### 5.1 Introduction

An IPMSM drive is usually controlled by a well-known strategy referred to as field oriented control (FOC) in which the d- and q-axis currents are controlled by two feedback loops independently [9, 92]. In the constant torque region when the voltage limit is not reached, the d- and q-axis current demands are generated to minimise the total losses. If the iron losses of an IPMSM are neglected in the losses minimisation, the resulting current demands follow the MTPA trajectory [57, 58]. In the constant power region, the inverter voltage reaches its limit, and appropriate field (or flux) weaken control is necessary in order to control the d- and q-axis currents. Flux weakening control strategies can be broadly classified into three categories: feed-forward based flux weakening (FF-FW), feedback based flux weakening (FB-FW) and the combination of feed forward and feedback (FF-FB) based flux weakening control [19, 35]. These control techniques are discussed in Chapter 1. It has been concluded that the FF-FB flux weakening control technique [51-55] has the advantages of both FF-FW [20, 35-39] and FB-FW [40-50] as it is robust to parameters variations and does not require back calculations of the anti-wind up of the current controller.

The implementation of this control method is often achieved by predefined look up tables (LUTs). In the previous work [47, 48], the current command LUTs are mostly generated with the assumption that the motor parameters are constant and the winding resistive voltage drop is neglected. A new losses minimization algorithm (LMA) is developed in Chapter 3 to generate d- and q-axis current demands for a given torque demand at a given speed under the voltage limit while minimising the total copper and iron losses of an IPMSM. This algorithm takes into consideration of the IPMSM parameter variations due to magnetic saturation effect and the voltage drop across the stator resistance. In this chapter, d- and q-axis command current look-up tables LUTs for an IPMSM used in experiments will be formulated based on the LMA proposed in Chapter 3. Since it has been shown in Chapter 4 that the iron losses of the utilised

IPMSM has negligible effect on the optimal current demands it is not considered in generating the non-linear current demand LUTs. These LUTs generated from the proposed method are advantageous over the conventional LUTs based IPMSM control in that the tracking of the optimal current demands leads to minimum losses operation with due account of the parameters variations and winding resistive voltage drop.

In this chapter, the control scheme for the implementation of the non-linear LUTs is discussed in section 5.2. The generating process of the non-linear LUTs is described in section 5.3. The performance of the control scheme with the SVPWM technique and LuPWM techniques is evaluated in section 5.4 by simulation study. The simulation results with SVPWM technique and LuPWM technique are demonstrated in section 5.3.3 and 5.3.4, respectively. It is shown that the LuPWM technique may result in a phase current distortion problem and therefore a solution is proposed in section 5.3.4.1. A comparative study of SVPWM, LuPWM and the modified Mod-LuPWM techniques is presented in section 5.3.5. Section 5.5 summarises the whole chapter.

## 5.2 IPMSM Control Scheme

The control strategy based on non-linear LUTs generated in this chapter are implemented using the control scheme depicted in Figure 5.1 [51]. In this control scheme three LUTs are utilised to control IPMSM. Two of these LUTs are the two dimensional d- and q- axis current demand  $(i_d^*, i_q^*)$  LUTs which are responsible for generating the optimal current demands for a given operating point. The inputs to these LUTs are the demand torque  $T_d$  and the maximum flux magnitude  $|\lambda|_{max}$  which is the difference between the feed forward flux component,  $|\lambda|_{ff}$ , based on losses minimisation, and the feedback flux component  $|\lambda|_{fb}$ . The feed forward,  $|\lambda|_{ff}$ , is the flux magnitude in the constant torque region for MTPA or minimum losses operation and it is determined from an one dimensional LUT with  $T_d$  as its input. The three LUTs are calculated by the LMA presented in Chapter 3. The feedback flux,  $|\lambda|_{fb}$ , is the output of the voltage feedback loop. The error signals between the d- and q-axis input

voltage vector  $(V_d^{r*}, V_q^{r*})$  and the output voltage vector  $(V_d^r, V_q^r)$  of the over modulation block, are filtered by two low pass filters, and are used as the input to the feedback loop. When the drive operates in the constant torque region, the voltage is below the maximum limit, and hFigure 5.1 is once the input and output voltage vectors of the over modulation block is the same, and  $|\lambda|_{fb} = 0$ , i.e., no flux weakening. At high speeds when field weakening is necessary, the over modulation block limits the magnitude of the reference voltage  $(V_d^{r*}, V_q^{r*})$  at the maximum available voltage  $V_{am}$  of  $V_{dc}/\sqrt{3}$ . Thus the magnitude of the voltage error vector generates the feedback flux  $|\lambda|_{fb}$  via the low pass filters. A tuning factor  $\omega_{MIcon}$  (rad/sec) is used to adjust the gain of the flux feedback loop  $\omega_{MIcon}$  should be chosen between the rated speed and the maximum speed of the IPMSM drive ( $\omega_{base} \leq \omega_{MIcon} \leq \omega_{max}$ ) [53]. The difference between  $|\lambda|_{ff}$  and  $|\lambda|_{fb}$  (see Figure 5.1) [53] forms the maximum available flux  $|\lambda|_{max}$  under a given operation condition which, in turn, is used as inputs to the dq non-linear LUTs.

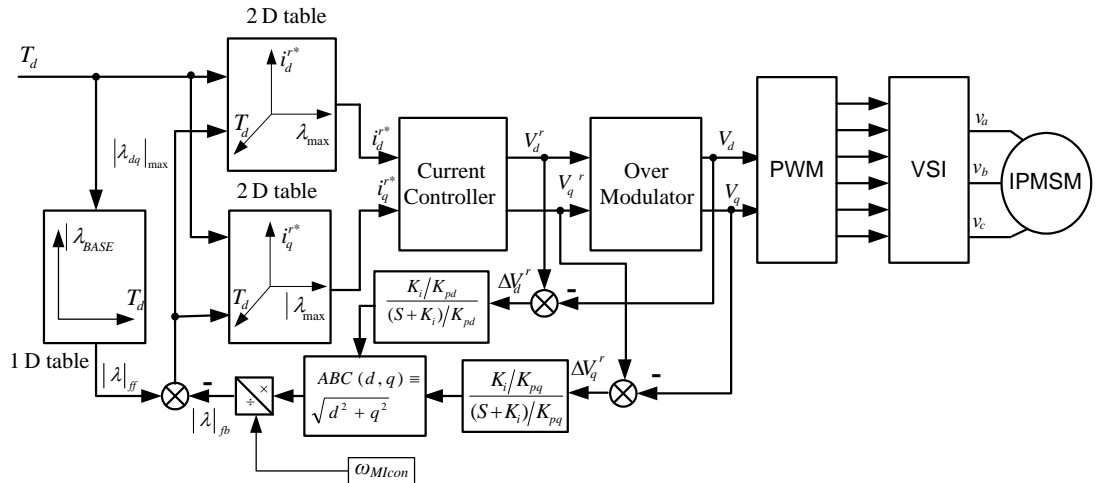


Figure 5.1 Schematic of IPMSM drive based on non-linear lookup tables generated by LMA [51].

### 5.3 Generation of Non-Linear Look Up Tables

In order to implement the minimum losses control, the optimal values of the d- and q-axis currents as functions of demand torque and stator flux are generated and stored in LUTs [91]. These LUTs can be then incorporated in a suitable IPMSM machine control structure as described in section 5.2. The method to generate d- and q-axis currents

LUTs using the optimal output points of the LMA over the torque and speed range of the IPMSM machine is presented in this section. This can be separated into two main steps which are discussed in sections 5.3.1 and 5.3.2, respectively.

### 5.3.1 Selection of Torque and Speed Operating Points

In section 3.5.1, it has been mentioned that the initial inputs to the LMA are divided into two types which are the constant ( $\omega_m$ ,  $T_d$ ) and variable inputs ( $L_d$ ,  $L_q$  and  $\lambda_m$ ) during the optimization process. The initial variable inputs are chosen at the rated speed and maximum torque of the utilised IPMSM. The interpolating will be processed with the varying inputs ( $L_d$ ,  $L_q$  and  $\lambda_m$ ) together with a given ( $\omega_m$ ,  $T_d$ ) to find the optimum solution as described in Chapter 3. A number of representative torque-speed points in Chapter 3, are used to validate the calculations of the LMA. The torque-speed points for generating the non-linear LUTs, however, need to be specified carefully to reduce the difficulties in arranging the resultant optimal current values in a LUT as much as possible. The speed and torque operating points ( $\omega_m$ ,  $T_d$ ) are chosen as the inputs with the help of the torque-speed profile of the IPMSM drive as shown in Figure 5.2. A set of torque values varied from  $0Nm$  to  $70Nm$  (the maximum torque) in a  $5Nm$  step basis is utilised. The speed is changed from  $0$  to  $4500rpm$  in a  $200rpm$  step basis. For the purpose of illustration a speed step of  $500rpm$  is shown in Figure 5.2. Also, the torque-speed envelope of the IPMSM denoted by the blue bold line in Figure 5.2 is considered in the generation process of the non-linear look-up tables. This will ensure that the computed optimal current demands from the non-linear LUTs will be always in the operating range of the IPMSM. Thus motor operating area is limited by the MTPA trajectory in the constant torque region (CTR) and by the maximum available current and voltage in the flux weakening region (FWR).

### 5.3.2 Generation of Base Flux, D-Axis and Q-Axis Currents LUTs

The non-linear LUTs should be able to generate an optimal value of the current demand components  $i_d^*$  and  $i_q^*$  under a specific torque  $T_d$  and maximum dq flux  $|\lambda_{dq}|_{max}$  calculated by Eqn. 5.1 [47, 48] via interpolation.

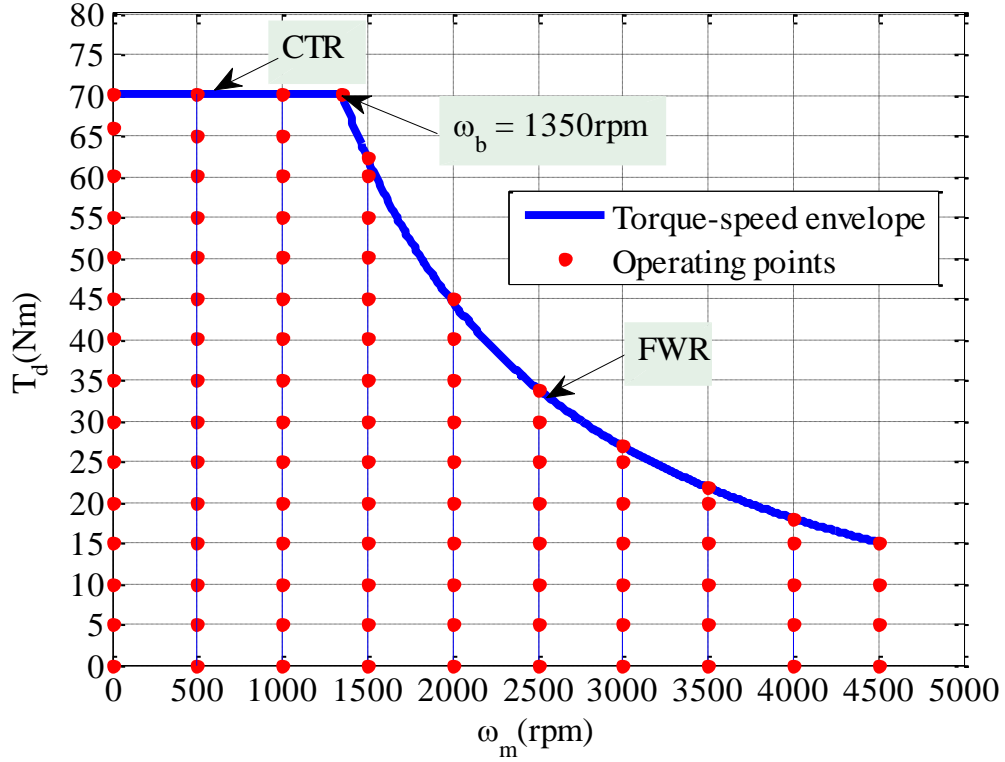


Figure 5.2 Input speed and torque for selected operating points  $(\omega_m, T_d)$  of the IPMSM.

$$\begin{aligned} \lambda_{dq}^2(i_d, i_q) &= v_d(i_d, i_q)^2 + v_q(i_d, i_q)^2 \\ &= (Ri_q/\omega_e + L_d(i_d, i_q)i_d + \lambda_m(i_q))^2 + (Ri_d/\omega_e - L_q(i_d, i_q)i_q)^2 \end{aligned} \quad 5.1$$

The first step is to calculate the optimal  $(i_d, i_q)$  and the corresponding flux magnitude  $\lambda_{dq}$  according to the torque-speed envelope input operating points shown in Figure 5.2. The resultant first iteration of the LMA under the given operating conditions  $(\omega_m, T_d)$  is the linear optimal solution of these operating points (this solution is calculated with the assumption that motor parameters are constant). Then, the optimization process is carried out as described in Chapter 3 and the non-linear optimal dq-current solution is generated. The variation of the  $i_q$  optimal current with the optimal

$i_d$  current for all the selected operating points in section 5.3.1 is depicted in Figure 5.3. The corresponding variation of the optimal flux magnitude  $\lambda_{dq}$  with the optimal  $i_d$  current is illustrated in Figure 5.4.

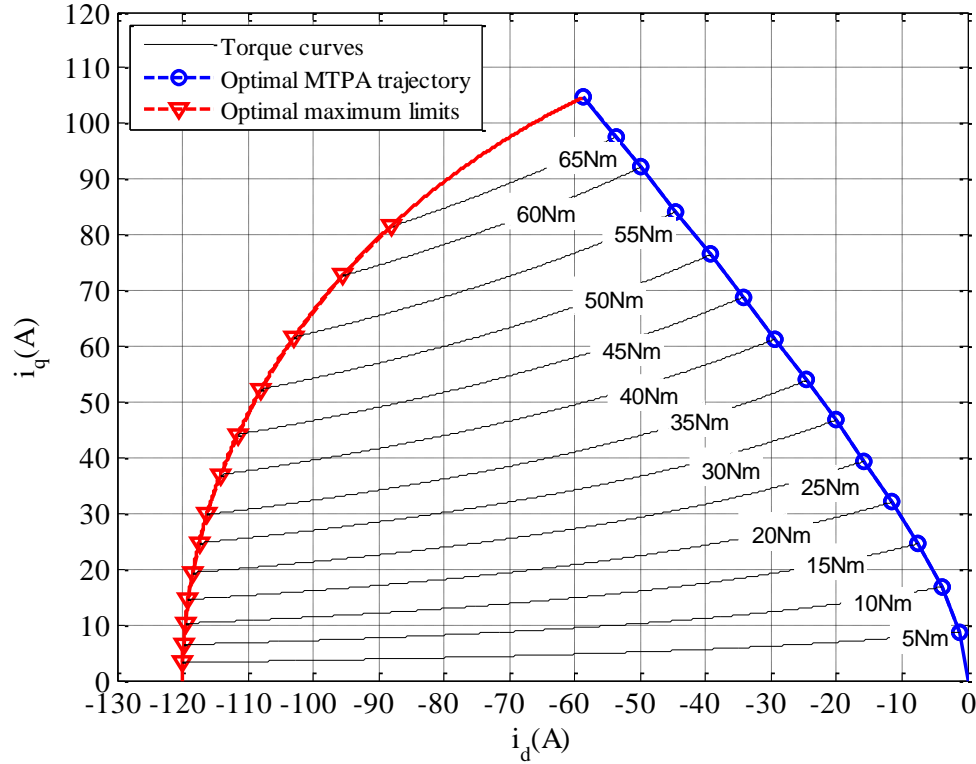


Figure 5.3 Variations of  $i_q$  with  $i_d$  and  $T_d$ .

As mentioned in section 5.3.1 the maximum allowed values of  $\lambda_{dq}$  is limited to maximum flux values of the IPMSM operating area. For example, the resultant optimal current vectors on the MTPA are limited to maximum allowed flux values of the generated optimal  $(i_d, i_q)$  current vector and consequently as the flux increases the current vector remains constant as illustrated in Figure 5.4. The limitation of the flux weakening region is defined in similar manner. As the limits of the LUTs are well-defined, the optimization process of the selected input operating points below the torque-speed envelope is then started as described in Chapter 3. Once the optimal solution of the whole selected input operating points is generated, the results will be stored in the LUTs with the inputs as torque and stator flux demands and the output is

the relevant dq-axis currents. The torque and flux demands are used as a row index and column index in the in the LUTs, respectively.

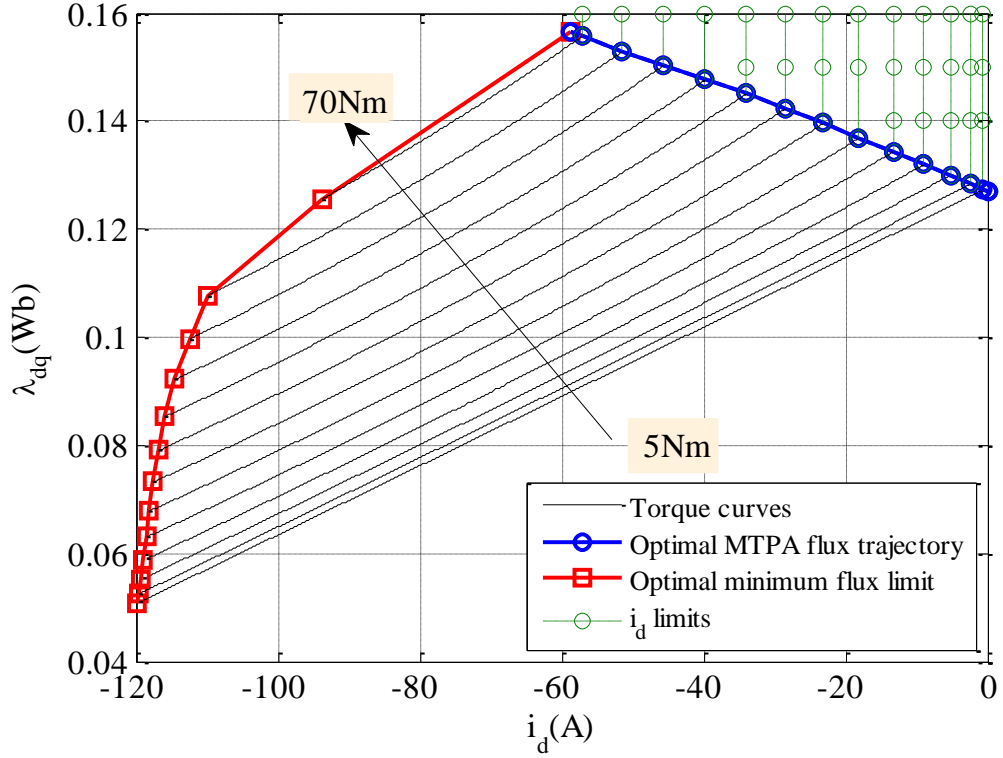


Figure 5.4 Variations and limitation of  $\lambda_{dq}$  with  $i_d$  and  $T_d$ .

The stator base flux ( $\lambda_{base}$ ) variation with the demand torque in the CTR (MTPA condition) is stored in a one dimensional LUT in order to generate the feed forward minimum losses base flux  $|\lambda|_{ff}$  [51]. The full generated non-linear look-up tables of the current  $i_d$  and  $i_q$  as well as the base flux ( $\lambda_{base}$ ) are shown in Figure 5.5, Figure 5.6 and Figure 5.7, respectively. It is noted that the stator base flux  $\lambda_{base}$  is a function of the DC-link voltage. In practice, this value varies according to the DC-link voltage variation providing that the machine is supplied via a battery pack when using in a traction application.

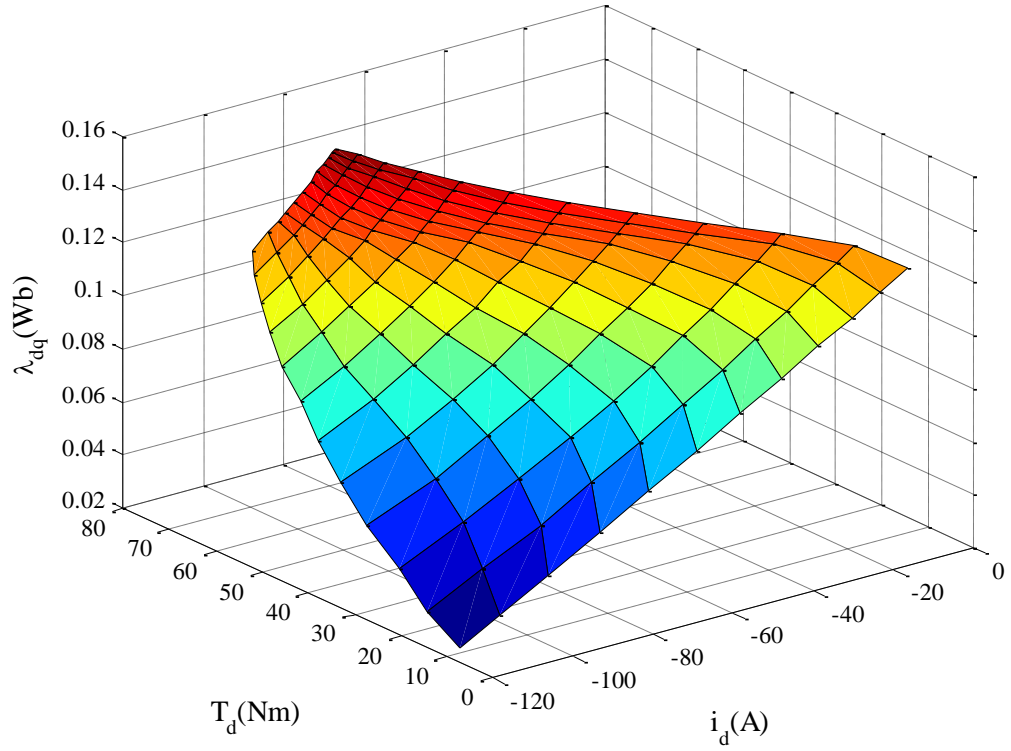


Figure 5.5 Look-up tables of variations of  $i_d$  with  $\lambda_{dq}$  and  $T_d$

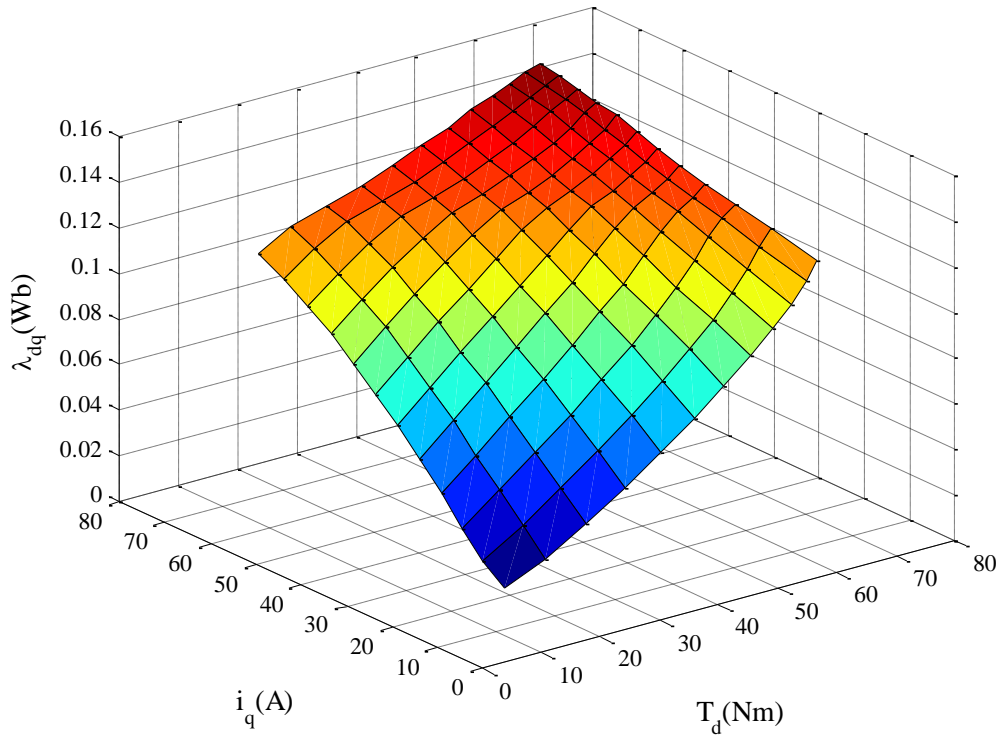


Figure 5.6 Look-up tables of variations of  $i_q$  with  $\lambda_{dq}$  and  $T_d$



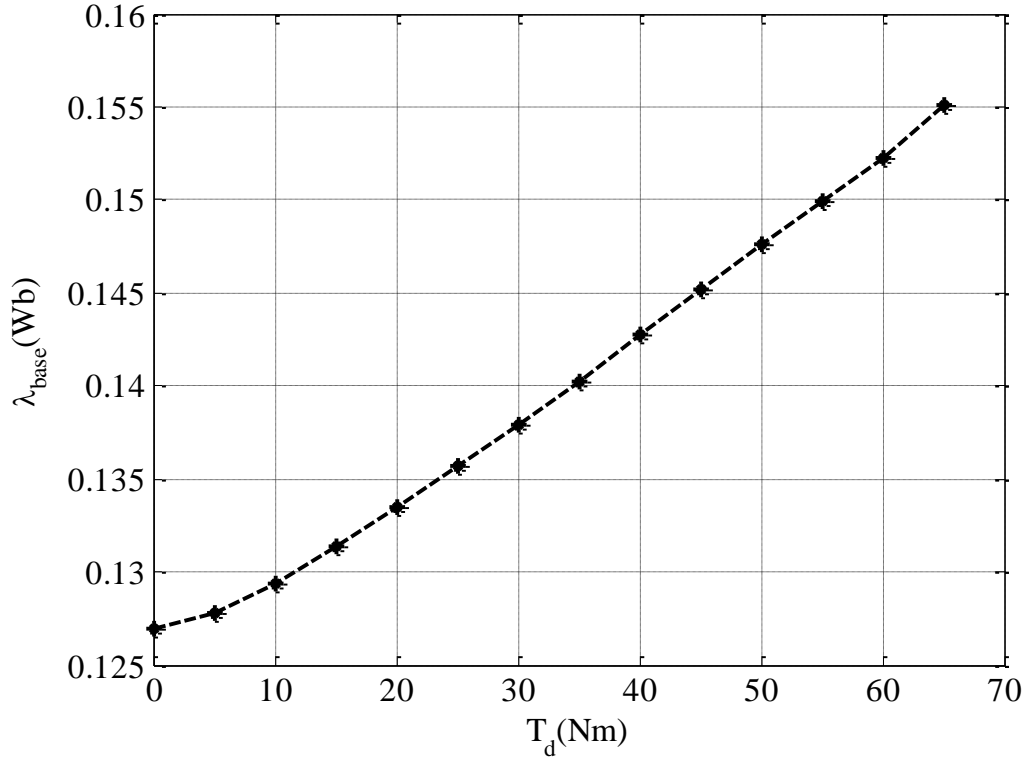


Figure 5.7 Look-up table of variations of  $\lambda_{base}$  with  $T_d$

## 5.4 Simulation Results

The control scheme given in Figure 5.1 is simulated using Simulink and SimPowerSystem toolbox. The proportional and integral terms of the feedback low pass filters ( $k_{pd}, k_{pq}, k_{id}, k_{iq}$ ) are calculated using the motor parameters and the cut-off frequency of the current controller ( $\omega_{cc}$ ) as given in Eqns. 5.3 to 5.4 [51].

$$k_{pd}(i_d, i_q) = L_d(i_d, i_q) \omega_{cc} \quad 5.2$$

$$k_{pq}(i_d, i_q) = L_q(i_d, i_q) \omega_{cc} \quad 5.3$$

$$k_{id} = k_{iq} = R \omega_{cc} \quad 5.4$$

According to this equation, the d- and q-axis proportional terms are  $L_d$  and  $L_q$  dependent and the integral terms are winding resistance dependent. The non-linearity effect of  $L_d$  and  $L_q$  is considered in the proportional terms by calculating the average value of  $L_d$  and

$L_q$  given by Eqn. 5.5 and 5.6,  $V_{no}$  respectively where  $L_{dmin}$  ( $L_{qmin}$ ) and  $L_{dmax}$  ( $L_{qmax}$ ) are the minimum and maximum values of the  $L_d$  ( $L_q$ ) values resultant from FEM analysis depicted in Figure 3.5 and Figure 3.6, respectively.

$$L_{dave} = \frac{L_{dmin} + L_{dmax}}{2} \quad 5.5$$

$$L_{qave} = \frac{L_{qmin} + L_{qmax}}{2} \quad 5.6$$

The average values  $L_{dave}$  and  $L_{qave}$  are then used to calculate an average inductance value  $L_{dqave}$  given by Eqn. 5.7.

$$L_{dqave} = \frac{L_{dave} + L_{qave}}{2} \quad 5.7$$

Consequently, equations 5.2 and 5.3 yields:

$$k_{pdave} = k_{pqave} = L_{dqave} \omega_{cc} \quad 5.8$$

The current controller parameters are calculated in a similar manner. The values of the parameters used to calculate Eqn. 5.5 to 5.8 are listed in Table 3.1.

Table 5.1 Parameters of IPMSM drive	
Minimum d-axis inductance ( $L_{dmin}$ ) [mH]	0.558
Minimum q-axis inductance ( $L_{qmin}$ ) [mH]	1.264
Maximum d-axis inductance ( $L_{dmax}$ ) [mH]	0.876
Maximum q-axis inductance ( $L_{qmax}$ ) [mH]	3.061

The cut-off frequency  $\omega_{cc}$  is chosen to be equal to the maximum frequency of the IPMSM drive which is about 1413 rad/sec (225Hz).

### 5.3.3 Simulation Results with SVPWM Technique

The performance of the IPMSM control scheme with the non-linear LUTs is evaluated in the CTR and FWR under the torque control mode. In the CTR, the simulated speed is set to  $1350\text{rpm}$  (the rated speed of the studied IPMSM). The demand torque is set to the rated torque of  $35\text{Nm}$  of the IPMSM, and to  $60\text{Nm}$  in order to validate the control scheme over the torque range. To evaluate the robustness of the control scheme under step torque condition, a dynamic simulation in which the torque is changed from  $10\text{Nm}$  to  $60\text{Nm}$  in a  $10\text{Nm}$  step basis at  $1350\text{rpm}$  is also performed. The simulation results of the CTR are illustrated in Figure 5.8 to Figure 5.13 and show that the minimum losses operation points obtained by the off-line calculations given in section 3.6 are well-tracked by the non-linear LUTs in the control scheme shown in Figure 5.1.

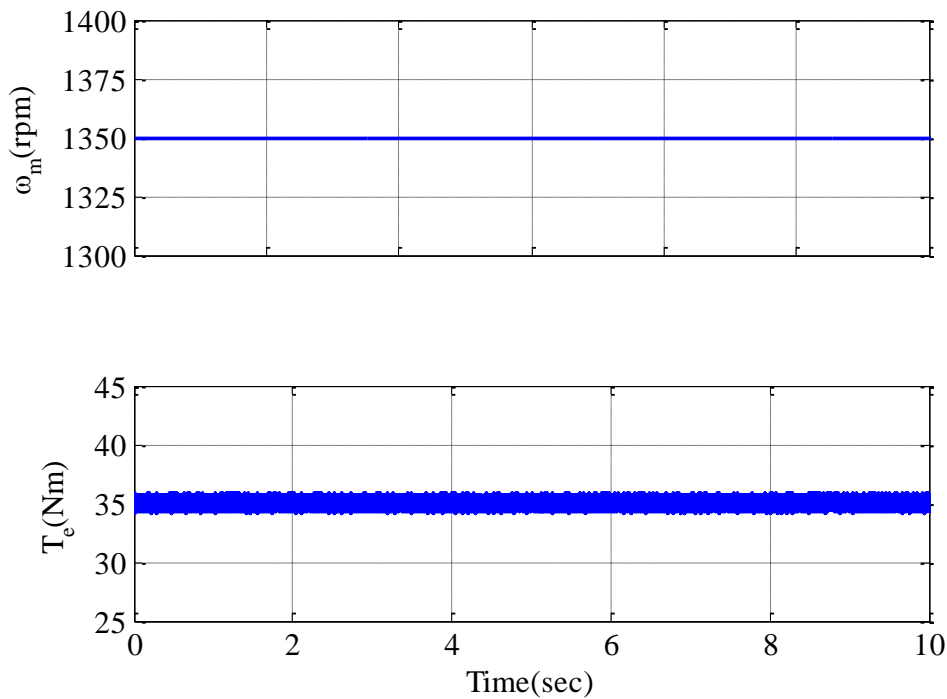


Figure 5.8 Torque and speed steady state response at  $\omega_m = 1350\text{rpm}$  and  $T_d = 35\text{Nm}$

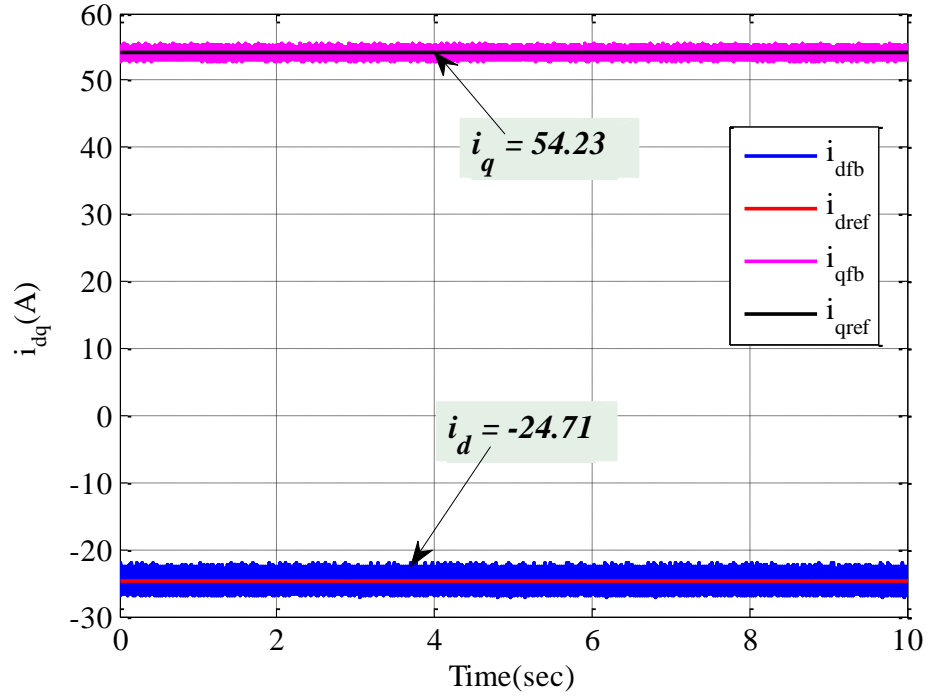


Figure 5.9  $i_d$  and  $i_q$  currents steady state response at  $\omega_m = 1350\text{rpm}$  and  $T_d = 35\text{Nm}$

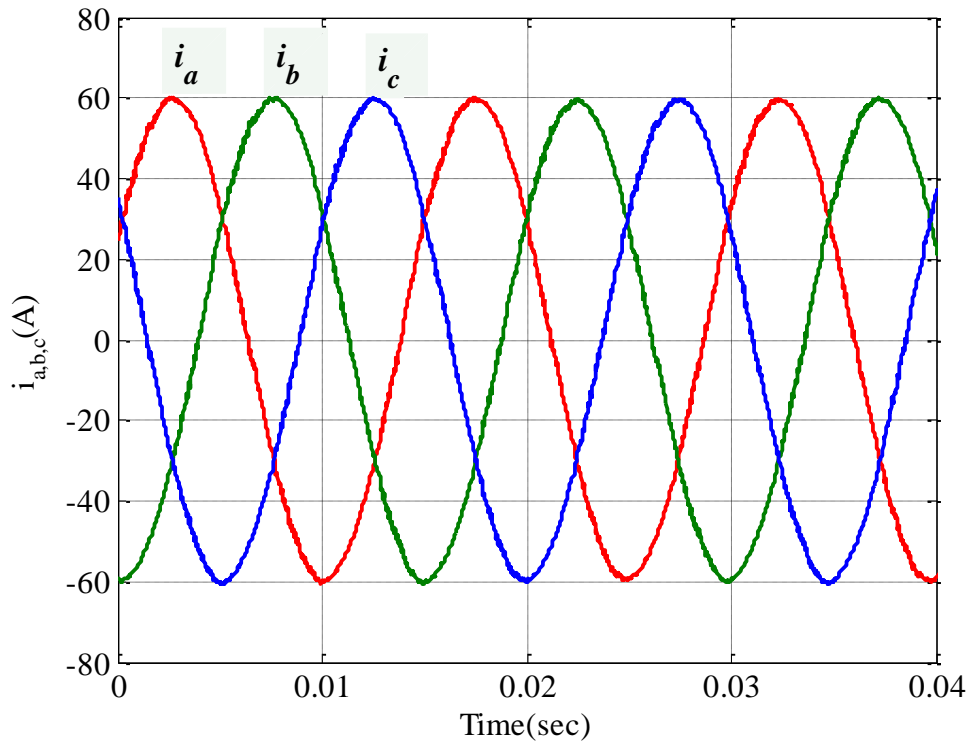


Figure 5.10 Phase currents response at  $\omega_m = 1350\text{rpm}$  and  $T_d = 35\text{Nm}$

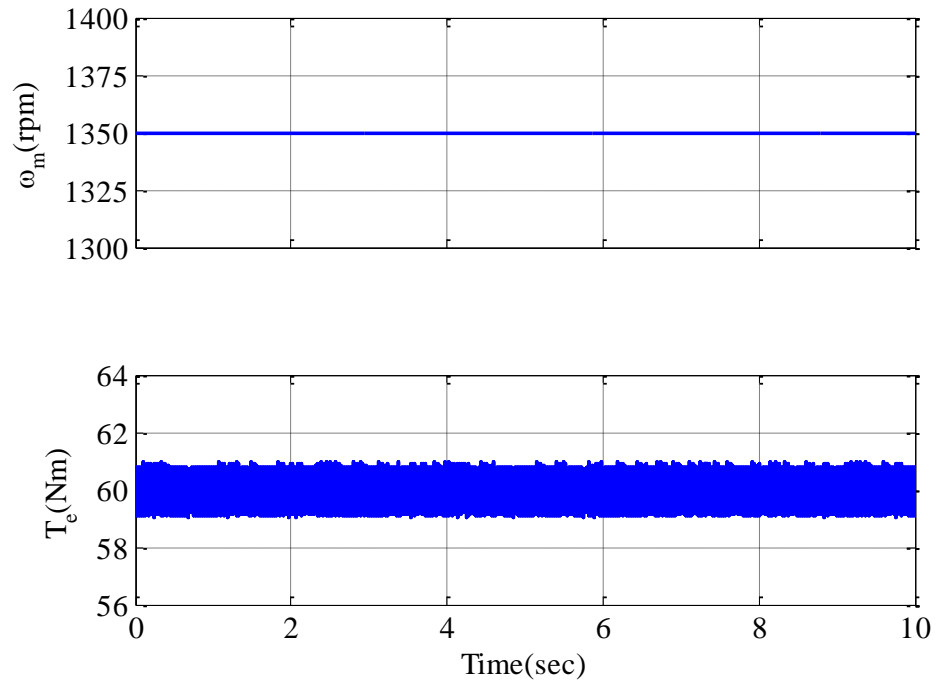


Figure 5.11 Torque and speed steady state response at  $\omega_m = 1350\text{rpm}$  and  $T_d = 60\text{Nm}$

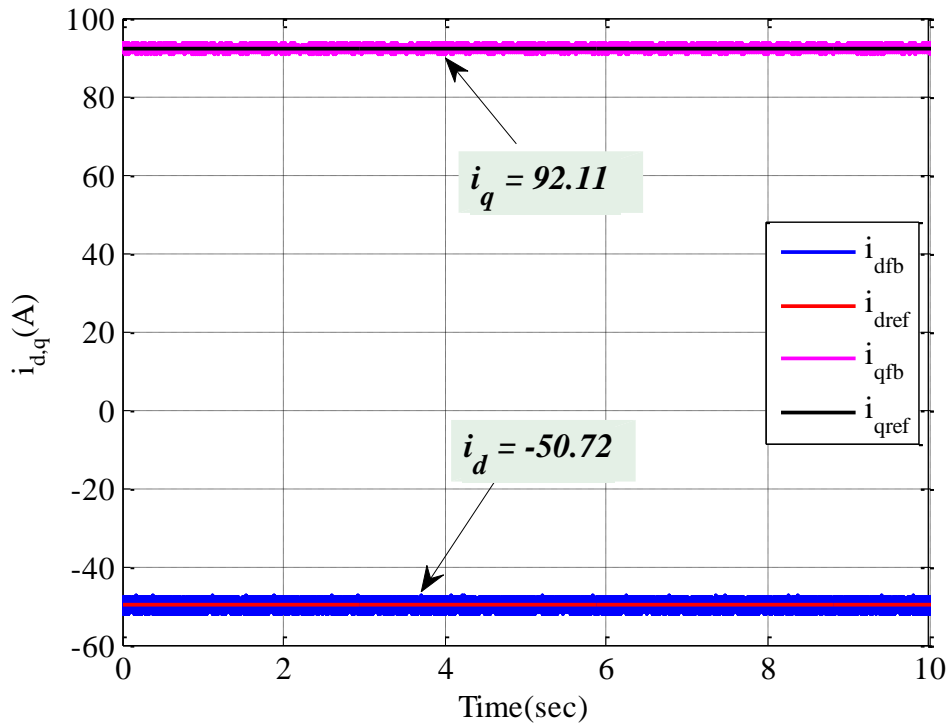


Figure 5.12  $i_d$  and  $i_q$  currents response at  $\omega_m = 1350\text{rpm}$  and  $T_d = 60\text{Nm}$

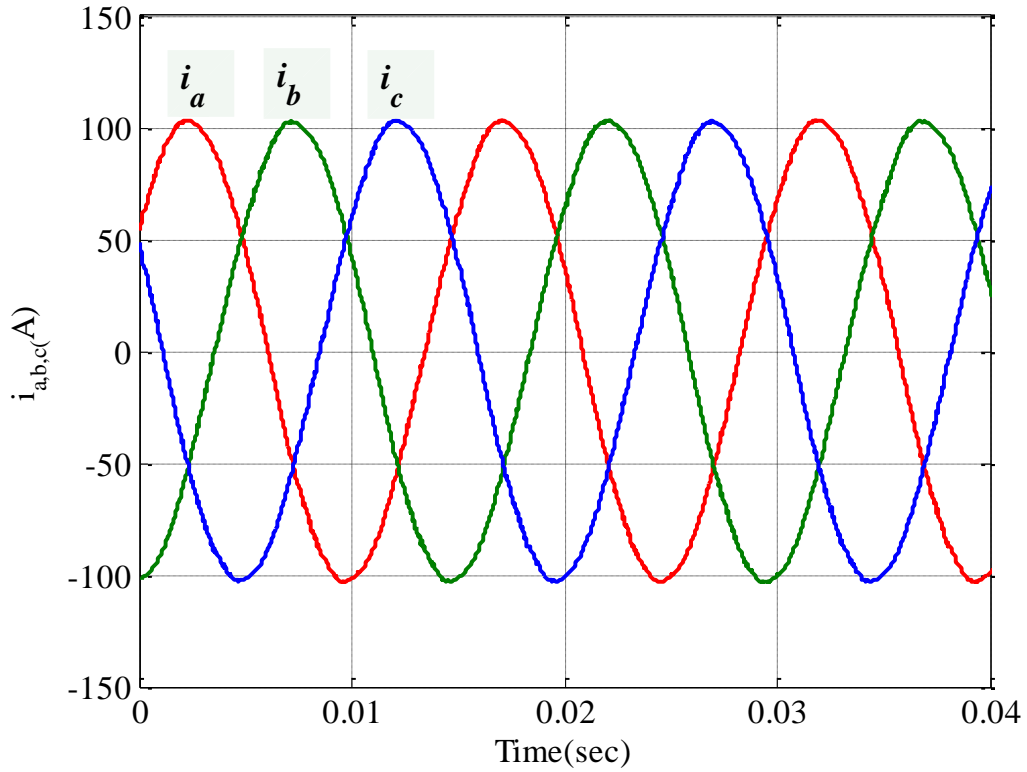


Figure 5.13 Phase currents response at  $\omega_m = 1350\text{rpm}$  and  $T_d = 60\text{Nm}$

The transient and steady state response of  $i_d$ ,  $i_q$  currents and the electromagnetic torque  $T_e$  at the rated speed ( $1350\text{rpm}$ ) and a torque of 0 to  $60\text{Nm}$  in a  $10\text{Nm}$  step basis are shown in Figure 5.14 to Figure 5.16 respectively. The results show the smooth transient responses achieved by the control scheme. The current demands produced by the non-linear LUTs are well-tracked by the control scheme in order to produce the demand torque from the IPMSM drive.

The simulation results under the flux weakening control of the IPMSM drive at different speeds and torques, over a full speed range operation, are shown in Figure 5.17 to Figure 5.22. Again the results show good agreement between the simulated dq-axis currents and the demand currents generated by the non-linear LUTs and consequently these currents satisfy the minimum IPMSM power losses operation described in Chapter 3. Thus the simulation results of the IPMSM under CTR and FWR demonstrate that the control scheme illustrated in Figure 5.1 can be used to implement the non-linear LUTs in order to fulfil the minimum power losses operation.

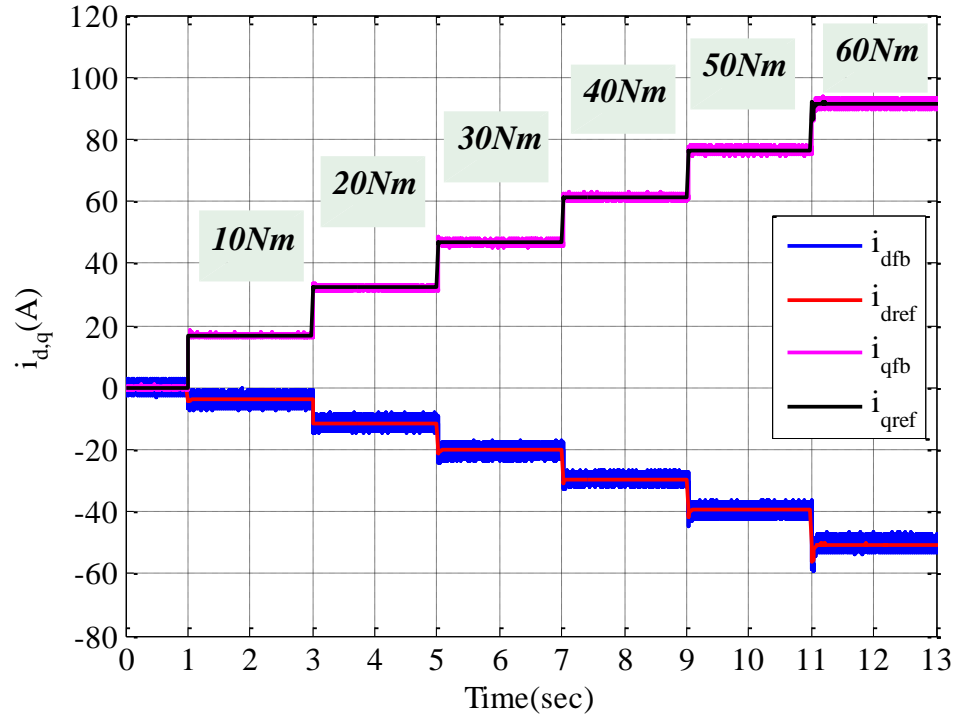


Figure 5.14  $i_d$  and  $i_q$  currents response at  $\omega_m = 1350rpm$  and  $T_d$  varied from 10 to 60Nm

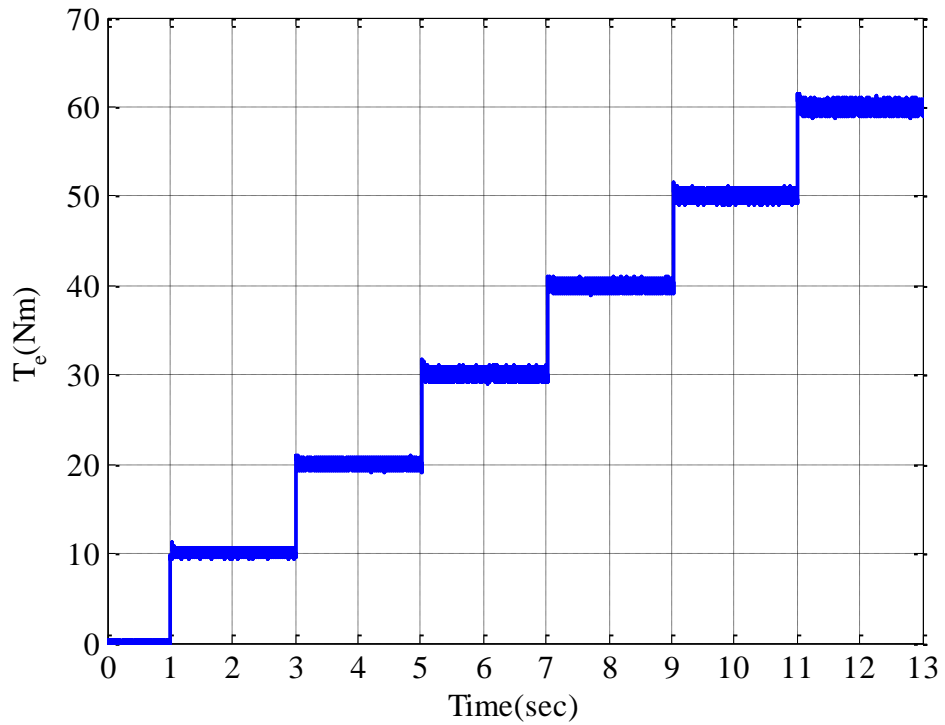


Figure 5.15 Torque response at  $\omega_m = 1350rpm$  and  $T_d$  varied from 10 to 60Nm

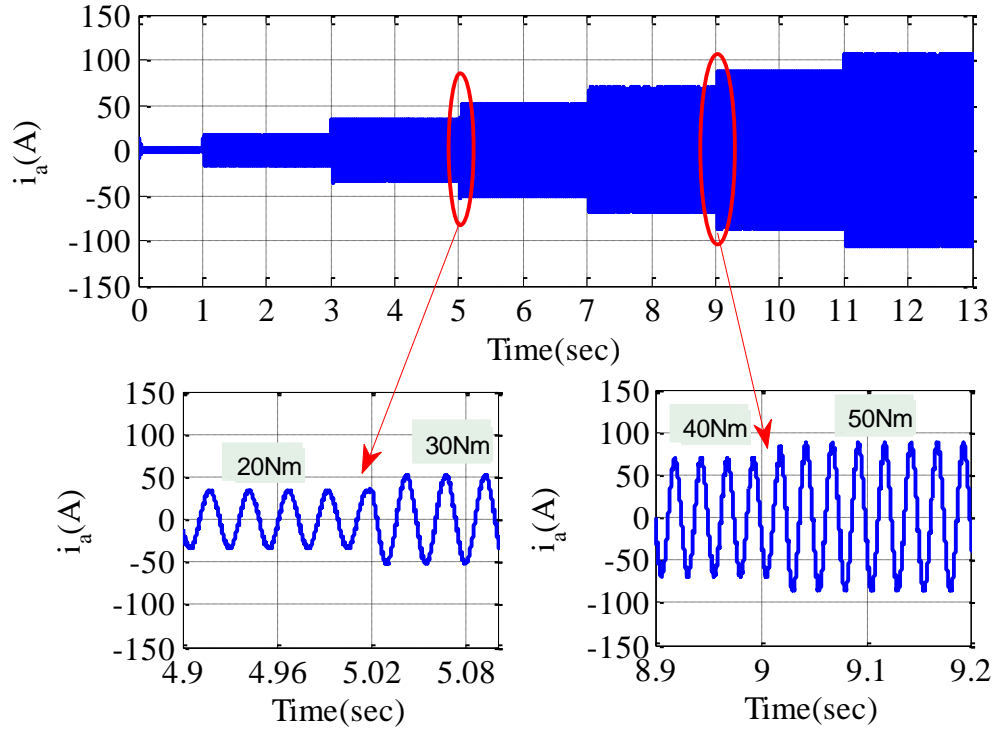


Figure 5.16 Phase current response at  $\omega_m = 1350rpm$  and  $T_d$  varied from 10 to 60Nm

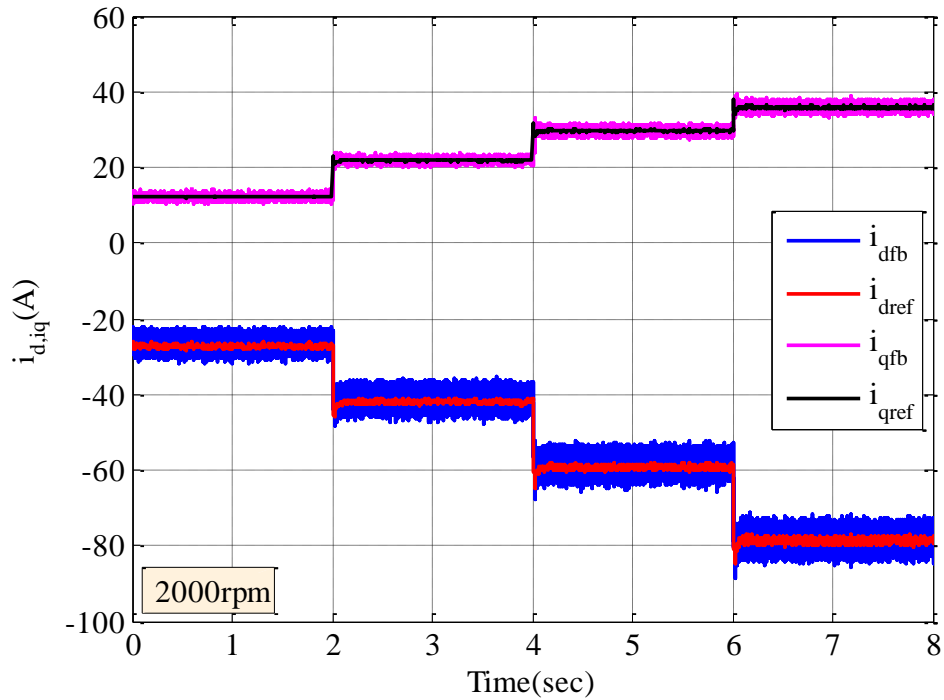


Figure 5.17  $i_d$  and  $i_q$  currents response at  $\omega_m = 2000rpm$  and  $T_d$  varied from 10 to 40Nm



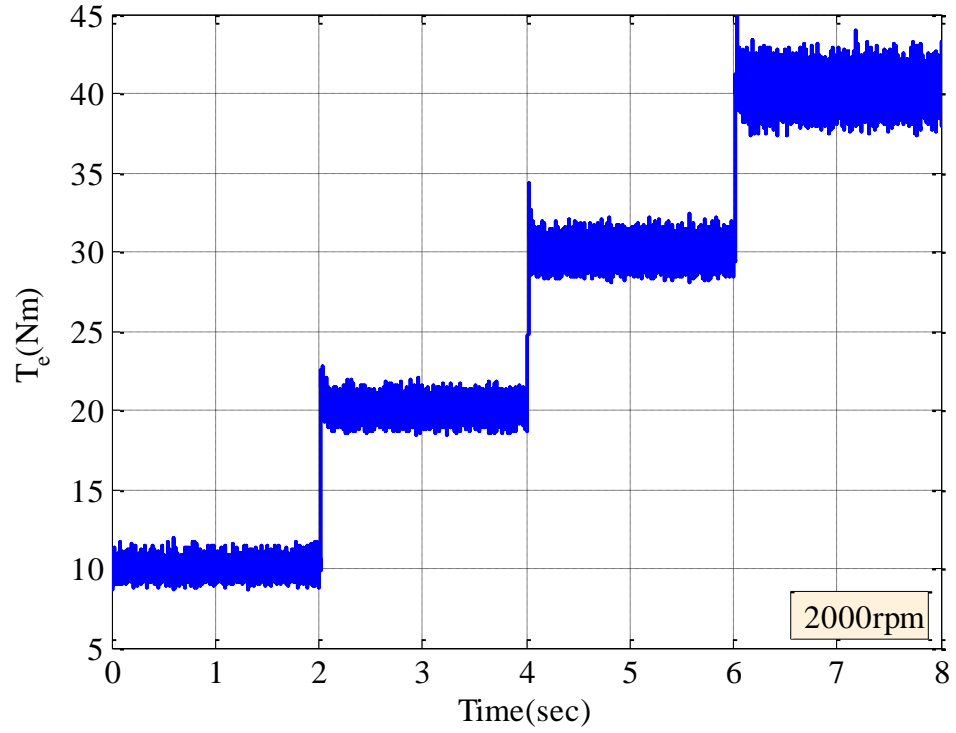


Figure 5.18 Torque response at  $\omega_m = 2000rpm$  and  $T_d$  varied from 10 to 40Nm

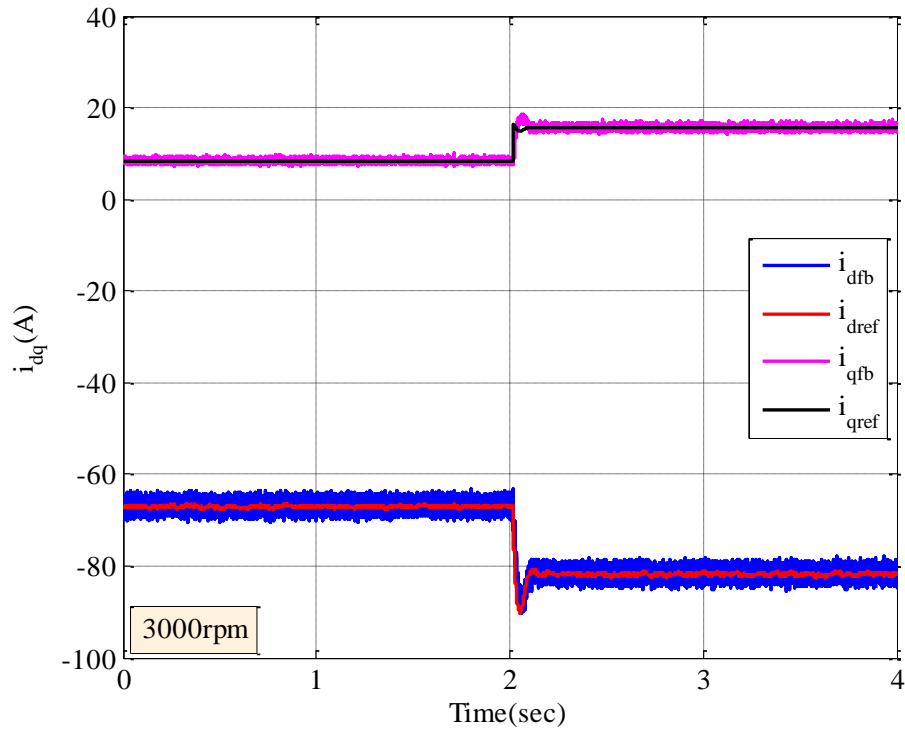


Figure 5.19  $i_d$  and  $i_q$  currents response at  $\omega_m = 3000rpm$  and  $T_d$  varied from 10 to 20Nm

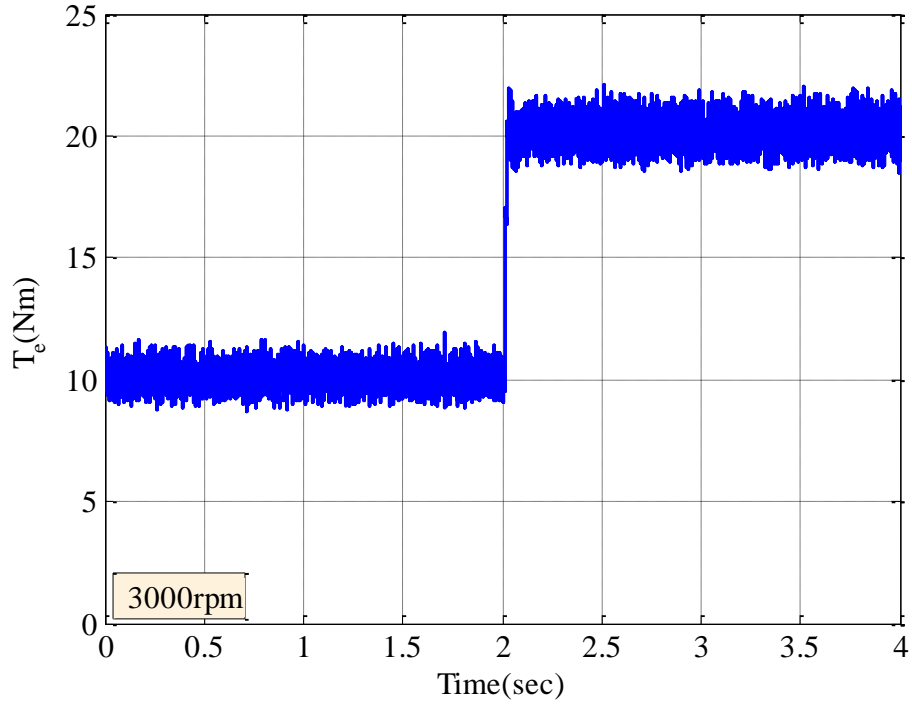


Figure 5.20 Torque response at  $\omega_m = 3000rpm$  and  $T_d$  varied from 10 to 20Nm

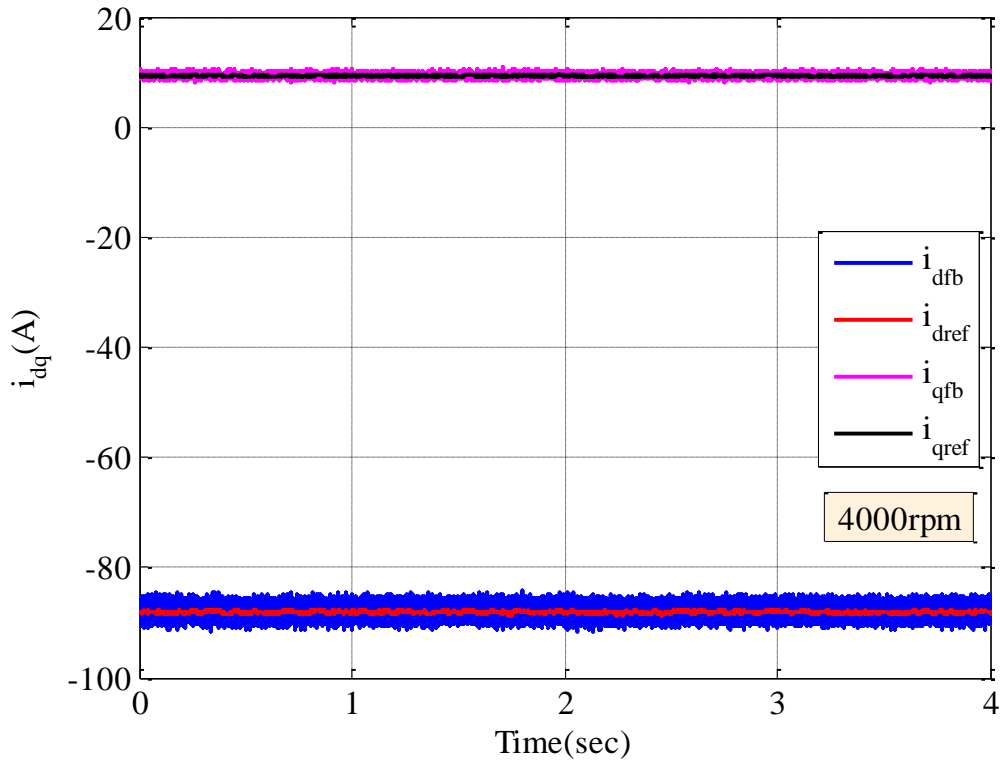


Figure 5.21  $i_d$  and  $i_q$  currents response at  $\omega_m = 4000rpm$  and  $T_d = 10Nm$

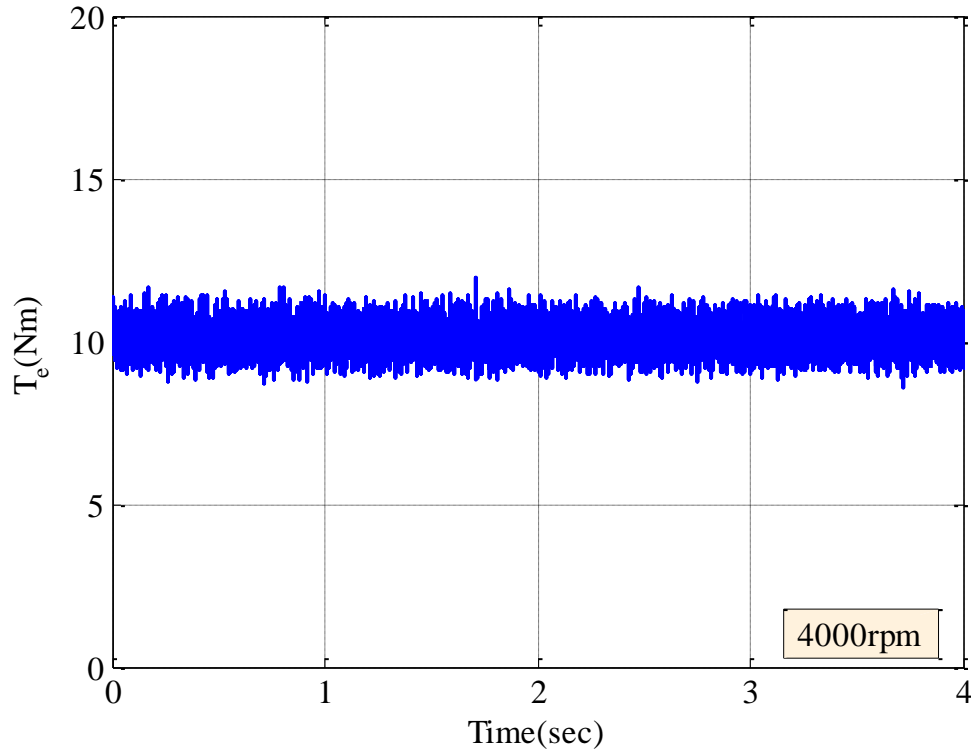


Figure 5.22 Torque and speed response at  $\omega_m = 4000rpm$  and  $T_d = 10Nm$

### 5.3.4 LuPWM Simulation Results, Identified Switching Problems and Proposed Solutions

The simulation results previously presented have shown that the non-linear LUTs can be employed to control the IPMSM over the full speed range with conventional SVPWM technique. In this section, the LuPWM technique described in section 2.4 is implemented for the IPMSM drive (see Figure 5.1) in order to reduce the peak-to-peak CMV and switching losses. This PWM is firstly examined in the low modulation region ( $m_a = 0.4$ ) at speed  $600rpm$ , torque  $10Nm$ , switching frequency ( $f_{sw}$ ) of  $8kHz$  and a dead time ( $t_d$ ) of  $3\mu s$ . The simulation waveforms of the phase currents, d- and q-axis currents, the torque and the peak-to-peak common mode voltage CMV are given in Figure 5.23 to Figure 5.25. It is evident that the phase current waveforms under the LuPWM (see Figure 5.23) are significantly distorted. This distortion leads to significant d- and q-axis current ripples and hence torque ripple as shown in Figure 5.24 and Figure 5.25, respectively.

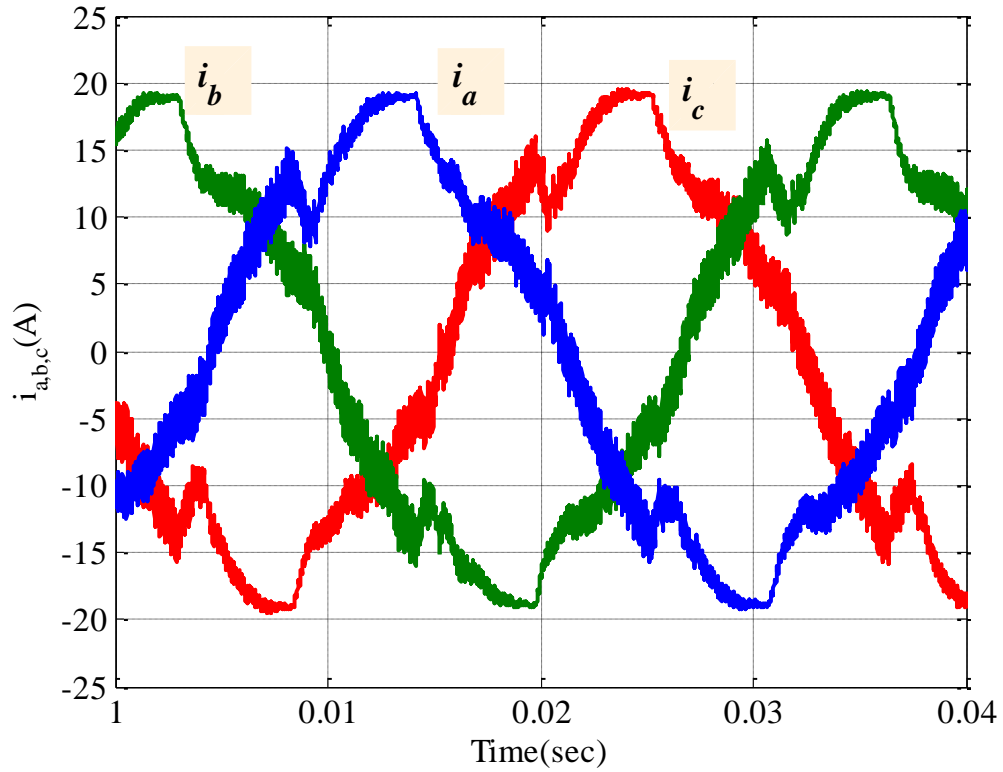


Figure 5.23 LuPWM phase current response at  $\omega_m = 600rpm$  and  $T_d = 10Nm$

Figure 5.26 shows the phase current waveforms during each sector for one hexagon period (in one hexagon period the sector number  $n$  changes from 1 to 6) where a distortion in the current waveforms occurs during the transitions between two sectors. The transition point is the time instant at which the reference voltage vector passes from one sector to another sector. Careful study of the current waveforms seen in Figure 5.26 indicates that the distortion occurs at each transition point. For example, the transition from sector 1 to 5 leads to a significant distortion in phase “ $b$ ” compared with the distortion in phases “ $a$ ” and “ $c$ ”. A transition from sector 4 to 6 leads to a considerable distortion in phase “ $c$ ” and the transition point of sector 5 to 4 results in the distortion in phase “ $a$ ”.

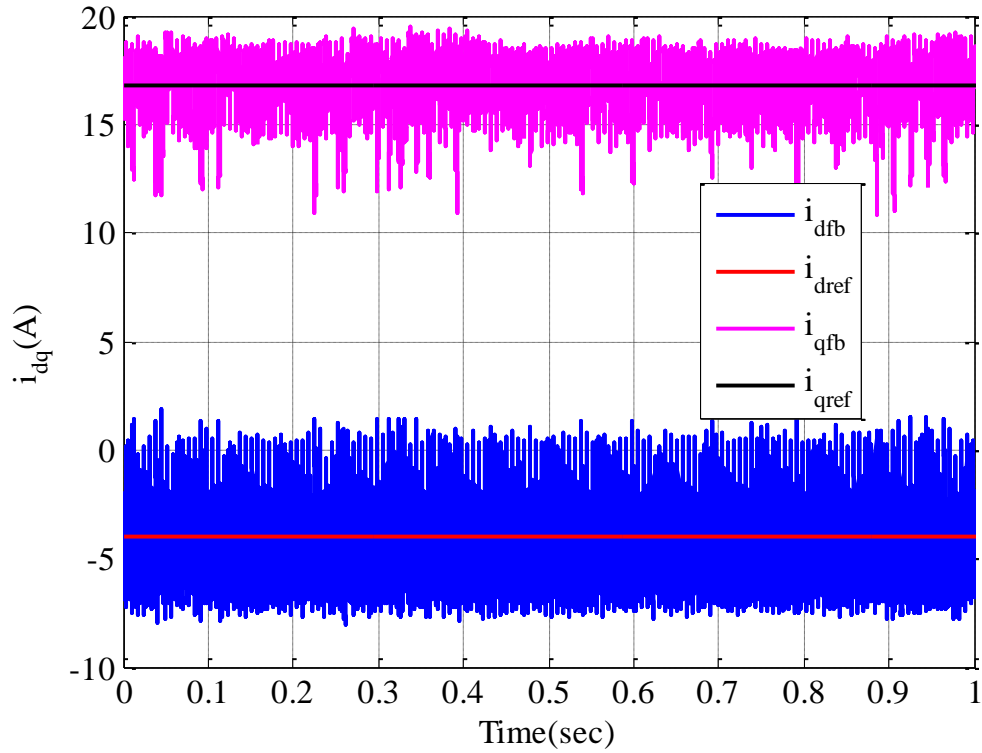


Figure 5.24 LuPWM  $i_d$  and  $i_q$  currents response at  $\omega_m = 600rpm$  and  $T_d = 10Nm$

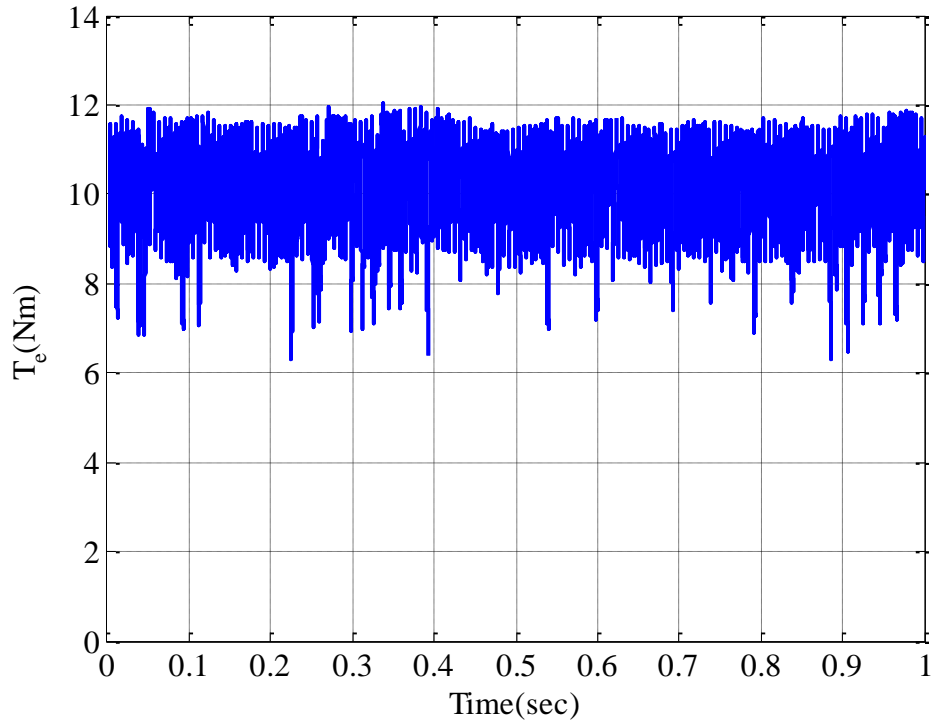


Figure 5.25 LuPWM torque response at  $\omega_m = 600rpm$  and  $T_d = 10Nm$

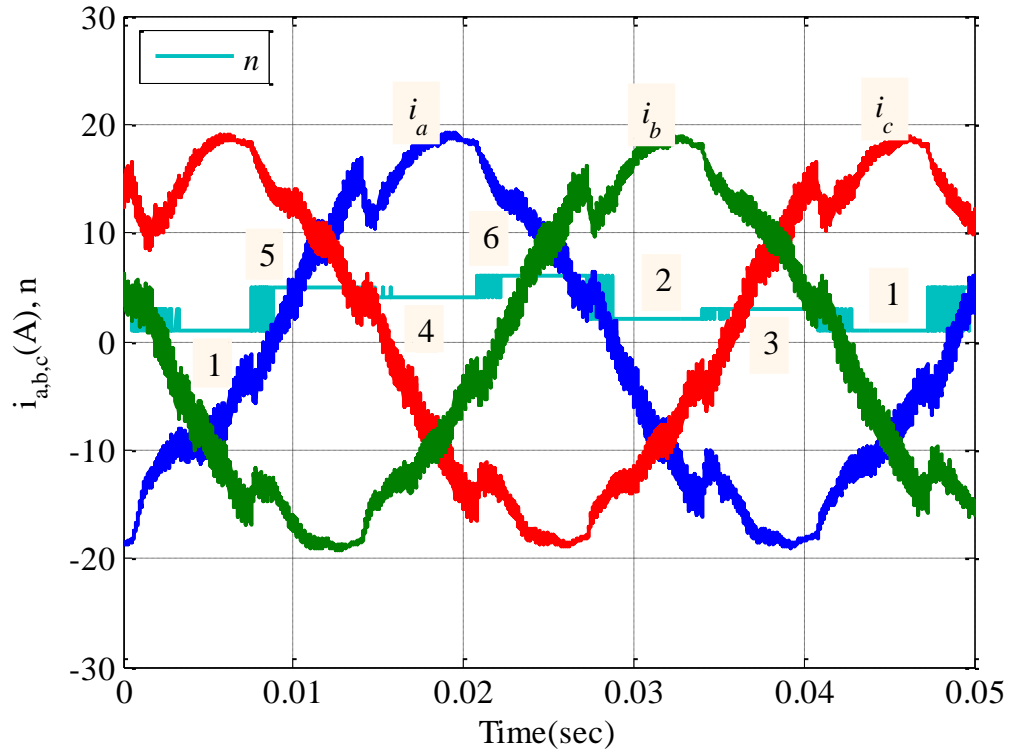


Figure 5.26 LuPWM phase current response at  $\omega_m = 600\text{rpm}$  and  $T_d = 10\text{Nm}$  for one hexagon period.

This distortion is due to the fact that the transition from one sector to the other, e.g., 1 to 5, 4 to 6 or 5 to 4, etc., illustrated in Figure 5.27 does not take place smoothly. For instance, at the transition point of sector 1 to 5, the pulse of phase “b” needs to change its state from “1” to “0” as shown in Figure 5.28. However, in the vicinity of the transition point the sector number is fluctuating between 1 and 5 (see Figure 5.28), resulting in undesirable switching and voltage distortion. The fluctuation in the sector number is caused by dq-axis voltages ripple. The dq-axis voltages are produced by the dq current controller which utilises the deviation of the dq feedback currents from the dq commands currents (see Figure 5.1) to generate these dq voltages. The resultant dq voltages are then transformed to alpha and beta voltage components by Clark transformation [23] to be used to calculate the magnitude and the direction of the reference voltage. This command voltage is then utilised by the LuPWM technique algorithm to determine a proper PWM pulse width and pattern for each phase. The ripple superimposed on the angle signal affects the electrical angle accuracy as shown in

Figure 5.29. This ripple leads to incorrect sector number and repeated transition as shown in Figure 5.28.

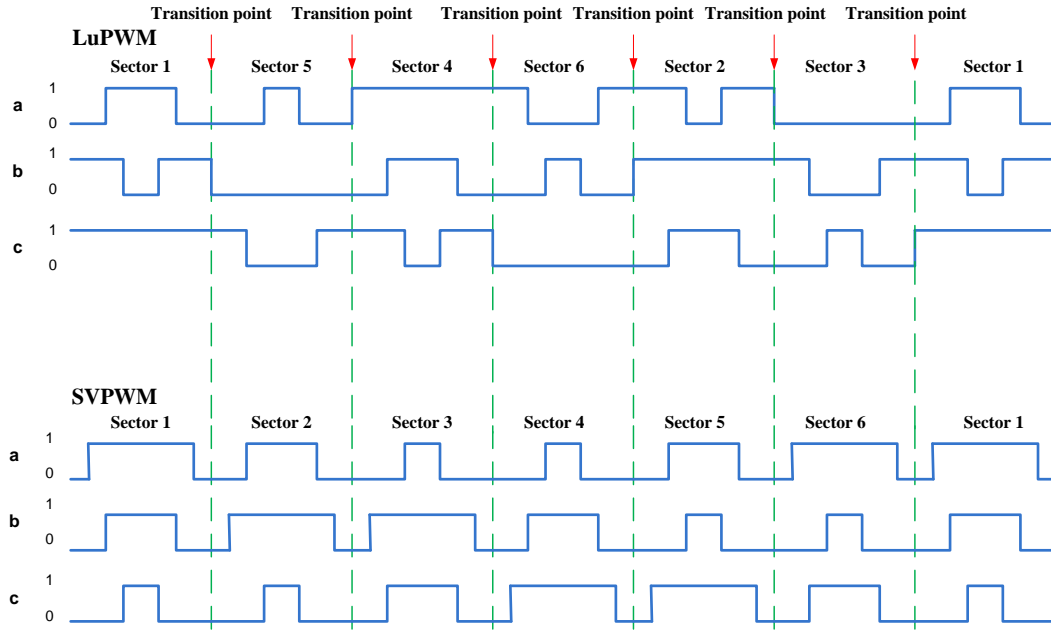


Figure 5.27 Switching sequence of LuPWM and SVPWM

The fluctuations in the sector number due to noise lead to a variation in the pulse state from “On” to “Off” and vice versa (see Figure 5.28). Therefore, a significant distortion in phase “b” at this point takes place. Although switching states of phases “a” and “c” remains constant during the transition from sector 1 to 5, the distortion in phase “b” voltage and current will propagate into them through electrical and magnetic couplings. At the transition from sector 5 to 4, phase “a” will be more distorted as its pulse state changes from “0” to “1”. The more distortion will take place in phase “c” at the transition point of sector 4 to 6 when its pulse state changes from “1” to “0”. Table 5.2 summarised the distortion occurrences at each transition point. For the purpose of comparison, the simulation results with the SVPWM technique under the same conditions are shown in Figure 5.30 to Figure 5.32. Figure 5.34 shows the zoomed-in phase current waveforms in one hexagon period. The d- and q-axis currents and torque waveforms shown in Figure 5.31 and Figure 5.32 are smoother compared with the corresponding waveforms given in Figure 5.24 and Figure 5.25 with LuPWM technique.

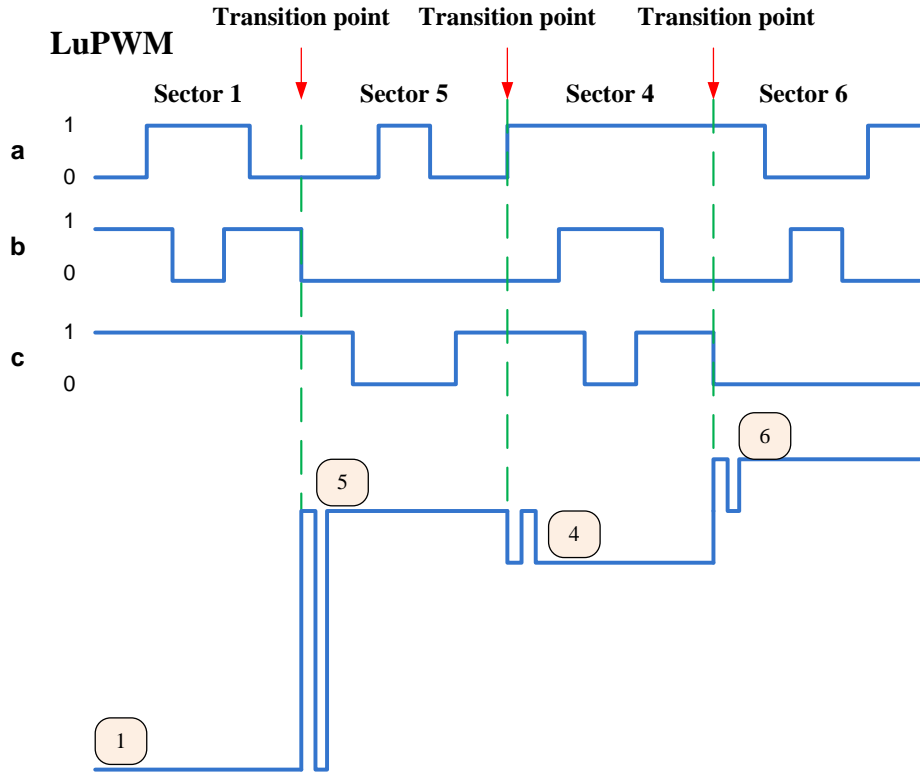


Figure 5.28 Fluctuation of sectors transition point in LuPWM (low region)

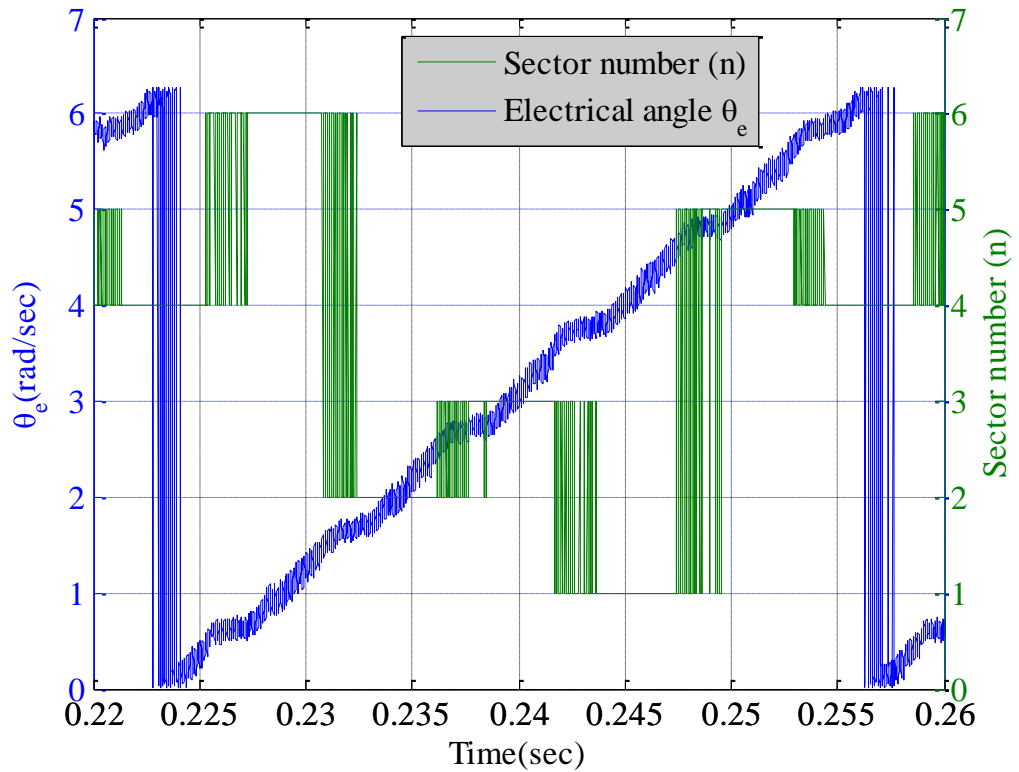


Figure 5.29 LuPWM electrical angle ripple



Table 5.2 Sector transition point and distorted phase		
Transition point		Most distorted phase
Current sector	Next sector	
1	5	<i>b</i>
5	4	<i>a</i>
4	6	<i>c</i>
6	2	<i>b</i>
2	3	<i>a</i>
3	1	<i>c</i>

The SVPWM technique produces smooth waveforms because its sector transitions take place during “zero” voltage state shown in Figure 5.27 in which all phases are at the “Off” state. Therefore, the angular ripple will have less influence on the switching state during the transitions as illustrated in Figure 5.34.

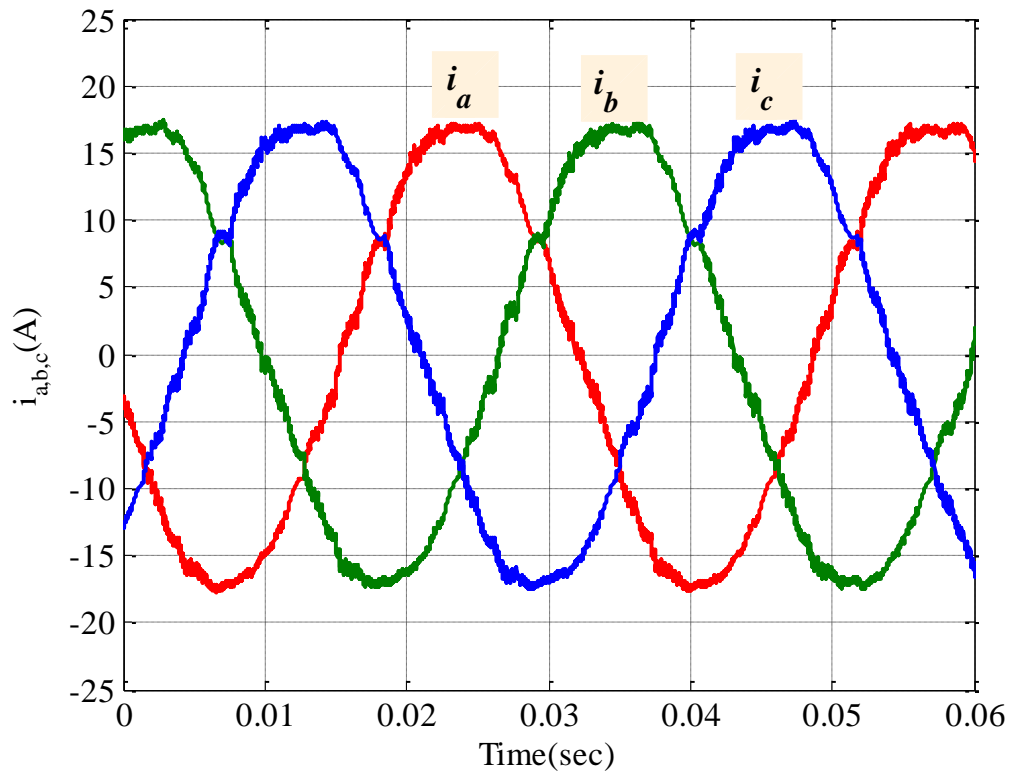


Figure 5.30 SVPWM phase current response at  $\omega_m = 600\text{rpm}$  and  $T_d = 10\text{Nm}$

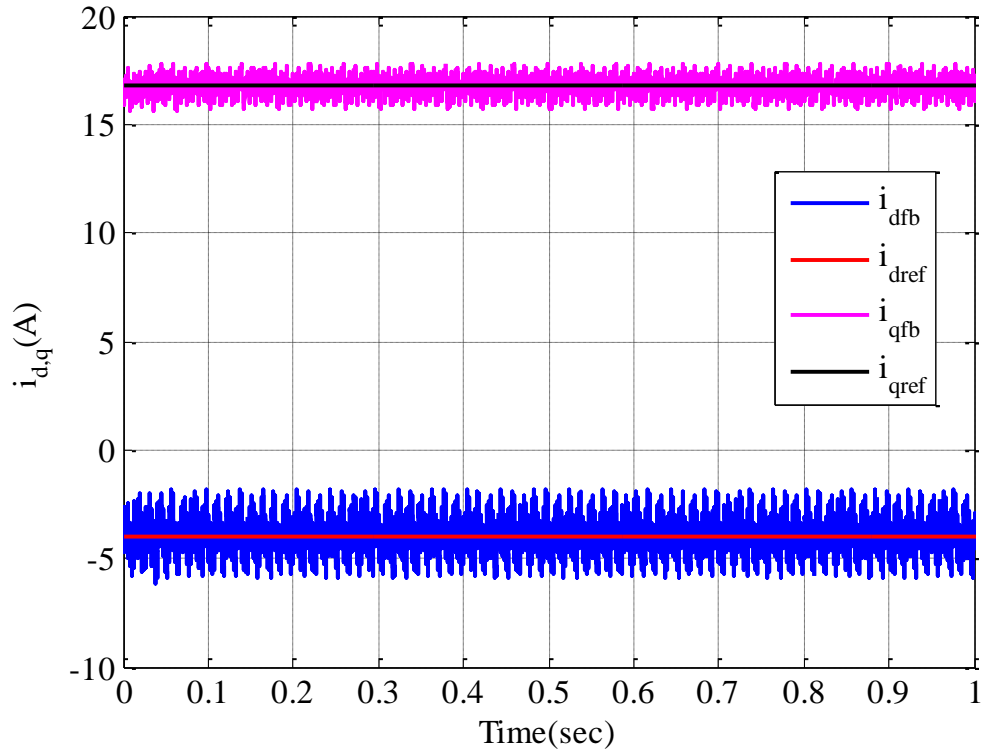


Figure 5.31 SVPWM  $i_d$  and  $i_q$  currents response at  $\omega_m = 600\text{rpm}$  and  $T_d = 10\text{Nm}$

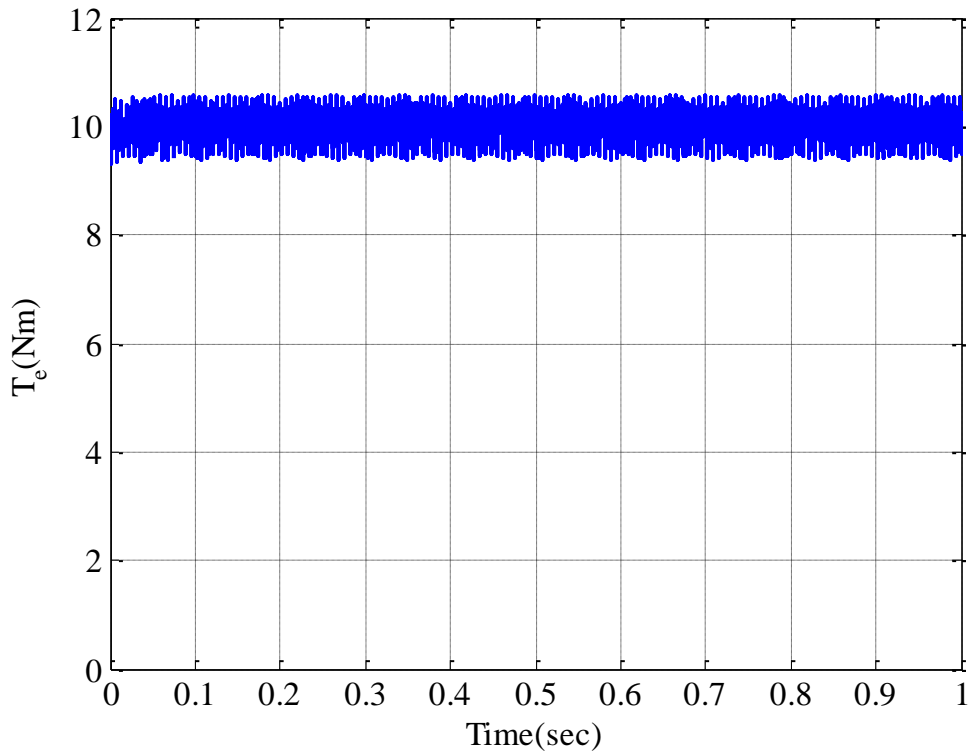


Figure 5.32 SVPWM torque response at  $\omega_m = 600\text{rpm}$  and  $T_d = 10\text{Nm}$

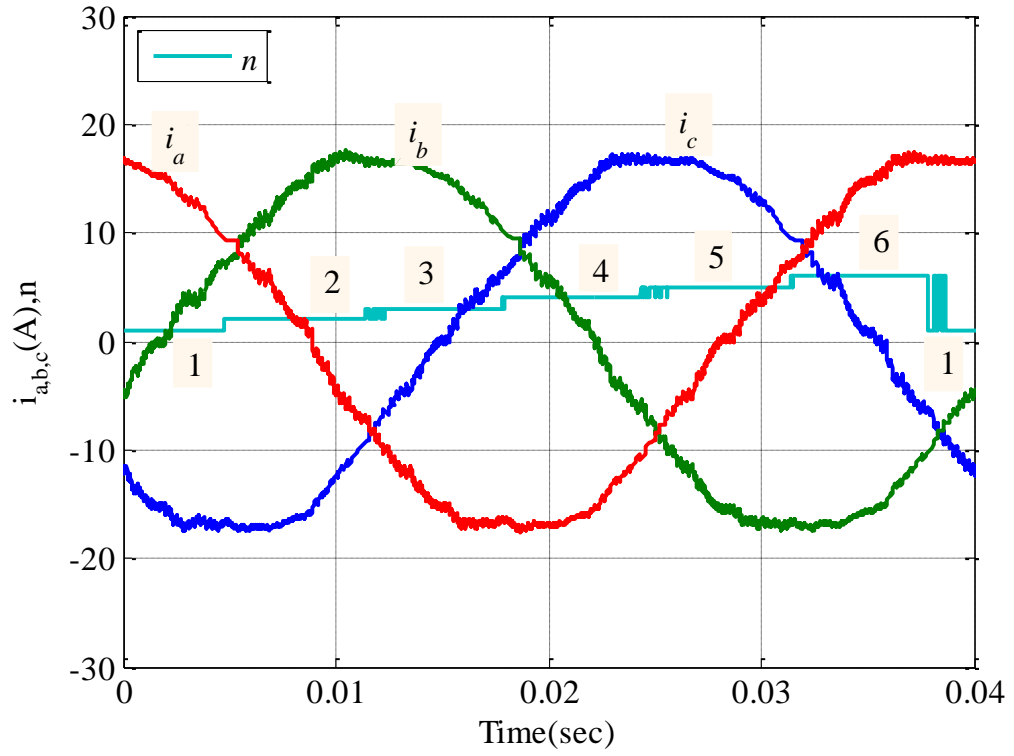


Figure 5.33 SVPWM phase current response at  $\omega_m = 600rpm$  and  $T_d = 10Nm$

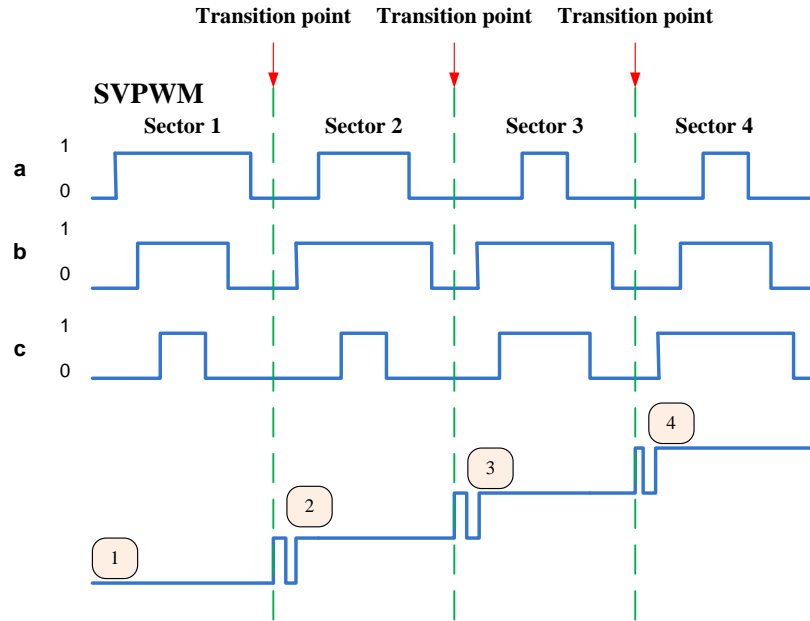


Figure 5.34 Fluctuation of sectors transition point in SVPWM (low region)

The influence of dead time is also investigated. Figure 5.35 shows the phase current simulation results with LuPWM under the same condition but with zero dead time. The results clearly show that the distortion in the current waveforms occur in the same pattern as those shown in Figure 5.23 regardless the dead time effects ( $3\mu s$ ).

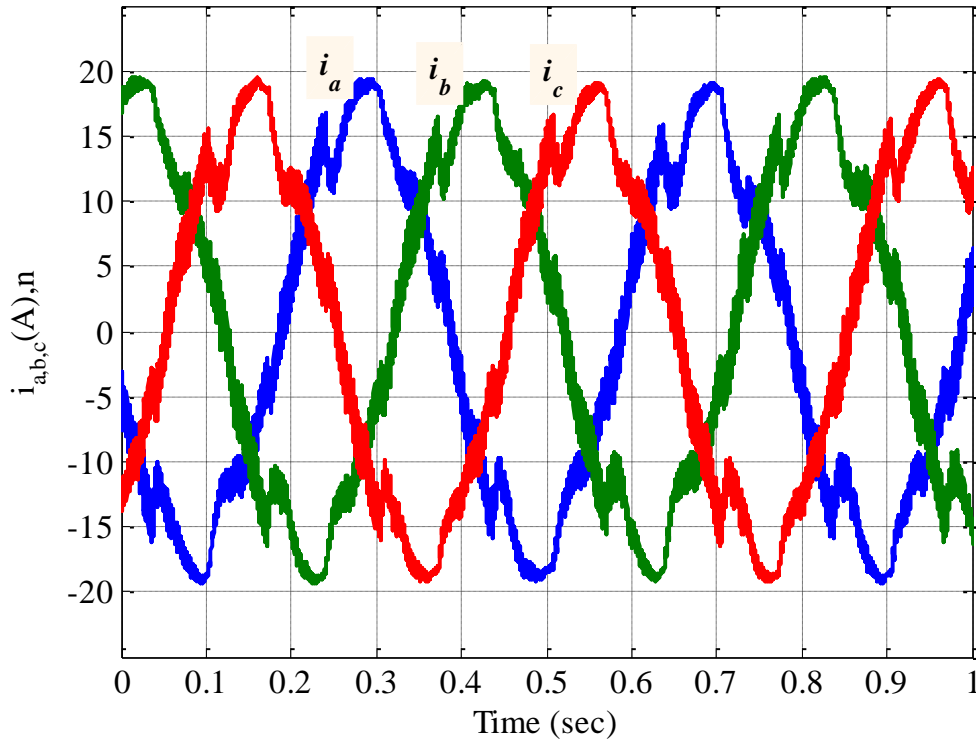


Figure 5.35 LuPWM phase current response at  $\omega_m = 600rpm$  and  $T_d = 10Nm$  without dead time

#### 5.3.4.1 Proposed solution of the LuPWM current waveform distortion

The foregoing analysis shows that the distortion of the current waveforms with the LuPWM technique occurs at the transition points from sector to sector in the hexagon. At each transition instant, the switching state of one phase change from “On” to “Off” or vice versa. The sector transitions will be smoother if the switching states in the current sector and the next sector are the same as the case with SVPWM technique.

The regions of the hexagon where the current waveforms distortion takes place are defined as the non-linear regions [93]. Figure 5.36 illustrates the non-linear regions of the LuPWM technique where the distortion occurs in the sector boundaries in the  $L$ -region and  $H$ -region.

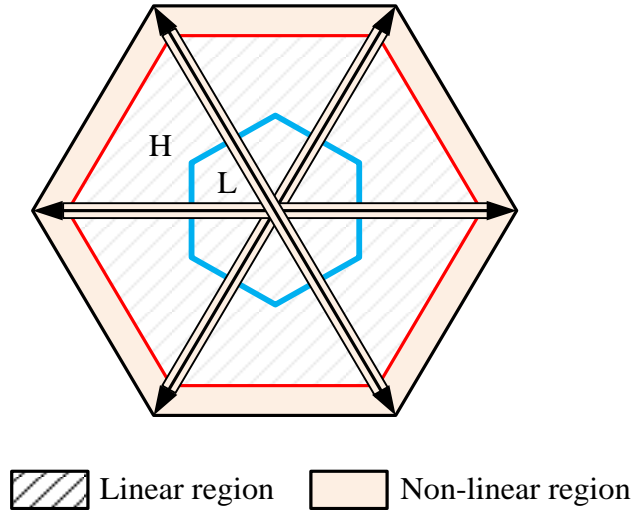


Figure 5.36 Linear and Non-linear regions of the LuPWM.

Therefore, the distortion problem of the current waveforms may be solved by making the transition process between the sectors smoother. In the previous studies [93-95], one solution has been suggested by combining LuPWM and SVPWM techniques. In the regions close to the transitions, SVPWM technique is employed. The problem of this solution is that the peak-to-peak of the CMV will be increased due to the use of SVPWM technique. The resultant CMV waveform is shown in Figure 5.37, where the peak-to-peak of the CMV increases from  $\pm V_{dc}/6$  ( $\pm 20V$ ) with LuPWM technique to  $\pm V_{dc}/2$  ( $\pm 60V$ ) with SVPWM technique. As a result, the use of SVPWM technique to avoid the problem of the distortion of the phase current waveforms will increase the CMV peak value. In addition, implementation of the combined LuPWM with SVPWM techniques will be more complex.

An alternative solution which is proposed in this thesis is to modify the existing LuPWM technique pulse pattern in the non-linear regions as shown in Figure 5.38. The

switching state of a pulse is kept constant in a small period around a transition instant. This will eliminate false switching due to angular ripple and the voltage error due to this will be evened out between the “Turn-On” and “Turn-Off” transitions. For example, in the conventional LuPWM technique at the transition point from sector 1 to 5 the switching state of phase “b” changes from “On” to “Off” (see Figure 5.38). In the modified LuPWM technique (Mod-LuPWM technique) this state is kept constant at “On” for a short period defined as the sectors transition period until the reference voltage vector passes from sector 1 to sector 5 and remains in sector 5. The same Mod-LuPWM switching technique can be used in the high modulation region.

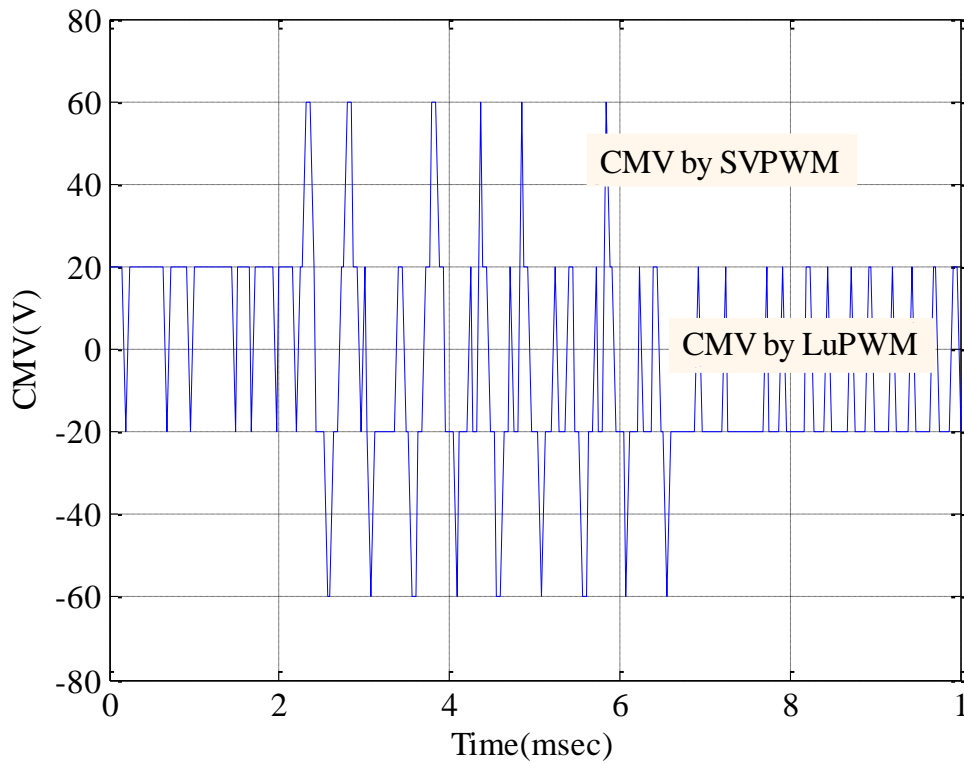


Figure 5.37 LuPWM and SVPWM in H-region at  $\omega_m = 1000\text{rpm}$  and  $T_d = 10\text{Nm}$

The start of the non-linear region of each sector (see Figure 5.36) is identified by a pre-calculated distortion angle ( $\theta_{dis}$ ) [93]. This angle is a function of the electrical angular position  $\theta_e$  and the modulation index  $m_a$ . Therefore, its value changes as these two

factors vary. It is noted that the angle ( $\theta_{dis}$ ) needs to be calculated for one sector due to the fact that PWM technique limits are symmetric and consequently the distortion angle of the other sectors can be determined by symmetry [93]. As an example of obtaining the angle ( $\theta_{dis}$ ) the fifth sector of the hexagon where the electrical angle is between  $240^\circ$  and  $300^\circ$  (see Figure 2.9 and Figure 2.10) will be considered.

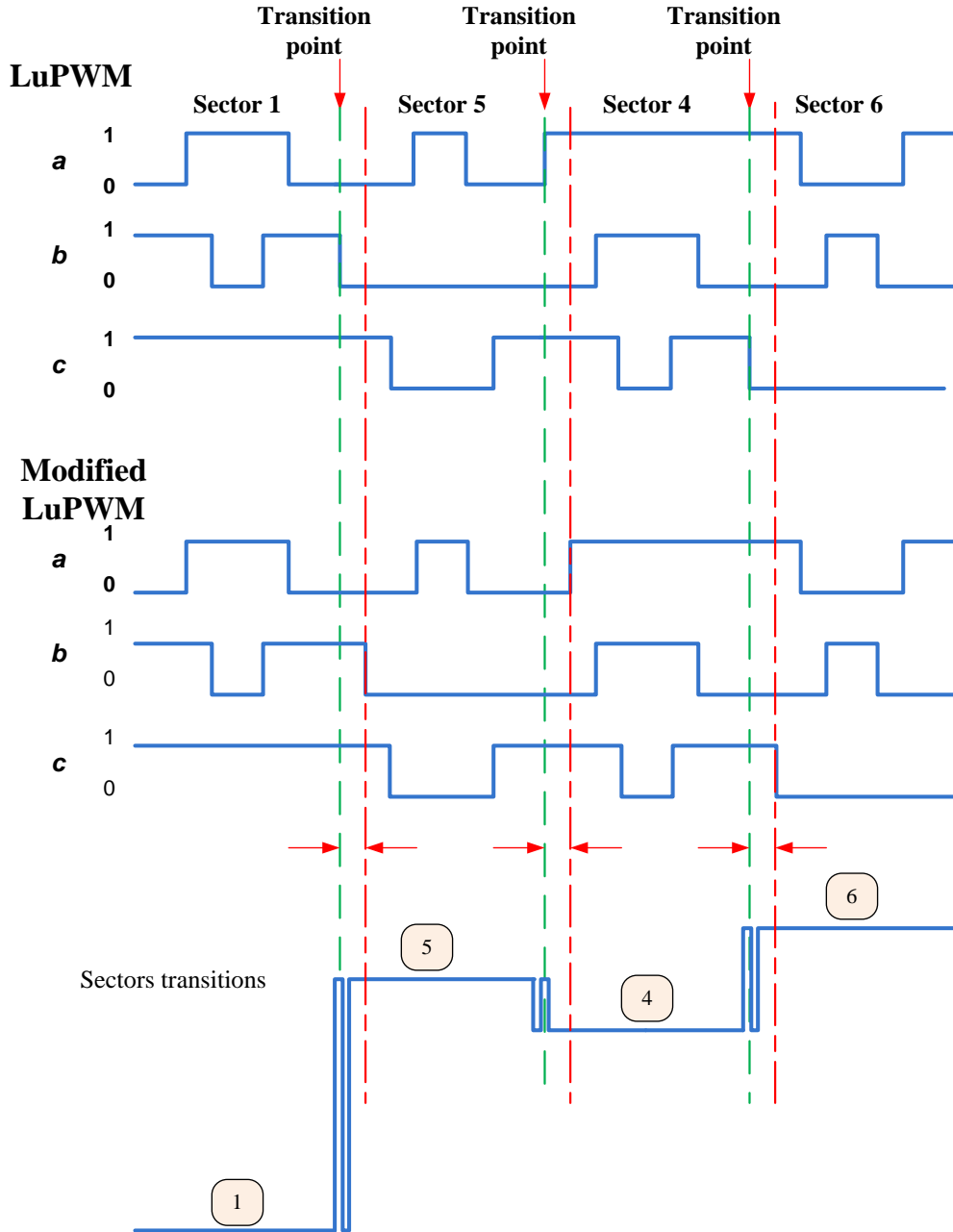


Figure 5.38 LuPWM and Mod-LuPWM switching pattern in low region

According to the modulation waveforms of the LuPWM technique given in Figure 2.9 and Figure 2.10, the phase “a” fundamental value  $v_a^*$  is given by [93]:

$$V_a^*(\theta_e) = V_a \cos(\theta_e) \quad 5.9$$

$$m_a = \frac{V_{com}}{V_{am}} = \frac{V_{com}}{V_{dc}/\sqrt{3}} \quad 5.10$$

$$V_{com} = \frac{\sqrt{3} m_a}{V_{dc}} = V_a \quad 5.11$$

Substituting from Eqn. 5.11 into Eqn. 5.9 yields:

$$V_a^*(\theta_e) = (\sqrt{3}m_a/V_{dc})\cos(\theta_e) \quad 5.12$$

The LuPWM technique zero signal  $V_0$  is given by Eqn.5.13 [17].

$$V_0 = \text{sign}(V_a^*) \left( \frac{V_{dc}}{2} \right) - V_a^* \quad 5.13$$

Substituting from Eqn. 5.13, the zero signal equation is obtained as given in Eqn. 5.14:

$$V_a(\theta_e) = (1/2) - (\sqrt{3}/V_{dc})m_a \cos(\theta_e + (2\pi/3)) \quad 5.14$$

The maximum duty cycle  $d_{max}$  of a PWM can be obtained by [93]:

$$d_{max} = 1 - (1/T_{sw})(3t_d + T_{MPW}) \quad 5.15$$

where  $T_{sw}$  is the switching period ( $125\mu s$ ),  $t_d$  is the dead time ( $3\mu s$ ) and  $T_{MPW}$  is the minimum pulse width ( $2\mu s$ ). According to [93], the angle of the start of the distortion can be calculated by Eqn.5.16:

$$d_{max} - (1/2) = V_a(\theta_e) + V_0(\theta_e) \quad 5.16$$



Substituting from Eqn. 5.12 and 5.14 into Eqn. 5.16 and by simplifying the resultant equation and normalization for  $V_{dc}$ , the maximum duty cycle  $d_{max}$  is related to the angle  $\theta_e$  by Eqn. 5.17.

$$d_{max} = (\sqrt{3}m_a/2)(\cos(\theta_e) + \sqrt{3} \sin(\theta_e)) + 1 \quad 5.17$$

Equation 5.17 can be numerically solved to obtain the angle  $\theta_e$  taking in consideration that  $d_{max}$  is computed by Eqn. 5.15 to be 0.912. The distortion angle  $\theta_{dis}$  can be calculated by [93] where  $300^\circ$  is the starting angle of sector 5 which has been taken as an example of these calculations:

$$\theta_{dis} = 300^\circ - \theta_e \quad 5.18$$

Table 5.3 Calculated distortion angle in each sector at $m_a = 0.7$		
$n$	Sector boundaries	$\theta_{dis}$ (degrees)
1	$210 \leq \theta_e < 270$	262.96
2	$90 \leq \theta_e < 150$	142.96
3	$150 \leq \theta_e < 210$	202.96
4	$330 \leq \theta_e < 30$	22.96
5	$270 \leq \theta_e < 330$	322.96
6	$30 \leq \theta_e < 90$	82.96

Figure 5.39 depicts the variation of the distortion angle ( $\theta_{dis}$ ) with the modulation index  $m_a$  in the fifth sector of the hexagon. It is noted that the distortion angle is maximum at low  $m_a$  and it reduces gradually as the  $m_a$  increases toward higher levels. This indicates that the distortion in the current phases is significant at the  $L$ -region of the hexagon ( $m_a \leq 0.6$ ) and it becomes less considerable at  $H$ -region ( $m_a > 0.6$ ). Table 5.3 gives an example of the calculated values of  $\theta_{dis}$  in the six hexagon sectors at  $m_a = 0.7$ . The LuPWM pulses at the hexagon sector boundaries are modified to be suitable for the aforementioned suggested solution (see Figure 5.38) as described in Table 5.4. The selection between the LuPWM and Mod-LuPWM techniques is based on comparison of the electrical angle  $\theta_e$  with the distortion angle  $\theta_{dis}$ . The Mod-LuPWM

technique is selected if the value of  $\theta_e$  is higher than  $\theta_{dis}$  and smaller than the upper limit of the current sector boundary otherwise the normal LuPWM technique is selected.

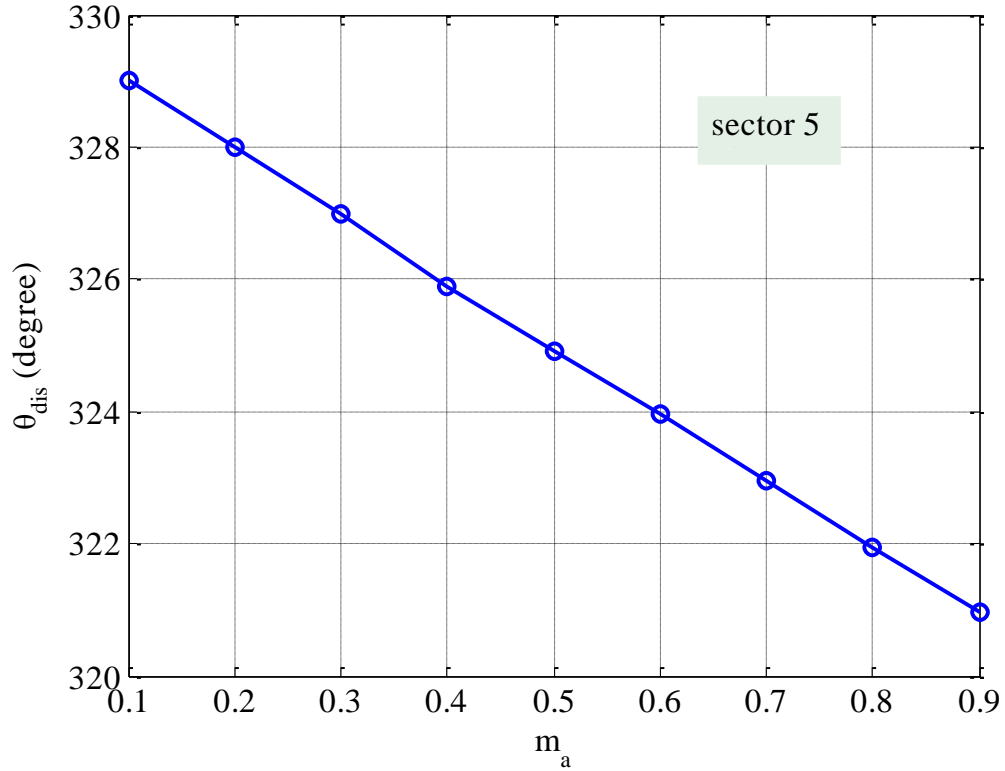


Figure 5.39 Variations of the distortion angle with the modulation index in sector 5

If	Pulse pattern	If	Pulse pattern
$210 \leq \theta_e < \theta_{dis}$	LuPWM	$\theta_{dis} \leq \theta_e < 270$	Mod-LuPWM
$90 \leq \theta_e < \theta_{dis}$	LuPWM	$\theta_{dis} \leq \theta_e < 150$	Mod-LuPWM
$150 \leq \theta_e < \theta_{dis}$	LuPWM	$\theta_{dis} \leq \theta_e < 210$	Mod-LuPWM
$330 \leq \theta_e < \theta_{dis}$	LuPWM	$\theta_{dis} \leq \theta_e < 30$	Mod-LuPWM
$270 \leq \theta_e < \theta_{dis}$	LuPWM	$\theta_{dis} \leq \theta_e < 330$	Mod-LuPWM
$30 \leq \theta_e < \theta_{dis}$	LuPWM	$\theta_{dis} \leq \theta_e < 90$	Mod-LuPWM

### 5.3.4.2 Simulation results of the Mod-LuPWM

The simulation results of the phase currents, d- and q-axis currents and torque of the proposed PWM algorithm at  $600rpm$  and  $10Nm$  are shown in Figure 5.40 to Figure 5.42, respectively. It is evident that the current waveforms are less distorted than those shown in Figure 5.23. Therefore, the Modified LuPWM (Mod-LuPWM) achieves better performance than the combined PWM (i.e. LuPWM and SVPWM techniques).

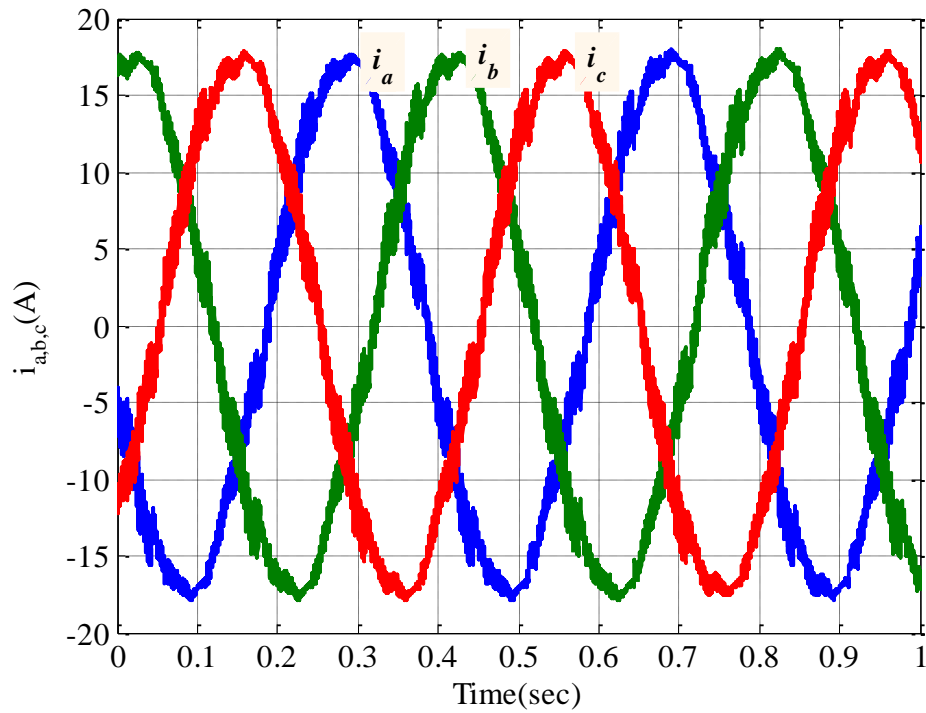


Figure 5.40 Mod-LuPWM phase current response at  $\omega_m = 600rpm$  and  $T_d = 10Nm$

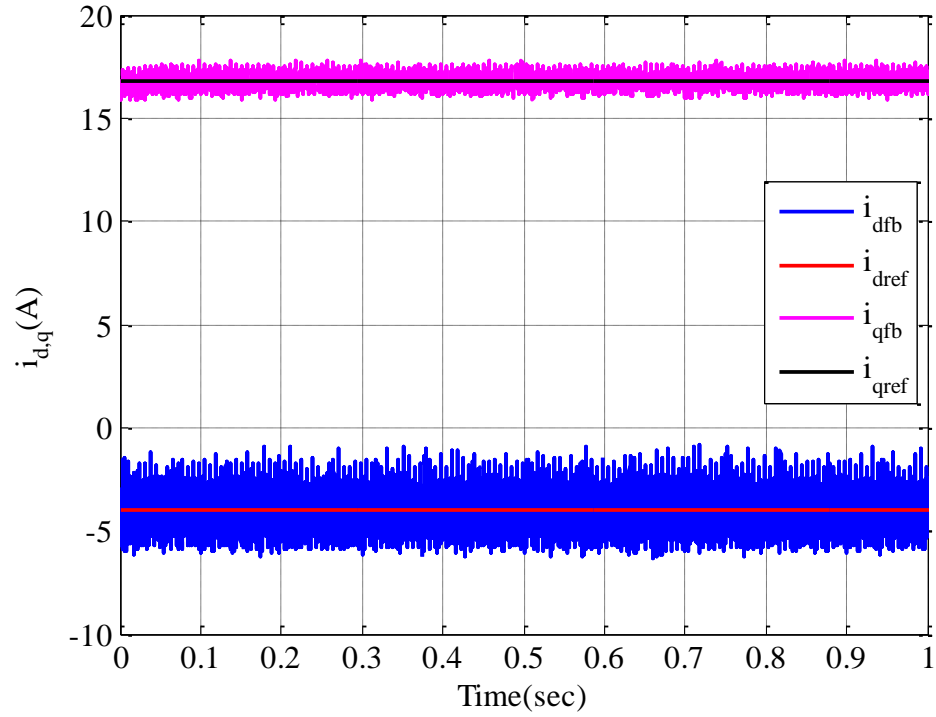


Figure 5.41 Mod-LuPWM  $i_d$  and  $i_q$  currents response at  $\omega_m = 600\text{rpm}$  and  $T_d = 10\text{Nm}$

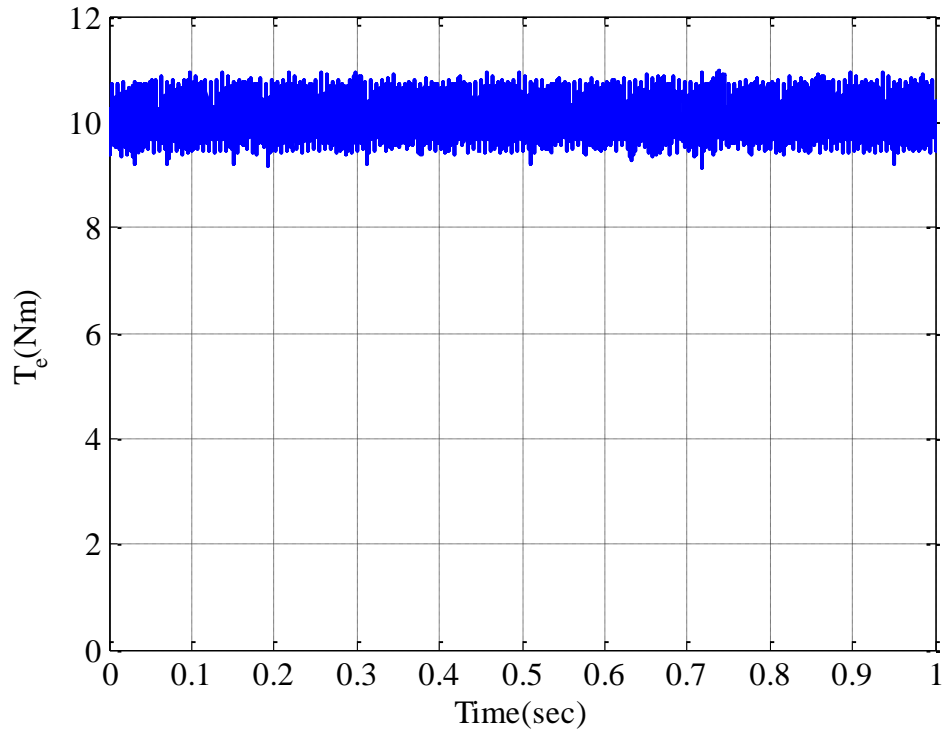


Figure 5.42 Mod-LuPWM Torque response at  $\omega_m = 600\text{rpm}$  and  $T_d = 10\text{Nm}$

### 5.3.5 Comparative Simulation Study of SVPWM, LuPWM and Mod-LuPWM

The SVPWM, LuPWM and Mod-LuPWM techniques are implemented by using the control scheme given in Figure 5.1. The simulated current and torque waveforms, and peak to peak CMV of these PWM techniques in the  $L$ - and  $H$ - regions of the  $(\alpha\beta)$  voltage hexagon are compared. The FFT harmonic analyses are generated for the current and voltage waveforms of the studied PWM techniques. In the  $L$ -region the IPMSM drive is run at  $600rpm$  and relatively high torque  $40Nm$ . The resultant phase current, torque,  $i_d$  and  $i_q$  currents, and CMV waveforms are shown in Figure 5.43 to Figure 5.46. It is noted that the Mod-LuPWM technique gives good current and torque waveforms compared with that produced by the traditional LuPWM technique. The current waveforms (see Figure 5.43) of the Mod-LuPWM technique are almost as good as the one generated by the SVPWM technique but its dq-current waveforms (see Figure 5.44) show a slightly higher ripple than that produced by SVPWM technique. This ripple can be clearly noticed in the torque waveforms (see Figure 5.45) where the Mod-LuPWM technique gives relatively low torque ripple compared with LuPWM technique. The torque ripple of the Mod-LuPWM is, however higher than that of the produced by the SVPWM technique. On the other hand, the SVPWM technique has the highest peak CMV amongst the studied PWM techniques (see Figure 5.46) where it is  $60V$  for SVPWM technique and  $40V$  for both LuPWM and Mod-LuPWM techniques. The CMV waveform produced by the LuPWM technique has higher distortion than that produced by the Mod-LuPWM technique. The Mod-LuPWM technique current waveforms (see Figure 5.43) are improved comparing with the waveforms of LuPWM technique without affecting the peak value of the CMV as both LuPWM and Mod-LuPWM techniques has the same peak value of the CMV ( $40V$ ) (see Figure 5.46). The above discussion is proved by performing the FFT analysis of the phase “a” voltage and current waveforms. The resultant harmonic orders are illustrated in Figure 5.47 and Figure 5.48 respectively. The FFT analysis shows that the LuPWM technique has the highest harmonic magnitudes amongst the studied PWMs especially the fifth and seventh harmonics compared with LuPWM and SVPWM techniques. The SVPWM technique has the lowest harmonic magnitude. This explains the high ripple of the LuPWM technique current waveforms (see Figure 5.43 to Figure 5.45).

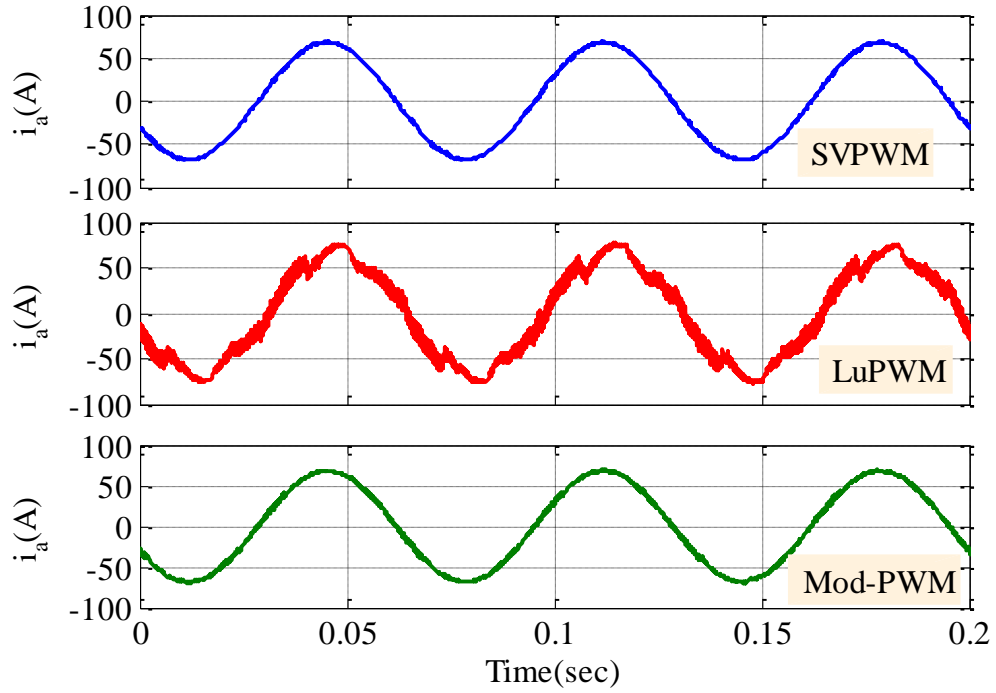


Figure 5.43  $i_a$  current of the studied PWMs at  $\omega_m = 600rpm$  and  $T_d = 40Nm$

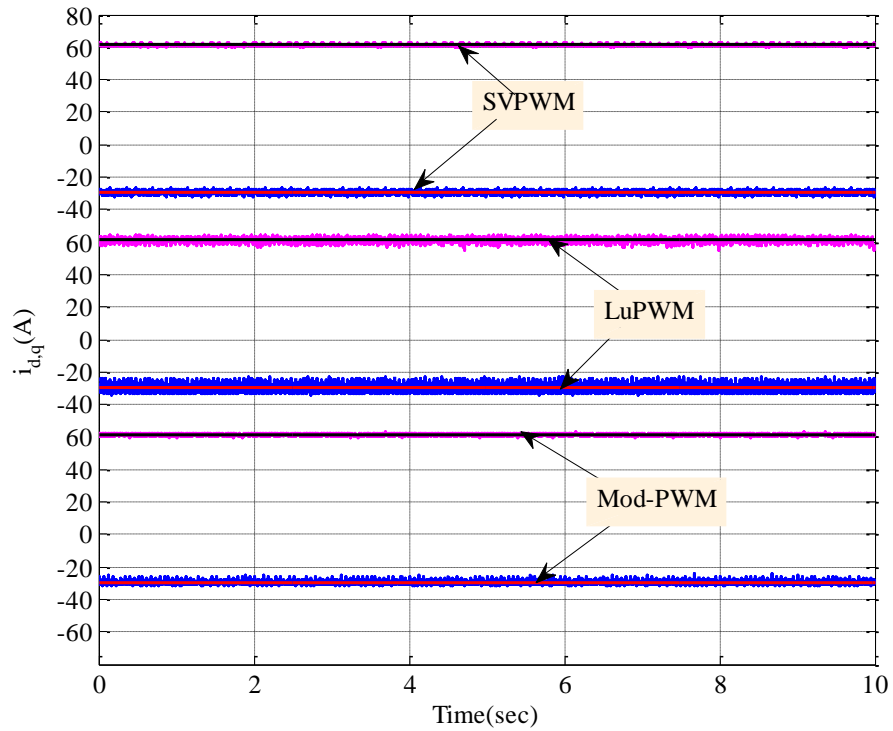


Figure 5.44  $i_d$  and  $i_q$  currents of the studied PWMs at  $\omega_m = 600rpm$  and  $T_d = 40Nm$

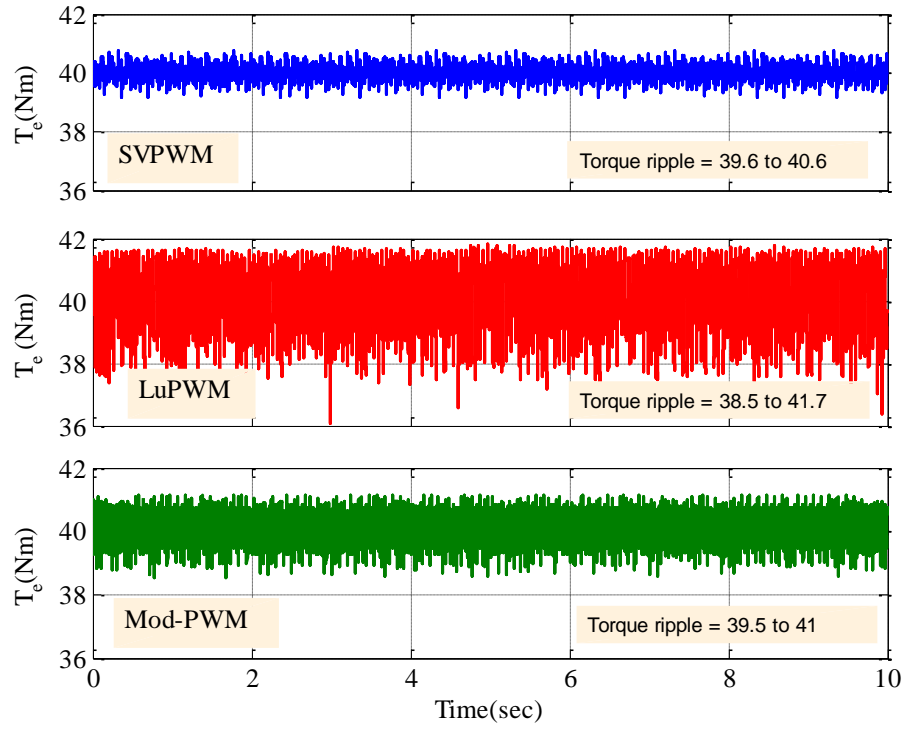


Figure 5.45 Torque response of studied PWMs at  $\omega_m = 600\text{rpm}$  and  $T_d = 40\text{Nm}$

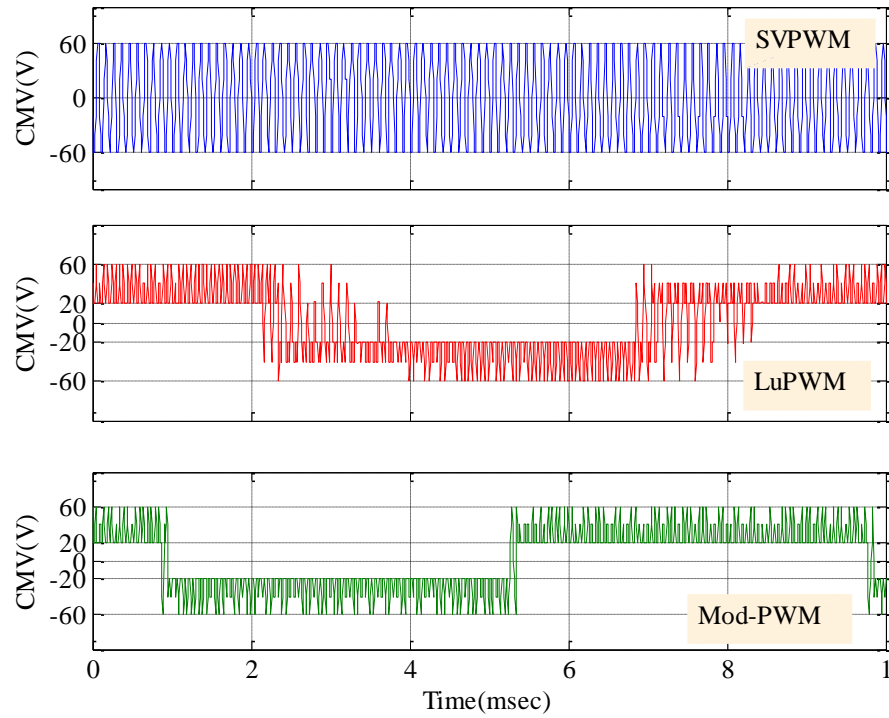


Figure 5.46 CMV of studied PWMs at  $\omega_m = 600\text{rpm}$  and  $T_d = 40\text{Nm}$

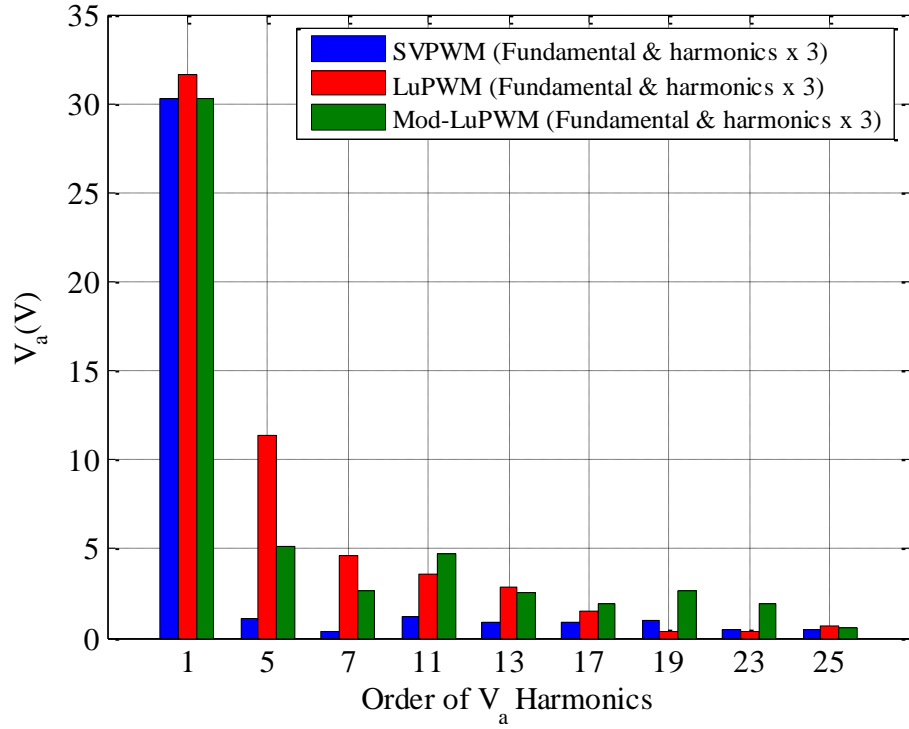


Figure 5.47 Phase voltage harmonic of studied PWMs at  $\omega_m = 600rpm$  and  $T_d = 40Nm$

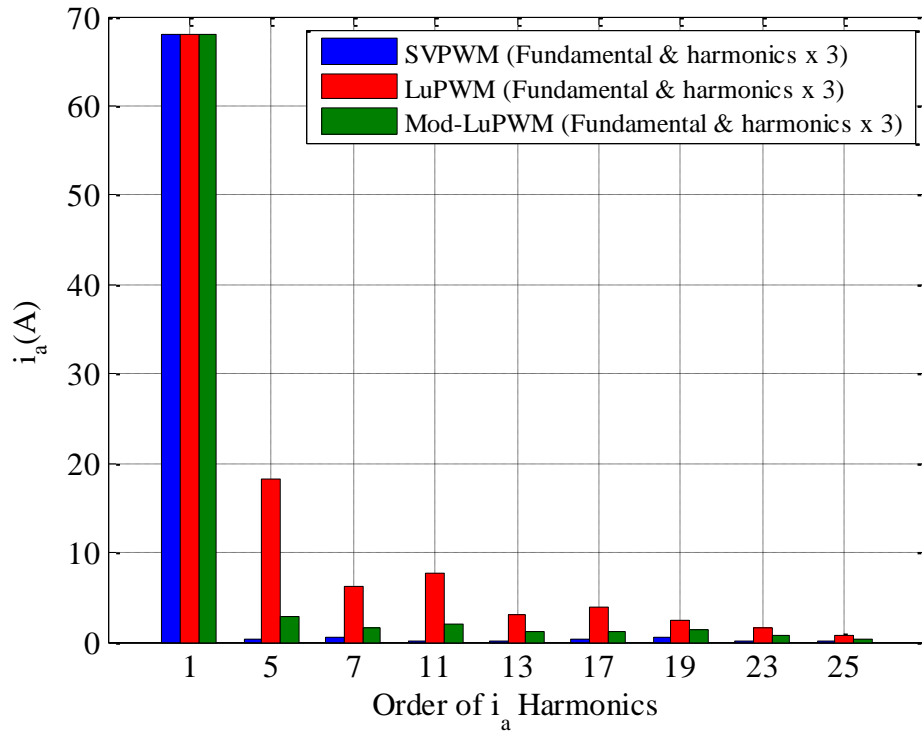


Figure 5.48 Phase current harmonic of the studied PWMs at  $\omega_m = 600rpm$  and  $T_d = 40Nm$



The FFT analysis also shows that the fundamental voltage of LuPWM technique is slightly higher than the fundamental voltage of both SVPWM and Mod-LuPWM techniques which are almost equal. The higher fundamental voltage of the LuPWM technique is again causing by the distortion of the voltage waveforms (see Figure 5.49) due to the electrical angle ripple (see Figure 5.29). The fundamental voltage of Mod-LuPWM technique is reduced to be almost equal to the SVPWM technique voltage by modifying the switching pattern of the LuPWM technique (see Figure 5.38).

The same analysis has been done for the *H*-region where the IPMSM drive is run at speed 1000rpm and torque 35Nm. The resultant simulation waveforms as well as the FFT analysis are illustrated in Figure 5.50 to Figure 5.55.

One can see that the simulation results as well as the harmonic analysis of the *H*-region almost follow the same trend of that produced in the *L*-region. The LuPWM current waveforms (see Figure 5.50) are however, more sinusoidal in their shape (i.e. has less distortion) compared with the current waveform produced in *L*-region (see Figure 5.43). This is again due to the fact that  $m_a$  is high and consequently the distortion angle is smaller than that in the *L*-region (see Figure 5.39). Therefore, the distortion region at the sector transition points is small which leads to reduce the distortion in the current waveforms.

The effect of reducing the distortion in the current waveforms can be clearly seen in the torque and current waveforms ripple which become lower. The magnitude of the fifth and seventh harmonic, Figure 5.54 and Figure 5.55, is smaller than that shown in Figure 5.47 and Figure 5.48.

It is noted that, the peak of the CMV of LuPWM as well as Mod-LuPWM techniques are reduced to 20V (see Figure 5.46 and Figure 5.53) compared with that produced by SVPWM technique which remains as high as the CMV in the low modulation region (60V).

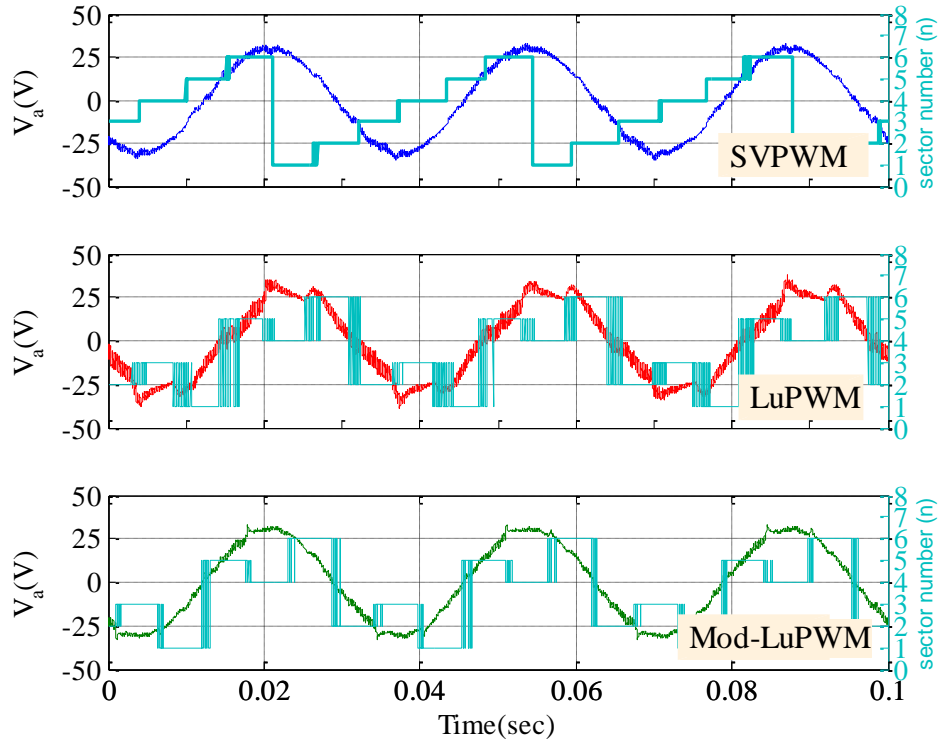


Figure 5.49 Phase current harmonic of studied PWMs at  $\omega_m = 600rpm$  and  $T_d = 40Nm$

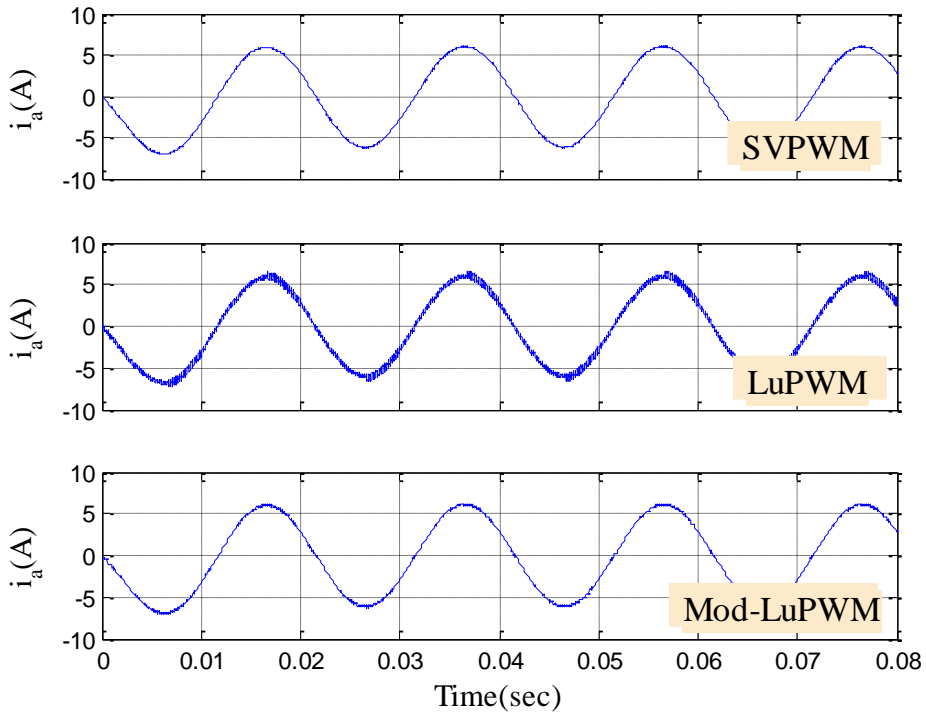


Figure 5.50  $i_a$  current of the studied PWMs at  $\omega_m = 1000rpm$  and  $T_d = 35Nm$

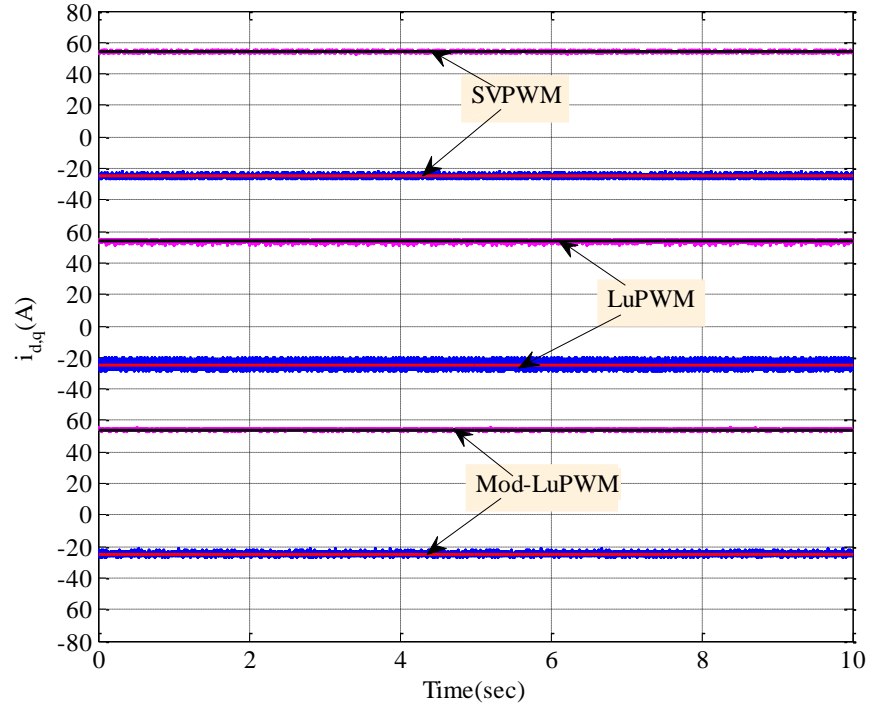


Figure 5.51  $i_d$  and  $i_q$  currents of the studied PWMs at  $\omega_m = 1000rpm$  and  $T_d = 35Nm$

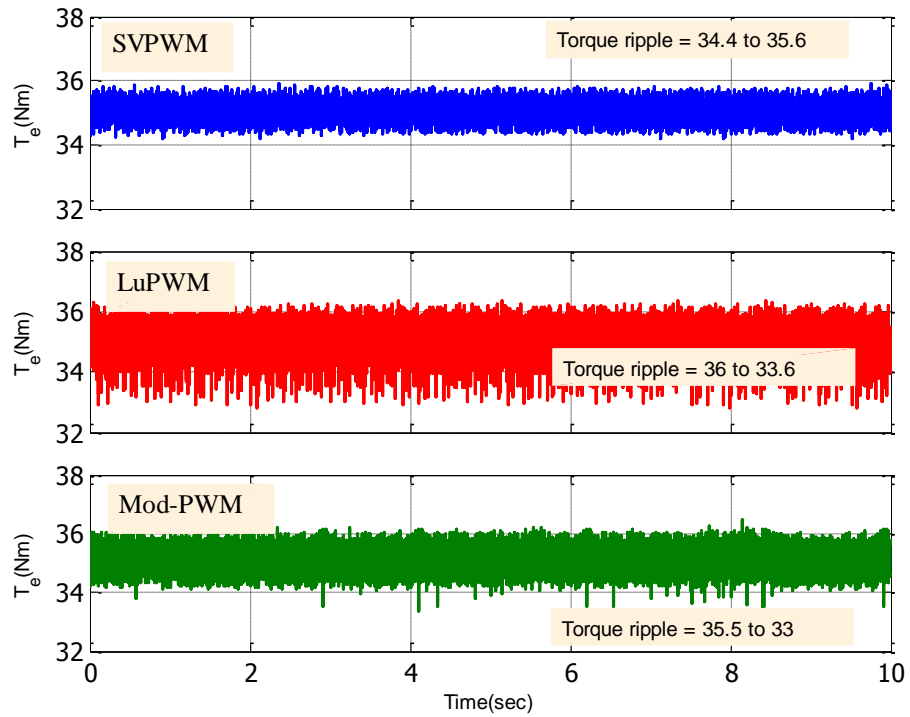


Figure 5.52 Torque response of the PWMs at  $\omega_m = 1000rpm$  and  $T_d = 35Nm$

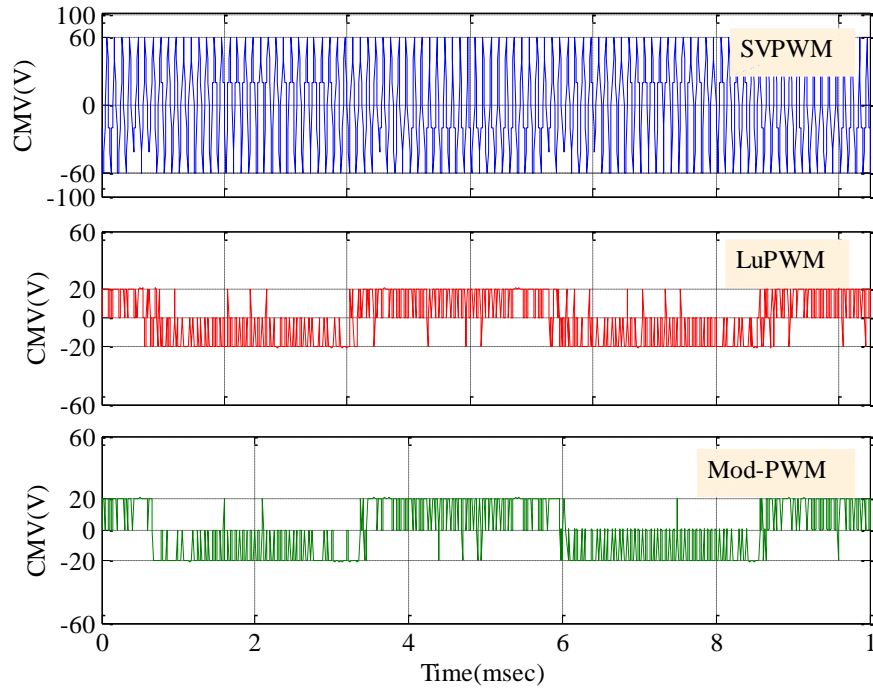


Figure 5.53 CMV of the studied PWMs at  $\omega_m = 1000rpm$  and  $T_d = 35Nm$

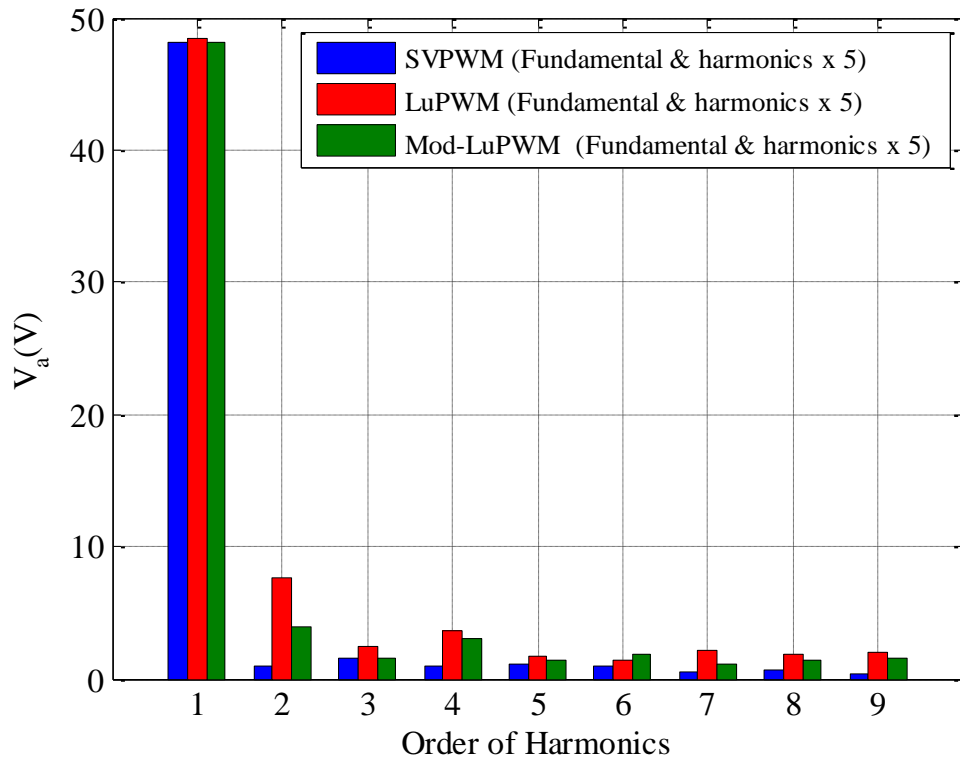


Figure 5.54 Phase voltage harmonics of studied PWMs at  $\omega_m = 1000rpm$  and  $T_d = 35Nm$

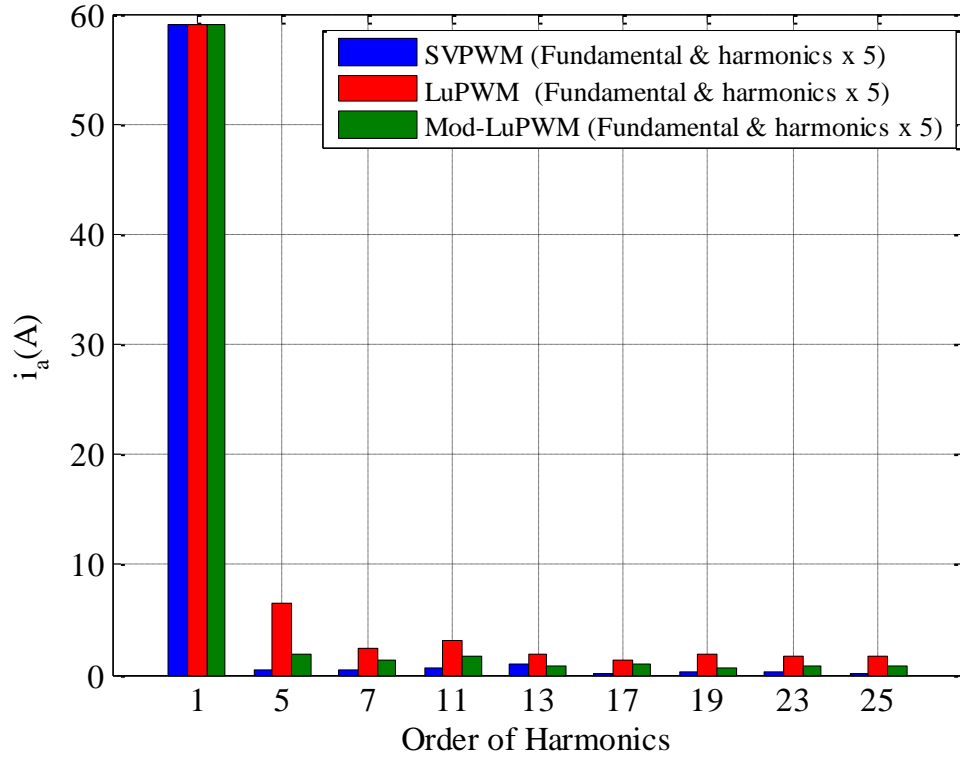


Figure 5.55 Phase current harmonics of the studied PWMs at  $\omega_m = 1000rpm$  and  $T_d = 35Nm$

## 5.5 Chapter Summary

In this Chapter, non-linear LUTs of the dq-axis current commands are generated based on the LMA described in Chapter 3 in order to control the IPMSM drive.

These non-linear LUTs are accounted for the parameters saturation effects and the voltage drop across the stator winding resistance. The input demand points ( $\omega_m$ ,  $T_d$ ) of the LUTs are selected according to the torque-speed profile to ensure that the whole speed and torque ranges (i.e. CTR and FWR of the IPMSM drive) are covered by the generated LUTs.

First, the optimal solution of the maximum speed-torque profile is calculated on the limits in order to well-defined the operation boundary of the IPMSM. Then, the optimal solutions of the area within the torque-speed envelope are calculated and the LUTs data are completed.

A FB-FF flux weakening control algorithm which combines the advantages of the FF-FW and FB-flux weakening control strategies is used to implement the constructed non-LUTs. A feedback flux magnitude is generated by passing a feedback dq voltage error signals through low pass filters. The resultant flux is used to correct the base flux (i.e. constant torque region flux magnitude) which is computed by a one dimensional LUT.

The simulation results with SVPWM technique in the constant torque region and the flux weakening region show smooth transient and steady state response indicating that the current controller is well-tuned. The results also show well agreement with the off-line calculations of the LMA presented in Chapter 3.

The SVPWM technique when replaced by the LuPWM technique, results in current waveform distortion. This distortion problem is caused by the fluctuation of the command voltage between sectors at the transition points. To be more specific, the undesirable ripple in the electrical angle signal which is used by the PWM algorithm in order to produce the PWM pulses due to the dq voltage ripple causes the sector fluctuations.

If the pulse state in the transition point needs to change from “On”/”Off” to “Off”/”On” then the fluctuation of the sector number will lead to a fluctuation in the pulse state which in turn leads to a distortion in the current waveforms.

It has been proven that by modifying the existing LuPWM technique switching pattern just before the transition point between the current and next sector is reached by the command voltage vector, the distortion problem can be reduced. This is achieved by keeping the state of the pulse of the LuPWM technique constant during the sector transition time until the reference voltage vector completely passing from the current sector to the next sector.

The modified LuPWM technique (Mod-LuPWM) shows smoother current waveforms compared with that of the traditional LuPWM technique when reserving the low CMV achievement of the LuPWM technique compared with the SVPWM technique.

## 6 EXPERIMENTAL VALIDATION

### 6.1 Introduction

The experimental validation of the theoretical and simulation studies obtained in Chapter 5 is described in this Chapter. The required experiments for this validation can be divided into two main tests. The first test is to implement the control scheme presented in Chapter 5 for constant torque and flux weakening control of the IPMSM drive. The second step is to compare the SVPWM, LuPWM and Mod-LuPWM techniques in terms of efficiency improvements and CMV reduction in the IPMSM drive system. The agreement between the simulation and experimental results is then evaluated and discussed.

For these purposes, an experimental test rig has been developed and described in section 6.2. The experimental results are presented in section 6.3 which is divided into three subsections 6.3.1, 6.3.2 and 6.3.3. Section 6.3.1 presents the experimental results of the IPMSM drive in the CTR and FWR regions. Section 6.3.2 compares experimental performance of the SVPWM, LuPWM and Mod-LuPWM techniques. Section 6.3.3 compares the experimental and simulated total power losses of the IPMSM drive. The whole chapter is summarised in section 6.4.

### 6.2 Hardware of the Experimental Work

A laboratory set up has been developed in order to implement the control scheme of the IPMSM drive under study described in Chapter 5. This experimental set up is also utilised to implement the SVPWM, LuPWM and the Mod-LuPWM techniques. The complete laboratory setup (test rig) and its control system is shown in Figure 6.1 [92].

The test rig (see Figure 6.1) mainly consists of an IGBT based voltage source inverter (VSI) with opto-isolation and gate drive circuit [92]. In addition, the direct voltage link (DC-link) power supply  $V_{dc}$  is connected to the DC input side of the VSI via a capacitive filter  $C_{dc}$  in order to reduce the voltage ripple [92].

Basically, the IPMSM drive is equipped by a position sensor (encoder) its outputs are sin and cos signals in the analogue to digital converter ADC range of 0 to  $\pm 2.5V$ . The voltage and current measuring sensors are utilised to provide the instantaneous values of the DC-link voltage and two stator phase currents. The third phase current is internally calculated from the two measured current values [92]. In addition to, the dSPACE control system which is responsible for receiving and sampling the measuring signals of the phase currents, DC-link voltage and the IPMSM rotor position. These signals are then internally utilised by the control algorithm of the IPMSM drive system. This control algorithm is implemented by the dSPACE real-time control desk interface in Simulink/Matlab environment in order to generate six PWM signals to achieve appropriate control of the IPMSM drive. The dead time and inversion board is designed and implemented to inverse and introduce the dead time value to the six PWMs signals generated by the dSPACE. A dynamometer is utilised to maintain the IPMSM drive under study at a fixed speed for operation in torque control mode. The components of the test rig and its control system are described in detail in the following sections.

### 6.2.1 Inverter

The utilised three-phase VSI consists of six IGBT switches and relevant free-wheeling diode per switch as shown in Figure 6.1. An intelligent power module (Mitsubishi-model number PM300CLA060) is chosen for the suggested test rig (see Figure 6.2). The specifications of this intelligent power module are listed in Table 3.1 which have been taken from its datasheet [96].

Additionally, for protection reasons, an isolated interface circuit (model number BP7B-LB) (see Figure 6.3) [97], which is especially designed to be implemented with the utilised intelligent power module, is employed. The interface board (BP7B-LB) safely delivers the gate drive signals from dSPACE to the intelligent power module (see Figure 6.3) via six opto-coupler IC (model VLA606-01R) (see Figure 6.3).



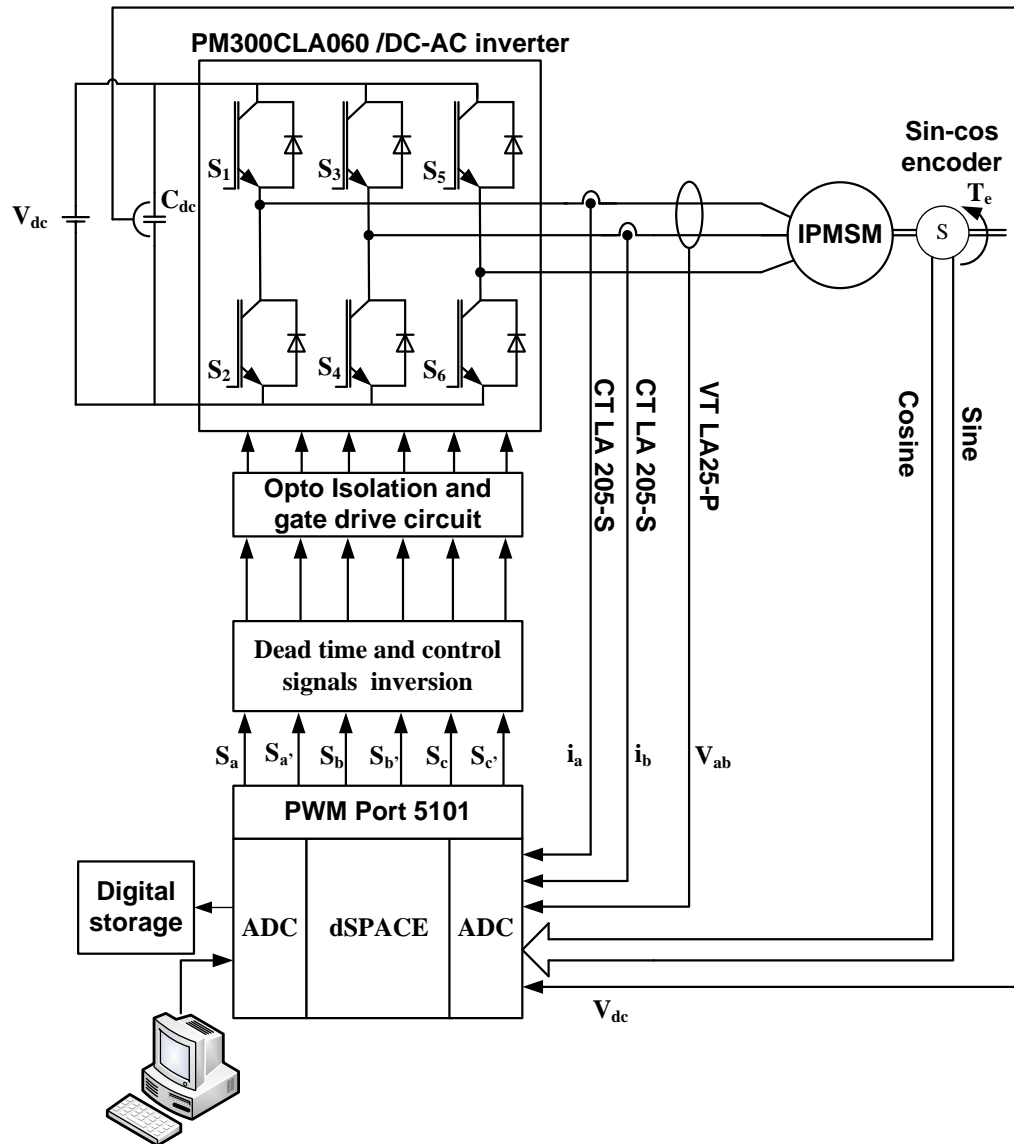


Figure 6.1 Experimental setup of the IPMSM drive.

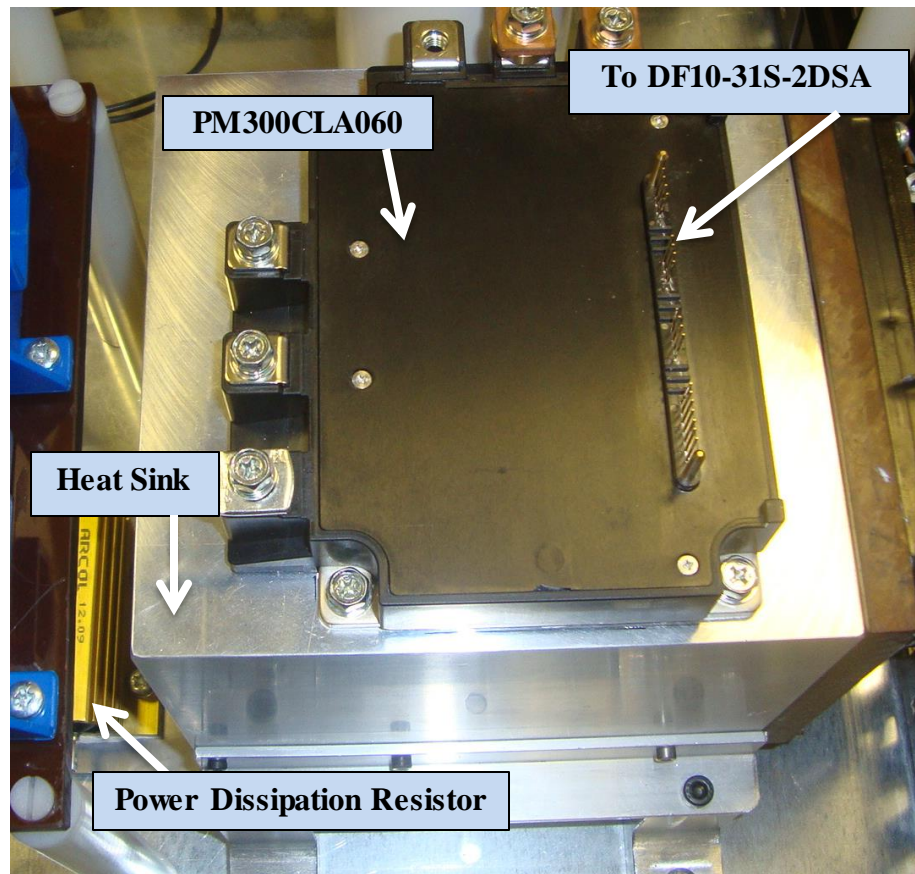


Figure 6.2 PM300CA060 situated on a heat sink.

The BP7B-LB is directly connected to the intelligent power module via a power module connector (model number DF10-31S-2DSA) (see Figure 6.2). The BP7B-LB is also equipped with three DC-to-DC converters (model number VLA106-24151, 24/15VDC) (see Figure 6.3) which are used to supply the high side control power for the intelligent power module. Additionally, a DC-to-DC converter (model number VLA106-24154, 24/24VDC) (see Figure 6.3) is used to supply the low side power control [97]. The intelligent power module may generate a fault detection feedback signal in the ADC range of 0V (i.e. fault) to 5V (i.e. no fault). The fault signal is provided to the dSPACE control system via a low speed opto-coupler which is implemented on the isolating board BP7B-LB. If a fault occurs, the relevant IGBT will be turned off by the intelligent power module [97]. The BP7B-LB layout circuit are shown in appendix A.

Table 6.1 PM300CA060/DC-AC inverter specifications	
Maximum Voltage Rating [V]	600
Maximum Current Rating (at 25° C)[A]	300
IGBT Forward Voltage Drop [V]	2.2
IGBT On State Resistance [ $\Omega$ ]	0.01
PWM switching frequency ( $f_{sw}$ ) [kHz]	$\leq 20$
Dead Time ( $t_d$ ) [ $\mu$ s]	$\geq 2$
Collector-Emitter Voltage ( $V_{CE}$ )[V]	15
Collector Dissipation ( $P_c$ ) (at 25° C) [W]	1041

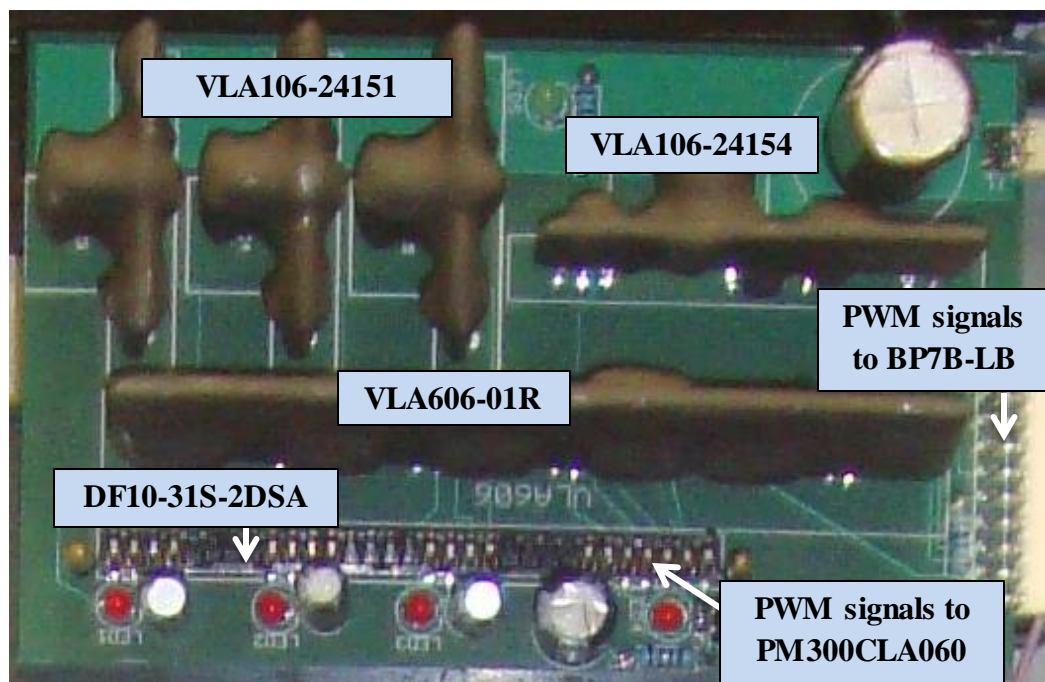


Figure 6.3 Intelligent power module interface BP7B-LB.

The intelligent power module is mounted on a heat sink (see Figure 6.2) with a cooling fan based on 500W losses assuming a temperature rise is 50°C ambient temperature. This heat sink helps to protect the intelligent power module's devices from overheating by dissipating heat into the surrounding area. A programmable grid source/sink DC power supply (model number LAB-GSS32-400-ISR-HMI-USB-CAN/400VDC/±100A) (see Figure 6.4) is used to supply the DC voltage for the utilised intelligent power module. This DC power supply has ability to sink the regenerating

energy from the IPMSM drive system if it operates in the regenerating mode. Two electrolytic capacitors of  $2200\mu F/450V$  are connected to the DC input side of the intelligent power module via a bus bar (see Figure 6.5). These capacitors reduce the ripple of the high-frequency DC-link voltage. A low inductance capacitor of  $0.22nF/1250V$  is connected to DC-link to maximize the intelligent power module switching frequency. When the inverter is disconnected from the power supply, the storage energy in the DC link voltage capacitors is dissipated using  $1.2k\Omega$  resistor as shown in Figure 6.2 .



Figure 6.4 The DC link voltage power supply.

### 6.2.2 PWM Control Signals Dead Time and Inversion Board

Dead-time control is achieved using the analogue circuit shown in Figure 6.6, which is connected at the output of the dSPACE PWM generator. The circuit utilises an inverter chip (model number 74HC14) to add a fixed time delay to the rising edge of the respective PWM signal. The dead-time is adjusted using the variable resistor RV3, whilst simultaneously measuring the TOP and BOTTOM gate drive signals at the



terminals on the power module for each half bridge circuit. The complete dead time and inversion board is shown in appendix A.

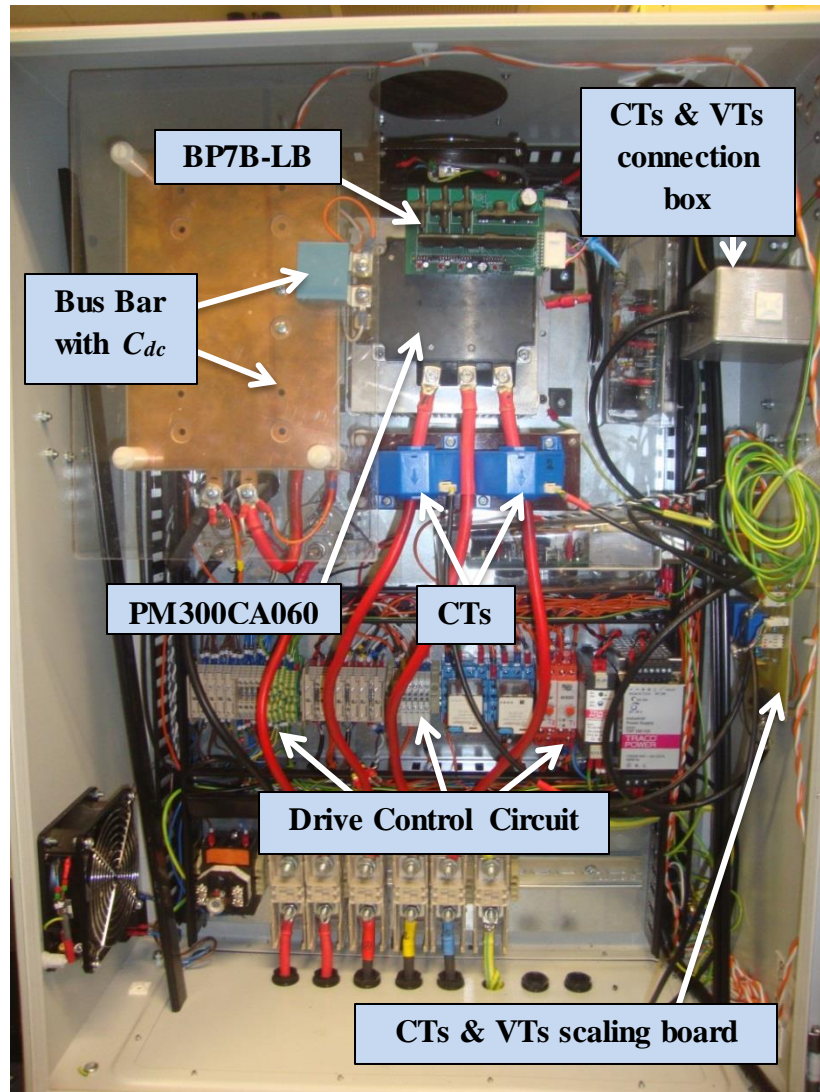


Figure 6.5 Developed drive system for IPMSM drive.

### 6.2.3 Voltage and Current Transducers

The feedback IPMSM currents need to be accurately measured for controlling the inverter. For this purpose, Hall Effect current transducers (CTs) (model number LEM LA205-S, bandwidth DC-100kHz) are employed as shown in Figure 6.7 (a). As the employed IPMSM phase windings are Y-connected, only two phase currents are

measured and sampled. The third phase current is internally computed via the Kirchoff circuit law. The DC link and phase voltages are measured using Hall Effect voltage transducers (VTs) (model number LV25P) (see Figure 6.7 (b)).

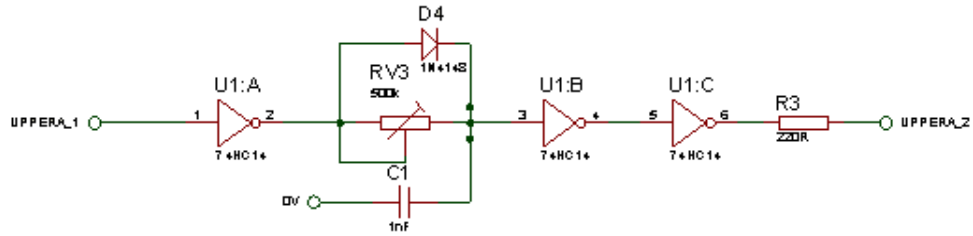


Figure 6.6 PWM dead time and inversion circuit for upper switch of phase “a”.

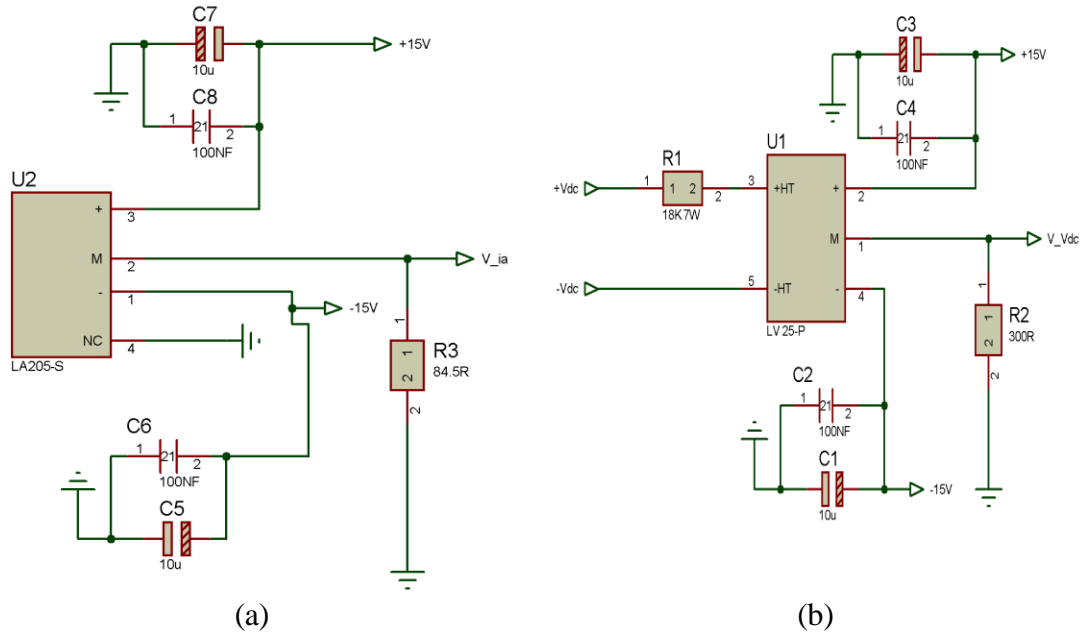


Figure 6.7 (a) Current transducers scaling circuits, (b) Voltage transducer scaling circuit.

The input to the CTs is 0-120A (the IPMSM drive maximum phase current). As dSPACE input voltage is limited to 5/10V, the output measuring voltage at terminal  $V_{ia}$  Figure 6.7 (a) is scaled between 0-5V by a resistor R3 of 84.5Ω/0.6W. The input voltage range to the VTs is 0-120VDC (IPMSM Maximum DC-link voltage) where the

primary resistor  $R_1$  of  $18k\Omega/3W$  is used to ensure that the primary current at maximum voltage (120V), will not exceed  $10mA$ . The measured output voltage at terminal  $V\_Vdc$  is scaled between 0-5VDC using a resistor  $R_2$  of  $300\Omega/0.25W$ . The current and voltage transducer measured signals are delivered to the dSPACE via a first-order unity-gain low-pass-filter circuit (see Figure 6.8) with a cut-off frequency of  $3 kHz$ . This value is selected as about 10 times of the maximum operating fundamental frequency of the tested IPMSM (225Hz at 4500rpm). This circuit is implemented in the drive enclosure using the CTs and VTs connection box, Figure 6.5. The layout of the CTs and VTs scaling circuit is provided in appendix A.

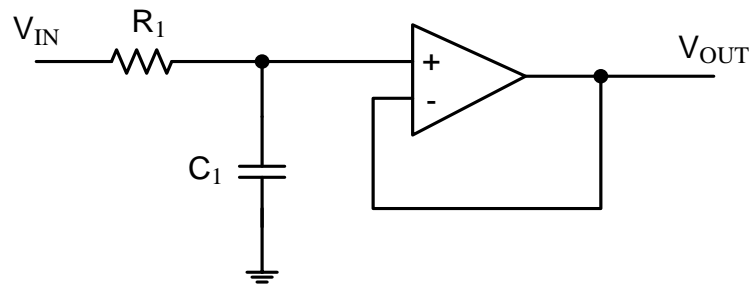


Figure 6.8 First-order unity-gain low-pass-filter.

#### 6.2.4 Inverter Power and Control Circuits

The power circuit of the developed inverter is shown in Figure 6.9. For protection purpose, the power circuit is fed from the mains input through an isolation switch (Isolator, see Figure 6.9) and five fuses (F1 to F5). Four power supplies units (PSUs) are used to supply the different circuits of the inverter where linear PSU ( $\pm 12/1A$  or  $\pm 15/1A$ ) is used to supply the CTs and VTs. Additionally, a switching mode PSU (24VDC/15A) is used to supply the inverter control circuits shown in Figure 6.10 and Figure 6.11, respectively. The isolated interface circuit (BP7B-LB) of the intelligent power module is fed by two power supplies which are a linear PSU ( $\pm 12/1A$  or  $\pm 15/1A$ ) and a switch mode PSU (5A/5A). The linear power supply is used to feed the DC-DC converters (VLA106-24151, 24VDC/ 15VDC) of the isolated interface circuit (BP7B-LB), Figure 6.3. The switch mode PSU (5V/5A) feeds the low side of PWM signals to

the isolated interface circuit. In addition, two fans are employed to circulate the air inside the inverter enclosure to keep it cooled (see Figure 6.9). The inverter control circuit is responsible for safely connect/disconnect the DC-link voltage power supply to the VSI through the DC-link capacitors (C1 and C2, Figure 6.11) which are implemented on the bus bar (see Figure 6.5). The control circuit consists of two parts as shown in Figure 6.10 and Figure 6.11, respectively. The functions of these two control circuits are described as follows:

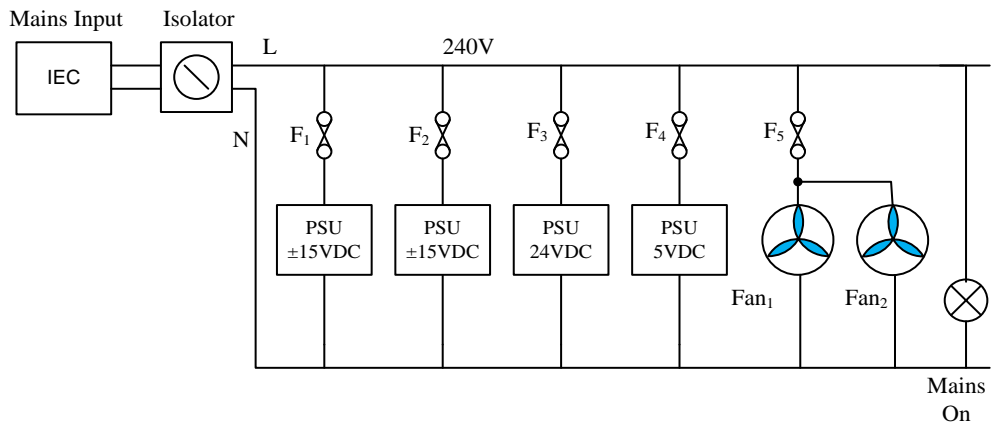


Figure 6.9 Power circuit of the inverter

- Once the drive is connected to the main input as shown in in Figure 6.9, the power supply 24VDC feeds the Stop (R) lamp through a fuse (F) and the normally closed (NC) relay contact  $R_{L1-3}$ . The lamp Stop (R) is turned “On” indicating that the power is connected properly to the drive power circuit.
- By pressing the Start (G) push button switch, the power supply 24VDC (see Figure 6.10) is connected to timers  $T_1$  and  $T_2$ , and relay  $R_{L1}$ .
- The relay contact  $R_{L1-3}$  (see Figure 6.10) is opened and the Stop (R) lamp is “Off”.
- The relay contact  $R_{L1-1}$  is closed and consequently the relay contact  $R_{L1-2}$  is closed too. The Start (Y) lamp is turned “On” indicating that the drive is properly started.



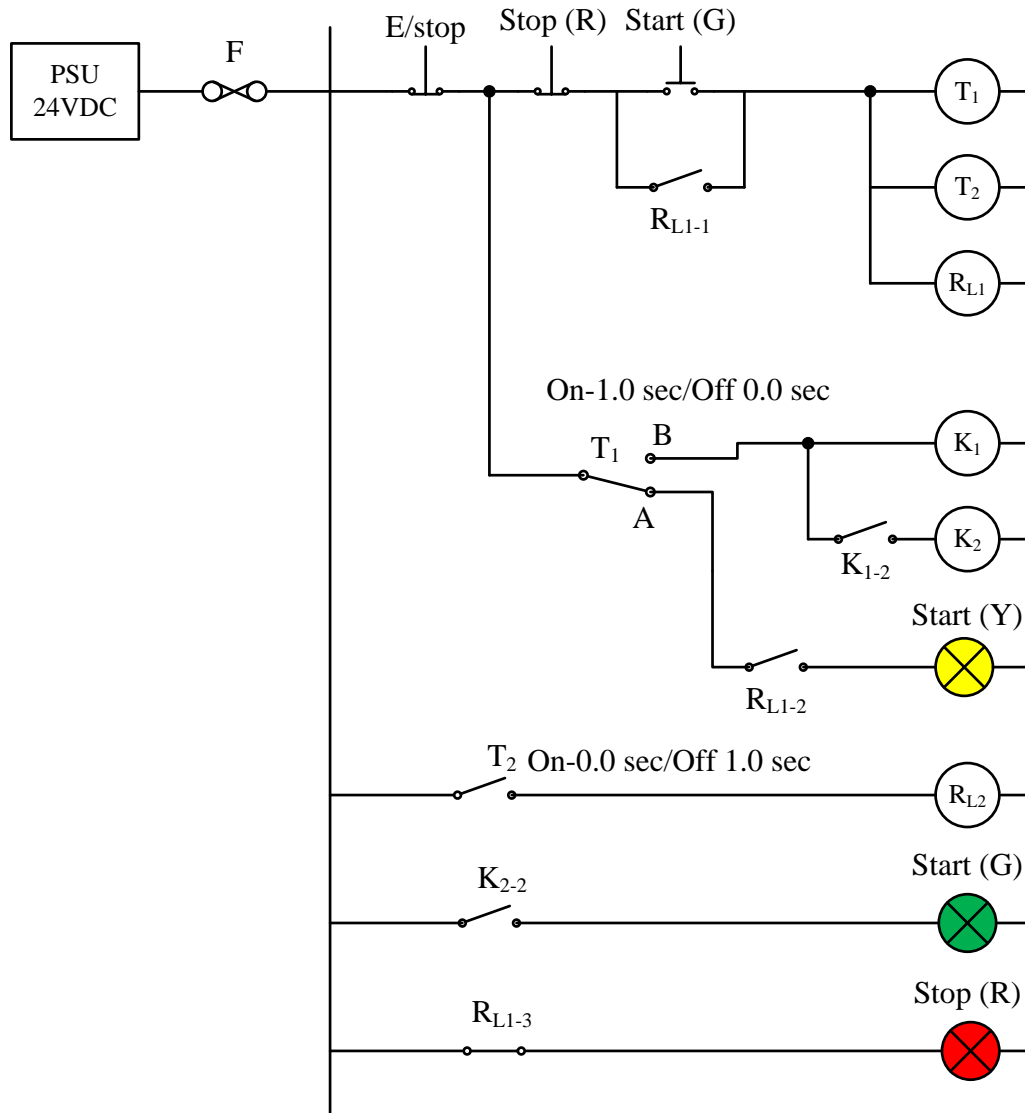


Figure 6.10 Control circuit of the inverter.

- The timer contact  $T_1$  is connected to the “B” position, a Kilovac 200 series contactor is activated and the contact  $K_{1-1}$  (see Figure 6.11) is connected. The positive side of the DC link power supply is now connected to the bus bar (capacitors  $C_1$  and  $C_2$ ).
- The timer  $T_1$  is adjusted to activate the contact  $K_{1-2}$  (see Figure 6.10) after one second from the closing of contact  $K_{1-1}$  (see Figure 6.11). This is because the Kilovac contactor needs about 12A to be activated. However, the 24VDC power supply rated current is about 15A. This means that two 24VDC/15A power supplies is required in order to activate the two Kilovac contactors utilised in the DC link

which will increase the drive cost. By allowing a delay time of 1 sec between their activation, then the power supply will be able to energize Kilovac contactor one by one therefore no additional power supply is required.

- As  $K_{2-1}$  is now activated (see Figure 6.11), the negative side of the DC link power supply is now connected to the bus bar.

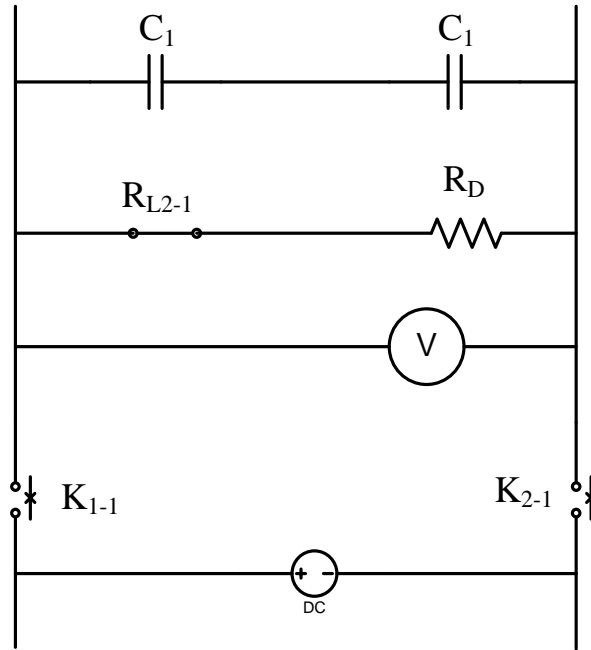


Figure 6.11 Control circuit of DC link capacitor power dissipation resistor.

- The contact  $K_{2-2}$  (see Figure 6.10) is closed and the Start (G) lamp is “On” indicating that the DC-link power supply is connected to the DC input side of the utilised intelligent power module.
- The contact  $T_2$  (see Figure 6.10) is closed and the relay  $RL_2$  (see Figure 6.11) is activated. Consequently, the contact  $RL_{2-1}$  (see Figure 6.11) is opened and no current flow from DC link power supply to the dissipation resistor  $R_D$ .
- The DC link voltage power supply can be disconnected from the bus bar by pressing the Stop (R) normally closed push buttons switch shown in Figure 6.10. The timers  $T_1$  and  $T_2$  and the relays  $RL_1$  and  $RL_2$  are deactivated (see Figure 6.10). The contact  $T_2$  is opened and the relay  $RL_2$  is deactivated. Therefore the contact  $RL_{2-1}$  (see

Figure 6.11) is closed and the storage power in the DC link capacitors  $C_1$  and  $C_2$  is dissipated by the resistor  $R_D$ .

- In emergency cases the inverter can be totally stopped by pressing the E/stop switch (see Figure 6.10).

### 6.2.5 Encoder

An angular magnetic encoder (model number AM256D01\_10) [98] is equipped in the IPMSM machine to measure the instantaneous rotor position. The encoder output signals are sampled into the dSPACE real-time control desk interface in Simulink/Matlab environment, via dedicated ADC as sin and cos waveforms in an ADC range of 0 to  $\pm 2.5V$  as shown in Figure 6.12 .

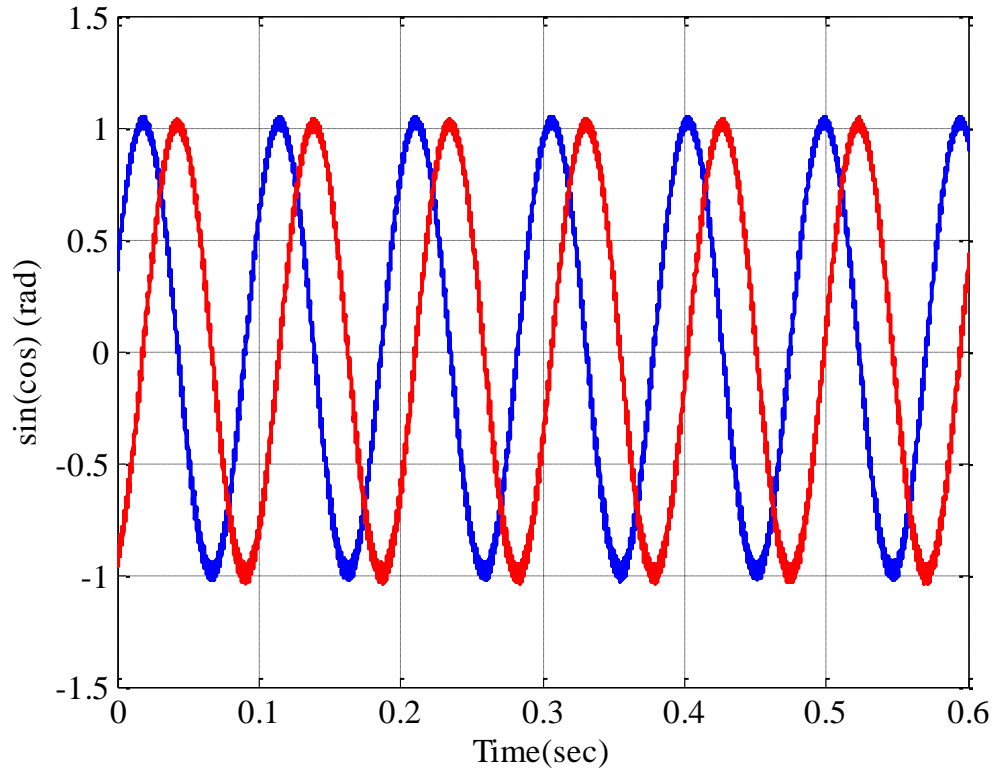


Figure 6.12 sine and cosine encoder signals.

The sin and cos signals are then converted into a representative angle using a Phase Locked Loop (PLL) [99] (see Figure 6.13). In the PLL, the encoder signals (sin and cos)

are transformed into dq-reference frame using Clark-Park transformation [22, 23]. The obtained d-axis signal is equal 1 which is the magnitude of the sin/cos signals. The resultant reference q-axis signal is compared with a zero signal (see Figure 6.13) and the PLL PI controller processes the resultant error. The proportional and integral gains of the PI controller are calculated using the following equations [99]:

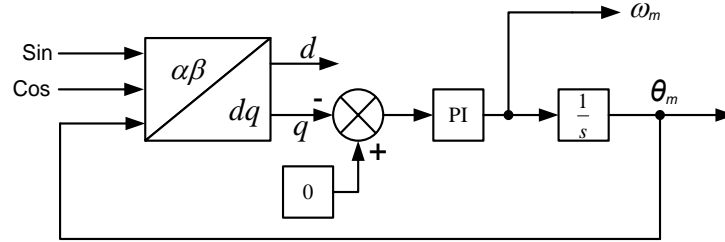


Figure 6.13 Block diagram of the utilised PLL.

$$\omega_c = 1/(\alpha T_s) \quad 6.1$$

$$T_i = \alpha^2 T_s \quad 6.2$$

$$K_p = (1/\alpha)(1/aT_s) \quad 6.3$$

where,  $\omega_c$  is the crossover frequency,  $\alpha$  is a normalized factor,  $T_s$  is the sampling time and  $a$  is a gain which is equal to the magnitude of the input signals to the PLL (i.e. sin or cos) [99]. The gains of the PI controller are listed in Table 6.2 taking into consideration that the gain  $\alpha$  is chosen to be 10 in order to speed up the PLL response.

Table 6.2 Gains of the phase locked loop PI controller					
$\alpha$	$a$	$T_s$ ( $\mu$ s)	$\omega_c$ (Hz)	$K_p$	$T_i$ ( $\mu$ s)
10	1	125	800	800	0.0125

The output of the PI controller is the mechanical speed  $\omega_m$  in rad/sec (see Figure 6.13) which is integrated to the mechanical angular position  $\theta_m$  in rad. As the dq-axis currents are regulated in the control scheme, care has been taken to ensure that the back-emf of the IPMSM machine for Phase “a” is aligned with the angular position derived from the PLL. However, a position delay has been noticed between the magnet position

and the encoder electrical output especially at high speed. This delay is due to an RC filter ( $10k\Omega/10nF$ ) implemented at the encoder output [98]. Therefore, the encoder nonlinearity which can be defined as the difference between the actual position of the magnet and the output from the encoder [98], needs to be compensated. To overcome this problem, the IPMSM drive is driven over its speed range starting from 500 to 4500rpm in a 500rpm step basis by a AVL dynamometer (model number AVL LIST GMBH-APA102/20- 20,000rpm/120KW/120Nm) and every time the resultant electrical angular position is realigned with phase “a” and the offset is recorded. The resultant electrical position offset for the full speed range of the IPMSM drive is depicted in Figure 6.14.

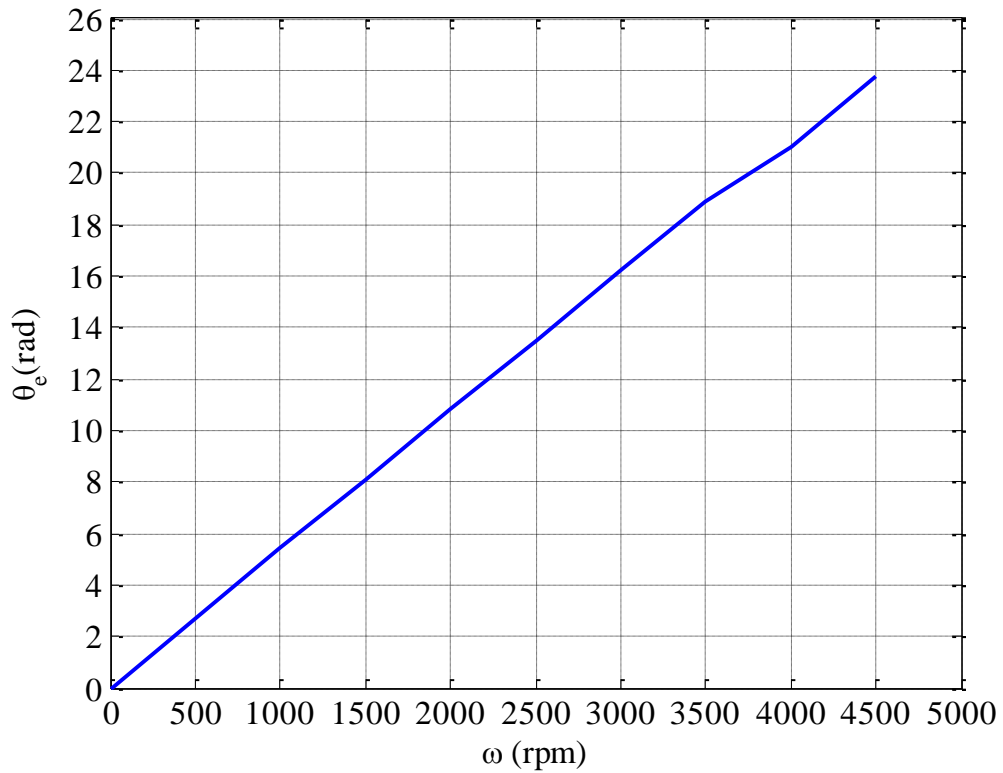


Figure 6.14 LUT of the electrical angular position offset.

The position offset for each speed is stored in a one dimensional LUT. The input to this LUT is the IPMSM mechanical speed and the output is the electrical position offset. The output of this LUT is added to the electrical angular position obtained by the PLL. The final resultant electrical angle is shown in Figure 6.15. Finally, phase “a” of the

back-emf of the IPMSM drive is aligned with the resultant electrical angular position as illustrated in Figure 6.16.

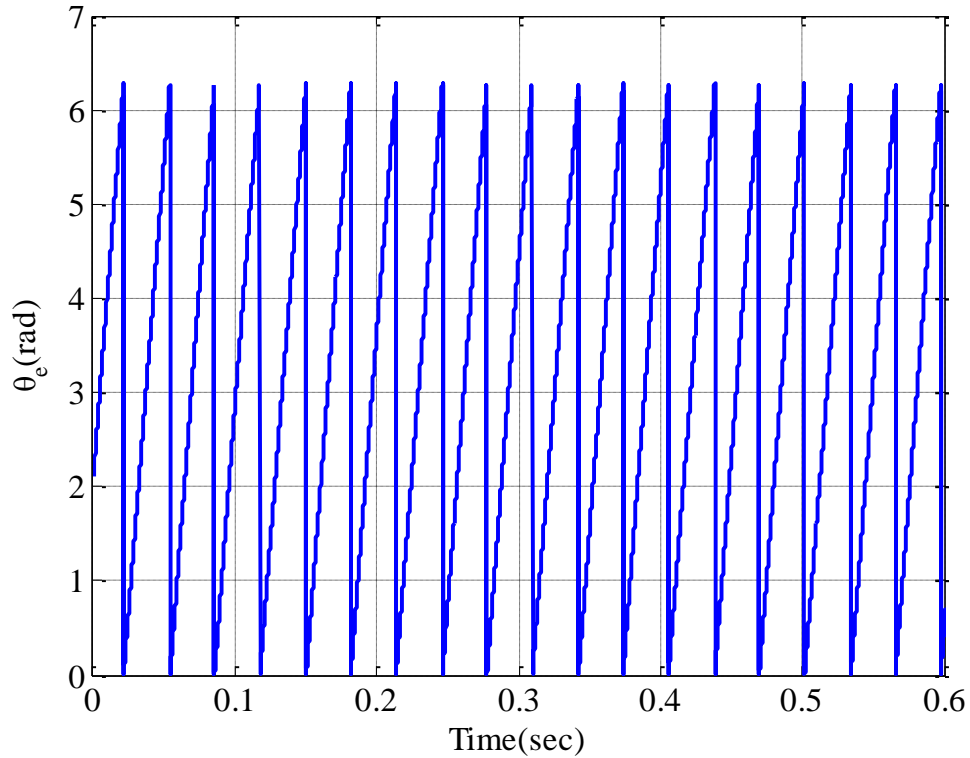


Figure 6.15 Final resultant electrical angular position after adding the delay offset.

### 6.2.6 dSPACE Control System

The control algorithm of the IPMSM drive is implemented using the dSPACE real-time interface in Simulink/Matlab environment (model number DS5001) as shown in Figure 6.17. The dSPACE ADC channels (model number DS2003) receives and samples the CTs, VTs and the sin and cos encoder signals for implementation of the control algorithm. The encoder signals are conditioned by the PLL (see Figure 6.17) after being employed to compute the speed and angular position of the IPMSM drive as described in section 6.2.5. The two stator phase current measured signals are used to calculate the third phase current. The instantaneous three stator phase current values are transformed to the feedback dq-axis current components via Clark-Park transformations [22, 23].

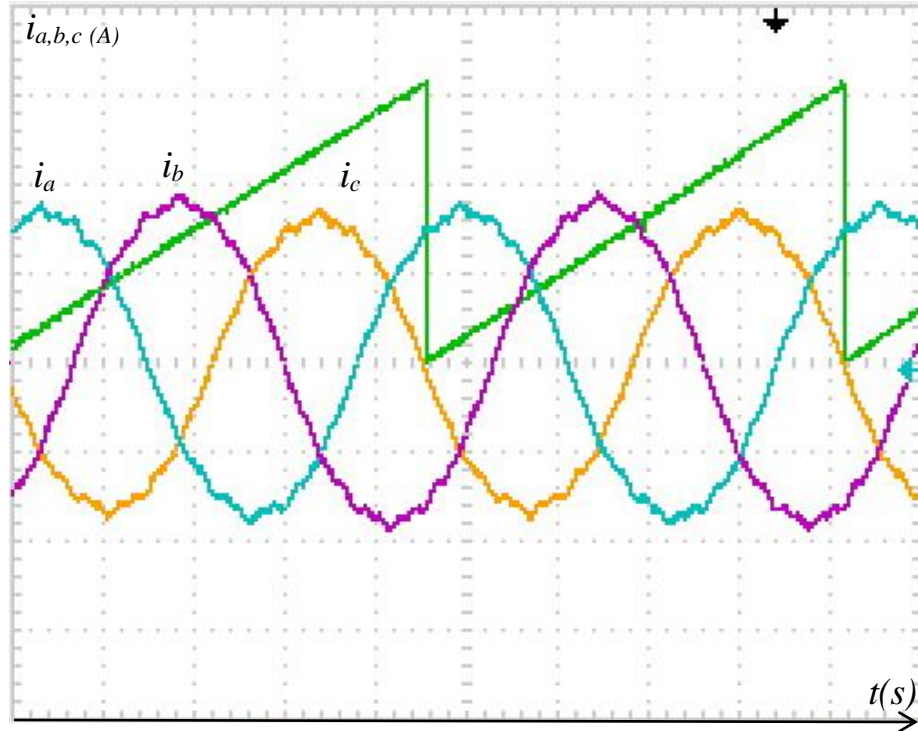
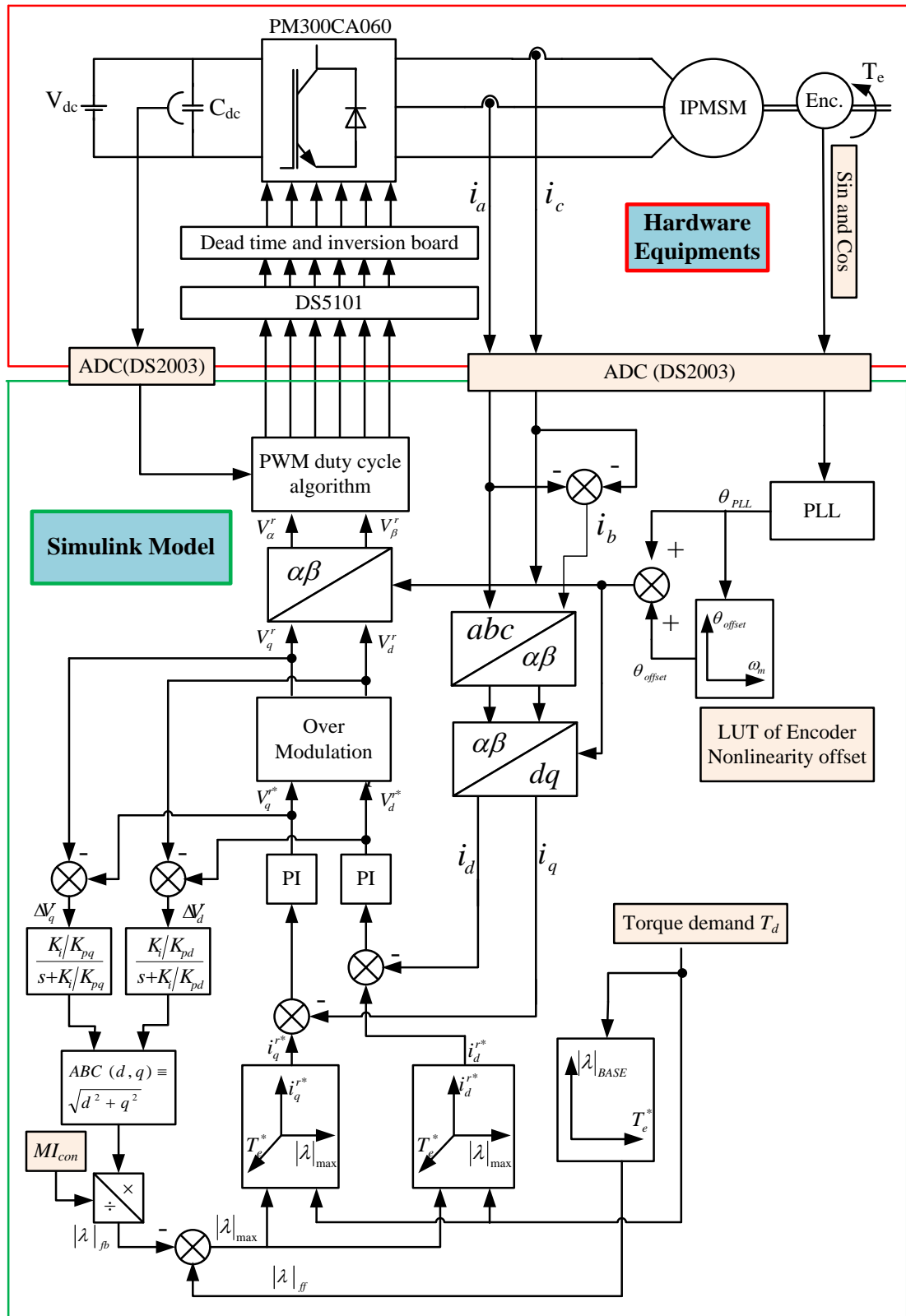


Figure 6.16 Alignment of back-emf of phase  $a$  with the electrical angular position.

The interface block which delivers these measured signals from the ADC to the Simulink model is shown in appendix A. The torque demand  $T_d$  is fed to the dq current demand and the base flux  $|\lambda|_{base}$  LUTs via the dSPACE real-time control desk shown in Figure 6.18. The values of  $T_d$  and the flux  $|\lambda|_{max}$  are utilised by the LUTs in order to generate the reference dq current components (see Figure 6.17). According to the applied torque demand  $T_d$ , the error in the dq current demand generated by non-linear LUTs and resultant feedback dq current components is processed by the  $PI$  current controllers in order to generate the required dq control voltages which are used to calculate the duty cycles of the three phase PWM switching signals to control the inverter gate drives of the utilised intelligent power module. The DC voltage, which is measured at the DC-link voltage terminals via the VT is utilised by PWM duty cycles calculation algorithm in order to compute the modulation index  $m_a$  for the control algorithm. The calculated duty cycles of the six PWM signals are provided to a dSPACE card (model number DS5101), then it generates the PWM switching signals. The generated PWM switching signals are delivered to the isolated interface circuit

(BP7B-LB) (see Figure 6.3) through the dead time and inversion board (see Figure 6.17). The PWM control signals are then delivered to the gate drives of the utilised intelligent power module. The interface block which delivers duty cycles from the Simulink model to the DS5101 is shown in appendix A. Figure 6.19 to Figure 6.23 describes the hardware connections of the test rig. The IPMSM drive is connected to the dynamometer (see Figure 6.19) via a mechanical coupling (see Figure 6.20). An accuracy torque transducer (200Nm rating, 0.2%) (model number 3410) (see Figure 6.20) is employed to sense the instantaneous torque, speed and output power of the tested IPMSM drive (see Figure 6.20). The power analyser (PA) is used to display the current and voltage waveforms, measure the electrical input power, the mechanical output power, and hence the efficiency of the IPMSM drive system (see Figure 6.21). A torque transducer display is used to monitor the produced torque, speed and output power of the tested IPMSM drive, Figure 6.22. The power analyser can also measure the input power to the inverter, and hence quantify the inverter efficiency. The three phase cables of the tested IPMSM are connected to the three output terminals of the VSI inverter through three high precision CTs (see Figure 6.19) of the PA (see Figure 6.21). The dSPACE PWM generated signals are delivered to dead time and inversion board box shown in Figure 6.23. The output PWM signals of this board are connected to the isolated interface circuit (BP7B-LB) (see Figure 6.3) through the PWM interface box (see Figure 6.23). Bayonet Neill-councilman (BNC) cables are used to feed the PWM signals from the output side of the PWMs interface box to the isolated interface circuit and then to the gate drive of the IGBT devices of the intelligent power module.





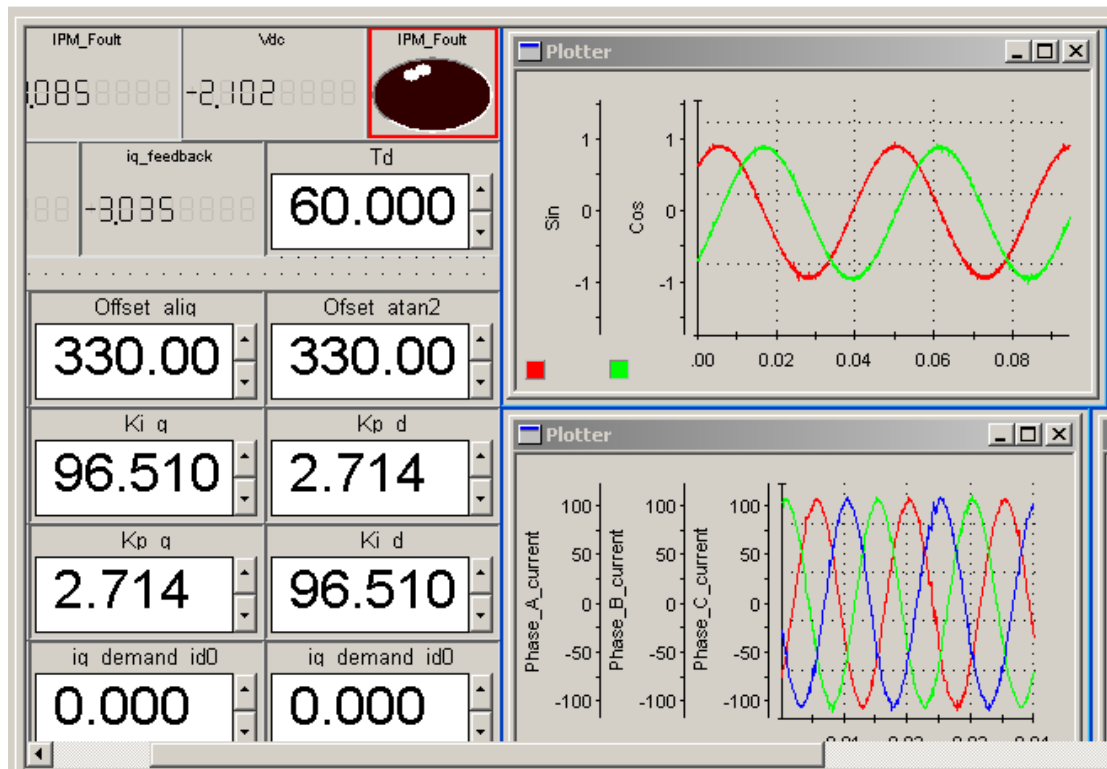


Figure 6.18 dSPACE Real-Time Control Desk.

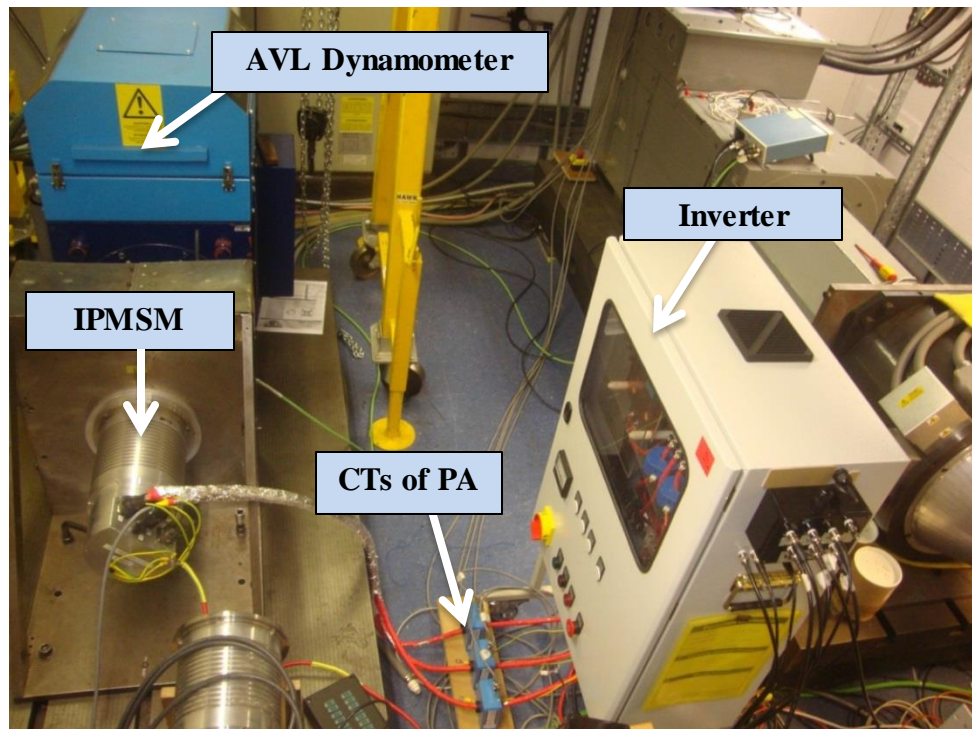


Figure 6.19 Connection between IPMSM, inverter, AVL dynamometer.

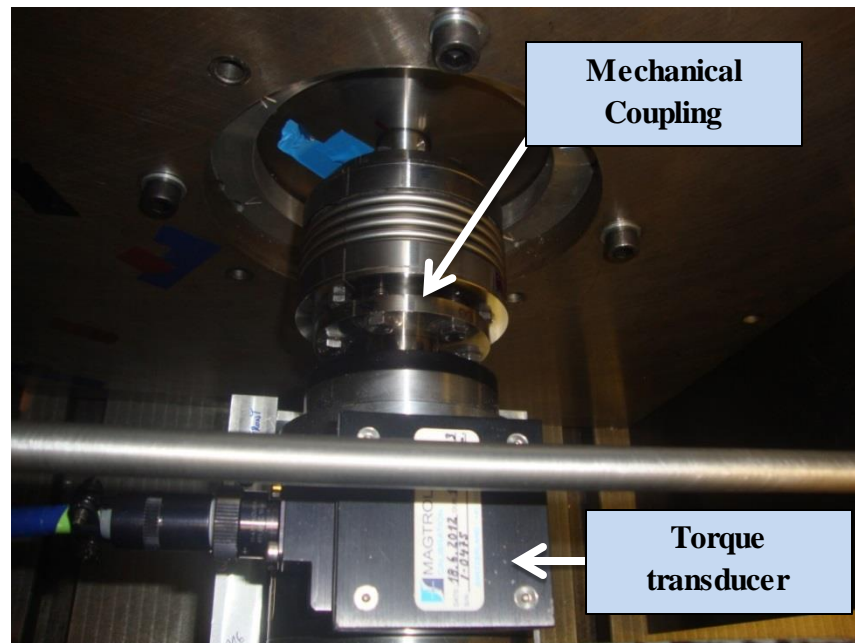


Figure 6.20 Torque transducer and coupling.

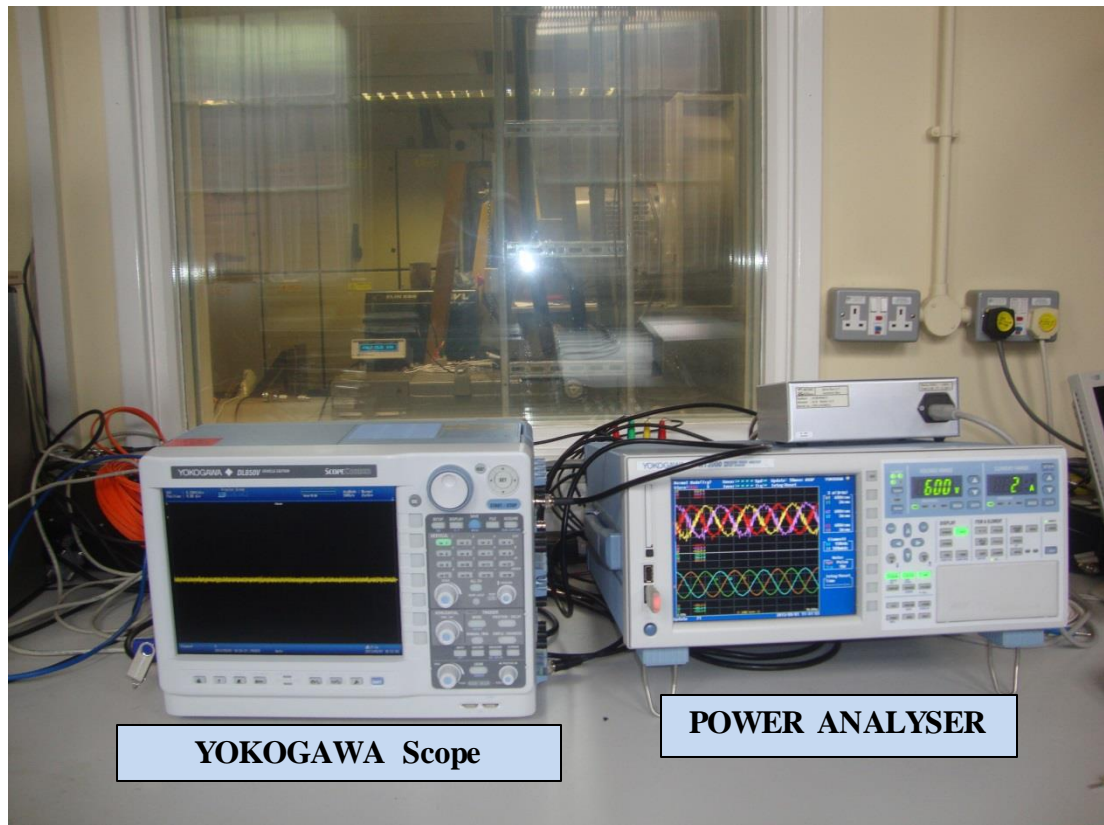


Figure 6.21 Torque waveform and power analyser displays.



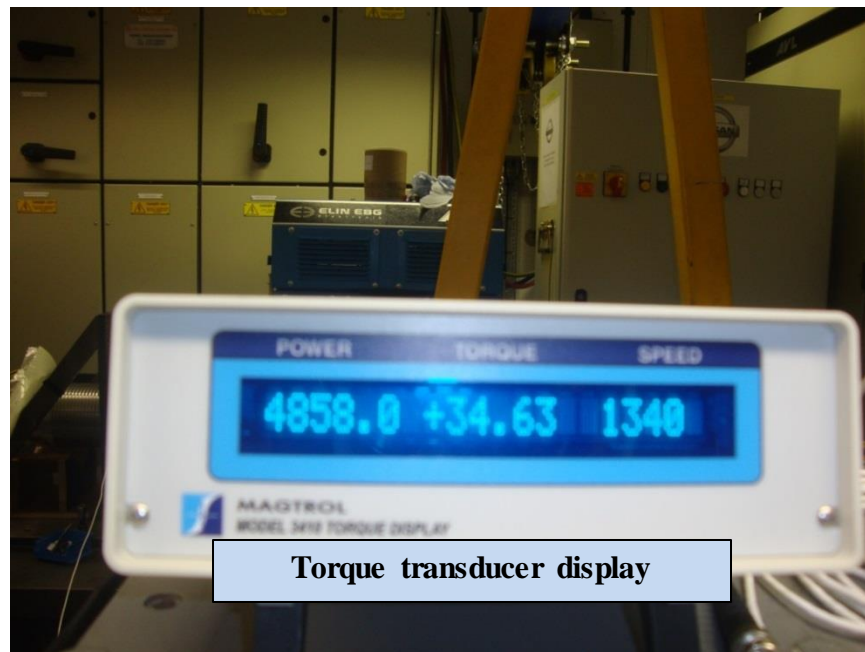


Figure 6.22 Torque transducer display.

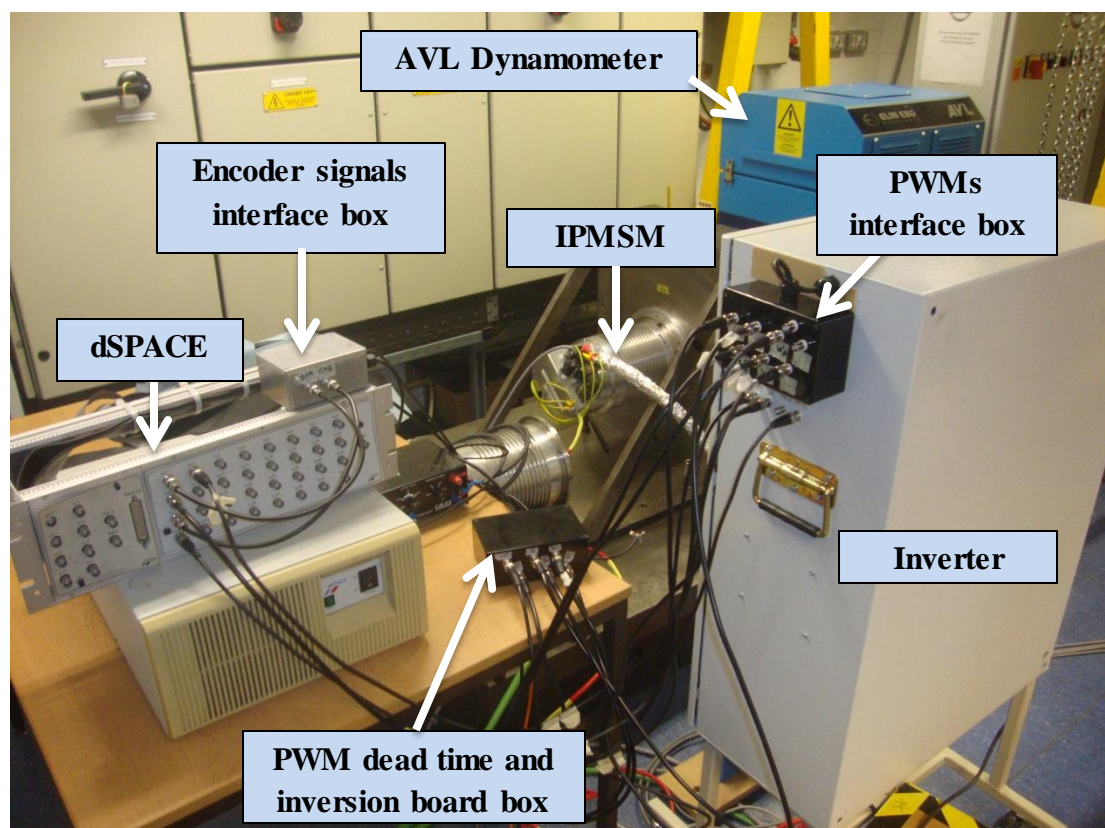


Figure 6.23 Connections between dSPACE, encoder and inverter.

### 6.3 Experimental Results

The simulation results of the studied IPMSM, which are presented in Chapter 5, are experimentally validated in this section. In the early stage of testing, the sinusoidal PWM (SPWM), SVPWM and LuPWM techniques are implemented and the inverter is tested with an inductive load in order to ensure the reliability of this test rig (some of the obtained experimental results by inductive load are given in Appendixes B and C).

The aforementioned test rig (see Figure 6.23) is used in order to run the IPMSM drive in the torque control mode while the AVL dynamometer regulates the IPMSM speed at a fixed value. The tuning of the current controller is done in similar manner of that described in Chapter 5. The obtained experimental results in the CTR and FWR are presented. The simulated and experimental total power losses are numerically compared. Additionally, an experimental comparison between the performance of SVPWM and Mod-LuPWM techniques in terms of drive efficiency and CMV reduction is discussed.

#### 6.3.1 Constant Torque and Flux Weakening Experimental Results

In order to experimentally evaluate the proposed control scheme, the IPMSM drive is tested in the CTR and FWR regions at the same speeds and demand torques that are used in the simulation control scheme presented in Chapter 5. It is noted that the well-known SVPWM technique is implemented to perform the CTR and FWR tests.

The test in the constant torque region is performed according to the following steps:

1. dSPACE is turned on and the Simulink control model is compiled.
2. The torque  $T_d$  is set to zero via the dSPACE real time control desk.
3. The DC-link power supply is turned on and its voltage and current limits are set to 120V (maximum DC-link voltage of the studied IPMSM) and 85A, respectively.
4. For safety reason, the AVL dynamometer speed limit is set to 1370rpm (just beyond the rated speed of the studied IPMSM) using the AVL control panel. The AVL maximum torque is limited to be the maximum torque of the IPMSM drive 70Nm.
5. The AVL is turned on and its speed is increased slowly to 200rpm.

6. The drive is turned on as described in section 6.2.4.
7. A small value of torque  $T_d$  for example  $5Nm$  is applied to the IPMSM and the generated current, voltage and torque waveforms are observed in order to ensure that the test rig is working properly. The torque  $T_d$  is again set to zero.
8. The speed of the AVL is increased slowly from  $200rpm$  to  $1350rpm$ .
9. The torque is slowly increased from  $0Nm$  to  $35Nm$  or above, and the results are recorded.

The sinusoidal current and voltage can be directly obtained by the PA. The torque waveforms can be obtained from the torque transducer by connecting its output to the Yokogawa scope shown in Figure 6.21. The  $dq$  current waveforms are, however, obtained by the dSPACE real-time control desk. Figure 6.24 to Figure 6.29 show the measured results of the IPMSM drive in the CTR at constant speed (rated speed =  $1350rpm$ ) and torque ( $35Nm$  and  $60Nm$ ). The experimental results show good agreements with the simulation results (see Figure 5.8 to Figure 5.13). The minimum operation power losses  $dq$  currents predicted by the LMA, which is presented in Chapter 3, are well-tracked by the non-linear LUTs generated in Chapter 5. To examine the dynamic response of the IPMSM drive under study, a torque demand from 0 to  $50Nm$  in a  $10Nm$  step basis is applied to the machine at the rated speed,  $1350rpm$ . The results under flux weakening control of the IPMSM drive are illustrated in Figure 6.30 to Figure 6.32. It is noted that the IPMSM drive is running at constant speed and varying applied load. The drawn current by the IPMSM drive changes linearly with the load leading to smooth transient and steady state response of  $dq$  currents and the electromagnetic torque  $T_e$  without overshoots or oscillations. This confirms that the control algorithm is well-designed and tuned. The figures also show good agreements with the simulation results depicted in Figure 5.14 to Figure 5.16. Figure 6.32 shows the smooth transient response of phase “a” from  $20Nm/40Nm$  to  $30Nm/50Nm$ . The IPMSM drive is also tested with a negative step torque (see Appendix B).

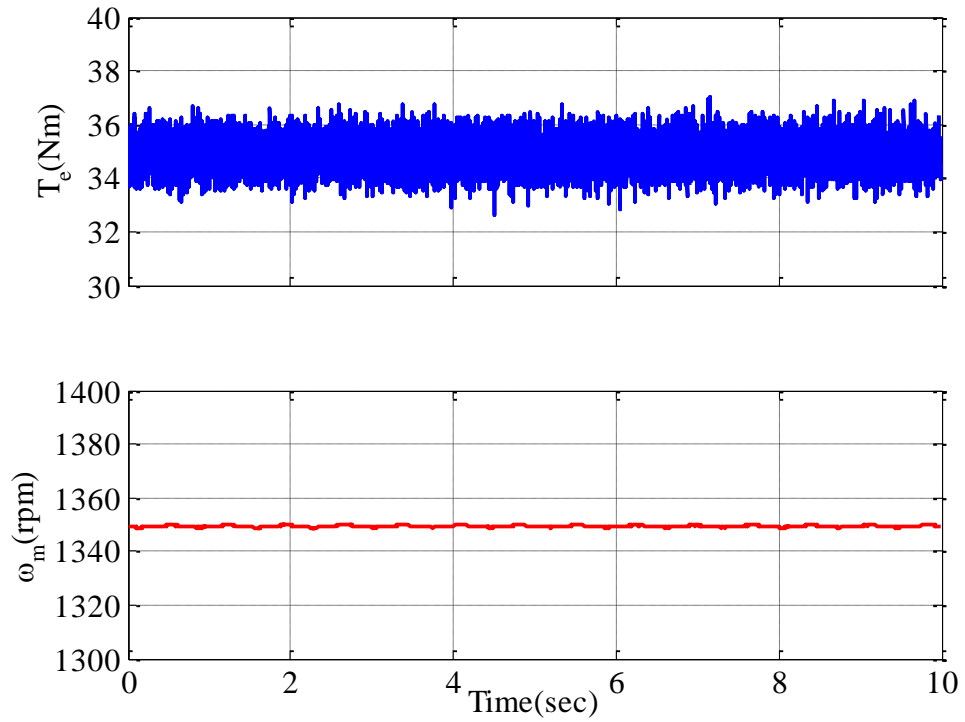


Figure 6.24 Torque and speed steady state response at  $\omega_m = 1350rpm$  and  $T_d = 35Nm$

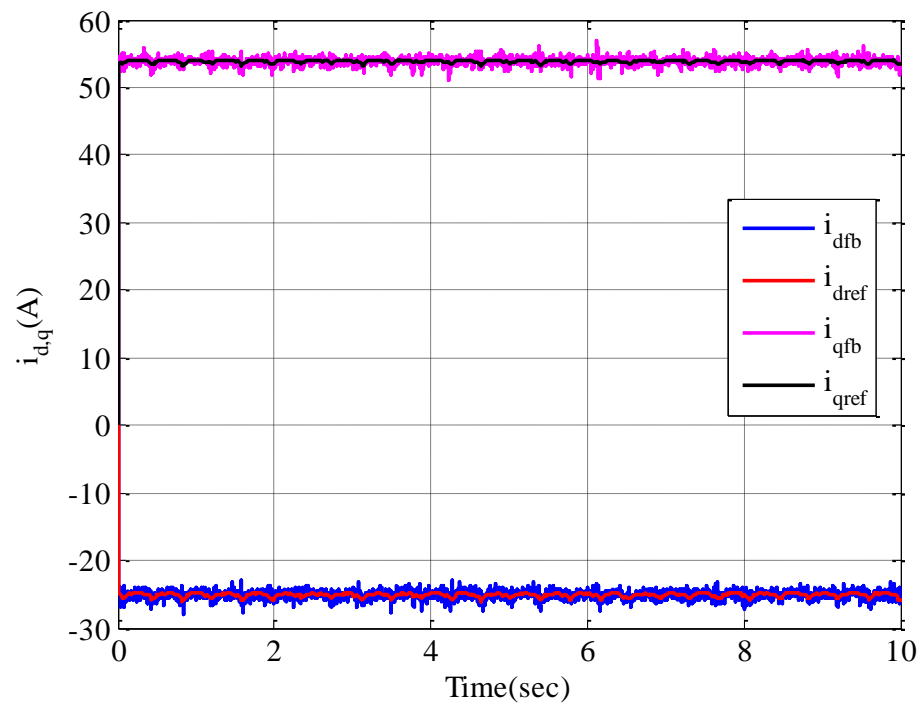


Figure 6.25  $i_d$  and  $i_q$  currents steady state response at  $\omega_m = 1350rpm$  and  $T_d = 35Nm$

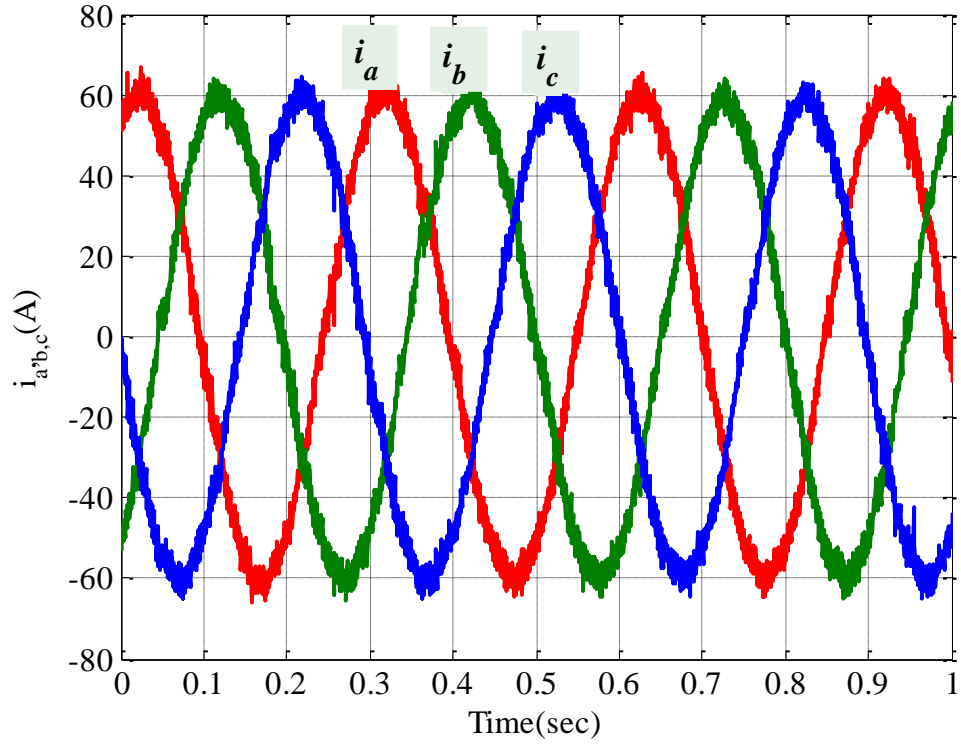


Figure 6.26 Phase currents response at  $\omega_m = 1350rpm$  and  $T_d = 35Nm$

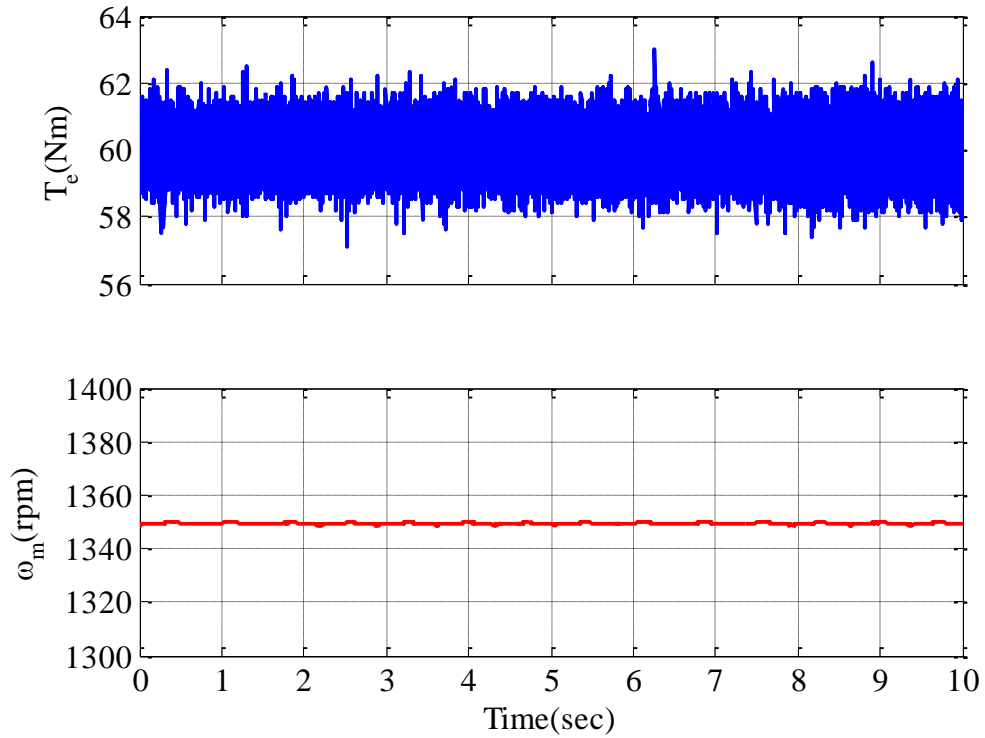


Figure 6.27 Torque and speed steady state response at  $\omega_m = 1350rpm$  and  $T_d = 60Nm$



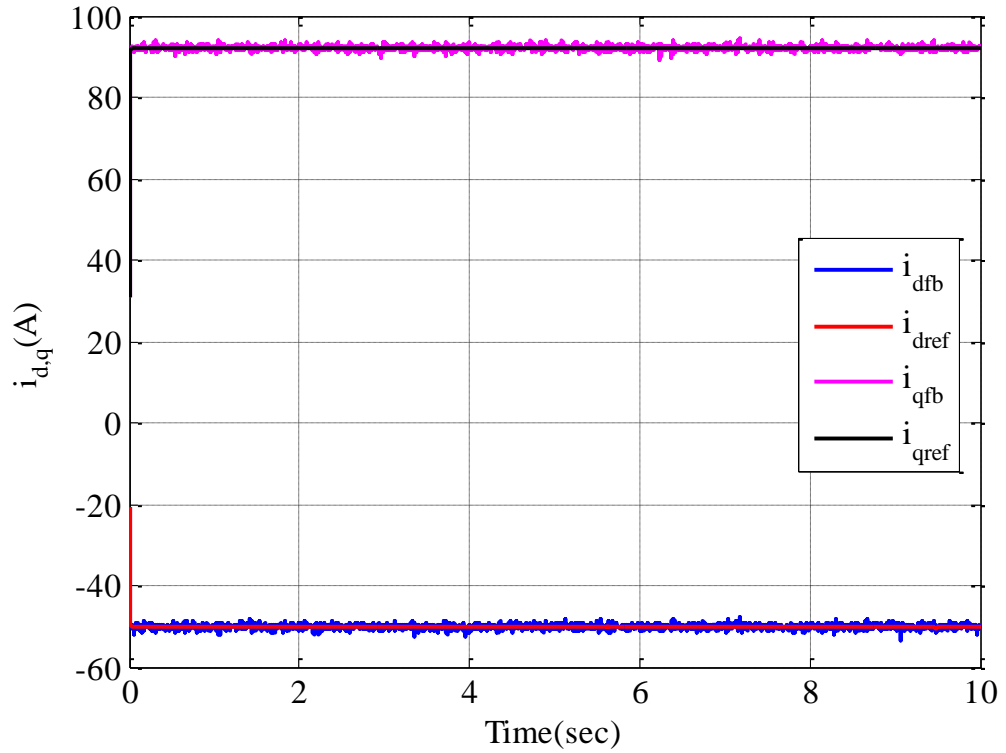


Figure 6.28  $i_d$  and  $i_q$  currents response at  $\omega_m = 1350rpm$  and  $T_d = 60Nm$

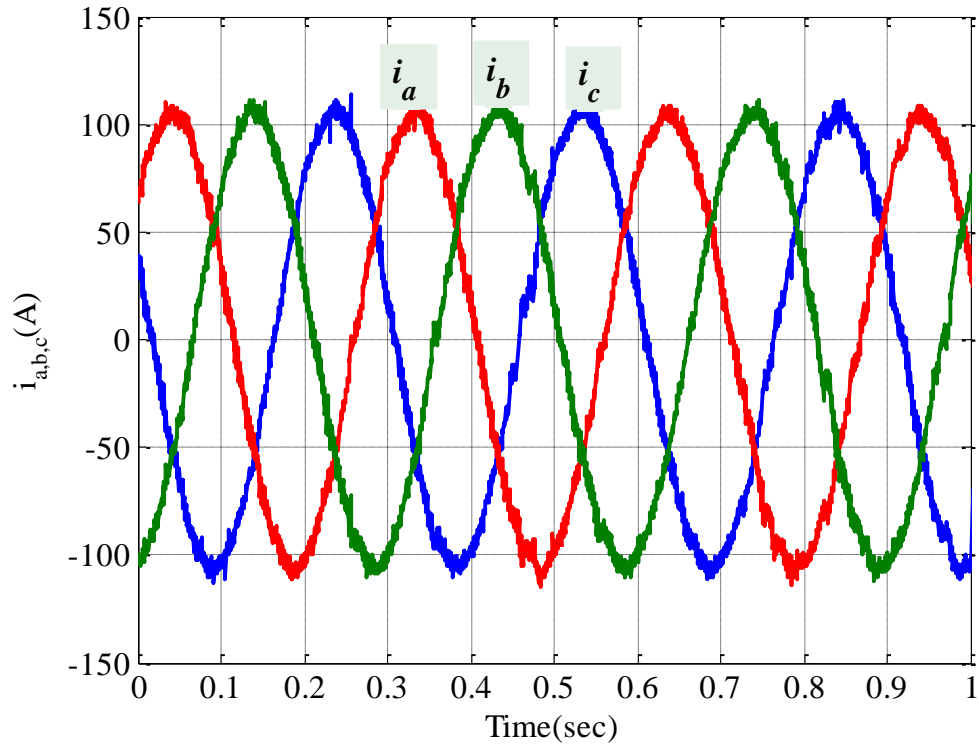


Figure 6.29 Phase currents response at  $\omega_m = 1350rpm$  and  $T_d = 60Nm$

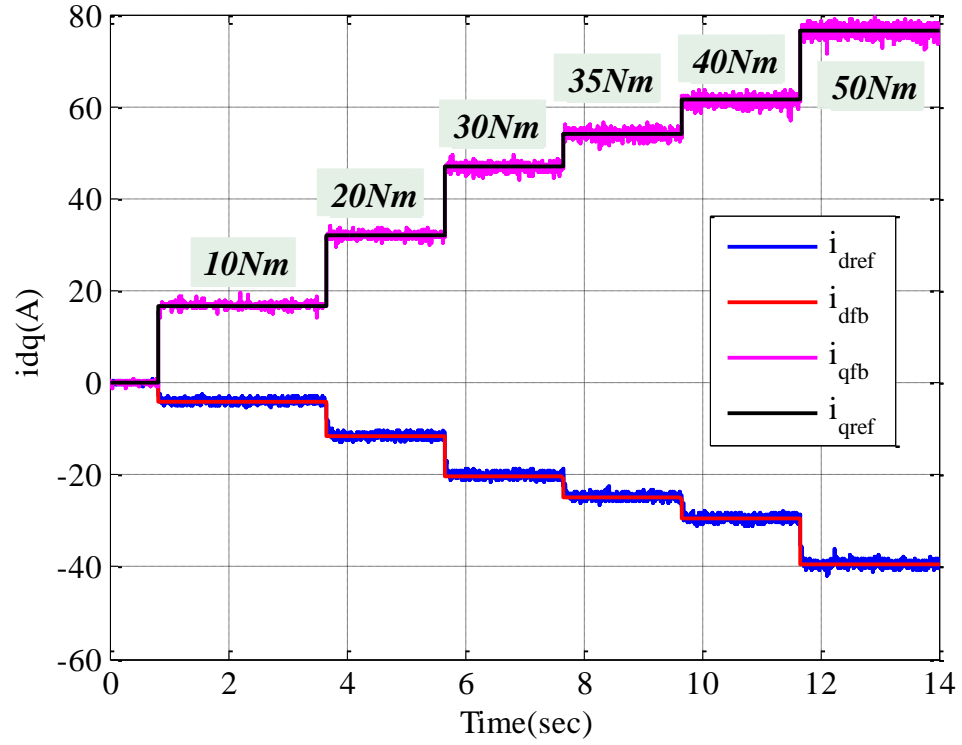


Figure 6.30  $i_d$  and  $i_q$  currents response at  $\omega_m = 1350\text{rpm}$  and  $T_d$  varied from 10 to  $60\text{Nm}$

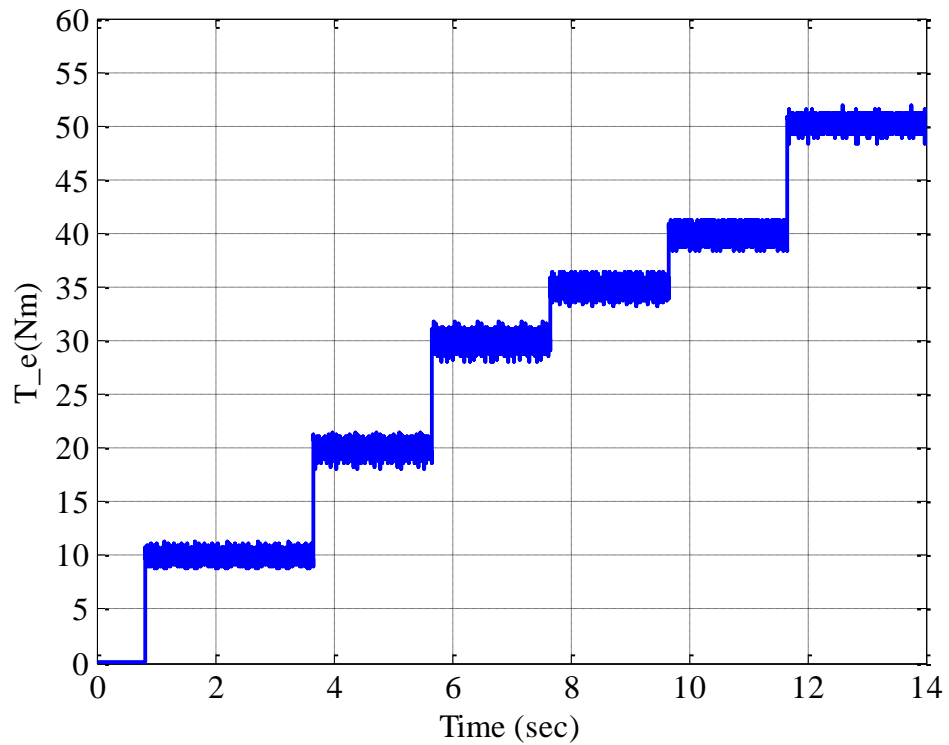


Figure 6.31 Torque response at  $\omega_m = 1350\text{rpm}$  and  $T_d$  varied from 10 to  $50\text{Nm}$

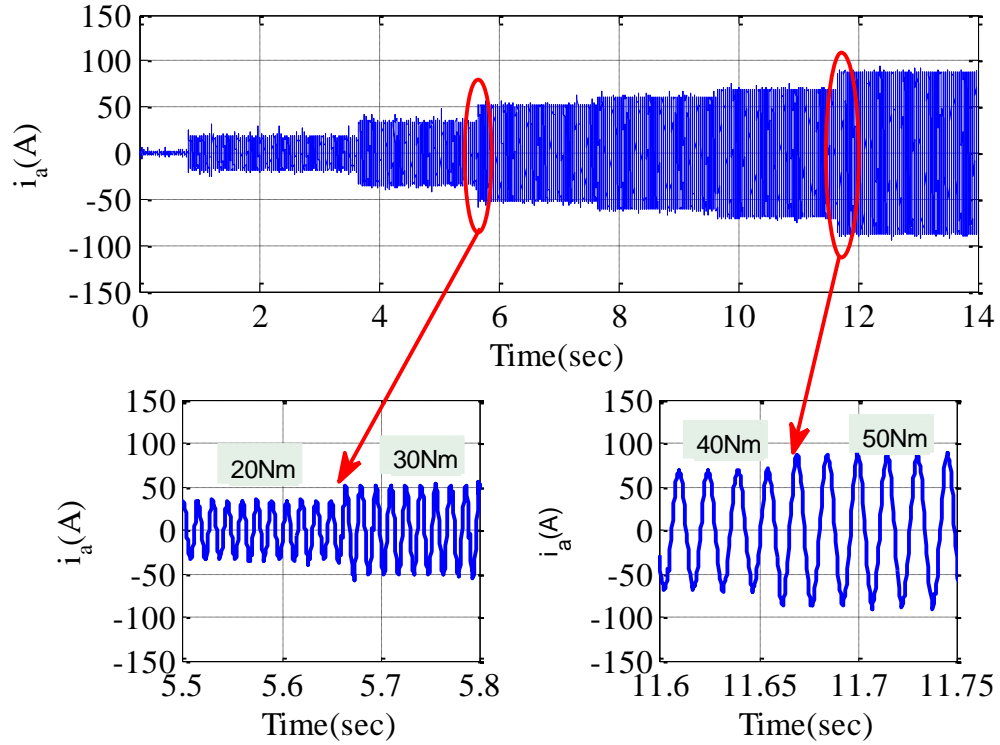


Figure 6.32 Phase current response at  $\omega_m = 1350rpm$  and  $T_d$  varied from 10 to 50Nm

In flux weakening region, the boundaries between the CTR and FWR region should be experimentally defined in order to identify the FW stating point at a given speed and torque. This is achieved according to the following steps:

1. The step from 1 to 7 in the CTR control test is repeated with the AVL speed is limited as 4500rpm (i.e. the maximum speed of the IPMSM drive) and the torque limit is set as 70Nm.
2. The torque is kept constant at 5Nm and the speed of the AVL is increased slowly until the phase voltages recorded by the PA reach to the maximum voltage  $V_m = V_{dc}/\sqrt{3}$  and then regulated by the voltage feedback loop to keep it constant. This phenomenon, when it occurs, indicates that the IPMSM drive enters the FW region.
3. Step 2 is repeated for different torques. The speed value, at which the FW operation of the IPMSM drive triggers, is recorded. The resultant curve that defined the starting point of the FW region for each torque is shown in Figure 6.33. This boundary is clearly defined the MTPA operation region of the studied IPMSM.

Consequently, for a given specific torque, if the motor operates beyond the speed defined by the MTPA curve, it will be in the FW region. It should be noted that the drive should not reach FW operation at  $35Nm/1350rpm$  (peak torque of  $70Nm$  or slightly lower) due to inverter voltage drop at  $1350rpm$ .

The IPMSM drive is then running at different speed under different demanded torques to investigate its responses in the FW control region. The experimental results are depicted in Figure 6.34 to Figure 6.40. Again, smooth response without oscillations can be observed. Also, good agreements with the simulated results presented in Chapter 5 are observed (see Figure 5.17 to Figure 5.22).

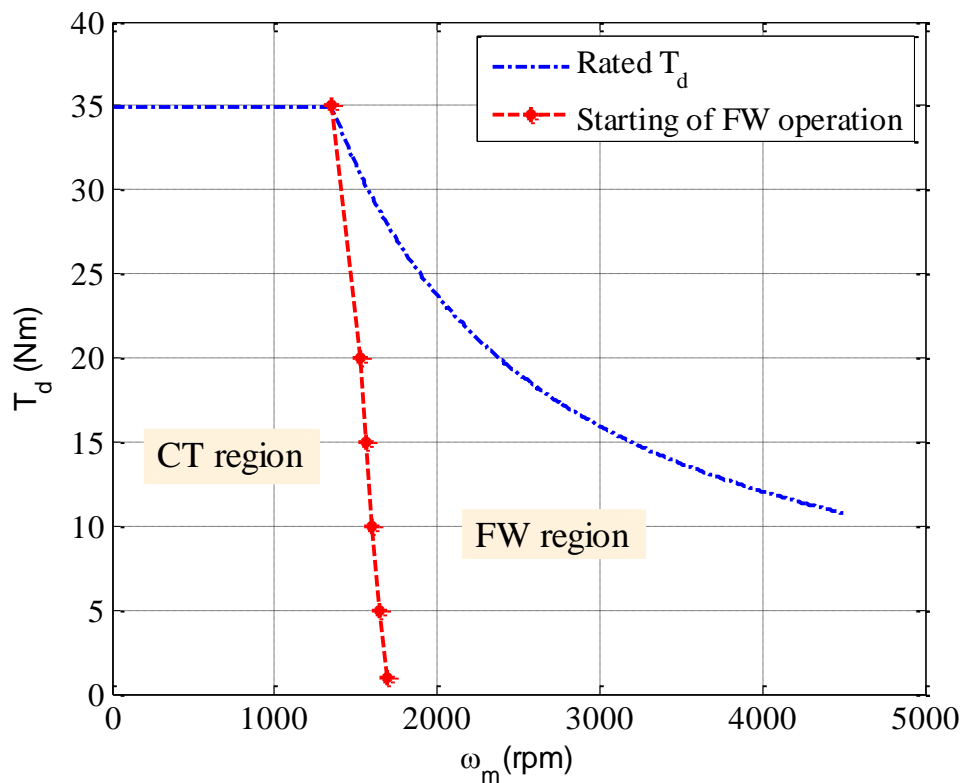


Figure 6.33 MTPA to FW line for  $V_{dc} = 120V$

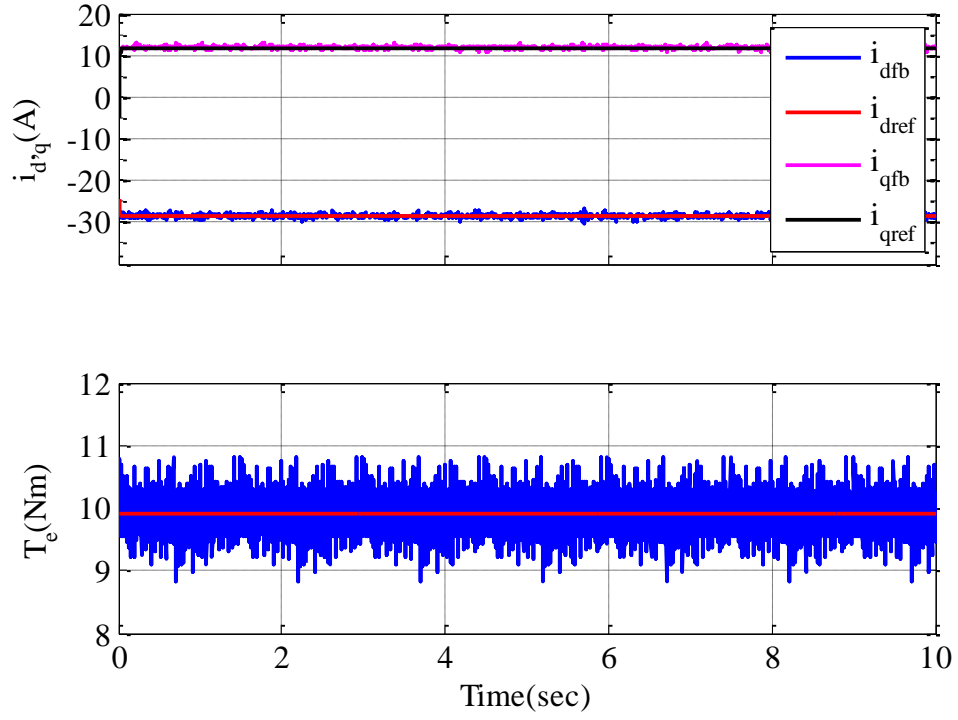


Figure 6.34  $i_d$  and  $i_q$  currents and torque response at  $\omega_m = 2000rpm$  and  $T_d = 10Nm$

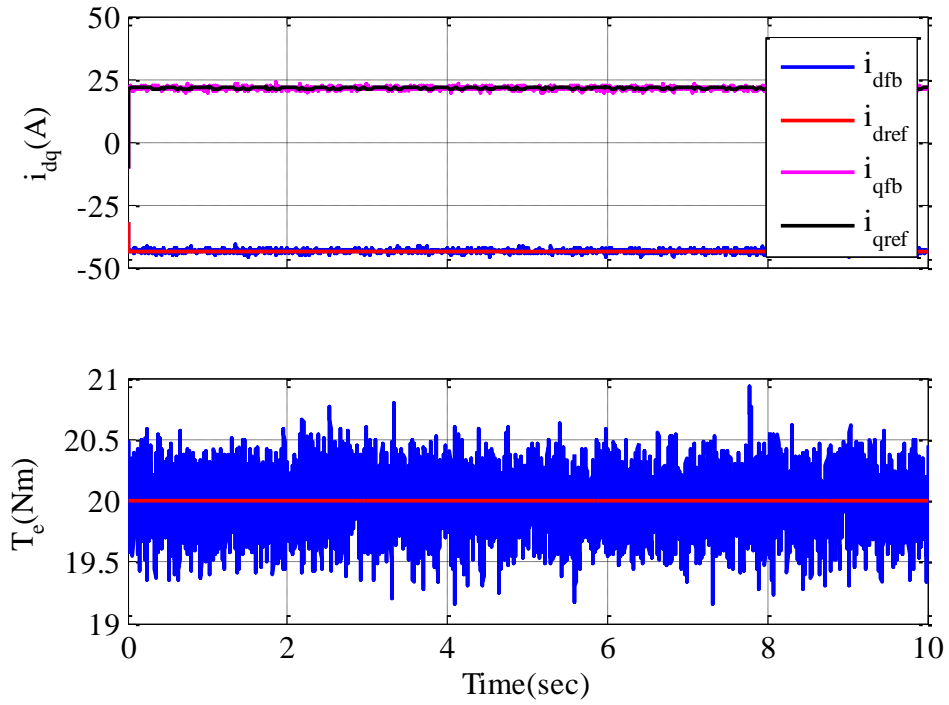


Figure 6.35  $i_d$  and  $i_q$  currents and torque response at  $\omega_m = 2000rpm$  and  $T_d = 20Nm$

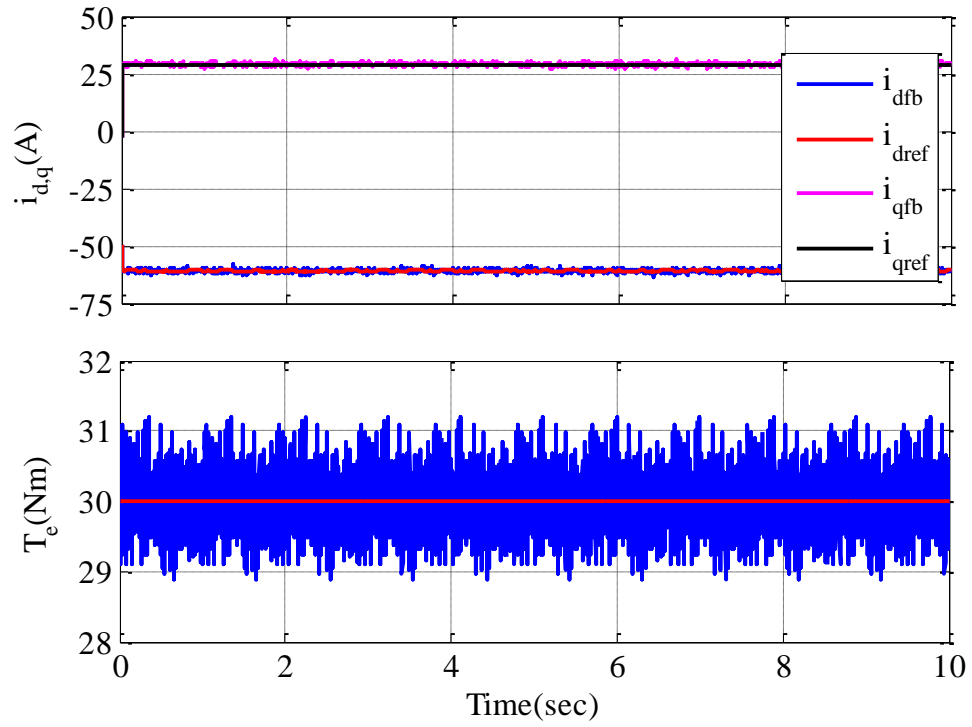


Figure 6.36  $i_d$  and  $i_q$  currents and torque response at  $\omega_m = 2000\text{rpm}$  and  $T_d = 30\text{Nm}$

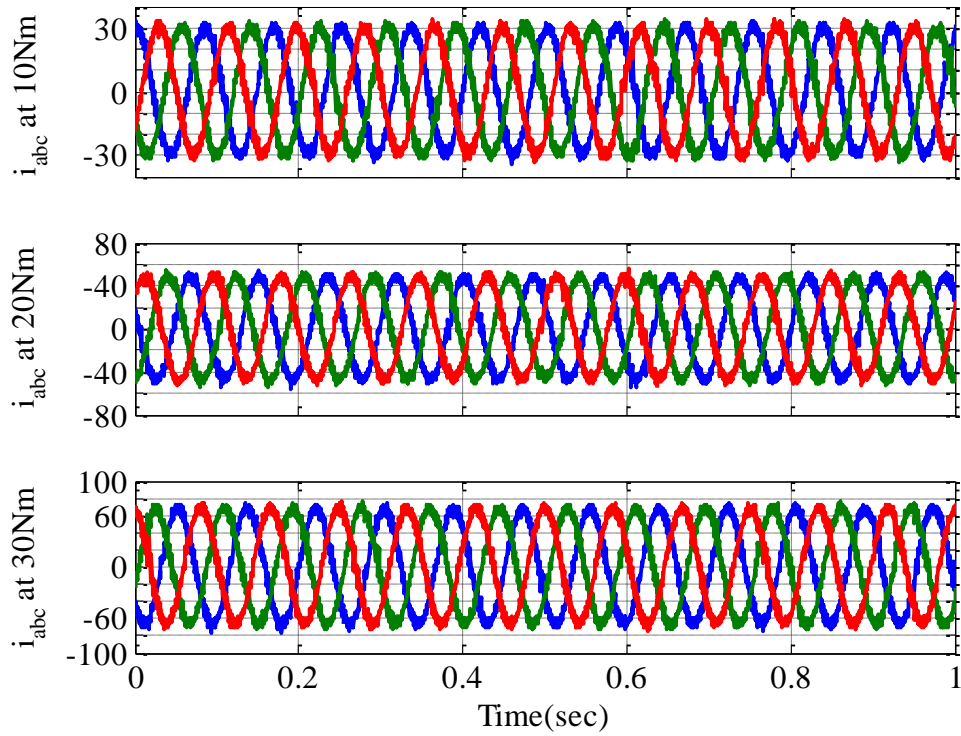


Figure 6.37 Phase currents at  $\omega_m = 2000\text{rpm}$  and  $T_d = 10\text{ Nm}$ ,  $20\text{ Nm}$  and  $30\text{Nm}$

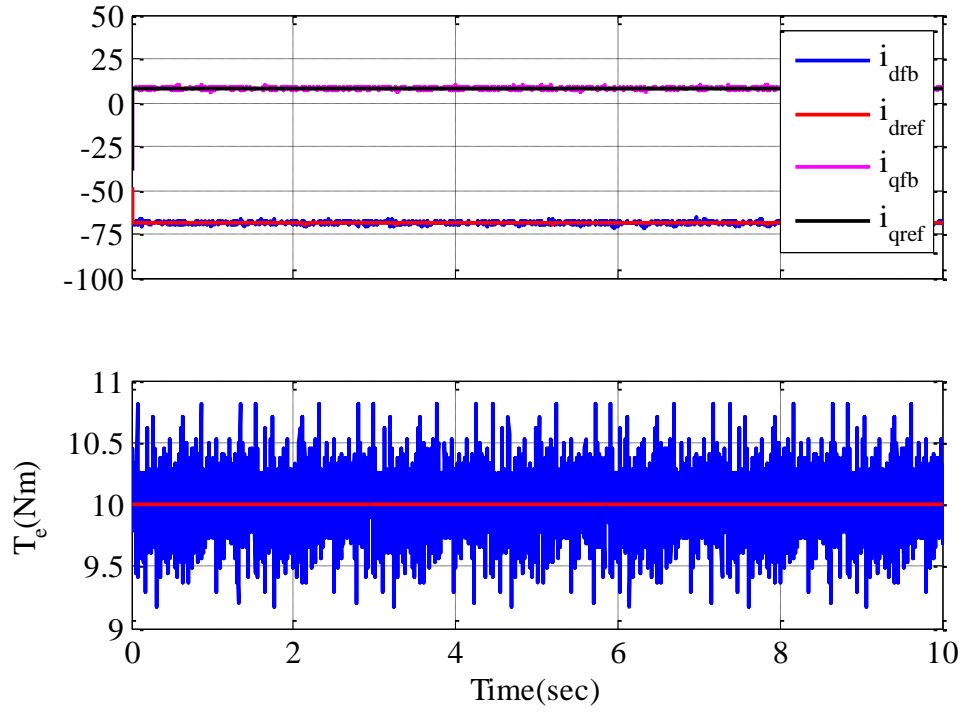


Figure 6.38  $i_d$  and  $i_q$  currents and torque response at  $\omega_m = 3000rpm$  and  $T_d = 10Nm$

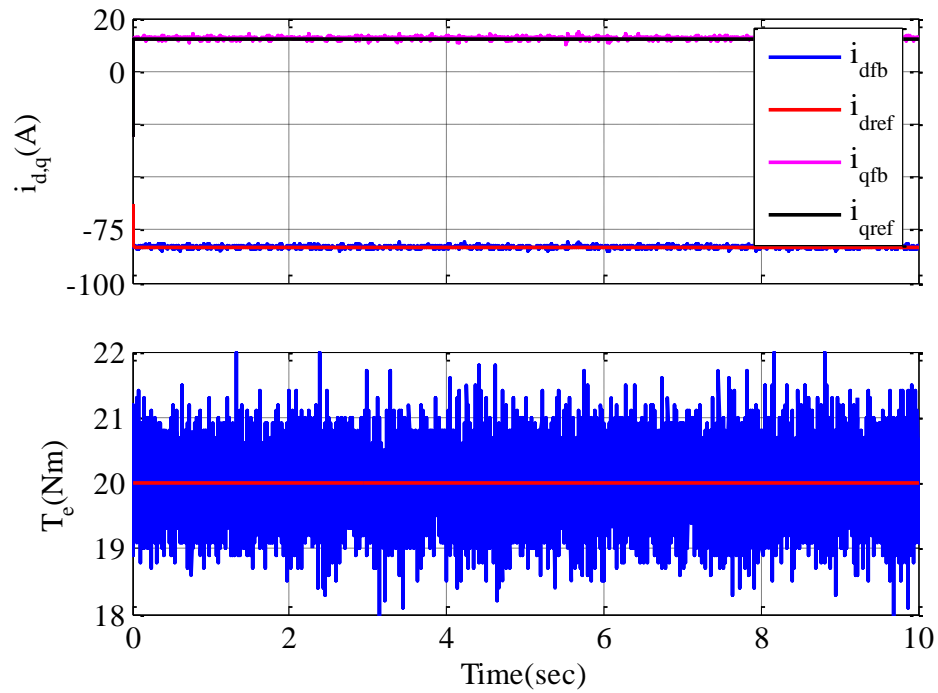


Figure 6.39  $i_d$  and  $i_q$  currents and torque response at  $\omega_m = 3000rpm$  and  $T_d = 20Nm$

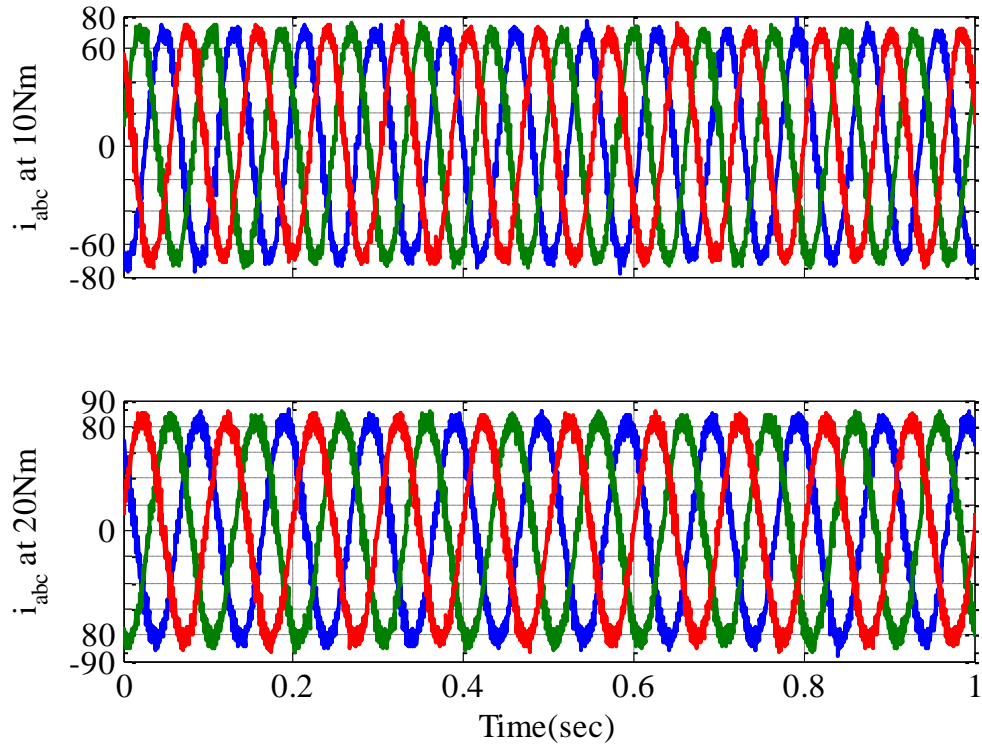


Figure 6.40 Phase currents at  $\omega_m = 3000\text{rpm}$  and  $T_d = 10\text{ Nm}$  and  $20\text{Nm}$

### 6.3.2 Experimental Comparative Study of SVPWM and Mod-LuPWM Techniques

In this section, the performances of the SVPWM and Mod-LuPWM techniques are experimentally compared to validate the simulation results presented in chapter 5.

As mentioned above, the LuPWM technique is tested with the inductive load in the  $L$ - and  $H$ -region and the results are shown in Figure 6.41 and Figure 6.42. It is noted that the phase current waveforms in the low and high modulation region are very smooth where no distortion take place at any time. This is due to the fact that under open loop operation, the electrical angular position is internally generated by a repeating sequence Simulink block in order to be used in the LuPWM algorithm. The angle cannot be generated by the inductive load as it is a stationary load. Therefore, the angle signal is very clean and smooth (see Figure 6.43), and consequently the sector transition of the



PWM pulses happen smoothly. As a result, the distortion in the current waveforms does not take place.

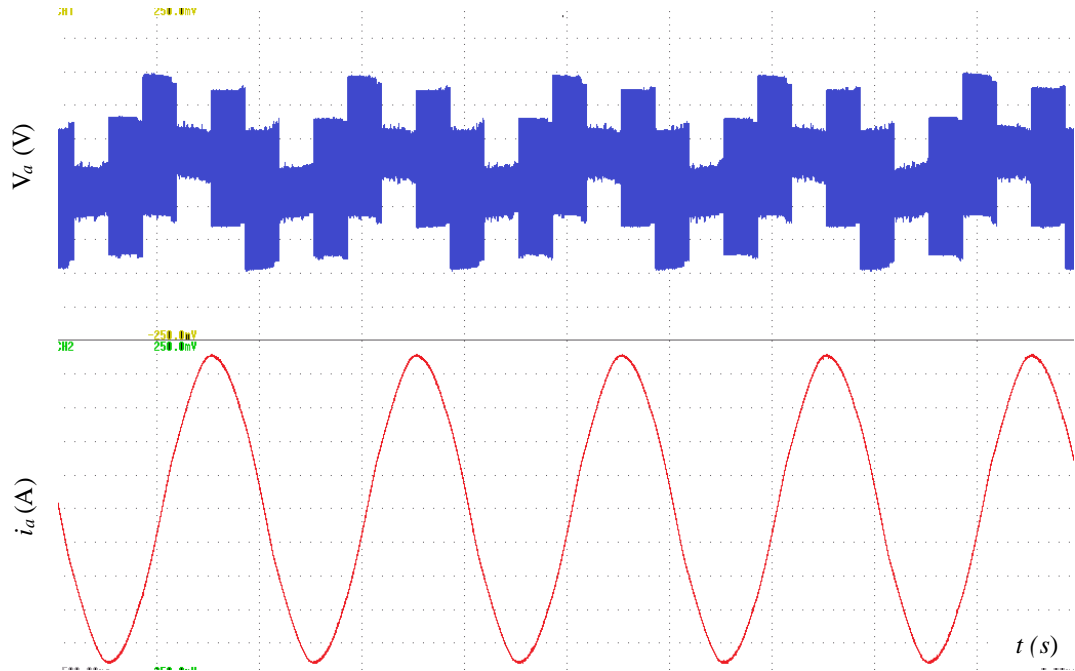


Figure 6.41 Voltage and current phases of the inductive load with LuPWM in the  $L$ -region.

However, it is noted that the simulation comparative study discussed in Chapter 5 considers the traditional LuPWM technique together with the SVPWM and Mod-LuPWM techniques. The LuPWM technique is not included in this experimental comparison as it could not be properly initialized due to the high distortion in the voltage and current waveforms in comparison with the Mod-LuPWM technique (see Figure 6.44). This distortion leads to short circuits of the DC-link voltage power supply. Figure 6.45 shows the DC-link current drawn by the drive at 200rpm and 10Nm (low modulation region  $m_a \leq 0.12$ ) where one can clearly see the short circuit created by this distortion in the DC-link power supply. The generated  $T_e$  in this modulation region is fully distorted as illustrated in Figure 6.46 which compares the torque waveforms produced by the LuPWM and Mod-LuPWM technique. As the drive may be damaged with the short circuit in the DC link power supply, a full test for the LuPWM technique is not considered in the experimental work.

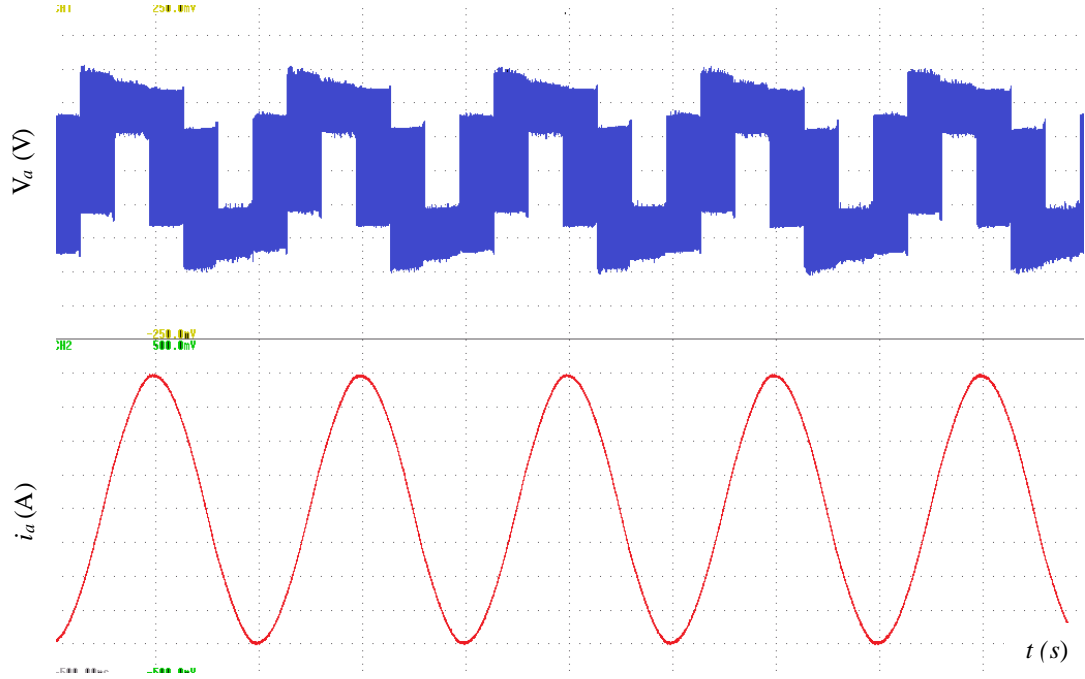


Figure 6.42 Voltage and current phases of the inductive load with LuPWM in the  $H$ -region.

The SVPWM and Mod-LuPWM techniques are implemented using dSPACE real-time interface Simulink/Matlab environment control systems. The aim of this test is to evaluate the Mod-LuPWM technique performance in comparison with the SVPWM technique. Therefore, the test is only performed in the CTR in a similar manner to the CTR control described in section 6.3.1. First, the IPMSM drive is run at a speed of  $600\text{rpm}$  and  $40\text{Nm}$  ( $L$ -region) with the implementation of SVPWM and Mod-LuPWM techniques, respectively. The CMV is measured as described in section 2.2, where the summation of the measured values of the inverter phase-to-zero output voltages  $V_{ao}$ ,  $V_{bo}$  and  $V_{co}$  (see Figure 2.1) is divided by three in order to calculate the CMV which is the neutral-to-zero voltage  $V_{no}$  (see Figure 2.1) according to Eqn.2.7.

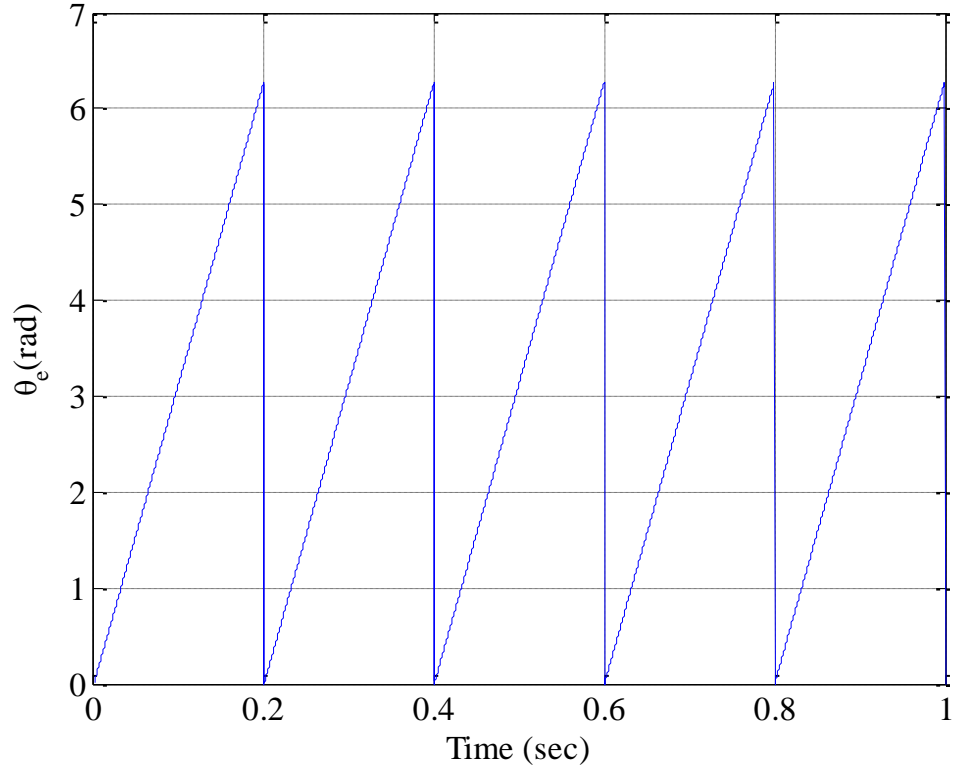


Figure 6.43 Electrical angular position generated by the Simulink repeating sequence block for open loop test with inductive load.

The resultant phase currents, the  $i_d$  and  $i_q$  current components, the torque  $T_e$  and the common mode voltage CMV waveforms of both SVPWM and Mod-LuPWM techniques are presented in Figure 6.47 to Figure 6.52. The results show that the d- and q-axis currents produced by the SVPWM and the Mod-LuPWM techniques (see Figure 6.48) successfully tracks the command dq values, however, the Mod-LuPWM technique generated higher ripple than SVPWM technique especially in  $i_d$  waveforms. Again, the high current ripple of the Mod-LuPWM technique is owing to the fact that the Mod-LuPWM technique uses only one zero vector in order to construct the command vector which leads to increase current harmonics due to the deviation of the machine currents from the fundamental currents [78]. Figure 6.49 illustrates the electromagnetic torque  $T_e$  generated by the studied PWMs techniques, where the ripple in the Mod-LuPWM technique is again higher than that produced by the SVPWM technique.

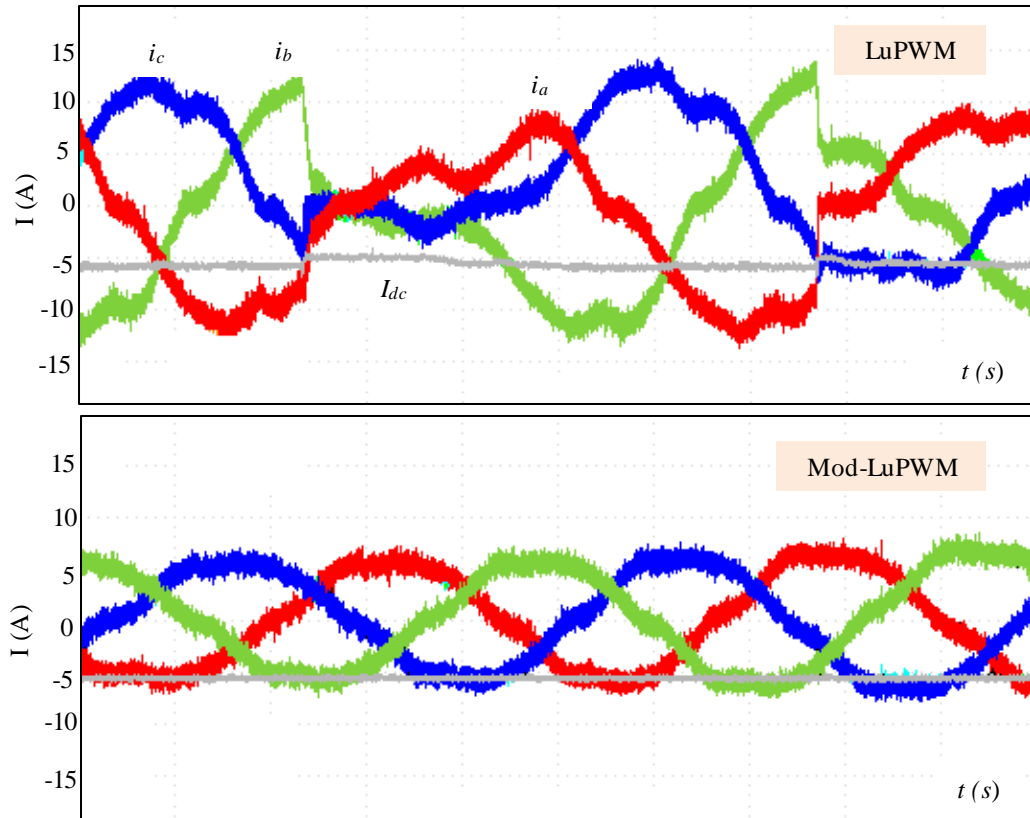


Figure 6.44 Phase currents of LuPWM and Mod-LuPWM at  $\omega_m = 200\text{rpm}$  and  $T_d = 10\text{Nm}$

The harmonic analysis of the phase voltage and phase current of both the SVPWM and Mod-LuPWM techniques are depicted in Figure 6.50 and Figure 6.51, respectively. The agreement between the harmonic analysis of the simulation results (see Figure 5.47 and Figure 5.48) and the experimental results (Figure 6.50 and Figure 6.51) can be clearly seen by comparing these figures. The fifth and seventh harmonic of the Mod-LuPWM technique are higher than that of the SVPWM technique leading to increase the torque ripple due to the increasing of the phase current ripple. These undesirable harmonics may lead to extra harmonic losses in the IPMSM drive [75].

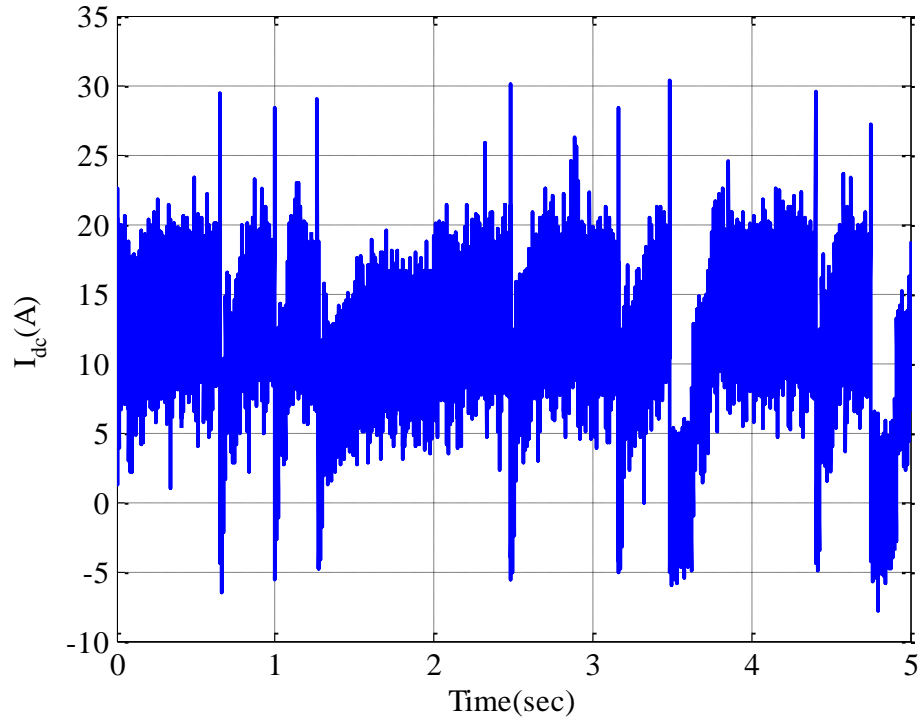


Figure 6.45 DC link current of LuPWM at  $\omega_m = 200\text{rpm}$  and  $T_d = 10\text{Nm}$

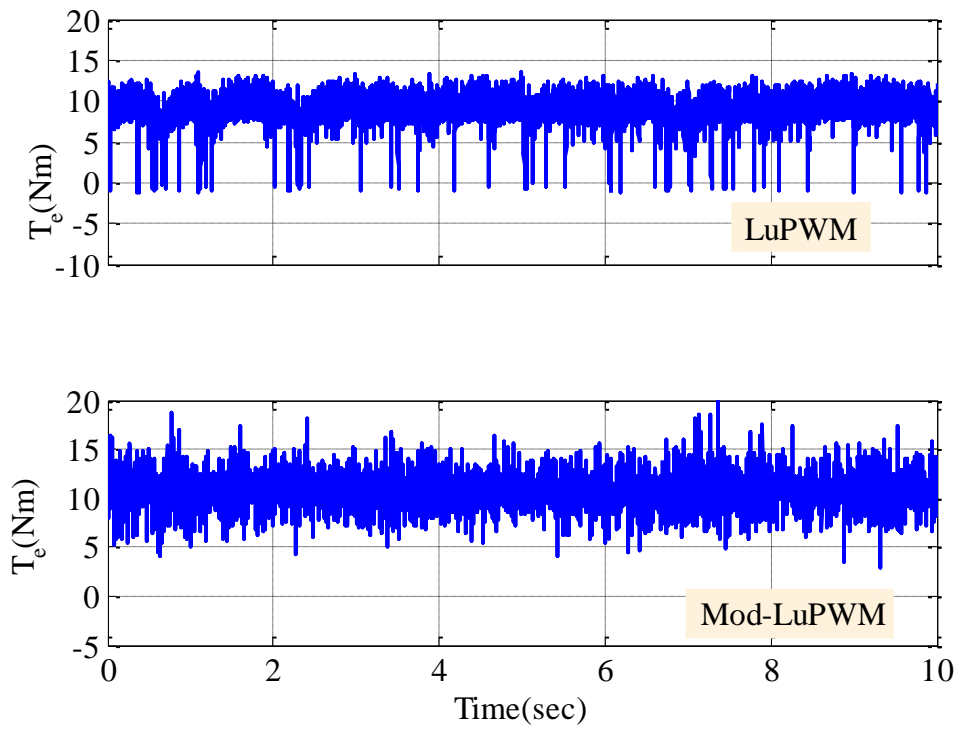


Figure 6.46 Torque response of LuPWM and Mod-LuPWM at  $\omega_m = 200\text{rpm}$  and  $T_d = 10\text{Nm}$

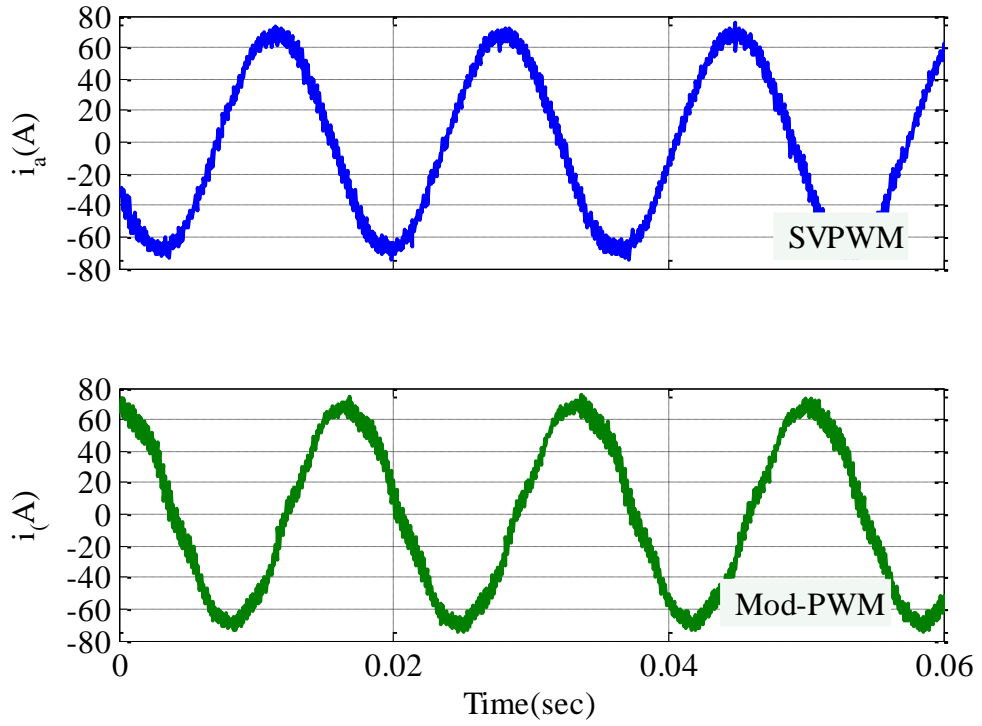


Figure 6.47  $i_a$  phase current of SVPWM and Mod-LuPWM at  $\omega_m = 600rpm$  and  $T_d = 40Nm$

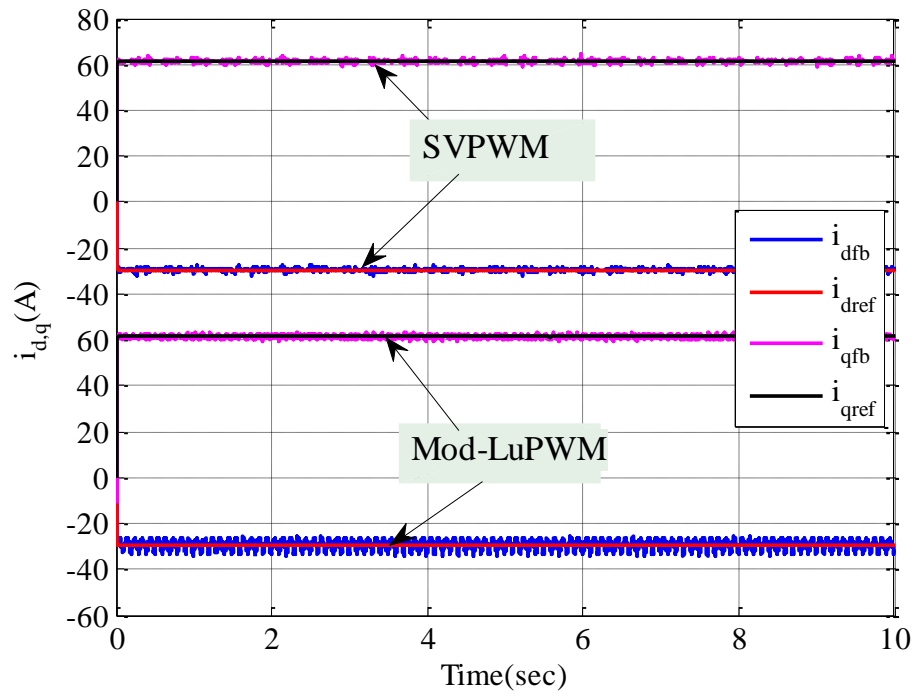


Figure 6.48  $i_d$  and  $i_q$  currents of SVPWM and Mod-LuPWM at  $\omega_m = 600rpm$  and  $T_d = 40Nm$

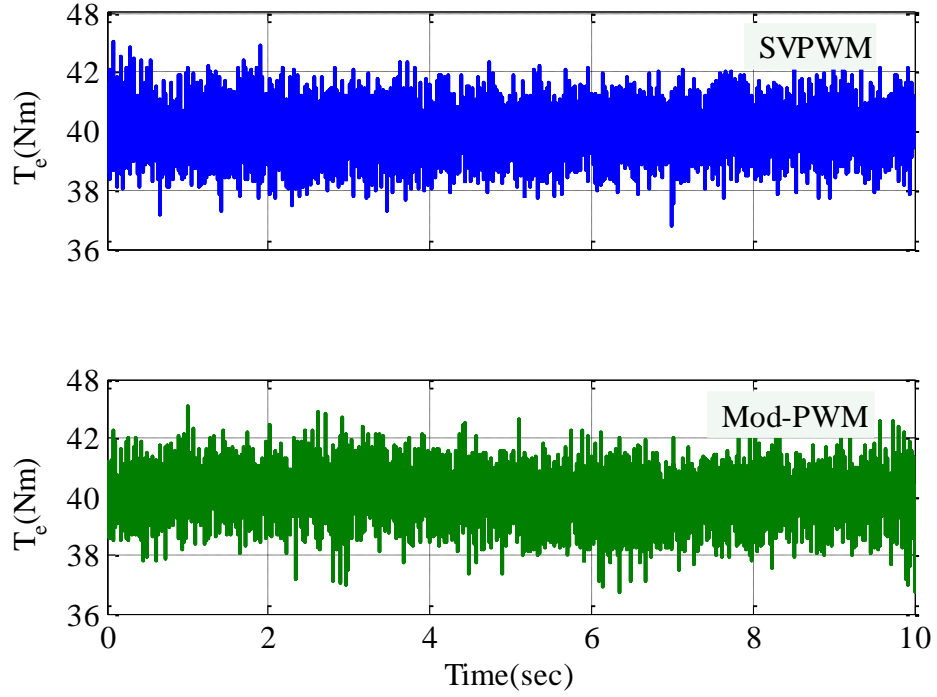


Figure 6.49 Torque response of SVPWM and Mod-LuPWM at  $\omega_m = 600\text{rpm}$  and  $T_d = 40\text{Nm}$

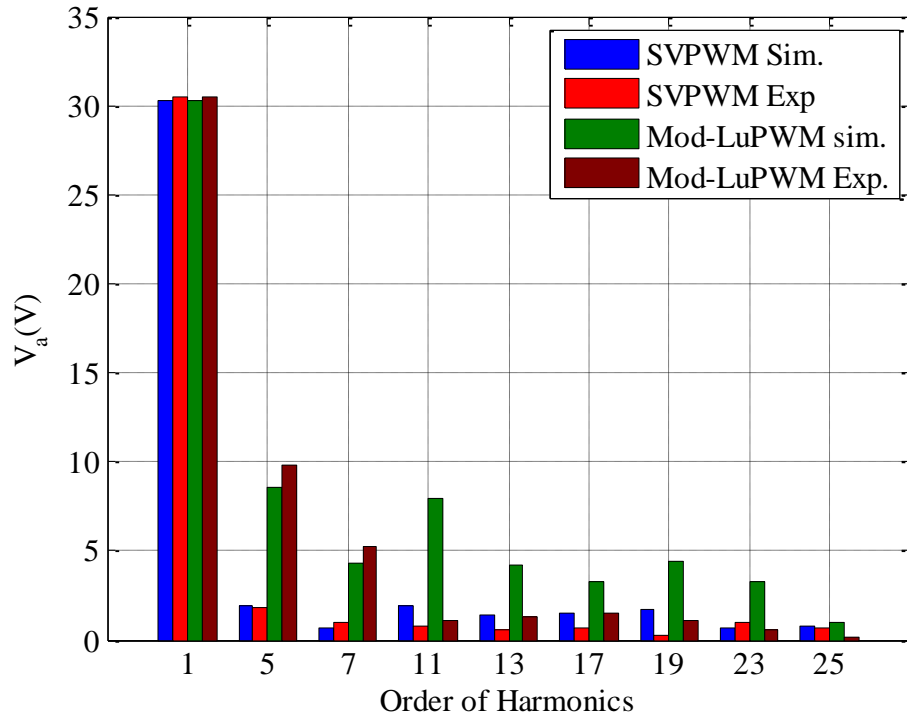


Figure 6.50 Simulation (Sim.) and experimental (Exp.) phase voltage harmonic of SVPWM and Mod-LuPWM at  $\omega_m = 600\text{rpm}$  and  $T_d = 40\text{Nm}$

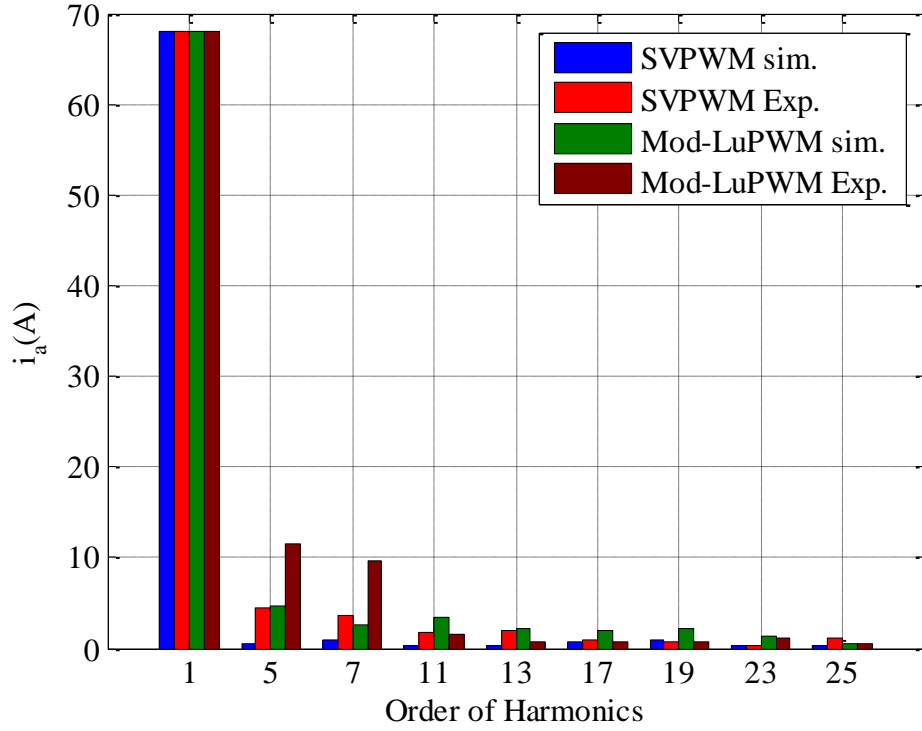


Figure 6.51 Simulation (Sim.) and experimental (Exp.) phase current harmonic of SVPWM and Mod-LuPWM at  $\omega_m = 600rpm$  and  $T_d = 40Nm$

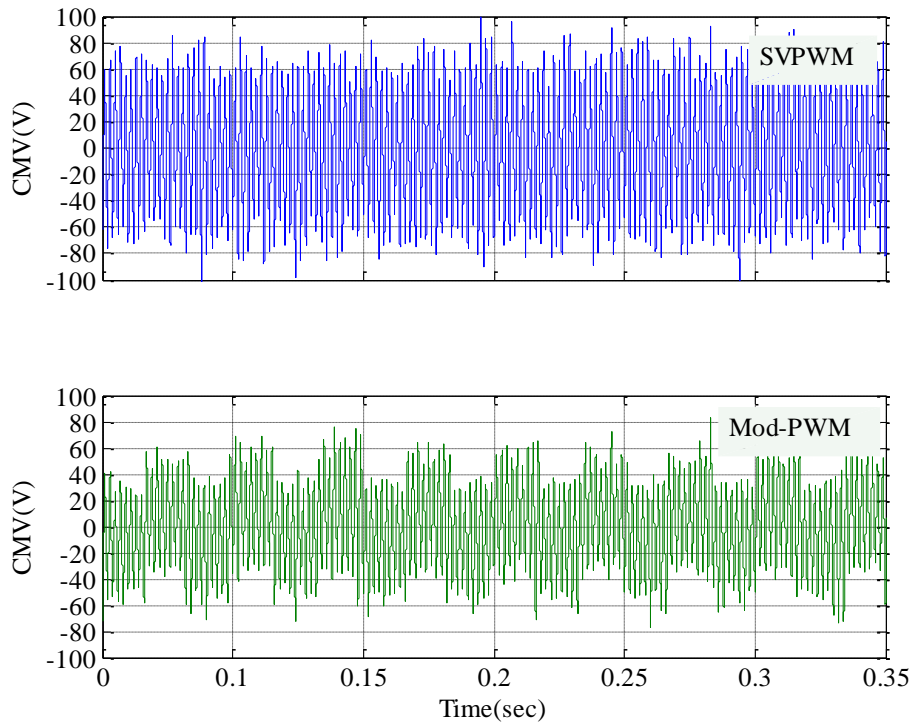


Figure 6.52 CMV of SVPWM and Mod-LuPWM at  $\omega_m = 600rpm$  and  $T_d = 40Nm$



Figure 6.53 to Figure 6.58 illustrates the obtained experimental results of the studied PWMs strategies at  $1000rpm$  and  $35Nm$  (H-region). The results are similar to that in the L-region (see Figure 6.47 to Figure 6.49). The phase voltage and current harmonics at this operation are shown in Figure 6.57 and Figure 6.58, respectively, and they are following the same trend in the low modulation region (see Figure 5.47 and Figure 5.48). The peak of the CMV of the SVPWM technique remains constant at about  $60V$  and the value of this voltage is reduced to about  $20V$  by implementing the Mod-LuPWM technique (see Figure 6.56). In general, the experimental results of the Mod-LuPWM technique show good agreement with its simulation results that are discussed in Chapter 5. Figure 6.60 to Figure 6.62 show the experimental phase voltage, phase current and the machine torque under SVPWM and Mod-LuPWM techniques which are directly obtained from the screen of the Yokogawa scope shown in Figure 6.21.

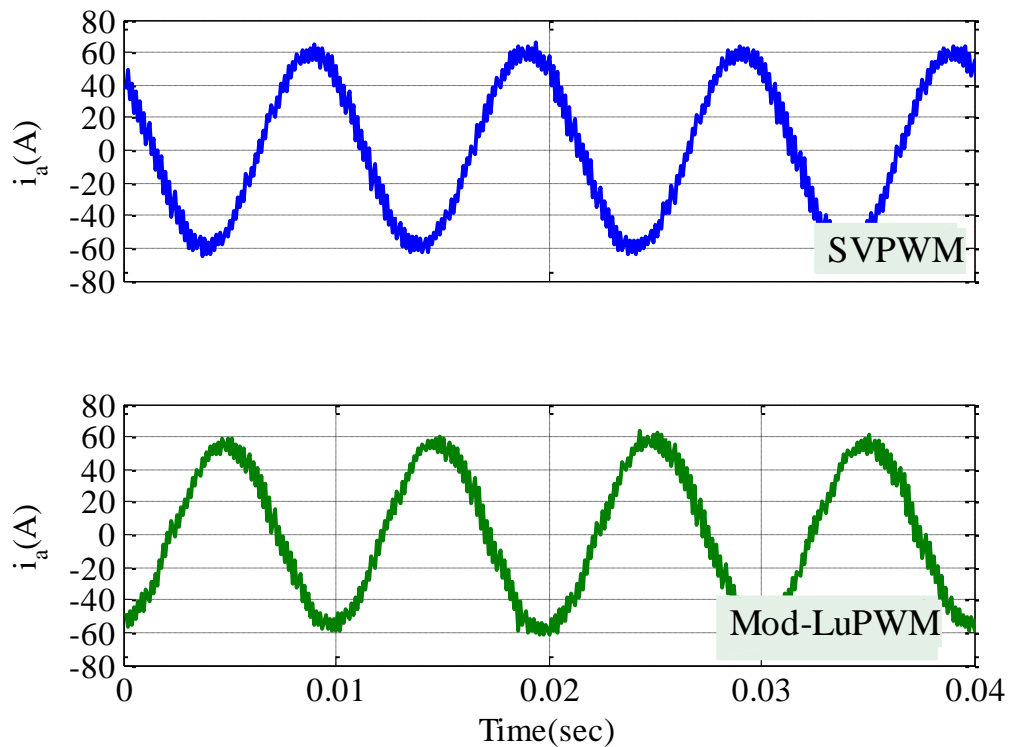


Figure 6.53  $i_a$  phase current of SVPWM and Mod-LuPWM at  $\omega_m = 1000rpm$  and  $T_d = 35Nm$

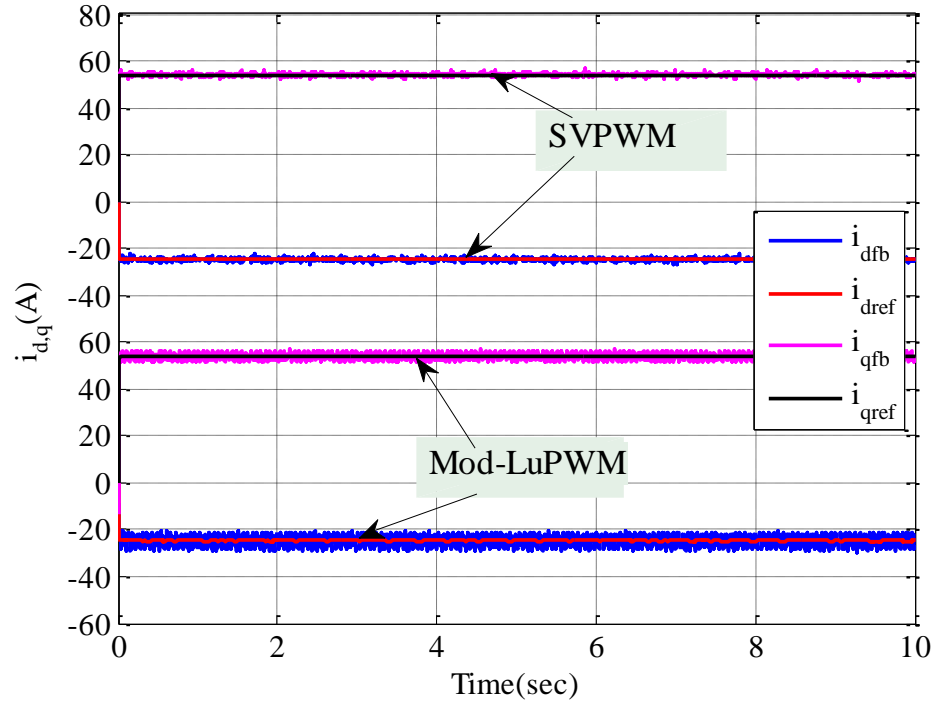


Figure 6.54  $i_d$  and  $i_q$  currents of SVPWM and Mod-LuPWM at  $\omega_m = 1000rpm$  and  $T_d = 35Nm$

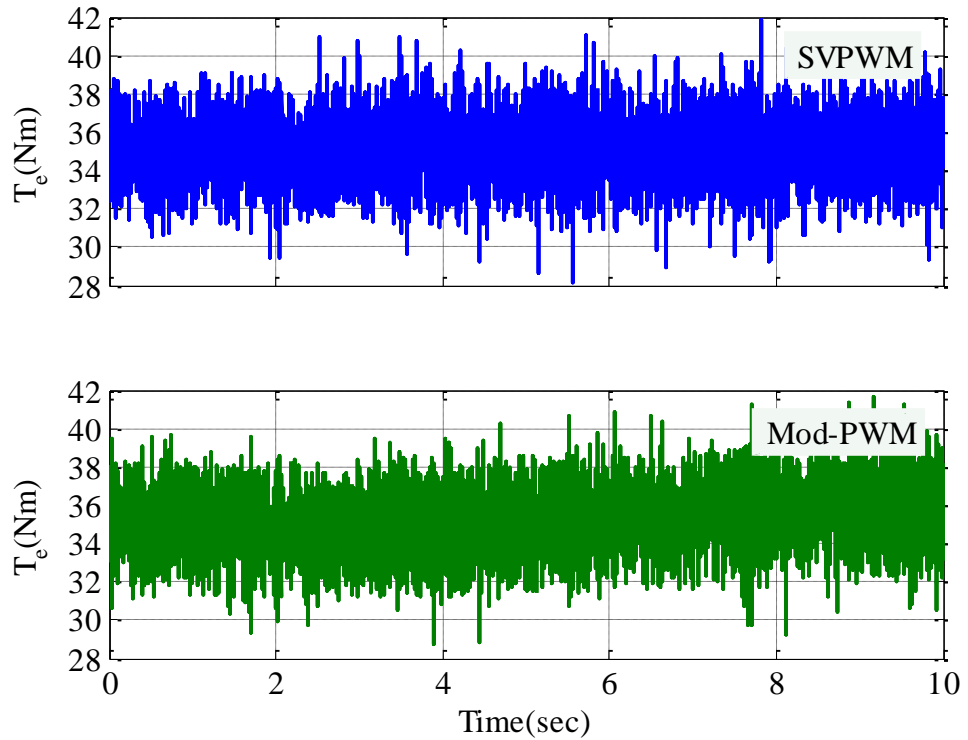


Figure 6.55 Torque response of SVPWM and Mod-LuPWM at  $\omega_m = 1000rpm$  and  $T_d = 35Nm$

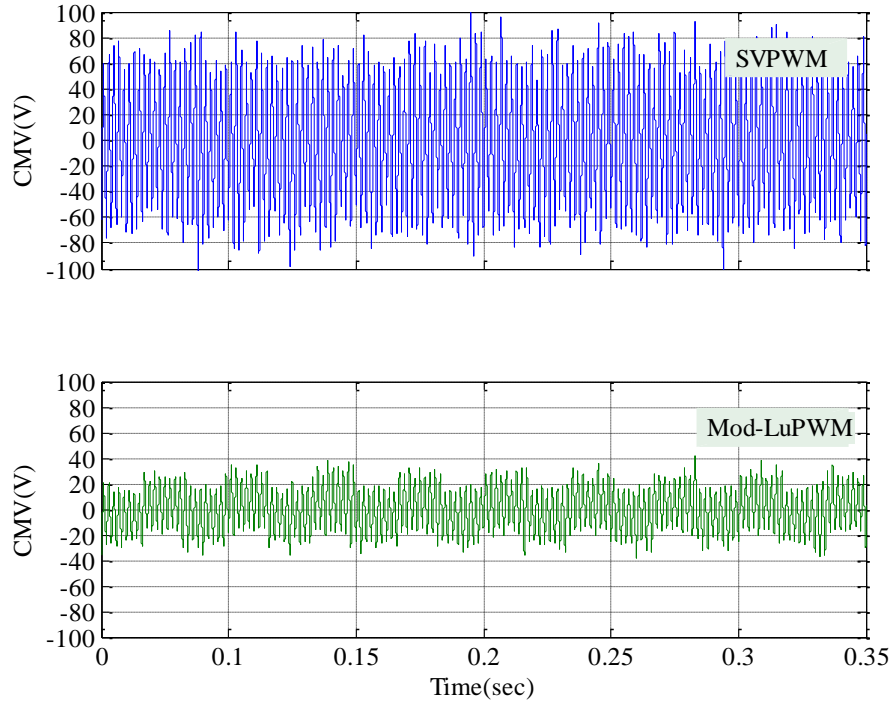


Figure 6.56 CMV of SVPWM and Mod-LuPWM at  $\omega_m = 1000rpm$  and  $T_d = 35Nm$

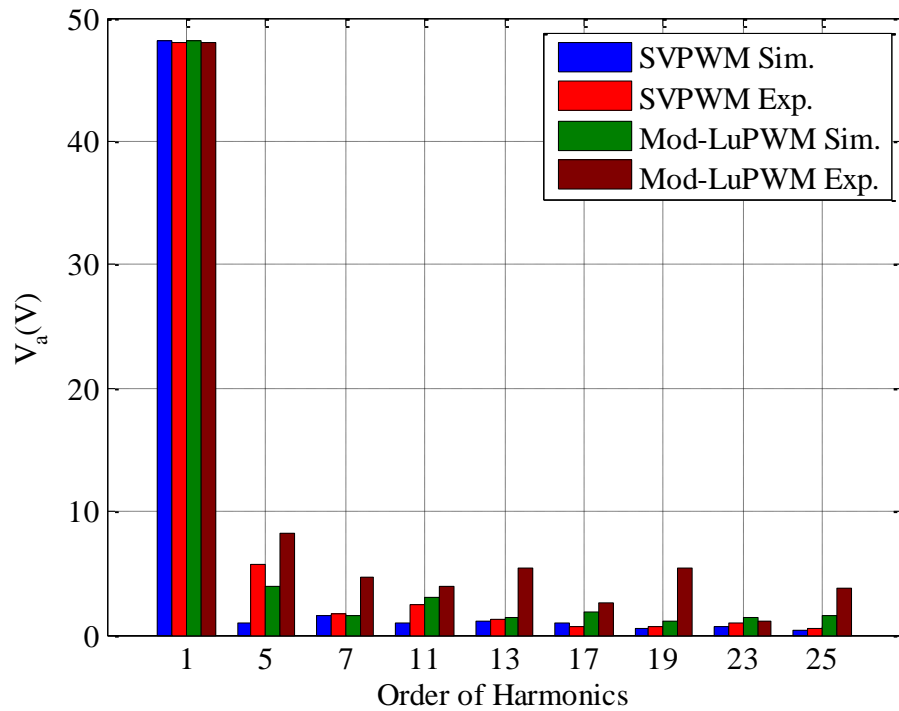


Figure 6.57 Simulation (Sim.) and experimental (Exp.) phase voltage harmonic of SVPWM and Mod-LuPWM at  $\omega_m = 1000rpm$  and  $T_d = 35Nm$

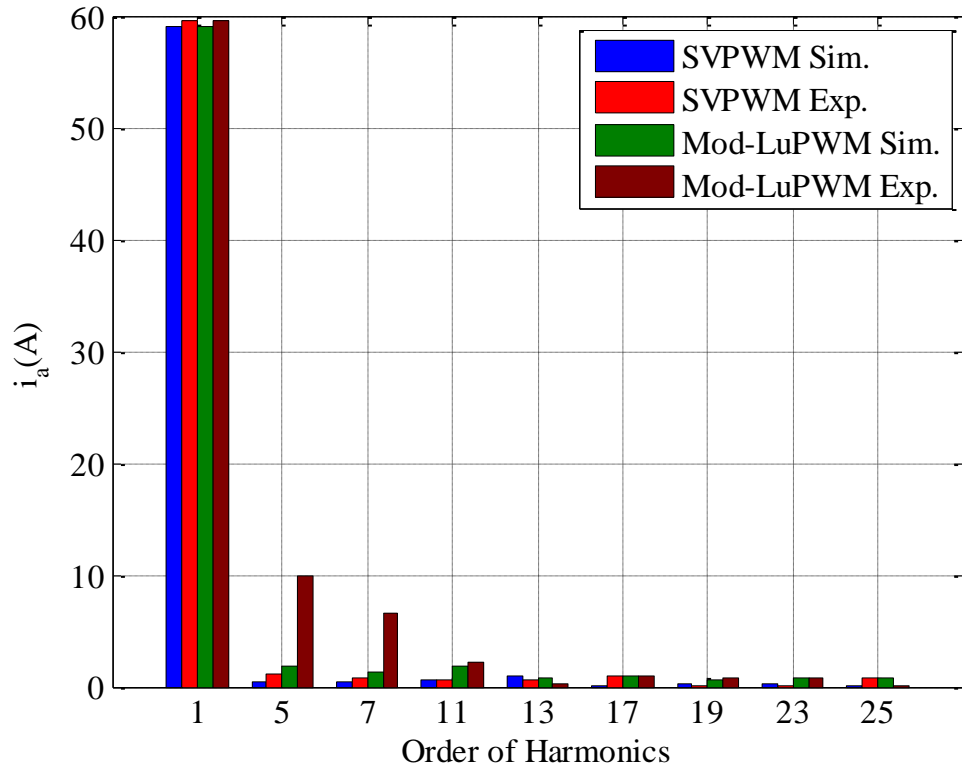


Figure 6.58 Simulation (Sim.) and experimental (Exp.) phase current harmonic of SVPWM and Mod-LuPWM at  $\omega_m = 1000rpm$  and  $T_d = 35Nm$

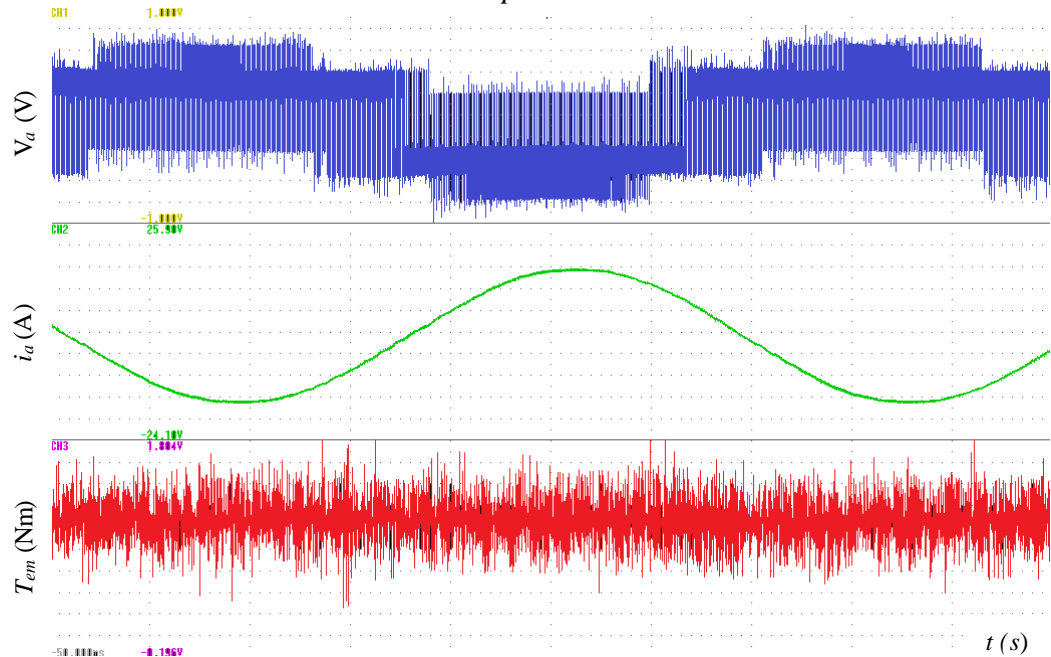


Figure 6.59 Phase voltage, phase current and torque waveforms of SVPWM  $\omega_m = 600rpm$  and  $T_d = 40Nm$

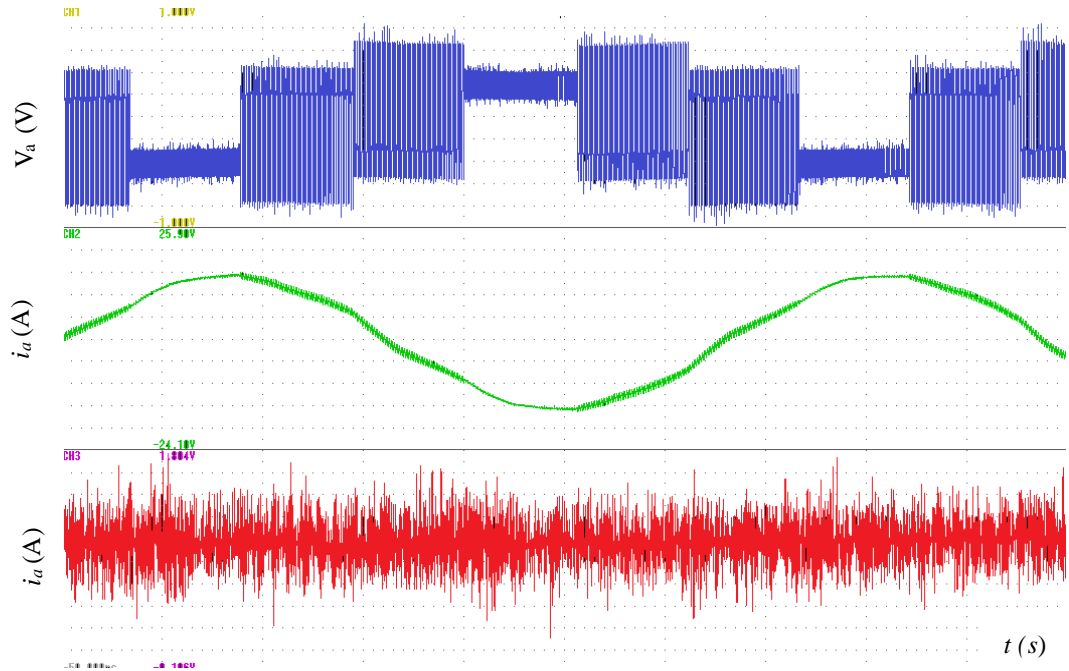


Figure 6.60 Phase voltage, phase current and torque waveforms of Mod-LuPWM  $\omega_m = 600rpm$  and  $T_d = 40Nm$

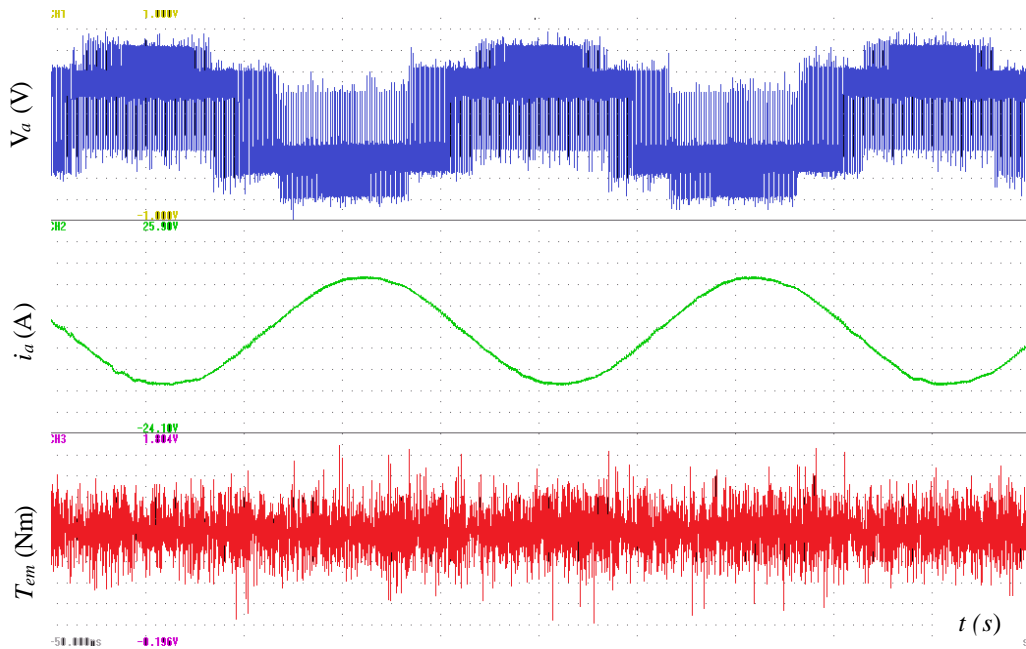


Figure 6.61 Phase voltage, phase current and torque waveforms of Mod-LuPWM  $\omega_m = 1000rpm$  and  $T_d = 35Nm$

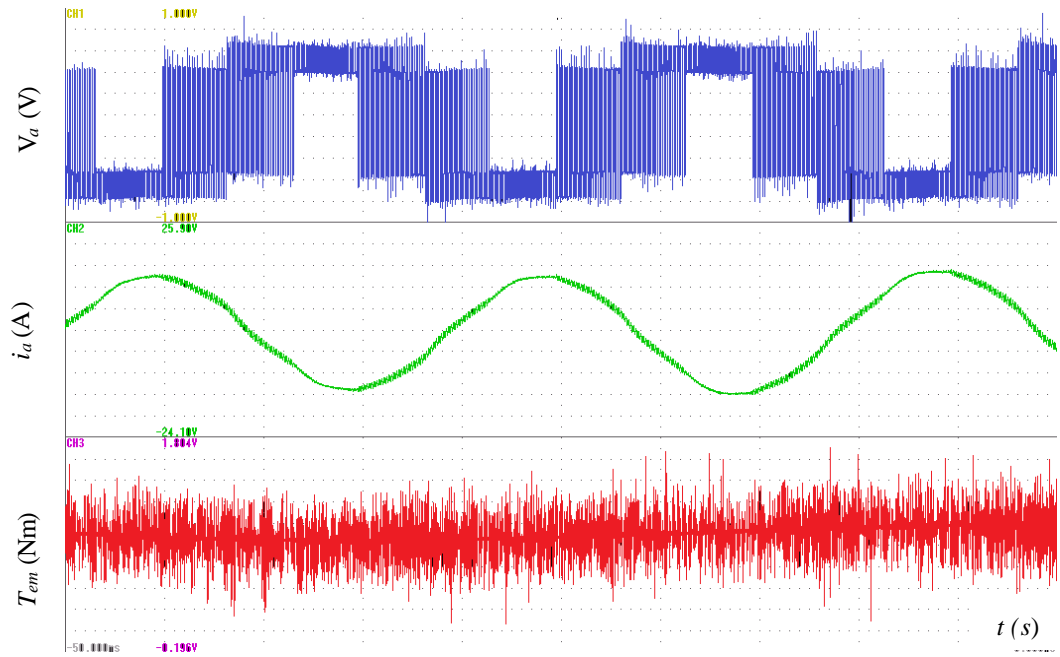


Figure 6.62 Phase voltage, phase current and torque waveforms of Mod-LuPWM  $\omega_m = 1000\text{rpm}$  and  $T_d = 35\text{Nm}$

### 6.3.3 Comparison of Simulated And Experimental Power Losses

The total power losses (i.e. copper and iron losses) predicted by the LMA in Chapter 3 and the resultant experimental total power losses are compared in this section. In addition, a comparison of the simulated and experimental inverter power losses with the SVPWM and Mod-LuPWM techniques is also achieved.

#### 6.3.3.1 Constant and Flux Weakening Region

The experimental total power losses of the motor (Exp.  $P_t$ ) can be calculated from the drive input power ( $P_{inp} = V_{dc}I_{dc}$ ), the drive output power ( $P_{out} = T_e \omega_m$ ) and the inverter losses ( $P_{inv}$ ) as given by Eqn. 6.4 [59].

$$P_t = P_{inp} - P_{out} - P_{inv} \quad 6.4$$

The powers  $P_{inp}$  and  $P_{out}$  can be directly measured by the power analyser described in section 6.2. The measured values of  $P_{inp}$  and  $P_{out}$  for a given  $\omega_m$  and  $T_d$  are listed in

Table 6.3. The experimental  $P_{inv}$  is the difference between  $P_{inp}$  and the VSI total output power as given by Eqn. 6.5.

$$P_{inv} = P_{inp} - (P_a + P_b + P_c) \quad 6.5$$

where,  $P_a$ ,  $P_b$  and  $P_c$  are the phase  $a$ ,  $b$  and  $c$  inverter output power, respectively, and they are measured and recorded by the PA. For example, at speed  $1350rpm$  and  $35Nm$  the measured  $P_{inp}$  is  $5561.65W$ ,  $P_{out}$  is  $4953.02W$  and  $P_a$ ,  $P_b$  and  $P_c$  (not shown in Table 6.3) are  $1692.5W$ ,  $1712.69W$  and  $1712.67W$  respectively. Substituting  $P_a$ ,  $P_b$  and  $P_c$  values into Eqn. 6.5 results in  $P_{inv} = 257.87W$ . Then, the total power losses  $P_t$  is obtained by substituting from  $P_{inp}$ ,  $P_{out}$  and  $P_{inv}$  in Eqn. 6.4 gives  $P_t = 350.76W$  as listed in Table 6.4. Similarly, the total experimental power losses for each given torque and speed in the CT region or FWR can be calculated. The resultant Exp.  $P_t$  for a given speed and torque are shown in Table 6.4. The predicted total power losses (LMA  $P_t$ ) which are directly calculated by the LMA for a given speed ( $\omega_m$ ) and demand torque ( $T_d$ ) described in Chapter 3, are also illustrated in Table 6.4.

Table 6.3 Experimental results of the IPMSM drive in CT and FW regions

	$\omega_m$ (rpm)	$T_d$ (Nm)	$P_{inp}$ (W)	$P_{out}$ (W)	$P_{inv}$ (W)
CTR	1350	35	5561.65	4953.02	257.87
		50	8210.90	6980.90	544.12
FWR	2000	10	2382.64	2093.40	135.02
		20	4735.28	4186.60	272.04
		30	7147.92	6280.20	405.06
	3000	20	7355.30	6290.70	332.40

Table 6.4 also compares the total power losses (copper and iron losses) obtained from the simulation results of the LMA and the experimental results (all motor losses such as copper losses, iron losses and stray losses etc.) in both the CTR and FWR.

Table 6.4 Simulation and experimental results of IPMSM drive power losses  $P_t$ 

	$\omega_m$ (rpm)	$T_d$ (Nm)	LMA $P_t$ (W)	Exp. $P_t$ (W)	% diff. $P_t$ (W)
CTR	1350	35	336.62	350.76	4.20
		50	649.28	685.81	5.62
FWR	2000	10	152.85	154.22	0.90
		20	267.96	285.64	3.24
		30	448.75	462.66	3.09
	3000	20	717	732.2	2.13

The results show close agreement between the simulated losses and experimental or actual power losses. It is noted that the maximum difference between these predicted and actual results is about 36.5W at 1350rpm and 50Nm in the CTR. In the FWR, however, the maximum difference between the predicted and actual power losses of the IPMSM drive is about 15.2W at 3000rpm and 20Nm. These differences between the predicted and measured power losses are due to the other motor losses that are not considered in the LMA optimization function such as the mechanical and stray losses [57, 58]. Additionally, in reality, the traction application with DC-link voltage supplied from battery system should be operated under extremely voltage reduction when the state-of-charge of the battery pack reduces. To realize this phenomenon, non-linear LUTs are generated with  $V_{dc} = 80V$  in order to investigate the reliability of the LMA and studied the IPMSM control scheme at relatively low DC-link voltage. The speed-torque profile of the IPMSM drive generated at 80V is shown in Figure 6.63 where the rated speed is reduced from 1350rpm at 120V to 900rpm at 80V. The same measurements and calculations that have been done for a DC-link voltage 120V are repeated for the voltage 80V in the FW region where the stator voltage reached the voltage limit. The measured power losses  $P_{inp}$ ,  $P_{out}$  and  $P_{inv}$  and offline simulated and experimental total  $P_t$  are listed in tables Table 6.5 and Table 6.6, respectively. The results are following the same trend of the results obtained at 120V (see Table 6.4).



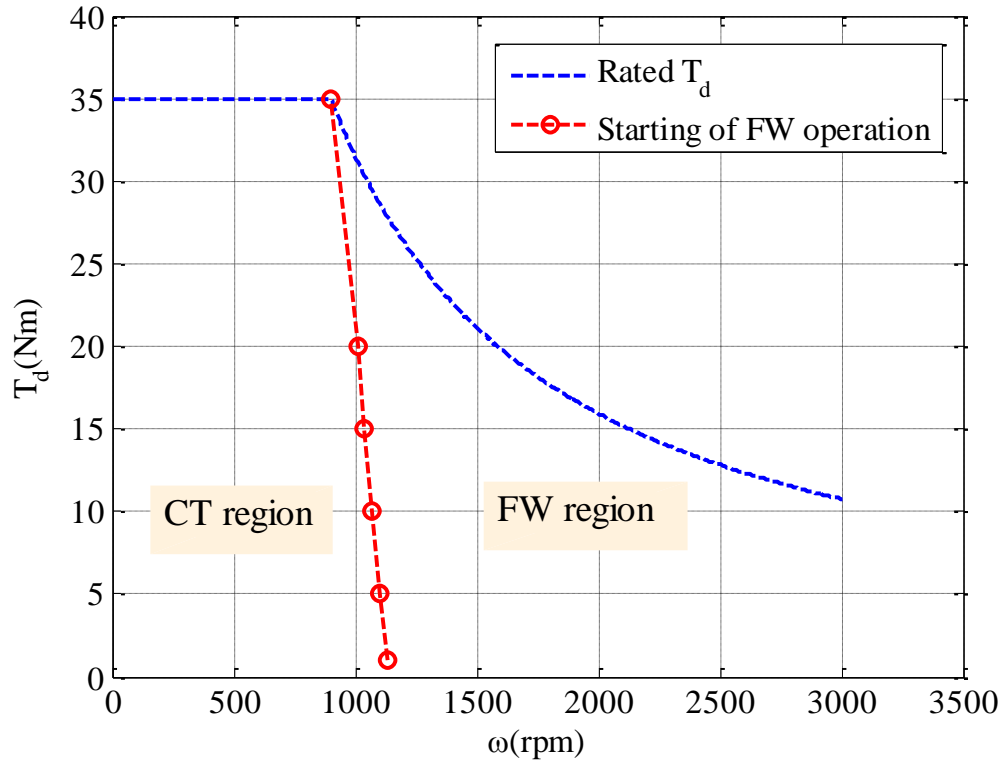
Figure 6.63 MTPA to FW line for  $V_{dc} = 80V$ 

Table 6.5 Experimental results of the IPMSM drive in CTR and FWR

	$\omega_m$ (rpm)	$T_d$ (Nm)	$P_{inp}$ (W)	$P_{out}$ (W)	$P_{inv}$ (W)
FW	1130	10	1344	1184.75	76.20
	1070	20	2440	2187.34	115.3
	2000	10	2391.7	2094.4	144.4

Table 6.6 Simulation and experimental results of the IPMSM drive total power losses  $P_t$ 

	$\omega_m$ (rpm)	$T_d$ (Nm)	$LMA P_t$ (W)	$Exp. P_t$ (W)	% diff. $P_t$ (W)
FW	1130	10	64.8	83.05	28.16
	1070	20	127.6	137.36	7.65
	2000	10	151.98	153.09	0.73

### 6.3.3.2 Inverter Losses with SVPWM and LuPWM Techniques

The experimental  $P_{inv}$  can be obtained from the measuring  $P_{inp}$  and phase  $a$ ,  $b$  and  $c$  power as discussed in the previous section. The inverter losses ( $P_{inv}$ ), which given by Eqn. 6.6, consists of the insulated gate bipolar transistors (IGBTs) power losses ( $P_{IGBT}$ ) and diode power losses ( $P_{Diod}$ ) [59, 73].

$$P_{inv} = P_{IGBT} + P_{Diod} \quad 6.6$$

The losses of an IGBT or a diode consist of the conduction losses ( $P_{CT/D}$ ) and switching losses ( $P_{swT/D}$ ) which are given by Eqns. 6.7 to 6.12 [72, 73].

$$P_{IGBT} = P_{CT} + P_{swT} \quad 6.7$$

$$P_{Diod} = P_{CD} + P_{swD} \quad 6.8$$

$$\begin{aligned} P_{CT} &= V_{CE0} I_{cav} + r_C I_{Crms}^2 \\ &= 6 \left\{ V_{CE0} I_o \left( \frac{1}{2\pi} + \frac{m_a \cos \varphi}{8} \right) + r_C I_o^2 \left( \frac{1}{8} + \frac{m_a \cos \varphi}{3\pi} \right) \right\} \end{aligned} \quad 6.9$$

$$\begin{aligned} P_{CD} &= V_{D0} I_{Dav} + r_D I_{Drms}^2 \\ &= 6 \left\{ V_{D0} I_o \left( \frac{1}{2\pi} - \frac{m_a \cos \varphi}{8} \right) + r_D I_o^2 \left( \frac{1}{8} - \frac{m_a \cos \varphi}{3\pi} \right) \right\} \end{aligned} \quad 6.10$$

$$P_{swT} = (E_{onT} + E_{offT}) f_{sw} \quad 6.11$$

$$P_{swD} = (E_{onD} + E_{offD}) f_{sw} \quad 6.12$$

where,  $V_{CE0}$  is the on-state forward voltage of the IGBT,  $V_{D0}$  is the on-state forward voltage of the diode;  $I_{cav}$ ,  $I_{Dav}$ ,  $I_{Crms}$  and  $I_{Drms}$  are the IGBT and diode average and root mean square values currents, respectively;  $r_C$  and  $r_D$  are the on state resistance of the IGBT and diode respectively;  $I_o$  is the peak output current;  $\cos(\varphi)$  is the power factor;  $E_{onT}$  and  $E_{onD}$  are the turn-on energy losses of the IGBT and diode, respectively; and

$E_{offT}$  and  $E_{offD}$  are the turn-off energy losses of the IGBT and diode, respectively. The turn-on losses of the diode is usually neglected [73]. The aforementioned parameters can be directly obtained from the datasheet of the utilised intelligent power module [96]. The turn-on and turn-off energy of the IGBT and diode are measured at a fixed condition and therefore should be scaled with the testing condition as given in Eqns. 6.13 and 6.14 [73].

$$E_{onT} = E_{onTref} \frac{V_{in} I_{in}}{V_{ref} I_{ref}} \quad 6.13$$

$$E_{offT} = E_{offTref} \frac{V_{in} I_{in}}{V_{ref} I_{ref}} \quad 6.14$$

where,  $E_{onTref}$  and  $E_{offTref}$  are the typical turn-on and turn-off energy values calculated from the typical switching losses curves of the utilised power module,  $V_{ref}$  and  $I_{ref}$  are the maximum voltage and current of the utilised power module given in Table 3.1 and,  $V_{in}$  and  $I_{in}$  are the input voltage and current. For example, at 600rpm and 40Nm with SVPWM technique the measured  $P_{inp}$  is 3188.54W (see Table 6.7),  $P_{out}$  is 2547.80W and  $P_a$ ,  $P_b$  and  $P_c$  (not shown in Table 6.7) are 987.7W, 983.5W and 976.2W respectively. Substituting from  $P_a$ ,  $P_b$  and  $P_c$  values in Eqn. 6.5 results in  $P_{inv} = 241.14W$ .

To obtain the predicted inverter losses at the same speed and torque demand, the resistances  $r_c$  and  $r_d$  are calculated from the power module datasheet, Figure 6.64 [73], where  $r_c = 0.01\Omega$  and  $r_d = 0.019\Omega$ ,  $m_a = 0.44$ ,  $\cos(\varphi) = 0.902$ ,  $V_{ce0} = 1.01V$ ,  $V_{d0} = 1.05V$ ,  $E_{onTref} + E_{offTref} = 0.024J/pulse$ ,  $E_{offDref} = 0.0132J/pulse$ ,  $V_{in} = 120V$ ,  $I_{in} = 68.09A$ . The predicted resultant total inverter losses under this condition are 236.54W as illustrated in Table 6.7. It is noted that the current harmonics produced by the Mod-LuPWM technique (see Figure 6.51 and Figure 6.58) are considered in the inverter losses calculations to accurately predict the actual inverter power losses. Equation 6.15 is utilised to include the current harmonic effects in the inverter losses calculations [100].

$$I_{rms} = \sqrt{I_0^2 + \sum_{j=1}^{\infty} \frac{I_j^2}{2}} \quad 6.15$$

where,  $j = 1, 2, \dots$ ,  $I_j$  is the magnitude of harmonic  $j$ . The harmonic values which produced by the SVPWM technique (see Figure 6.51 and Figure 6.58) is quite small compared with that under the Mod-LuPWM technique, and therefore their effects can be neglected.

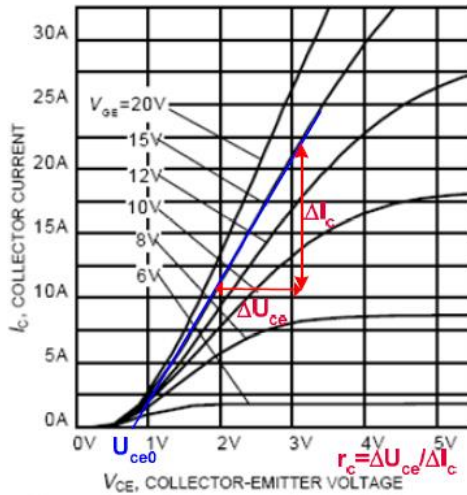


Figure 6. Typical output characteristic ( $T_j = 175^\circ\text{C}$ )

(a)

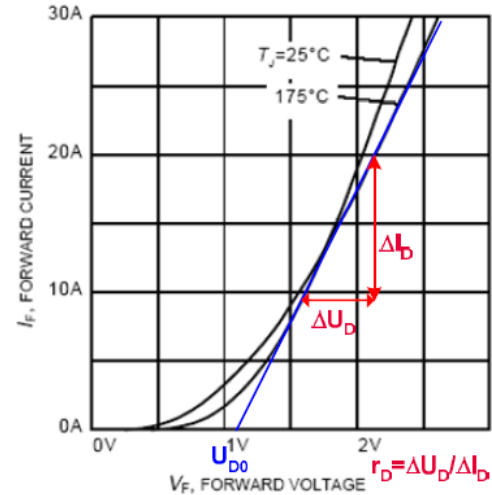


Figure 27. Typical diode forward current as a function of forward voltage

(b)

Figure 6.64 Determining of the initial voltage and resistance values from the graph of (a) Transistor (b) Diode [73].

Finally, the experimental and simulated power inverter losses results are presented in Table 6.7. It is noted that there are small differences between the simulated and experimental power losses produced by the SVPWM and Mod-LuPWM techniques which may be caused by the measurement errors existing in measuring instruments (i.e. noises, offsets, and finite accuracy, etc.). Based on simulation study in Chapter 2, it is proved that the LuPWM technique may reduce the switching losses by one third compared with conventional PWM techniques. However, Table 6.7 illustrates that employing the Mod-LuPWM technique under closed-loop control may cause significant increase in conduction losses as it also produces undesirable low-frequency voltage and current harmonics, especially the fifth and seventh harmonics.

The obtained experimental power losses of the VSI, IPMSM and IPMSM drive losses with the SVPWM and Mod-LuPWM techniques are illustrated in Table 6.8. The results clearly show that implementation of the Mod-LuPWM technique does not enhance the drive efficiency as the input power drawn by the IPMSM drive with Mod-LuPWM technique is higher than that drawn with SVPWM technique for almost the same output power. This is true in the low modulation region (600rpm/40Nm) and high modulation region (1000rpm/35Nm) due to high current harmonics. The current harmonics of the Mod-LuPWM technique also increase the total power losses of the studied IPMSM machine and consequently, the total IPMSM drive losses which are the summation of the inverter and IPMSM machine losses. Therefore, the overall efficiency of the IPMSM drive with the Mod-LuPWM technique will drop to lower levels than that achieved by the SVPWM technique. The Mod-LuPWM technique may achieve better performance than the SVPWM technique with high switching frequency applications where the switching losses are considerably high. As maximum predicted switching losses of the inverter under the conventional SVPWM technique at 600rpm and 40Nm (see Table 6.7) are just around 13.51W due to low DC-link voltage compared with 223.03W for the conducting losses, implementation of the Mod-LuPWM technique to reduce the switching losses will not improve the drive efficiency. However, if the DC-linkage voltage and the switching frequency increase, the benefits of the Mod-LuPWM technique in reducing total converter losses could be obvious. To investigate that, the DC-link voltage is increased to 600V and the switching frequency is increased to 20 kHz (the maximum DC voltage and switching frequency of the utilised power module). However, the speed and torque are kept constant at 600rpm/1000rpm and 40Nm/35Nm in order to maintain the conduction losses constant. The predicted switching losses are calculated under these conditions according to Eqns. 6.11 to 6.14 and the obtained results are demonstrated in Table 6.9. One can see that the inverter power losses with the Mod-LuPWM technique is lower than that with the SVPWM technique by about 1.87% which may lead to improve the overall drive efficiency. The switching losses are, however, increases from 13.51W to 200.55W with the SVPWM technique and from 10.59 to 132.36 with the Mod-LuPWM technique at speed 600rpm and torque 40Nm. The Mod-LuPWM technique considerably decreases the switching losses of the drive

which leads to improve the inverter efficiency. Thus, it is expected that it will enhance the drive efficiency. Similar phenomenon is expected in the high modulation region where the speed is  $1000rpm$  and the torque is  $35Nm$  (see Table 6.9)

Table 6.7 Simulation and experimental results of the IPMSM drive total power losses  $P_t$  at 120VDC

$PWM$	$\omega_m(rpm)$	$T_d(Nm)$	$P_{inp}(W)$	$P_{out}(W)$	$P_{CD}(W)$	$P_{sw}(W)$	$P_{inv}(W)$		% diff.(W)
			Exp.	Exp.	Sim.	Sim.	Sim.	Exp.	
SVPWM	600	40	3188.54	2547.80	223.03	13.51	236.54	241.14	1.94
Mod-LuPWM		40	3292.85	2545.21	283.30	10.59	293.89	307.32	4.57
SVPWM	1000	35	4382.21	3732.29	177.76	11.71	189.47	218.96	15.56
Mod-LuPWM		35	4461.68	3734.19	190.90	8.1915	199.09	222.75	11.88

Table 6.8 Experimental results of the inverter losses, IPMSM power losses and the IPMSM drive power losses at 120VDC

$PWM$	$\omega_m(rpm)$	$T_d(Nm)$	$P_{inp}$	$P_{out}$	$P_{inv}$	Exp. $P_t$	Exp. $P_{drive}$	$\eta(\%)$
			(W)	(W)	(W)	(W)	(W)	
			Exp.	Exp.	Exp.	Exp.	Exp.	
SVPWM	600	40	3188.54	2547.80	241.14	399.6	640.74	79
Mod-LuPWM		40	3292.85	2545.21	307.32	440.33	747.65	77
SVPWM	1000	35	4382.21	3732.29	218.96	430.96	649.92	85
Mod-LuPWM		35	4461.68	3734.19	222.75	504.74	727.49	84

Table 6.9 Simulation and predicted results of the studied IPMSM total power losses  $P_t$  at 120VDC and 600VDC

$PWM$	$\omega_m$	$T_d$	$P_{CD}(W)$	$P_{CD}(W)$	$P_{sw}(W)$	$P_{sw}(W)$	$P_{inv}(W)$	$P_{inv}(W)$
	(rpm)	(Nm)	120V/8kHz	600V/20kHz	120V/8kHz	600V/20kHz	120V/8kHz	600V/20kHz
SVPWM	600	40	223.03	223.03	13.51	200.55	236.54	423.58
Mod-LuPWM		40	283.30	283.30	10.59	132.36	293.89	415.66
SVPWM	1000	35	177.76	177.76	11.71	155.14	189.47	332.9
Mod-LuPWM		35	190.90	190.90	8.1915	102.39	199.09	293.29



## 6.4 Chapter summary

In this chapter, the experimental validation of the simulation results discussed in chapter 5, are presented. A complete laboratory setup is developed and the test rig components such as inverter components (intelligent power module and its interface), measuring devices (CTs, VTs, encoder) and their signals scaling and filtering, dSPACE hardware control system, the generation of six PWMs signals, the dead time and PWMs signal inverting, are described.

The first part validates the performance of the non-linear LUTs based control of IPMSM drives that were described and simulated in chapter 3 and 5, respectively in both the CTR and FWR. The experimental results show good agreements with those obtained by simulation. The results demonstrate that the proposed control scheme can be effectively used to achieve the optimal control of the IPMSM drive in the constant torque and FW regions at high or low DC-link voltage values.

In the second part of the experimental validation process, the Mod-LuPWM technique is implemented in order to evaluate its performance in the L- and H- regions in the CTR compared with the SVPWM technique. The comparison considers quality of the current and torque waveforms, peak-to-peak CMV reduction and the inverter losses. In chapter 2, a simulation study shows that the LuPWM technique and consequently Mod-LuPWM technique can reduce the switching losses of the VSI by about one third compared with the conventional SVPWM technique. However, the experimental results show that it will increase the inverter conduction losses due to higher total harmonic distortion in currents, and consequently reduces the overall efficiency of the IPMSM drive system. This is because the switching frequency and the DC-link voltage of the drive system are relative low, and hence switching losses value is quite small compared to the conduction losses. The DC linkage voltage and the switching frequency are increased to the maximum allowed values of the utilised power module (i.e. 600V, 20kHz) in order to predict the switching losses and demonstrate the benefit of implementing the Mod-LuPWM technique in high voltage operation. The load current is kept constant in order to maintain constant conduction losses levels at 120VDC. The calculated results show

that the Mod-LuPWM technique successfully improves the efficiency of the inverter by reducing the switching losses.

## 7 CONCLUSION AND FUTURE WORK

### 7.1 Conclusion

This chapter summarises the thesis research work and discusses the future work that can be developed based on this research. This PhD research aims to improve the efficiency of an IPMSM drive system and it considers the IPMSM controllable losses, the inverter losses and common mode voltage. In terms of the IPMSM power losses, a LMA has been developed in order to minimize the copper and iron losses in both the constant and flux weakening operating regions of the IPMSM drive accounting for the d-q inductances and flux linkage saturation effect, and the stator winding resistive voltage drop which have been neglected generally in the previous studies. To reduce the inverter switching losses as well as the CMV which has adverse effects on the motor bearings and causes electromagnetic interference, a modified discontinuous PWM technique is developed and implemented for this purpose.

Modern PWMs such as NSPWM, AZPWM and LuPWM techniques that are aimed to reduce the CMV, are investigated and compared with the conventional SVPWM technique in *Chapter 2*. The investigation is performed by comparing the PWMs switching pattern, voltage linearity, minimization of switching losses and the ability to reduce the CMV. Comparisons between SVPWM, NSPWM and AZPWM techniques have been already investigated in the previous studies but the LuPWM technique has not been fully considered. The investigation results clearly show the advantage and disadvantage of each PWM technique. For example, SVPWM technique has the smoothest current waveforms among the studied PWM techniques and it is able to operate in the very low and high modulation regions of the  $\alpha\beta$  voltage hexagon space but it produces high switching losses and high CMV especially during the switching interval of the zero vectors. The AZPWM technique has the ability to reduce the CMV which covers the whole regions of the hexagon but it does not reduce the switching losses. In addition, it generates high ripples in the current waveforms which lead to high undesirable torque ripple, especially in the low modulation region. Despite the fact that NSPWM technique reduces both the CMV and the inverter switching losses, its duty

cycles are only applicable in the high modulation region. On the other hand, the LuPWM technique can reduce both the CMV and the switching losses. In addition, it operates in both the low and high modulation region, although its current waveforms have more distortions in the low modulation region due to voltage harmonic. The scalar implementation of the LuPWM technique which has not been well-covered in the previous work is described in details in this chapter and the simulation results show that this PWM technique is applicable to IPMSM drives.

**Chapter 3** presents a new power LMA in order to minimize the copper and iron losses of the IPMSM drive in the CTR and FWR. For each single speed and demand torque the LMA computes the optimal d- and q-axis current demands off-line. The results that cover the entire torque-speed operating range can be stored in LUTs for real-time implementation. The proposed LMA is able to predict minimum power losses operation that is very close to the actual values due to the fact that it takes into account the parameters variations, the resistive voltage drop and it consider both the copper and iron losses in the overall speed range of the IPMSM drives. In addition to, the initial values of the LMA are chosen to be the linear optimal solution (i.e. the solution calculated with the assumption of constant parameters) which is the closest initial values to the actual optimal solution. This leads to reduce the searching time and the number of iterations required to reach the optimal point by the LMA. The LMA provides a flexible means of accounting various factors that may affect minimum losses operations, such as the inductance, flux linkage variations with current and the resistive voltage drop, etc. It is also applicable to surface mounted permanent magnet machine (SPMSM) drives. The optimisation function of the LMA can be expanding to include extra power losses types such as stray losses or inverter losses as long as their models are available.

**Chapter 4** utilised the LMA presented in Chapter 3 to investigate the influence of magnetic saturation, resistive voltage drop and iron losses on minimum losses operation of the IPMSM drive. Comprehensive off-line calculations are performed using the LMA. The parameters saturation effects are studied over the speed and torque range of the IPMSM drive and the results are compared with that under linear parameters assumption. The results clearly show the significant differences between the power losses calculated with linear and non-linear parameters especially at high torque

demand. Consequently, it is concluded that the parameters saturation effect should not be neglected and should be included in any losses minimisation in order to reduce the errors between the predicted and the actual optimal solution or the total power losses. The second part of this chapter investigates the influence of the stator winding resistive voltage drop which has been typically neglected in the previous works on minimum losses operation. It is concluded that the resistive voltage drop can strongly affect the minimum operating points of the IPMSM at high speeds as neglecting this voltage drop leads to less negative d-axis current and insufficient field weakening flux. Therefore, the current control will saturate and consequently the demand torque will not be achieved. The voltage deficit will be more significant at high torque level due to the fact that the resistive voltage drop being proportional to current or torque. The effect of the iron losses on the optimum operation of the IPMSM drive has been investigated in both the CTR and FWR. The off-line simulation results in the CTR show that the copper losses are dominant. Consequently, including the iron losses in the losses minimisation in the CTR of the IPMSM drive causes a small difference in the optimal d-axis current (7.45% at 1350rpm and 60Nm). In the FWR the IPMSM drive operates under the current and voltage limits, therefore only one solution that satisfies these constraints can be obtained. As a result, the d-axis optimal current level differs slightly with and without consideration of iron losses. It is concluded that the iron losses effect of an IPMSM is mainly depending on the machine design and the materials used to build it.

**Chapter 5** explains how to utilise the LMA presented in chapter 3 in controlling the IPMSM drive, implements LuPWM technique and compares it with SVPWM technique. The LMA is used to generate non-linear LUTs of the d- and q-axis current demands which are incorporated into an IPMSM control scheme. The new non-linear LUTs have advantage over the traditional LUTs in that they generate the current demand for minimum losses operation with due account for the IPMSM parameters nonlinearity and the resistive voltage drop across the stator windings. According to the simulation results in the CTR and FWR of this control scheme, the current demands generated from the LUTs are well-tracked. This demonstrates that the non-linear LUTs which facilitate minimum losses operation can be successfully implemented in the IPMSM drive. The second part of chapter 5 focuses on investigating the performance of

the LuPWM technique the IPMSM drive and comparing it with the SVPWM technique. The simulation results show that the phase current waveforms are highly distorted with LuPWM technique especially in the regions close to at the sector transitions. The cause of this distortion has been identified. It has been shown that the ripple in the rotor angular position leads undesirable switching events and hence voltage distortion. This ripple causes the sector transition to fluctuate between the current and the next sectors. In the SVPWM technique switching states are kept constant during the transition time between any two sectors in the hexagon and consequently the switching state is not affected by the angular position ripple. The switching state of the LuPWM technique change from “On”/”Off” to “Off”/”On” during the sector transition time, and this leads to switching state fluctuation with presence of ripple on rotor position. Therefore, a noticeable distortion is observed in the phase current waveforms. To solve this problem and to make the current waveforms produced by the LuPWM technique more sinusoidal, the pulse pattern of the conventional LuPWM technique is modified by holding the last pulse state just before the sector transition point is started and continue to hold it constant until the voltage command vector has passed from the current sector to the next sector with sufficient margin. In this way, the impact of the angular position ripple is eliminated or reduced. The proposed Mod-LuPWM technique is successfully implemented and simulated in the CTR using the IPMSM drive control scheme and the results show smooth current waveforms compared with that under the conventional LuPWM technique. It is clearly shown that the proposed Mod-LuPWM technique successfully reduces the peak-to-peak CMV compared with the conventional SVPWM technique. However, voltage distortion is increased due to the modification of the sector transition. Consequently, the current waveforms contain the fifth and seventh harmonics which may increase the drive losses. Nevertheless the control scheme that is used to implement the Mod-LuPWM technique operates under closed loop condition which has not been reported in the previous work.

**Chapter 6** presents the experimental validation of the simulation results obtained in Chapter 5. The obtained experimental current and torque waveforms in the CT region and FW region agree with the simulation results which, in turn, validate the non-linear LUTs generated based on the LMA. The agreement between the simulation and

experimental results produced by the Mod-LuPWM technique is also observed. The total power losses predicted by the LMA is smaller than the actual power losses (i.e. power losses measured by the power analyser) as some other losses are not considered in the LMA optimization process such as mechanical losses and rotor eddy current losses. Another important conclusion is that according to the simulation study in Chapter 2, the Mod-LuPWM technique can successfully reduce switching losses by about one third and the peak-to-peak of the CMV comparing with the traditional SVPWM technique. However, employment of the Mod-LuPWM does not improve the overall efficiency of the drive due to the fact that it generates low-harmonic currents comparing with SVPWM technique.

## **7.2 Future Works**

This thesis has considered control algorithms for IPMSM drives with accounting for machine non-linearity and inverter losses together with reduction the CMV. As always, there are many more interesting aspects that should be consider as future works

1. As the proposed control method for IPMSM depends on machine parameters and machine mathematical model, a search method using advance control techniques to determine the optimum operating point online without requirements of machine parameters and machine mathematical model in both the CTR and FWR regions are essential for future works. This is under studying by another PhD student.
2. Since it has been demonstrated that the Mod-LuPWM technique can reduce the CMV, its effects on the bearing current and the EMI should be further investigated.
3. The IPMSM drive is developed for traction applications where the DC-link voltage supplied by a battery pack may vary considerably during operations. 3D-LUTs may be used to take into consideration of this variation and provide another area for further improvement.
4. The proposed control method is based on vector control technique. As traction applications often require torque control, direct torque control techniques for IPMSM drives with non-linear parameter and minimum losses should be studied.
5. As the proposed control method based on torque control mode as this is often required by traction application, a drive system with speed control mode which may

apply to traction applications, in cruise control for example, is necessary for future work.



## Appendix A: Experimental Set Up

### A.1. Isolated Interface Layout

The layout of the isolated interface circuit (model number BP7B-LB) is shown in Figure A. 1 [97] where the three upper PWM signals ( $W_P$ ,  $V_P$ ,  $U_P$ ) and the three lower PWM signals ( $W_N$ ,  $V_N$ ,  $U_N$ ) are delivered to the input side of opto-couplers VLA606-01R via connector J2. This connector is supplied by a 5V/5A switching power supply.

The six output PWM signals of the opto-coupler are delivered to the utilised intelligent power module by the L-series intelligent power module connector J3. This connector is also used to deliver the fault signals of the upper switches ( $W_{Fo}$ ,  $V_{Fo}$ ,  $U_{Fo}$ ) and lower switches ( $Fo$ ). Three DC-DC converters VLA106-24151 supplied the upper PWM signals connector side. The lower PWM signal side is fed by one DC-DC converter VLA106-24154 or VLA106-24151. The connector J1 applies a 24/1A to the input side of these DC-DC converters.

### A.2. Layout of The CT's And VT's Measuring Board

The scaling measuring boards of the CTs and VTs are shown in Figure A. 3 where it is designed using the Protus program.

### A.3. PWM Dead Time and Inversion Boards

The PWM signals dead time and inversion board are depicted in Figure A. 2.

### A.4. dSPACE ADC to Simulink Interface BLOCKS

Figure A. 4 shows the DAC to Simulink model interface blocks. The input measuring signals of the CTs, VTs, encoder sin and cos signals, and the intelligent power module fault signal is delivered to the Simulink model using the Simulink block (model number DS2003\_B1) shown in Figure A. 4(a). The scaling between dSPACE and Simulink is done by multiplying all these measuring signals by 10.

The duty cycles of the three phases are delivered to the PWM card (DS5101) via the Simulink block shown in Figure A. 4(b) where scaling between Simulink and dSPACE is internally achieved by the dSPACE.

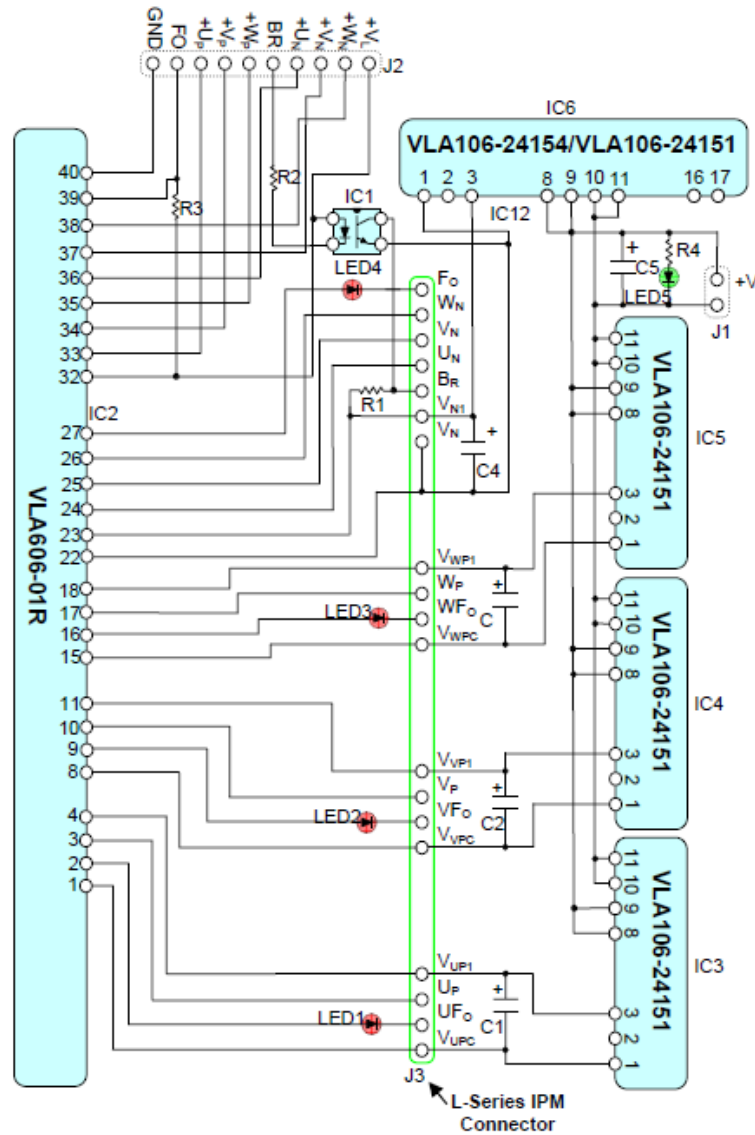


Figure A. 1 Isolated interface layout model BP7B-LB.

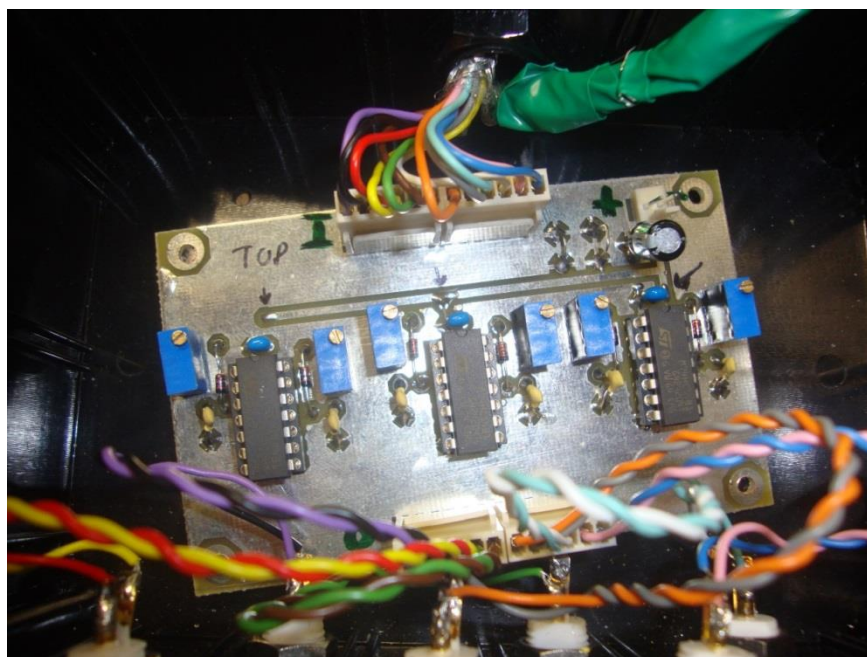


Figure A. 2 Complete circuit of the PWM signals dead time and inversion board.

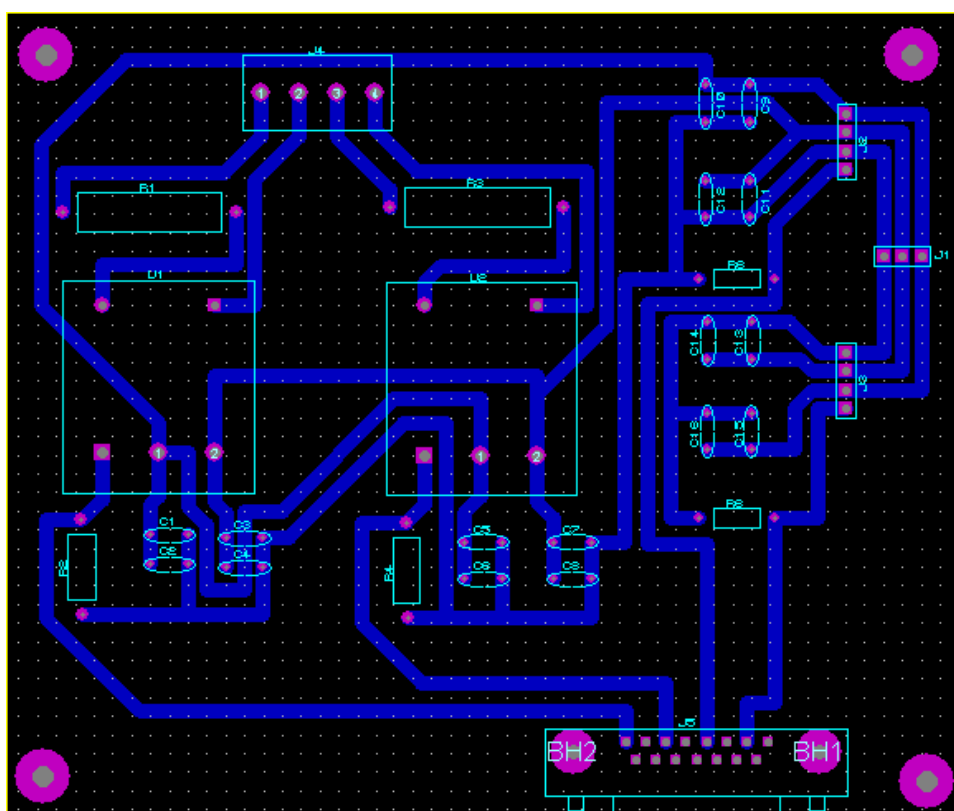


Figure A. 3 CTs and VTs scaling measuring board.

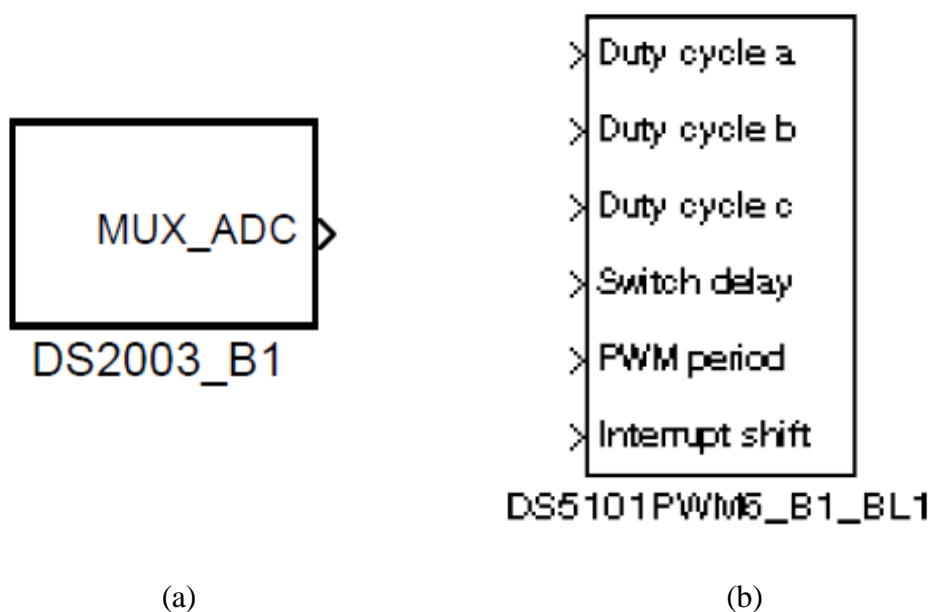


Figure A. 4 dSPACE Simulink interface blocks (a) input signal (b) PWM signals.

## Appendix B: Additional Experimental Results

### B.1. Encoder Signals

The encoder sin and cos signals, and the mechanical and electrical positions calculated by the utilised PLL are depicted in Figure B. 1 and Figure B. 2, respectively. These signals are obtained by the dSPACE control desk. The back-emf phase “a” of the IPMSM is aligned with electrical angular position as shown in Figure B. 3 which is obtained by the dSPACE control desk.

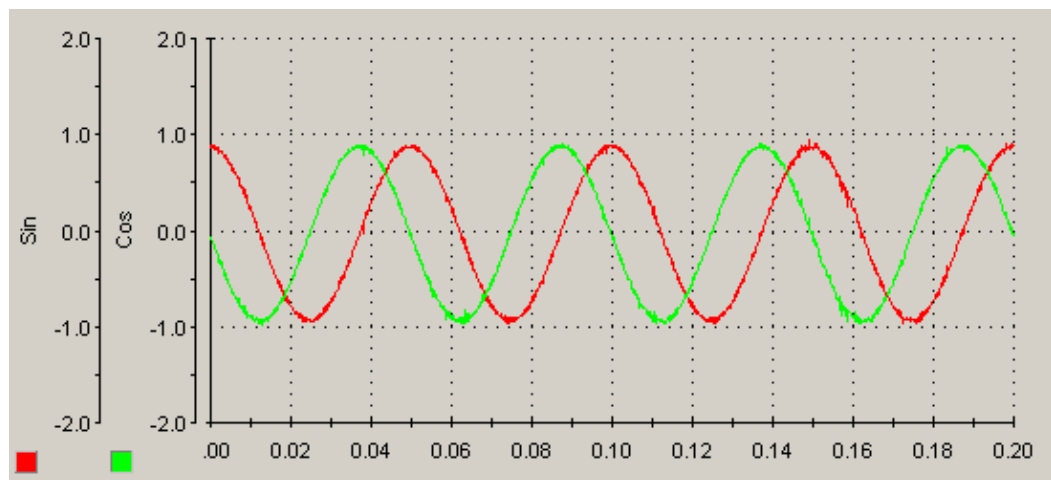


Figure B. 1 Encoder sin and cos signals.

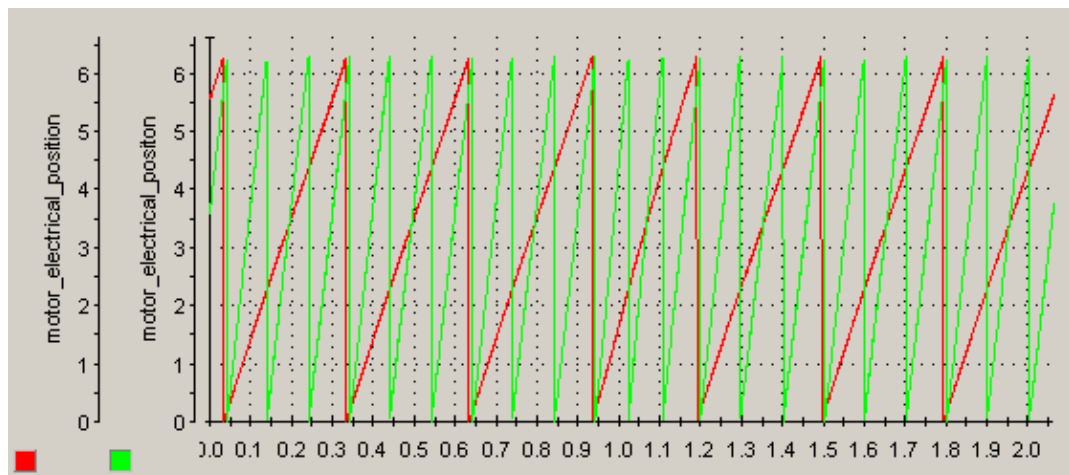


Figure B. 2 Electrical and mechanical position calculated by the PLL.

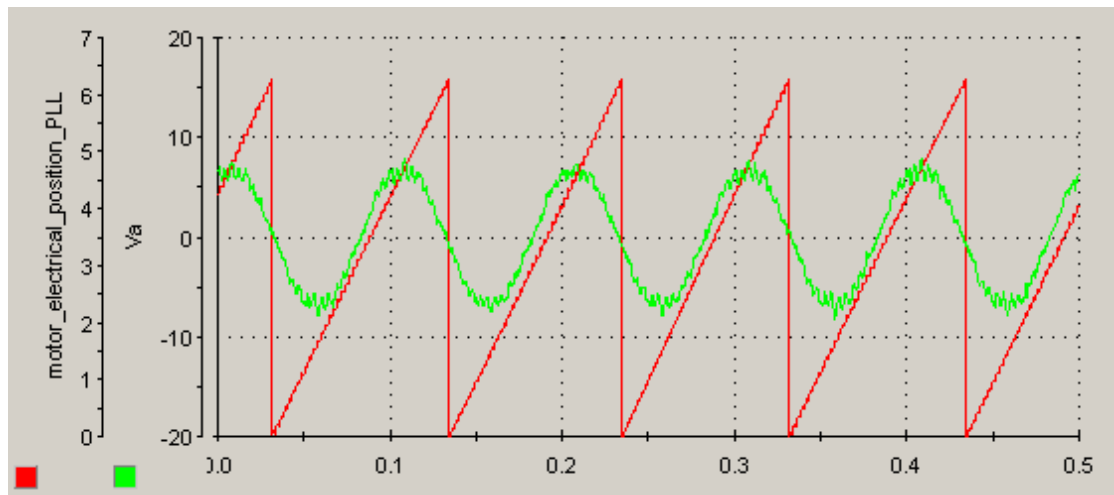


Figure B. 3 Alignment of back-emf phase “a” with the electrical angle.

## B.2. Inductive Load Results with SVPWM

Figure B. 4 and Figure B. 5 illustrate the voltage and current phases of the utilised inductive load with the SVPWM technique.

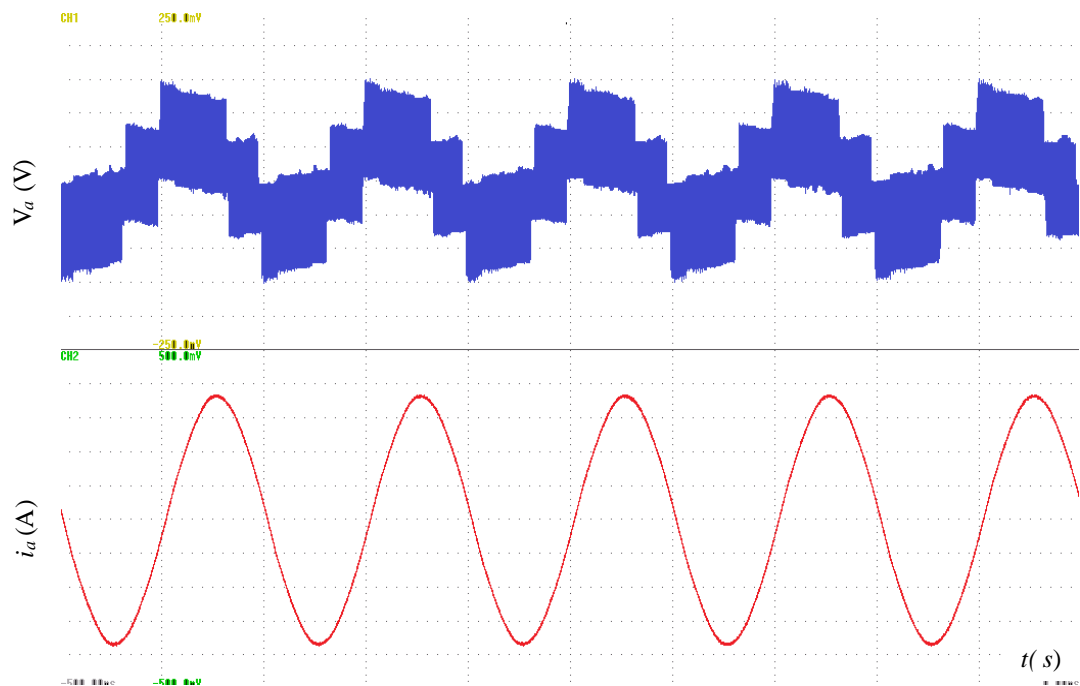


Figure B. 4 Voltage and current phases of the inductive load with SVPWM in the  $L$ -region.

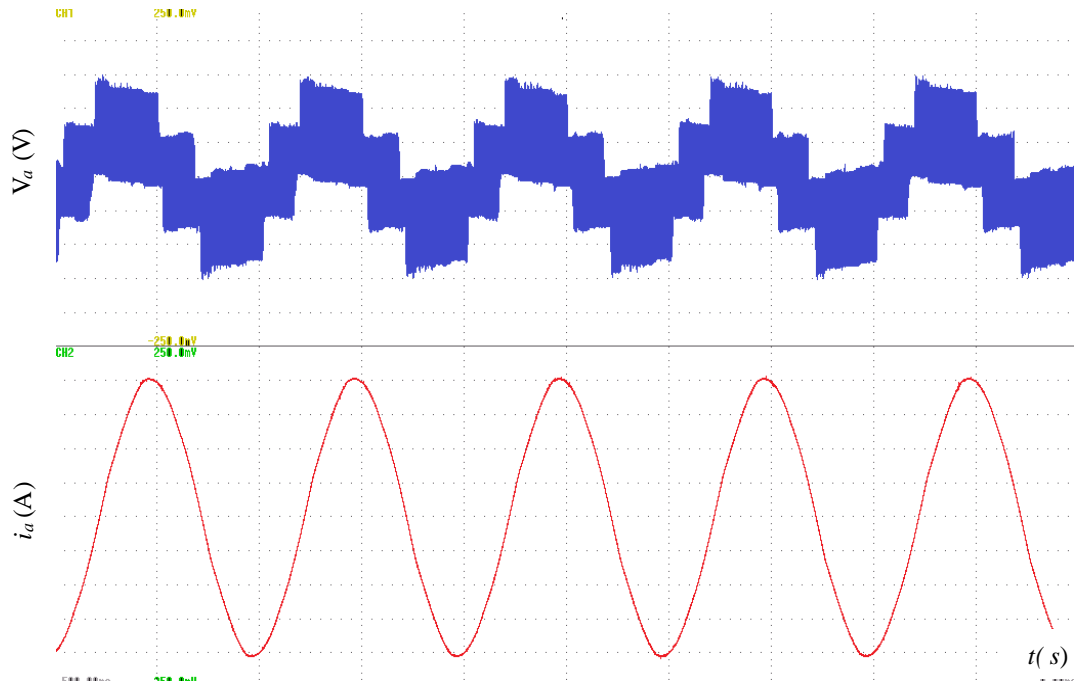


Figure B. 5 Voltage and current phases of the inductive load with LuPWM in the  $H$ -region.

### B.3. IPMSM Drive Results with SPWM Technique

The IPMSM drive is tested using the traditional sinusoidal PWM (SPWM) technique in the constant torque region before is driven by the SVPWM and LuPWM techniques in order to evaluate the test rig as SPWM technique is simple and easy to be implemented. Figure B. 6 and Figure B. 7 illustrate the d-and q-axis current, and the torque waveforms when a step torque is applied to the IPMSM drive.

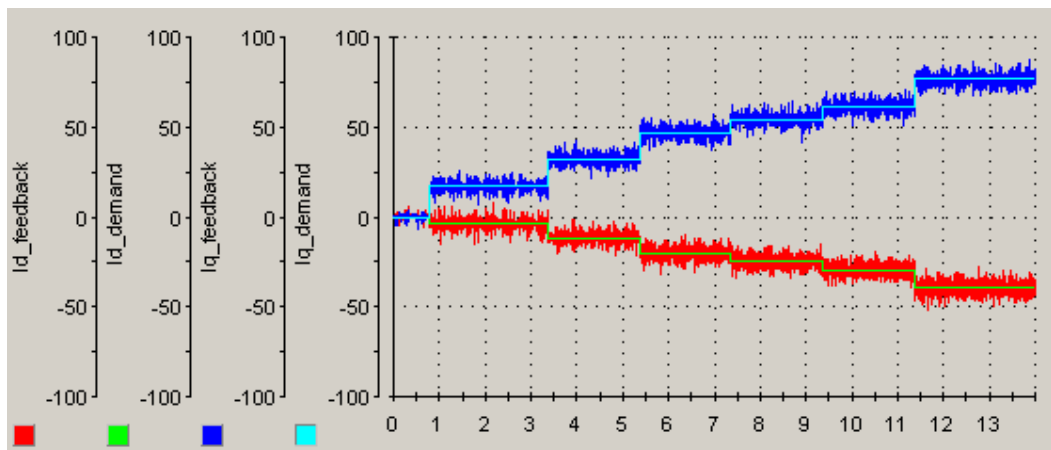


Figure B. 6  $i_d$  and  $i_q$  current waveforms of the IPMSM drive with SPWM.

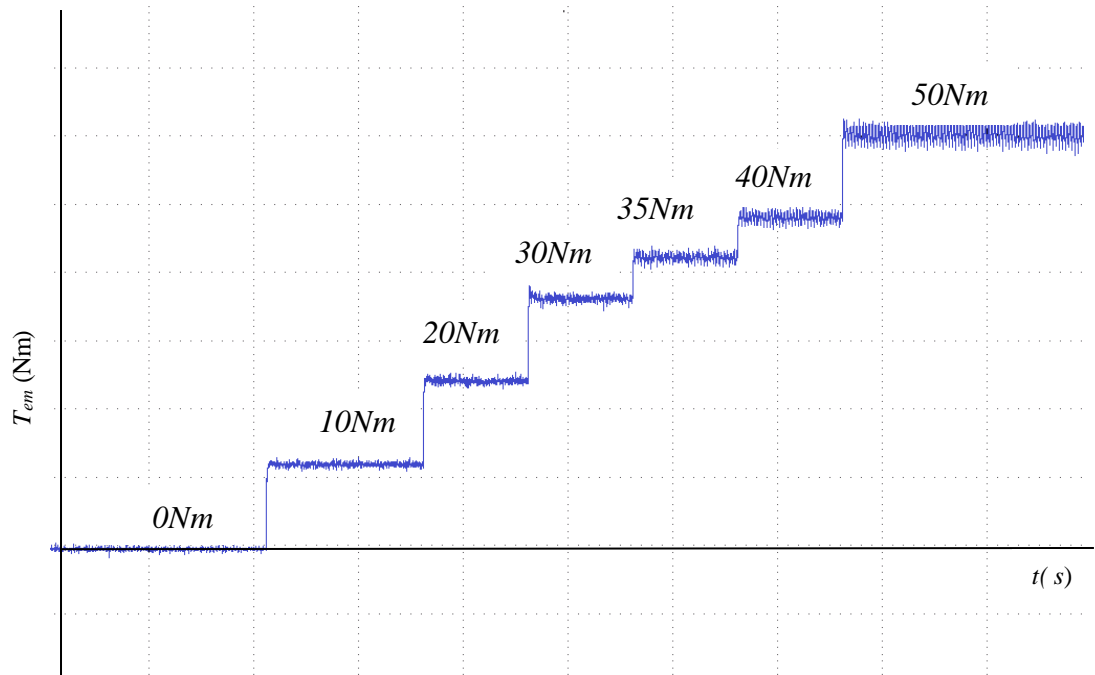


Figure B. 7 Torque waveforms of the IPMSM drive with SPWM.

#### B.4. IPMSM Drive Results with Negative Torque

The IPMSM drive is tested with a negative step torque is applied in the constant torque region. The obtained d-and q-axis current demands and torques are illustrated in Figure B. 8 and Figure B. 9 respectively. Again the results show smooth transient response and stable steady state response. The current demands are well-tracked by the well-tuned current controller.

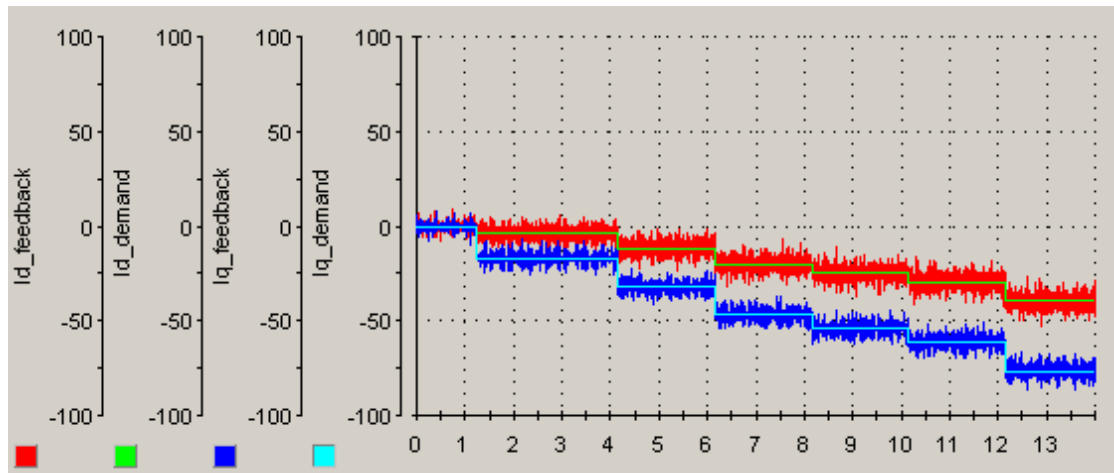


Figure B. 8  $i_d$  and  $i_q$  current of the IPMSM drive with SVPWM.



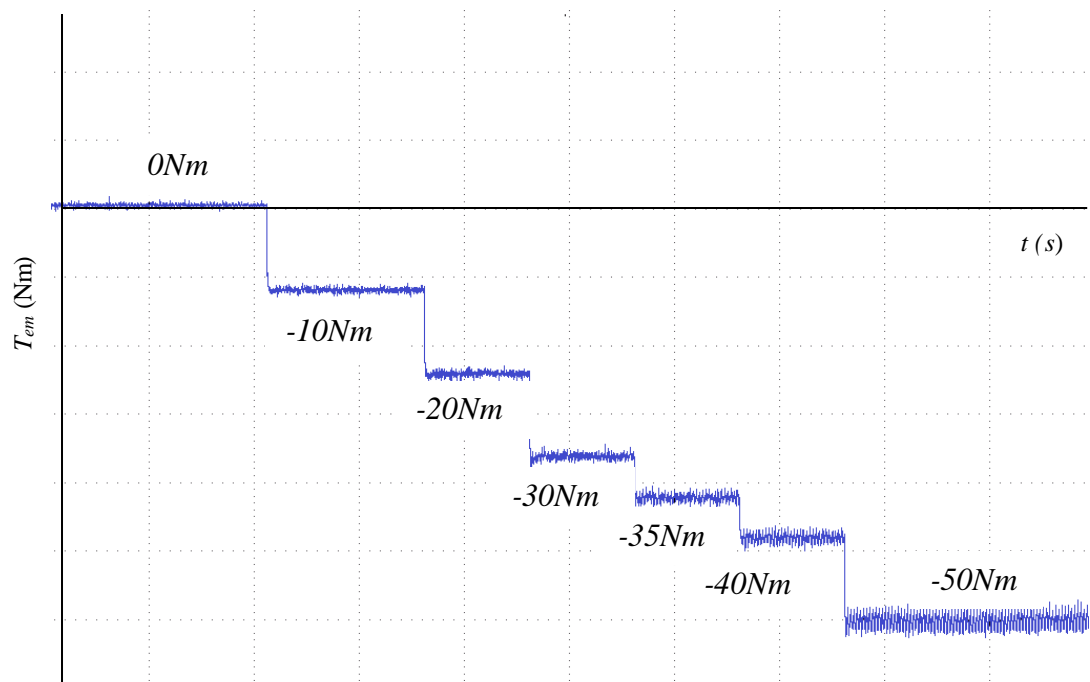


Figure B. 9 Negative torque waveforms of the IPMSM drive with SVPWM.

## Appendix C: LuPWM implementation

The LuPWM has been implemented successfully using DS1015 where the resultant pulse waveforms of phases  $a$ ,  $b$  and  $c$  are shown in Figure C. 1. The inverter legs output of the LuPWM in each sector in the low and high modulation region are shown in Figure C. 2 and Figure C. 3, respectively taken in consideration that these pulses are generated under open loop conditions.

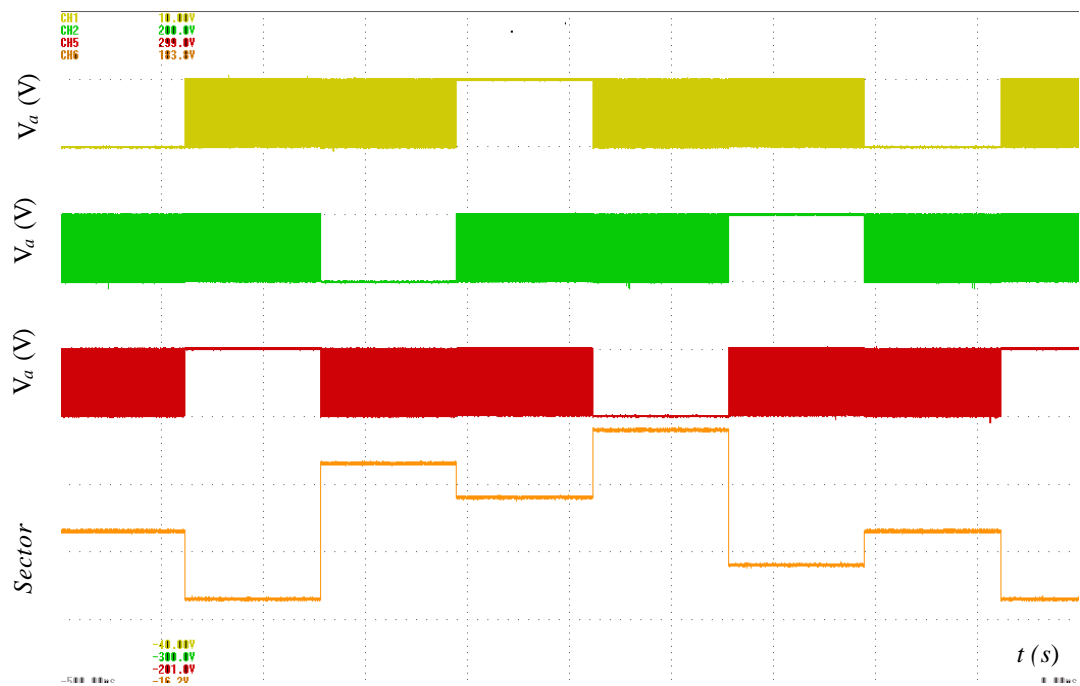


Figure C. 1 Phase  $a$ ,  $b$  and  $c$  inverter legs output voltages, and sector transition

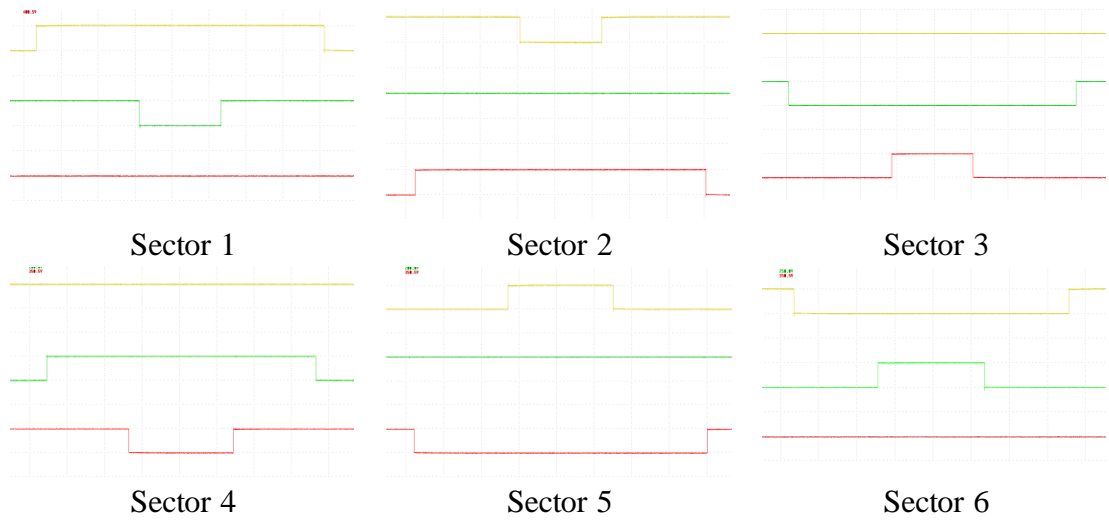


Figure C.2 Switching of low region sector 1 to 6

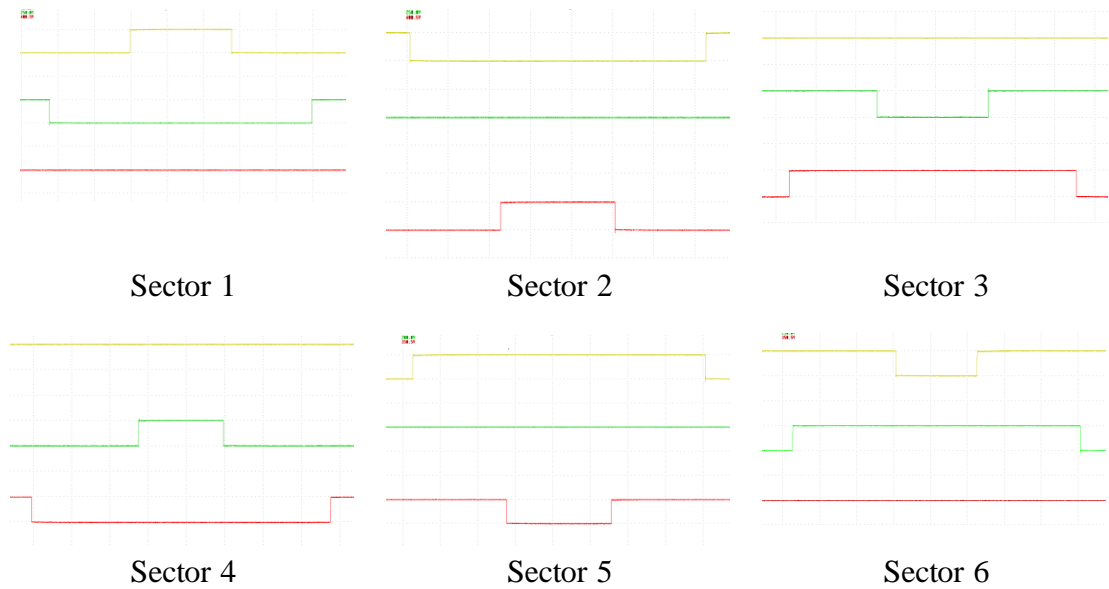


Figure C.3 Switching of high region sector 1 to 6

## References

- [1] S. Wahsh, "Past present future of electrical vehicle," in *Power System Conference, 2008. MEPCON 2008. 12th International Middle-East*, 2008, pp. 119-123.
- [2] S. Lixin, "Electric vehicle development: The past, present and future," in *Power Electronics Systems and Applications, 2009. PESA 2009. 3rd International Conference on*, 2009, pp. 1-3.
- [3] X. D. Xue, K. Cheng, and N. C. Cheung, "Selection of electric motor drives for electric vehicles," in *Power Engineering Conference, 2008. AUPEC '08. Australasian Universities*, 2008, pp. 1-6.
- [4] Toyota, "Toyota Prius 2004 ".
- [5] J. Wu-Shun and C. Wei-Liang, "Design and Implementation of a Charge Equalization Using Positive/Negative Pulse Charger," in *Industry Applications Conference, 2007. 42nd IAS Annual Meeting. Conference Record of the 2007 IEEE*, 2007, pp. 1076-1081.
- [6] T. Reddy, *Linden's handbook of batteries*, fourth ed. U.S: MCGraw-Hill Professional, 2010.
- [7] X. Wei, Z. Jianguo, G. Youguang, W. Shuhong, W. Yi, and S. Zhanghai, "Survey on electrical machines in electrical vehicles," in *Applied Superconductivity and Electromagnetic Devices, 2009. ASEMD 2009. International Conference on*, 2009, pp. 167-170.
- [8] M. Zeraoulia, M. E. H. Benbouzid, and D. Diallo, "Electric motor drive selection issues for HEV propulsion systems: A comparative study," *Vehicular Technology, IEEE Transactions on*, vol. 55, pp. 1756-1764, 2006.
- [9] K. T. Chau, C. C. Chan, and L. Chunhua, "Overview of permanent-magnet brushless drives for electric and hybrid electric vehicles," *Industrial Electronics, IEEE Transactions on*, vol. 55, pp. 2246-2257, 2008.
- [10] L. Chang, "Comparison of AC drives for electric vehicles-a report on experts' opinion survey," *Aerospace and Electronic Systems Magazine, IEEE*, vol. 9, pp. 7-11, 1994.

- [11] J. R. Hendershot and T. J. E. Miller, *Design of brushless permanent-magnet motors*. United States: Magna Physics 1994.
- [12] K. D. Hoang, "Direct and indirect torque control of low-cost and fault-tolerant permanent magnet brushless AC drives," in *Department of Electronic and Electrical Engineering*. vol. PhD UK: University of Sheffield, 2011.
- [13] G. Ledwich, "Current source inverter modulation," *Power Electronics, IEEE Transactions on*, vol. 6, pp. 618-623, 1991.
- [14] D. Ke, L. Peiguo, X. Jian, and C. Jian, "Comparative study on current control for three-phase SVPWM voltage-source converter in synchronous rotating frame using complex vector method," in *Power Electronics Specialist Conference, 2003. PESC '03. 2003 IEEE 34th Annual*, 2003, pp. 695-700 vol.2.
- [15] E. P. Wiechmann, P. Aqueveque, R. Burgos, and J. Rodriguez, "On the efficiency of voltage source and current source inverters for high-power drives,," *Industrial Electronics, IEEE Transactions on*, vol. 55, pp. 1771-1782, 2008.
- [16] N. Mohan, T. M. Undeland, and P. R. Robbins, *Power electronics converters, applications and design*. United State: John Wiley and Sons, Inc, 2003.
- [17] A. M. Hava, R. J. Kerkman, and T. A. Lipo, "Simple analytical and graphical methods for carrier-based PWM-VSI drives," *Power Electronics, IEEE Transactions on*, vol. 14, pp. 49-61, 1999.
- [18] A. Iqbal, A. Lamine, I. Ashraf, and Mohibullah, "Matlab/Simulink model of space vector PWM for three-phase voltage source inverter," in *Universities Power Engineering Conference, 2006. UPEC '06. Proceedings of the 41st International*, 2006, pp. 1096-1100.
- [19] L. Dongyun and N. C. Kar, "A review of flux-weakening control in permanent magnet synchronous machines," in *Vehicle Power and Propulsion Conference (VPPC), 2010 IEEE*, pp. 1-6.
- [20] S. Morimoto, Y. Takeda, T. Hirasaka, and K. Taniguchi, "Expansion of operating limits for permanent magnet motor by current vector control considering inverter capacity," *Industry Applications, IEEE Transactions on*, vol. 26, pp. 866-871, 1990.
- [21] B. K. Bose, *Prentice hall-modern power electronics and AC drives*. United States of America: Prentice Hall PTR, 2002.

- [22] R. H. Park, "Two-reaction theory of synchronous machines, generalized method of analysis, Part I," *AIEE*, pp. 716-730, 1929.
- [23] P. C. Krause and C. H. Thomas, "Simulation of symmetrical induction machinery," *IEEE Trans. Power App. Sys*, vol. PAS.84, pp. 1938-1953, 1965.
- [24] T. M. Jahns, G. E. Kliman, and T. W. Neumann, "Interior permanent magnet synchronous motors for adjustable-speed drive," *IEEE Trans. Ind. Appl*, vol. IA-22, pp. 738-747, 1986.
- [25] F. Zidani, M. Nait-Said, R. Abdessemed, and A. Benoudjit, "Comparative study by numerical simulation of induction machine performances in vector and scalar control," in *System Theory, 1998. Proceedings of the Thirtieth Southeastern Symposium on*, 1998, pp. 483-487.
- [26] P. T. Krein, F. Disilvestro, I. Kanellakopoulos, and J. Locker, "Comparative analysis of scalar and vector control methods for induction motors," in *Power Electronics Specialists Conference, 1993. PESC '93 Record., 24th Annual IEEE*, 1993, pp. 1139-1145.
- [27] C. Wei, K. T. Chau, J. Z. Jiang, Y. Fan, and Z. Wang, "Scalar control of a new phase-decoupling permanent magnet synchronous motor for servo application," in *Industry Applications Conference, 2005. Fourtieth IAS Annual Meeting. Conference Record of the 2005*, 2005, pp. 1762-1769 Vol. 3.
- [28] M. F. Rahman, L. Zhong, and K. W. Lim, "A direct torque controlled interior permanent magnet synchronous motor drive incorporating field weakening," in *Industry Applications Conference, 1997. Thirty-Second IAS Annual Meeting, IAS '97., Conference Record of the 1997 IEEE*, 1997, pp. 67-74 vol.1.
- [29] B. Chunyuan, R. Shuangyan, and M. Liangyu, "Study on Direct Torque Control of Super High-speed PMSM," in *Automation and Logistics, 2007 IEEE International Conference on*, 2007, pp. 2711-2715.
- [30] L.-H. Hoang, "Comparison of field-oriented control and direct torque control for induction motor drives," in *Industry Applications Conference, 1999. Thirty-Fourth IAS Annual Meeting. Conference Record of the 1999 IEEE*, 1999, pp. 1245-1252 vol.2.
- [31] B. Bossoufi, M. Karim, A. Lagrioui, and S. Ionit, "Performance analysis of direct torque control (DTC) for synchronous machine permanent magnet

- (PMSM)," in *Design and Technology in Electronic Packaging (SIITME)*, 2010 *IEEE 16th International Symposium for*, 2010, pp. 237-242.
- [32] G. Pfaff, A. Weschta, and A. F. Wick, "Design and experimental results of a brushless AC servo drive," *IEEE Tran. Ind. Appl*, vol. IA-20, pp. 814-821, 1984.
- [33] P. Pillay and R. Krishnan, "Modelling, simulation, and analysis of permanent-magnet motor drives, part I: the permanent-magnet synchronous motor drive," *IEEE Trans. Ind. Appl*, vol. 25, pp. 265-273, 1989.
- [34] S. Morimoto, M. Sanada, and Y. Takeda, "Wide-speed operation of interior permanent magnet synchronous motors with high-performance current," *Industry Applications, IEEE Transactions on*, vol. 30, pp. 920-926, 1994.
- [35] M. Tursini, E. Chiricozzi, and R. Petrella, "Feedforward flux-weakening control of surface-mounted permanent-magnet synchronous motors accounting for resistive voltage drop," *Industrial Electronics, IEEE Transactions on*, vol. 57, pp. 440-448, 2010.
- [36] Z. Xin and L. Hui, "Flux-weakening control of permanent magnet synchronous motor using in electric vehicles," in *Power Electronics and Motion Control Conference, 2009. IPEMC '09. IEEE 6th International*, 2009, pp. 1050-1054.
- [37] M. M. Islam Chy and M. N. Uddin, "Analysis of flux control for wide speed range operation of IPMSM drive," in *Power Engineering, 2007 Large Engineering Systems Conference on*, 2007, pp. 256-260.
- [38] D. Jiang, D. Zhu, X. Jiang, M. Seto, M. Kimata, A. Satake, and S. Azuma, "Research of control system of permanent magnet brushless synchronous motor for EV," in *Power Electronics and Motion Control Conference, 2000. Proceedings. IPEMC 2000. The Third International*, 2000, pp. 353-358 vol.1.
- [39] K. Jang-Mok, P. Kitae, K. Seog-Joo, S. Seung-Ki, and K. Jung-Lock, "Improved dynamic performance of interior permanent magnet synchronous motor drive in flux-weakening operation," in *Power Electronics Specialists Conference, 1996. PESC '96 Record., 27th Annual IEEE*, 1996, pp. 1562-1567 vol.2.
- [40] S. D. Sudhoff, K. A. Corzine, and H. J. Hegner, "A flux-weakening strategy for current-regulated surface-mounted permanent-magnet machine drives," *Energy Conversion, IEEE Transactions on*, vol. 10, pp. 431-437, 1995.

- [41] D. S. Maric, S. Hiti, C. C. Stancu, and J. M. Nagashima, "Two improved flux weakening schemes for surface mounted permanent magnet synchronous machine drives employing space vector modulation," in *Industrial Electronics Society, 1998. IECON '98. Proceedings of the 24th Annual Conference of the IEEE*, 1998, pp. 508-512 vol.1.
- [42] D. S. Maric, S. Hiti, C. C. Stancu, J. M. Nagashima, and D. B. Rutledge, "Two flux weakening schemes for surface-mounted permanent-magnet synchronous drives. Design and transient response considerations," in *Industrial Electronics, 1999. ISIE '99. Proceedings of the IEEE International Symposium on*, 1999, pp. 673-678 vol.2.
- [43] S. Jong-Hwan, K. Jang-Mok, and S. Seung-Ki, "A new robust SPMSM control to parameter variations in flux weakening region," in *Industrial Electronics, Control, and Instrumentation, 1996., Proceedings of the 1996 IEEE IECON 22nd International Conference on*, 1996, pp. 1193-1198 vol.2.
- [44] K. Jang-Mok and S. Seung-Ki, "Speed control of interior permanent magnet synchronous motor drive for the flux weakening operation," *Industry Applications, IEEE Transactions on*, vol. 33, pp. 43-48, 1997.
- [45] Y. Young-Doo and S. Seung-Ki, "New flux weakening control for surface mounted permanent magnet synchronous machine using gradient descent method," in *Power Electronics, 2007. ICPE '07. 7th International Conference on*, 2007, pp. 1208-1212.
- [46] J. Simanek, J. Novak, O. Cerny, and R. Dolecek, "FOC and flux weakening for traction drive with permanent magnet synchronous motor," in *Industrial Electronics, 2008. ISIE 2008. IEEE International Symposium on*, 2008, pp. 753-758.
- [47] B. Bon-Ho, N. Patel, S. Schulz, and S. Seung-Ki, "New field weakening technique for high saliency interior permanent magnet motor," in *Industry Applications Conference, 2003. 38th IAS Annual Meeting. Conference Record of the*, 2003, pp. 898-905 vol.2.
- [48] R. U. Lenke, R. W. De Doncker, K. Mu-Shin, K. Tae-Suk, and S. Seung-Ki, "Field weakening control of interior permanent magnet machine using improved



- current interpolation technique," in *Power Electronics Specialists Conference, 2006. PESC '06. 37th IEEE*, 2006, pp. 1-5.
- [49] K. Tae-Suk and S. Seung-Ki, "Novel Antiwindup of a Current Regulator of a Surface-Mounted Permanent-Magnet Motor for Flux-Weakening Control," *Industry Applications, IEEE Transactions on*, vol. 42, pp. 1293-1300, 2006.
- [50] L. Ping-Yi and L. Yen-Shin, "Novel voltage trajectory control for flux weakening operation of surface mounted PMSM drives," in *Industry Applications Society Annual Meeting, 2008. IAS '08. IEEE*, 2008, pp. 1-8.
- [51] K. Tae-Suk, C. Gi-Young, K. Mu-Shin, and S. Seung-Ki, "Novel flux-weakening control of an IPMSM for quasi-six-step operation," *Industry Applications, IEEE Transactions on*, vol. 44, pp. 1722-1731, 2008.
- [52] R. Dolecek, J. Simanek, J. Novak, and O. Cerny, "Dynamics of a feedback optimal-current-vector flux-weakening strategy for traction permanent-magnet synchronous motors," in *Advanced Electromechanical Motion Systems & Electric Drives Joint Symposium, 2009. ELECTROMOTION 2009. 8th International Symposium on*, 2009, pp. 1-6.
- [53] C. Gi-Young, K. Mu-Shin, K. Tae-Suk, and S. Seung-Ki, "Novel flux-Weakening control of an IPMSM for quasi six-step operation," in *Industry Applications Conference, 2007. 42nd IAS Annual Meeting. Conference Record of the 2007 IEEE*, 2007, pp. 1315-1321.
- [54] G. Gallegos-Lopez, F. S. Gunawan, and J. E. Walters, "Optimum torque control of permanent-magnet AC Machines in the field-weakened region," *Industry Applications, IEEE Transactions on*, vol. 41, pp. 1020-1028, 2005.
- [55] G. Gallegos-Lopez and S. Hiti, "Optimum Current Control in the Field-Weakened Region for Permanent Magnet AC Machines," in *Industry Applications Conference, 2007. 42nd IAS Annual Meeting. Conference Record of the 2007 IEEE*, 2007, pp. 2154-2160.
- [56] S. Bolognani, S. Calligaro, R. Petrella, and F. Pogni, "Flux-weakening in IPM motor drives: Comparison of state-of-art algorithms and a novel proposal for controller design," in *Power Electronics and Applications (EPE 2011), Proceedings of the 2011-14th European Conference on*, pp. 1-11.

- [57] C. Mademlis, J. Xypteras, and N. Margaris, "Loss minimization in surface permanent-magnet synchronous motor drives," *Industrial Electronics, IEEE Transactions on*, vol. 47, pp. 115-122, 2000.
- [58] C. Mademlis, I. Kioskeridis, and N. Margaris, "Optimal efficiency control strategy for interior permanent-magnet synchronous motor drives," *Energy Conversion, IEEE Transactions on*, vol. 19, pp. 715-723, 2004.
- [59] L. Junggi, N. Kwanghee, C. Seoho, and K. Soonwoo, "Loss-minimizing control of PMSM with the use of polynomial approximations," *Power Electronics, IEEE Transactions on*, vol. 24, pp. 1071-1082, 2009.
- [60] S. Morimoto, Y. Tong, Y. Takeda, and T. Hirasu, "Loss minimization control of permanent magnet synchronous motor drives," *Industrial Electronics, IEEE Transactions on*, vol. 41, pp. 511-517, 1994.
- [61] O. Solomon and P. Famouri, "Control and efficiency optimization strategy for permanent magnet brushless AC motors," in *Industrial Electronics, 2009. ISIE 2009. IEEE International Symposium on*, 2009, pp. 505-512.
- [62] M. N. Uddin and F. Abera, "Online loss minimization based vector control of IPMSM drive," in *Electric Machines and Drives Conference, 2009. IEMDC '09. IEEE International*, 2009, pp. 30-35.
- [63] C. Mademlis and N. Margaris, "Loss minimization in vector-controlled interior permanent-magnet synchronous motor drives," *Industrial Electronics, IEEE Transactions on*, vol. 49, pp. 1344-1347, 2002.
- [64] C. Cavallaro, A. O. Di Tommaso, R. Miceli, A. Raciti, G. R. Galluzzo, and M. Trapanese, "Efficiency enhancement of permanent-magnet synchronous motor drives by online loss minimization approaches," *Industrial Electronics, IEEE Transactions on*, vol. 52, pp. 1153-1160, 2005.
- [65] S. Vaez, V. I. John, and M. A. Rahman, "An on-line loss minimization controller for interior permanent magnet motor drives," *Energy Conversion, IEEE Transactions on*, vol. 14, pp. 1435-1440, 1999.
- [66] M. Nasir Uddin and B. Patel, "Loss minimization control of interior permanent magnet synchronous motor drive using adaptive backstepping technique," in *Industry Applications Society Annual Meeting, 2013 IEEE*, 2013, pp. 1-7.

- [67] K. Hyunbae, J. Hartwig, and R. D. Lorenz, "Using on-line parameter estimation to improve efficiency of IPM machine drives," in *Power Electronics Specialists Conference, 2002. pesc 02. 2002 IEEE 33rd Annual*, 2002, pp. 815-820 vol.2.
- [68] Y. A. R. I. Mohamed and T. K. Lee, "Adaptive self-tuning MTPA vector controller for IPMSM drive system," *Energy Conversion, IEEE Transactions on*, vol. 21, pp. 636-644, 2006.
- [69] P. Niazi, H. A. Toliyat, and A. Goodarzi, "Robust maximum torque per ampere (MTPA) control of PM-assisted synRM for traction applications," *Vehicular Technology, IEEE Transactions on*, vol. 56, pp. 1538-1545, 2007.
- [70] K. Sungmin, Y. Young-Doo, S. Seung-Ki, K. Ide, and K. Tomita, "Parameter independent maximum torque per ampere (MTPA) control of IPM machine based on signal injection," in *Applied Power Electronics Conference and Exposition (APEC), 2010 Twenty-Fifth Annual IEEE*, 2010, pp. 103-108.
- [71] Y. Dejun, O. Sehoon, and Y. Hori, "A novel traction control for EV based on maximum transmissible torque estimation," *Industrial Electronics, IEEE Transactions on*, vol. 56, pp. 2086-2094, 2009.
- [72] W. Jiabin and D. Howe, "Design optimization of radially magnetized, iron-cored, tubular permanent-magnet machines and drive systems," *Magnetics, IEEE Transactions on*, vol. 40, pp. 3262-3277, 2004.
- [73] M. Rafiq, F.-U.-H. Mohammed, M. Yaqoob, and T. Thiringer, "Analysis of power losses and efficiency up to 60 kW DC-DC converter for hybrid electric vehicle with different inductive core materials," in *Industrial Electronics (ISIE), 2013 IEEE International Symposium on*, 2013, pp. 1-5.
- [74] F. Abrahamsen, F. Blaabjerg, J. K. Pedersen, and P. B. Thøgersen, "Efficiency-optimized control of medium-size induction motor drives," *Industry Applications, IEEE Transactions on*, vol. 37, pp. 1761-1767, 2001.
- [75] A. M. Hava and E. Un, "Performance analysis of reduced common-mode voltage PWM methods and comparison with standard PWM methods for three-phase voltage-source inverters," *Power Electronics, IEEE Transactions on*, vol. 24, pp. 241-252, 2009.

- [76] C. Xiaomeng, Q. Wenlong, L. Haifeng, and F. Yang, "An improved two-phase PWM strategy for inverters in electric vehicle," in *Vehicle Power and Propulsion Conference, 2008. VPPC '08. IEEE*, 2008, pp. 1-5.
- [77] Z. Yonggao, G. Yanli, and L. Lizhong, "Study on a common-mode voltage suppression method with high performance for the three-level diode-clamped inverter," in *Industrial Electronics (ISIE), 2012 IEEE International Symposium on*, 2012, pp. 539-544.
- [78] H. W. Van der Broeck, H. C. Skudelny, and G. V. Stanke, "Analysis and realization of a pulsewidth modulator based on voltage space vectors," *Industry Applications, IEEE Transactions on*, vol. 24, pp. 142-150, 1988.
- [79] E. Un and A. M. Hava, "A Near-state PWM method with reduced switching losses and reduced common-mode voltage for three-phase voltage source inverters," *Industry Applications, IEEE Transactions on*, vol. 45, pp. 782-793, 2009.
- [80] L. Haifeng, Q. Wenlong, C. Xiaomeng, F. Yang, and Z. Xing, "A Novel PWM Technique With Two-Phase Modulation," *Power Electronics, IEEE Transactions on*, vol. 22, pp. 2403-2409, 2007.
- [81] P. H. Mellor, R. Wrobel, and D. Holliday, "A computationally efficient iron loss model for brushless AC machines that caters for rated flux and field weakened operation," in *Electric Machines and Drives Conference, 2009. IEMDC '09. IEEE International*, 2009, pp. 490-494.
- [82] J. Goss, P. H. Mellor, R. Wrobel, D. A. Staton, and M. Popescu, "The design of AC permanent magnet motors for electric vehicles: A computationally efficient model of the operational envelope," in *Power Electronics, Machines and Drives (PEMD 2012), 6th IET International Conference on*, pp. 1-6.
- [83] H. Lu, X. Cheng, W. Qu, X. Zhang, and Y. Fan, "A new PWM strategy to reduce the common-mode voltage," in *TENCON 2006. 2006 IEEE Region 10 Conference*, 2006, pp. 1-4.
- [84] S. Tunyasirirut, S. Srilad, and T. Suksri, "Comparison power quality of the voltage source inverter type SVPWM and SPWM technique for induction motor drive," in *SICE Annual Conference, 2008*, 2008, pp. 241-246.

- [85] G. Oriti, A. L. Julian, and T. A. Lipo, "A new space vector modulation strategy for common mode voltage reduction [in PWM invertors]," in *Power Electronics Specialists Conference, 1997. PESC '97 Record., 28th Annual IEEE, 1997*, pp. 1541-1546 vol.2.
- [86] L. Yen-Shin and S. Fu-San, "Optimal common-mode Voltage reduction PWM technique for inverter control with consideration of the dead-time effects-part I: basic development," *Industry Applications, IEEE Transactions on*, vol. 40, pp. 1605-1612, 2004.
- [87] L. Yen-Shin, C. Po-Sheng, L. Hsiang-Kuo, and J. Chou, "Optimal common-mode voltage reduction PWM technique for inverter control with consideration of the dead-time effects-part II: applications to IM drives with diode front end," *Industry Applications, IEEE Transactions on*, vol. 40, pp. 1613-1620, 2004.
- [88] N. O. Cetin and A. M. Hava, "Scalar PWM implementation methods for three-phase three-wire inverters," in *Electrical and Electronics Engineering, 2009. ELECO 2009. International Conference on*, 2009, pp. I-447-I-451.
- [89] P. K. Pillay, R., "Modeling of permanent magnet motor drive," *on Industrial Electronics, IEEE Transactions*, vol. 35, pp. 537-541, 1988.
- [90] D. Y. Ohm, "Dynamic model of M synchronous motors ": Drivetech, Inc., Blacksburg, Virginia, [www.drivetechinc.com](http://www.drivetechinc.com).
- [91] H. Aorith, J. Wang, and P. Lazari, "A new loss minimization algorithm for interior ermanent magnet synchronous machine drives," in *Electric Machines & Drives Conference (IEMDC), 2013 IEEE International*, 2013, pp. 526-533.
- [92] S. Dwivedi and B. Singh, "Vector control vs direct torque control comparative evaluation for PMSM drive," in *Power Electronics, Drives and Energy Systems (PEDES) & 2010 Power India, 2010 Joint International Conference on*, pp. 1-8.
- [93] B. A. Welchko, S. E. Schulz, and S. Hiti, "Effects and compensation of dead-time and minimum pulse-width limitations in two-level PWM voltage source inverters," in *Industry Applications Conference, 2006. 41st IAS Annual Meeting. Conference Record of the 2006 IEEE*, 2006, pp. 889-896.
- [94] A. M. Hava, R. J. Kerkman, and T. A. Lipo, "A high-performance generalized discontinuous PWM algorithm," *Industry Applications, IEEE Transactions on*, vol. 34, pp. 1059-1071, 1998.

- [95] A. M. Hava, x, and N. O. etin, "A generalized scalar PWM approach with easy implementation features for three-phase, three-wire voltage-source inverters," *Power Electronics, IEEE Transactions on*, vol. 26, pp. 1385-1395, 2011.
- [96] Misubishi, "PM300CLA060," 2012, <http://www.datasheeteeltib.com>.
- [97] Powerex, "BP7B-LB," 2012, <http://www.datasheeteeltib.com>.
- [98] RLS, "AM256D01\_10," <http://resouces.renishaw.com/en/download/data-sheet-am256-rotary-magnetic-encoder-ic--48868>.
- [99] V. Kaura and V. Blasko, "Operation of a phase locked loop system under distorted utility conditions," *Industry Applications, IEEE Transactions on*, vol. 33, pp. 58-63, 1997.
- [100] R. W. Erickson, "Power and RMS values of fourier series." vol. 2014.